

Comb based Optical Signal Processing



Zihan Geng

B. ENG Monash University & Central South University

This dissertation is submitted for the degree of Doctor of Philosophy at

Monash University

Department of Electrical and Computer Systems Engineering,

Monash University, Clayton, Australia

October 2018

I would like to dedicate this thesis to my loving parents Hongmei Nan and Qi Geng.

Declaration and Copyright

I hereby declare that this dissertation is written by myself and it has not been submitted for any other degree or qualification at any university or equivalent institution. Most of this dissertation is original, and all the contents that are the work of others have been clearly stated in the dissertation.

© Zihan Geng 2018.

I certify that I have made all reasonable efforts to secure copyright permissions for third-party content included in this thesis and have not knowingly added copyright content to my work without the owner's permission.

Zihan Geng
October 2018

Acknowledgements

I would like to acknowledge my main supervisor, professor Arthur Lowery, for all he has contributed to my research. You are highly knowledgeable and experienced in optical communications. You support us to do research in a bright and spacious laboratory full of cutting-edge equipment. You read my paper drafts and offered me valuable feedback. You showed me the way to the world of leading technologies and outstanding people.

I also want to acknowledge my vice supervisor, Dr. Bill Corcoran for his great support to my research. You motivated and instructed me in most of my research work, and your passion for research encourages me to pursue knowledge.

To Arthur's post-doctoral research fellows - Dr. Deming Kong, Dr. Leimeng Zhuang, Dr. Chen Zhu and Dr. Valery Rozental, you helped me to troubleshoot my experiments whenever I had a problem. You invited me to join your research and helped me to learn more.

To my seniors, Dr. Monir Morshed, Dr. Benjamin Foo, Ms. Yiwei Xie, Mr. Binhuang Song, Mr. Qibing Wang, Mr. Jignesh Jokhakar and my junior Mr. Tianyu Wang. We spent a great time doing research together and helped each other. You are an awesome group of people to work with.

To people I worked with in Technical University of Denmark - Dr. Pengyu Guan, Dr. Francesco da Ros, Dr. Edson Porto da Silva, Dr. Leif Katso Oxenlowe and Dr. Hao Hu. Thank you for assisting my research and helping me to fit in life in Denmark.

I would like to acknowledge Australian Research Council's Centre of Excellence in ultra-high bandwidth devices for optical systems, CUDOS (CE110001018), ARC Laureate Fellowship (FL130100041) schemes and Monash University for funding my research.

Finally, to my parents, Hongmei Nan and Qi Geng. You gave me my life and raise me up. You encouraged me, supported me for years. My appreciation goes beyond words.

Abstract

Because of the increasing use of video content, penetration of mobile devices and growth in the demand for cloud computing, data traffic has been growing tremendously in recent years. Digital signal processing (DSP) based on electronics provides a substantial portion of signal processing in optical communications. However, electronic devices are facing challenges in terms of bandwidth and latency in high capacity networks.

Optical signal processing (OSP) takes advantage of the physical properties of optical elements to manipulate optical signals, so it saves the effort of optical-to-electrical-optical (O-E-O) conversions. Unlike DSP, which processes each channel bit-by-bit, OSP is capable of simultaneously processing multiple channels over a wide bandwidth with a negligible delay. Thus, OSP can be used to work around the limitations of electronics, potentially providing signal processing with high capacity, low latency and low power consumption [1].

To harness the ultra-broadband potential of OSP, optical frequency combs provide a key resource. An optical frequency comb is composed of evenly spaced spectral lines. For OSP applications, the advantages of optical frequency combs are the broadband coverage and the coherence among frequency comb lines.

This thesis explores new applications of frequency comb-based OSP to overcome the limitations of electronics devices, providing photonic alternatives or enhancements to improve tomorrow's communication systems.

Table of contents

1	Introduction	1
1.1	Topic and motivation	1
1.2	Fiber-optic communications background	2
1.3	Optical signal processing	5
1.4	OSP and DSP	6
1.5	Study objectives	6
1.6	Original contributions	7
1.7	Thesis structure	8
1.8	Publications	10
2	Optical signal processing fundamentals	13
2.1	OSP based on nonlinear optics	14
2.1.1	Second-order susceptibility	15
2.1.2	Third-order susceptibility	18
2.2	OSP based on linear optics	21
2.2.1	FIR filters based on Mach-Zehnder interferometers	21
2.2.2	IIR filters based on ring resonators	23
3	Frequency Comb Generation and Manipulation	27
3.1	Prior art in frequency comb generation	28
3.1.1	Actively mode-locked lasers	29
3.1.2	Passively mode-locked lasers	31
3.1.3	ERGO pulse generating laser	31
3.1.4	Microring resonator based frequency comb generation	32
3.1.5	Optoelectronic frequency comb generation	33
3.2	Comb generation simulations and experiments	34
3.2.1	Principle of comb generation with a phase modulation	34
3.2.2	Flat top frequency comb generation - simulation	36

3.2.3	Flat-top frequency comb generation - experiment	37
3.3	Short pulse characterization	38
3.3.1	Autocorrelation measurement methods	38
3.3.2	Autocorrelation measurement of experimental results	40
3.4	Comb repetition rate manipulation	41
3.4.1	Motivation for comb repetition rate manipulation	41
3.4.2	Design principle	43
3.4.3	Device description	47
3.4.4	Experiment and results	48
3.5	Conclusion	52
4	Optical sampling based on frequency combs	55
4.1	Overview on optical sampling	56
4.2	Sagnac loops	57
4.2.1	Linear loop mirrors	58
4.2.2	Nonlinear-optical loop mirror	58
4.2.3	Nonlinear Sagnac interferometer with a control signal	60
4.3	FWM sampling	61
4.4	Enhancing Nyquist-shaped signal detection bandwidth using optical pre-sampling	62
4.4.1	Motivation	62
4.4.2	Operational principle	64
4.4.3	Simulation setup	66
4.4.4	Simulation results	67
4.4.5	Experimental setup	69
4.4.6	Experimental results	70
4.4.7	Alternative implementation with a PPLN chip	73
4.5	Noise-bandwidth-reduced all-optical sampling based on a temporal integrator	75
4.5.1	Motivation	76
4.5.2	Operational principle	76
4.5.3	Experimental setup	79
4.5.4	Results and discussions	80
4.6	Conclusion	81
5	Frequency combs for WDM aggregation	83
5.1	Introduction	84
5.2	WDM wavelength quantizer	85

5.2.1	Principle of optical arbitrary frequency shifting	86
5.2.2	Experimental setup and results	86
5.3	Full C-band Nyquist-WDM Generation	90
5.3.1	Device characterization	92
5.3.2	Experimental system	92
5.3.3	Results and discussion	93
5.4	Conclusions	95
6	Time-lenses in optical communication systems	97
6.1	Introduction	98
6.1.1	Principle of complete OFT and complete-scaling time-lens	101
6.1.2	Principle of spectral imaging time-lens	102
6.2	Time-lenses for time-division multiplexing (TDM) of optical OFDM channels	104
6.2.1	Time-lens based symbol compression for TDM	104
6.2.2	Time-lens design guidelines	106
6.2.3	Numerical simulations and results	108
6.2.4	System penalty analysis - Nonlinear effects	112
6.2.5	Third-order dispersion	116
6.3	All-optical OFDM demultiplexing with OFT and sinc sampling	117
6.3.1	Principle	118
6.3.2	Experimental setup	121
6.3.3	Results and discussions	123
6.4	Conclusion	125
7	Conclusion	127
7.1	Achievements and future work	127
7.2	Recent advances in the OSP enabling technologies	133
	References	135

Chapter 1

Introduction

1.1 Topic and motivation

As the speed and the capacity of optical communication systems increases, we need new techniques to increase the speeds of signal generation, processing and reception.

The majority of optical communications use the optical C-band (1530-1565 nm), which occupies a 4.4-THz bandwidth. However, the bandwidth of electronic devices is limited to tens of gigahertz. For example, state-of-art high-speed digital sampling oscilloscopes have 256-GSa/s sampling rates and 103-GHz analog bandwidths [2]. To simultaneously manipulate optical signal over the 4.4-THz bandwidth, a great number of electronic devices are required to work in parallel.

In comparison, optical devices can be engineered to cover the entire C-band, or even C- and L-band [3, 4]. As such, optical signal processing (OSP) provides ultra-high-speed signal processing over a wide bandwidth, providing potential benefits where digital signal

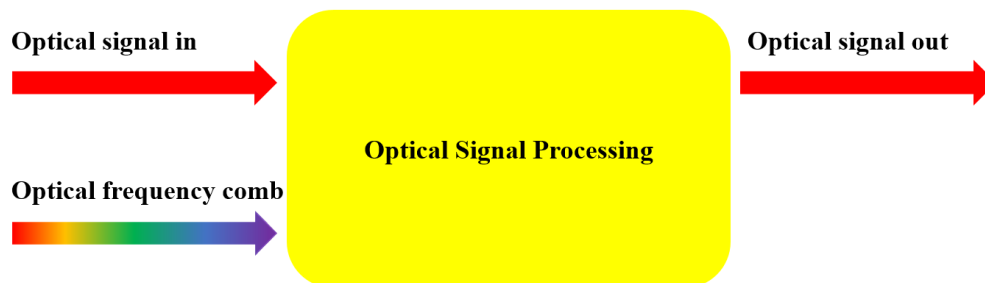


Fig. 1.1 Research topic.

processing (DSP) is limited by analog-digital conversion speeds, numerical complexity or logic resource limitations.

In commercial optical communication systems, OSP has been used for wavelength routing, intradyne mixing in coherent receivers, and optical amplification. Commercialization of more complex OSP functions, including those proposed in this thesis, relies on the advance of OSP enabling techniques such as photonic integrated circuits and frequency comb generation.

As illustrated in Fig. 1.1, this research is to enhance or replace some of the electrical signal processing functions with frequency comb-based optical signal processing. The interaction of an optical signal with an optical frequency comb in a photonic device results in broadband signal processing. In this thesis, the processes investigated include optical sampling, ultra-precise optical filtering and time-frequency conversion (i.e. Fourier transforms). By combining the new optical processing approaches with the mature digital signal processing techniques, the intrinsic ultra-high bandwidth of optical processing can complement the flexibility of electronics to provide a precise and robust data manipulation for optical communications.

1.2 Fiber-optic communications background

Fiber-optic communication is a process of transmitting information from one place to another by sending light through a fiber. In the past years, optical fibers have largely replaced copper wire for telecommunications, owing to significantly higher bandwidth, vastly lower attenuation at high frequencies and immunity to electromagnetic interference [5].

Optical fiber communication systems date back to the 1970s. In 1970, Kao and Hockham pioneered the development of low-loss optical fiber [6]. In 1977, General Telephone and Electronics tested and deployed the world's first fiber-based live telephone traffic running at 6 Mbps in California. In the 1990s, EDFA enabled optical power amplification of several hundreds times [7]. Coherent detection was proposed by Delange in 1970 [8] and it is widely used in today's long-haul optical communication systems. The invention of wavelength division multiplexing (WDM) revolutionized optical communications by increasing system capacity dramatically [9]. 1-Tbit/s on-off-keying (OOK) transmission with 50 WDM channels was reported in 1996 [10]. The advance of digital coherent signal processing in the 2000s enables compensation of transmission impairments and advanced modulation formats with high spectral efficiency [11–14]. In 2012, 100-Tbit/s pulse-density modulation (PDM)-64 quadrature amplitude modulation (QAM) transmission over 240-km single-mode single-core fiber was achieved [15]. Recently, space division multiplexing (SDM) in multi-mode or multi-core fibers adds the fifth degree-of-freedom to optical communications [16–21].

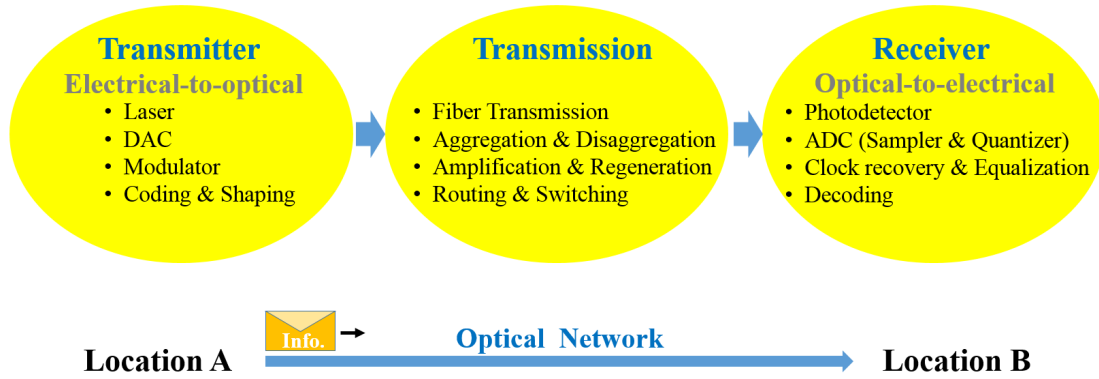


Fig. 1.2 Key components of optical communication systems.

In 2018, Suzuki and Nakazawa's group experimentally demonstrated a 10.16-Pbps dense SDM/WDM transmission over 11.3-km 6-mode 19-core fiber across the C+L band [22]. Elastic networking [23] and photonic integrated circuits (PIC) [24, 25] are currently being researched, and they may become the key enabling technologies for the next generation optical communication systems.

As shown in Fig. 1.2, fiber-optic communication requires a transmitter, a transmission link, and a receiver. In a state-of-art transmitter, the digital signal is coded by an application specific integrated circuit (ASIC). A digital-to-analog converter (DAC) converts digital numbers to an analog signal [26]. The signal is modulated onto a lightwave carrier emitted from a vertical-cavity surface-emitting laser (VCSEL) [27, 28], a distributed feedback laser (DFB) or an external cavity laser (ECL) [29, 30]. A semiconductor laser can be directly modulated by its driving current or externally modulated by a Mach–Zehnder interferometer (MZI) [31].

In the transmission process, the optical signals from different transmitters are multiplexed together to share a single fiber. Due to power loss along the fiber, the optical signals are amplified by erbium-doped fiber amplifiers (EDFA) [7] or regenerated by repeaters [32]. The signal can be routed and switched by reconfigurable optical add-drop multiplexers (ROADM).

At the receiver, the optical signal is converted to an electrical signal through photodetection. A transimpedance amplifier (TIA) converts the photocurrent to voltage and amplifies the electrical signal [33]. Types of photodiodes include: p-i-n photodiodes and avalanche photodiodes. The continuous electrical signal is sampled by an electrical sampler and becomes a discrete signal. A quantizer maps the electrical voltage of each sample to digital numbers. In the end, digital signal processing compensates transmission distortion and decodes the signal. In a coherent system, transmitter I/Q skew and bandwidth limitation diminish the system performance.

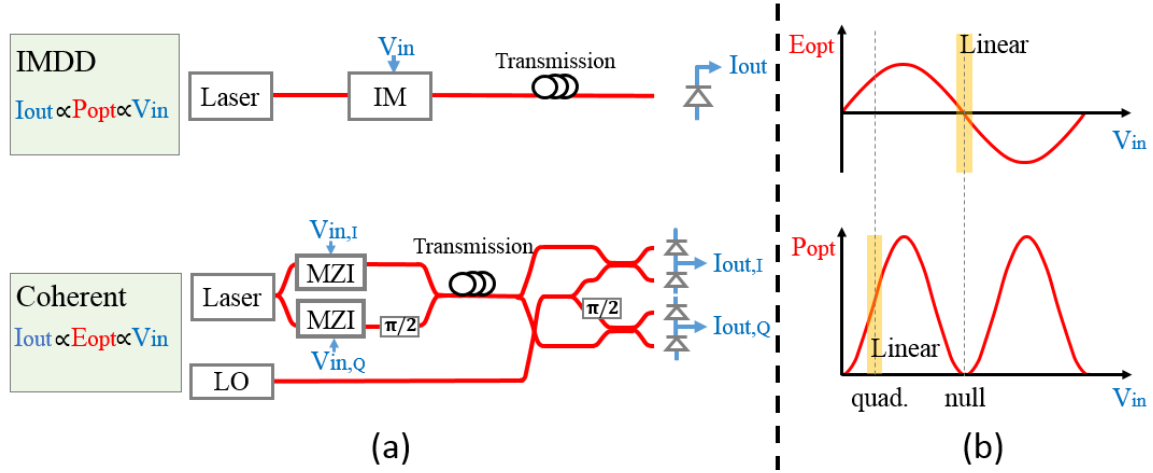


Fig. 1.3 (a) IMDD and coherent back-to-back systems. (b) The electro-optic transfer characteristic of a Mach Zehnder modulator.

There are two sets of ideally distortion-less transmitter and receiver combinations commonly used in optical communication systems: intensity modulation with direct detection (IMDD) and field modulator with coherent detection. IMDD is shown in Fig. 1.3, the light from the laser is intensity modulated by a RF signal (V_{in}) using an external modulator. The intensity modulator is biased at quadrature point to obtain the linear transfer from the input RF voltage to the output optical power (P_{opt}). The transmitted optical signal is detected by a photodiode (PD), which performs square-law detection. The output current of the PD (I_{out}) is proportional to the power (P_{opt}) of the optical signal, which equals to the square of the optical field (E_{opt}). The output current of the PD can be converted to a voltage by a transimpedance amplifier (TIA). The IMDD scheme is not sensitive to the randomly changing carrier phase and the state of polarization (SOP), thus it is easy to implement.

In a coherent system, the single-polarization transmitter is composed of two MZIs and a 90-degree phase shifter for in-phase (I) and quadrature (Q) modulation. The modulators are biased at the null point for linear mapping from the RF voltage to the optical field (E_{opt}). The optical field is extracted by the interference between the optical signal and a local oscillator (LO) in a 90-degree hybrid. The outputs of the balanced-PD are inner product between the I or Q signal and LO phasors. A polarization division multiplexed (PMD) signal can be detected by a polarization-diverse coherent receiver which is composed of two polarization beam splitters (PBS) and two phase-diverse coherent receivers shown in Fig. 1.3 (a, bottom).

In brief, IMDD implies optical intensity modulation and detection. Coherent systems use optical field modulation and detection. Normally, coherent schemes are used in long-haul transmissions for high capacity and low sensitivity. IMDD is widely used in short-haul

communications for simplicity and low cost. The original works in this thesis are related to both of IMDD and coherent systems.

This thesis includes novel OSP applications for transmitters, transmission and receivers. For example, in Chapter 4 a WDM quantizer is proposed for signal aggregation. In Chapter, 5 optical Nyquist filters are used for signal shaping in the transmitter. In Chapter 6, to solve the receiver bandwidth limitation problem, a time-lens based OFDM receiver is demonstrated.

1.3 Optical signal processing

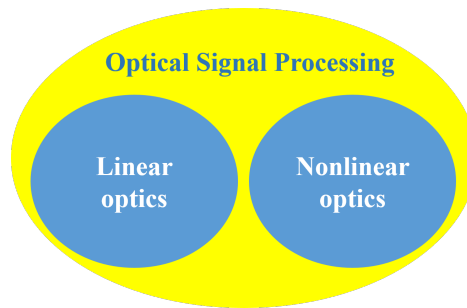


Fig. 1.4 Optical signal processing based on linear and nonlinear optics.

Optical signal processing covers techniques that processes data in the optical domain. In contrast to electronic logic, which processes discrete bits, optical signal processing operates on continuous waveforms [34]. For example, optical amplifiers can process the broadband optical signal. The time it takes to optically amplify the signal does not scale with the number of bits.

As shown in Fig. 1.4, OSP is based on linear optics or nonlinear optics. Examples of linear optics are dispersion compensating fibers, filters and couplers. In this thesis, linear OSP applications are implemented on photonic integrated circuits (PIC) for:

- Optical clock frequency multiplication
- Nyquist-WDM generation.

Nonlinear optics takes place in highly nonlinear fibers (HNLF), semiconductor optical amplifiers (SOA), periodically poled lithium niobate (PPLN) etc. In this thesis, applications of nonlinear OSP are:

- Optical sampling
- WDM aggregation
- AO-OFDM demultiplexing
- Compression of OFDM symbols.

1.4 OSP and DSP

Digital signal processing (DSP) plays an essential role in maximizing data capacity per wavelength channel with advanced modulation formats [35] and spectrally efficient wavelength multiplexing such as orthogonal frequency-division multiplexing (OFDM) [36] and Nyquist WDM [37]. Also, DSP extends optical transmission distances by compensating transmission impairments such as group-velocity dispersion (GVD) [38], polarization-mode dispersion (PMD) [39] and nonlinear distortion [40]. In recent years, nonlinear Fourier transforms (NFT) [41], probabilistic shaping [42], Kramers-Kronig receivers [43] and MIMO-DSP for multimode optical transmission [44] have been investigated.

Digital signal processing is supported by a well-developed supply chain of electronic integrated circuits. However, advances in electronic integrated circuit speed has been slowing down due to the increase of the leakage current across each transistor [45, 46], the physical limits for subthreshold slope and the limits on heat removal [47]. In the near future, CMOS technology is approaching the end of Moore's law [48].

Optical signal processing is promising for future optical communications, providing orders of magnitude higher transmitting and processing speed than most electronics [49]. Optical signal processing can be achieved with femtosecond response times, giving a terahertz operation bandwidth [50–52]. Except for the broadband coverage, OSP has the potential of further increasing the signal processing speed by fully exploring the five optical signal processing dimensions - amplitude, phase, frequency, polarization and space.

From the system point of view, the next generation optical communication is the combination of high-speed optical signal processing and flexible digital signal processing. For example, CMOS-compatible photonic circuits are designed for the transitions between electronics and photonics [53, 54].

1.5 Study objectives

Optical signal processing based on optical frequency combs enables a wide range of high-speed optical signal processing applications in IMDD and coherent communication systems [55–59]. The strategic goal of this research project is to propose and explore comb-based optical signal processing methods to improve the current fiber-optic communication systems.

The main objectives of the study were to:

- Survey fiber optics communication systems and fundamentals of all-optical signal processing, including photonic integrated circuits and nonlinear optics.
- Identify applications of optical signal processing in optical communication systems such as

optical sampling, time-lenses, WDM aggregation, OFDM generation, OFDM demultiplexing, Nyquist-OTDM generation, Nyquist-WDM generation, Nyquist-WDM detection.

- Propose novel optical signal processing methods that may be useful for optical communications.
- Demonstrate novel ideas using simulations and experiments of optical signal generation, transmission and detection.
- Characterise photonic integrated circuits and design telecom applications.

1.6 Original contributions

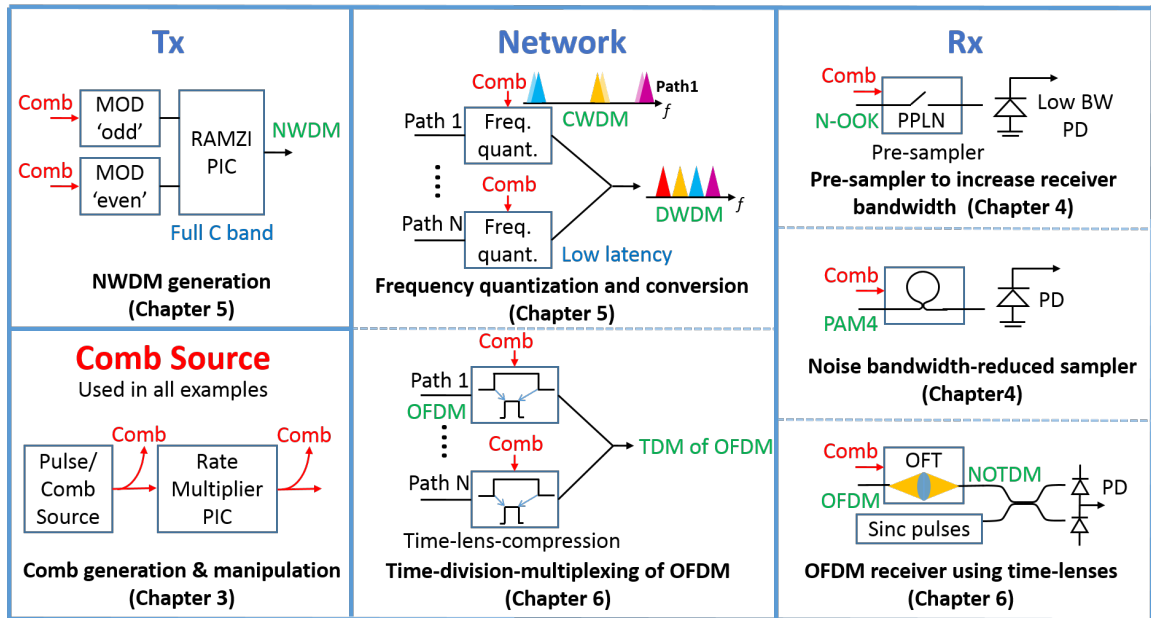


Fig. 1.5 Applications of the work explored in this thesis, from transmitter, through the network, and at the receiver.

As shown in Fig. 1.5, this thesis explores seven examples of frequency comb based optical signal processing in various parts of optical communication systems, ranging from transmitters, transmission links to receivers.

- Experimental demonstration of optical clock multiplication on a photonic integrated circuit. This work is presented in Ref. [60] and Chapter 3 of this thesis.
- Experimental demonstration of optical pre-sampling to alleviate the degradation of Nyquist-shaped signals in a receiver with insufficient bandwidth. This work is presented in Ref. [61] and Chapter 4 of this thesis.
- Experimental demonstration of optical sampling with noise suppression. This work is

presented in Ref. [62] and Chapter 4 of this thesis.

- Experimental demonstration of all-optical wavelength conversion that is robust to input frequency drift. This work is presented in Ref. [63] and Chapter 5 of this thesis.
- Experimental demonstration of Nyquist-WDM generation with Nyquist-shaped optical interleavers on a photonic integrated circuit. This work is presented in Ref. [64] and Chapter 5 of this thesis.
- Simulation of OFDM symbol compression with time-lenses and time division multiplexing of the compressed symbols. This work is presented in Ref. [65] and Chapter 6 of this thesis.
- Experimental demonstration of AO-OFDM demultiplexing based on a time-lens and optical sinc sampling. This work is presented in Chapter 6 of this thesis.

1.7 Thesis structure

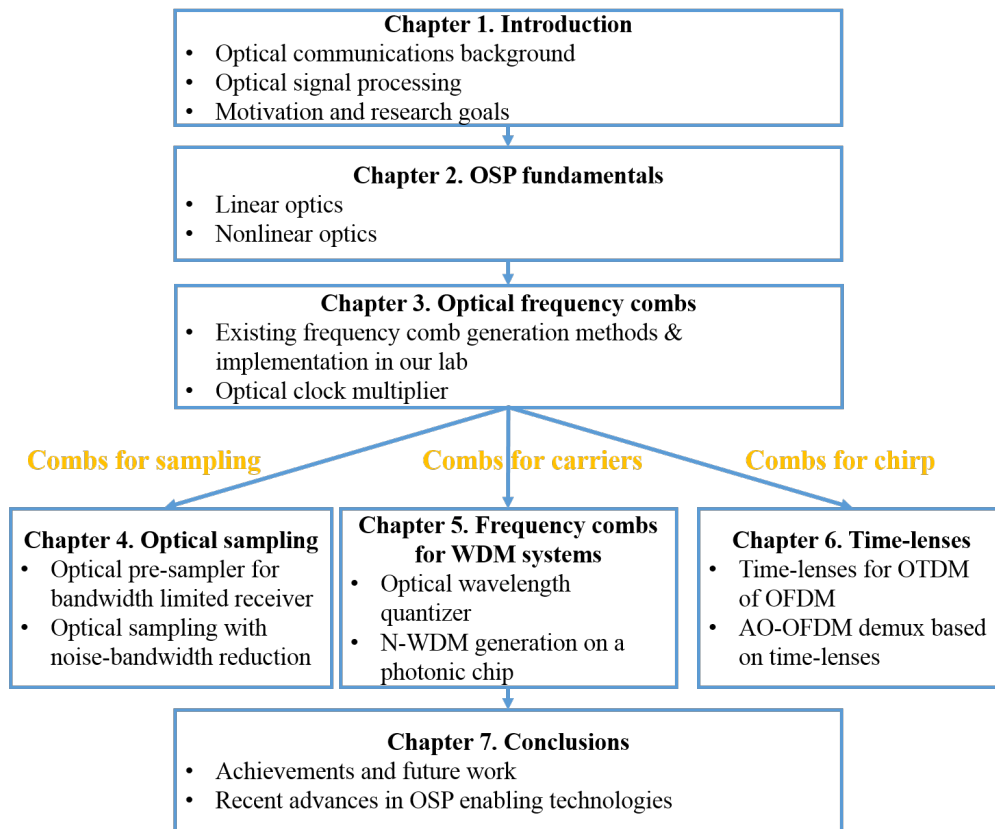


Fig. 1.6 Thesis structure.

The thesis structure is shown in Fig. 1.6. Chapter 1 includes the basic concepts and history of fiber-optic communications, the background of optical signal processing, research goals, original contributions and thesis outline.

Chapter 2 introduces fundamental knowledge of optical signal processing. Optical signal processing can be categorized into OSP based on nonlinear optics and linear optics. Nonlinear optics include nonlinear optical mixing such as four-wave mixing (FWM), self-phase modulation (SPM), cross-phase modulation (XPM) and second-harmonic generation (SHG). A substantial part of linear optics based OSP is implemented on photonic integrated circuits that act as finite impulse response (FIR) or infinite impulse response (IIR) filters.

Chapter 3 begins with the comparison of existing frequency comb generation methods. One of the methods is selected as a guideline for building a frequency comb source in our lab. The novel work is frequency comb manipulation for optical clock multiplication.

Chapter 4 includes two new applications of optical sampling using a frequency comb as sampling short pulses. An optical pre-sampler is proposed to tackle receiver bandwidth limitation problem for Nyquist-shaped signal detection. Another work is optical sampling with noise bandwidth suppression.

Chapter 5 presents WDM aggregation using optical frequency combs as carriers. An optical wavelength quantizer is proposed to overcome the frequency drifting problem of the incoming signal. The FWM between the frequency comb and the signal results in wavelength conversion and multiple consecutive copies of the signal. In another work, NWDM generation with aggregation and Nyquist shaping over entire C-band on a photonic chip is demonstrated.

Chapter 6 explains the concept and different configurations of time-lenses. Two novel applications of time-lenses are included in this chapter. The first one is OTDM of OFDM based on time-lenses. Each OFDM channel is temporally compressed by time-lenses allowing time-division multiplexing by couplers. The purpose is to give a strict condition for time-lenses in order to analysis every cause of system penalties. This work may be useful for people who want to design or debug their time-lens systems. The other application is broadband AO-OFDM demultiplexing. The time-lens performs a Fourier transform and transforms the OFDM signal into a Nyquist OTDM signal. Thus the channels can be detected by time-division demultiplexing through optical sampling.

Chapter 7 concludes the research outcomes and discusses possible future work.

1.8 Publications

Published journal papers:

- **Z. Geng**, B. Corcoran, C. Zhu, and A. Lowery, “Time-lenses for time-division multiplexing of optical OFDM channels,” *Opt. Express* 23, 29788-29801 (2015).
- **Z. Geng**, Y. Xie, M. Burla, C. G. H. Roeloffzen, M. Hoekman, L. Zhuang, A. J. Lowery, “Photonic integrated circuit implementation of a sub-GHz-selectivity frequency comb filter for optical clock multiplication,” *Opt. Express* 25 (22), 27635-27645 (2018).
- Y. Xie, **Z. Geng**, L. Zhuang, etc. “Programmable optical processor chips: toward photonic RF filters with DSP-level flexibility and MHz-band selectivity,” *Nanophotonics* 7(2), 421-454 (2018).
- Y. Xie, **Z. Geng**, D. Kong, L. Zhuang and A. J. Lowery, “Selectable-FSR 10-GHz Granularity WDM Superchannel Filter in a Reconfigurable Photonic Integrated Circuit,” *J. Lightwave Technol.*, 36(13), 2619-2626 (2018).
- D. Kong, **Z. Geng**, B. Foo, V. Rozentel, B. Corcoran, and A. Lowery, “All-optical digital-to-analog converter based on cross-phase modulation with temporal integration,” *Opt. Lett.* 42(21), 4549-4552 (2018).
- B. Corcoran, **Z. Geng**, V. Rozentel and A. Lowery, “Cyclic spectra for wavelength-routed optical networks,” *Opt. Lett.* 42, 1101-1104 (2017).

Published conference papers:

- **Z. Geng**, C. Zhu, B. Corcoran, A. Boes, A. Mitchell, J. Hart, and A. Lowery, “WDM Wavelength Quantizer,” in *Asia Communications and Photonics Conference (ACP)*, Wuhan, China, pp. AF3B.2 (2016). Best Student Paper Award
- **Z. Geng**, L. Zhuang, B. Corcoran, B. Foo, and A. J. Lowery, “Full C-band Nyquist-WDM Interleaver Chip,” in *Optical Networking and Communication Conference (OFC)*, Los Angeles, America, pp. M2J.6 (2017).
- **Z. Geng**, B. Corcoran, A. Boes, A. Mitchell, L. Zhuang, Y. Xie and A. J. Lowery, “Mitigation of Electrical Bandwidth Limitations using Optical Pre-Sampling,” in *Optical Networking and Communication Conference (OFC)*, Los Angeles, pp. Tu2I.4 (2017).
- **Z. Geng**, B. Corcoran, D. Kong, B. Foo and A. Lowery, “Noise Suppression based on All-optical Temporal Integrator,” in *CLEO: Science and Innovations*, pp. SM1C.2 (2018).
- B. Corcoran, **Z. Geng**, V. Rozentel, L. Zhuang, M. Lillieholm and A. J. Lowery, “Photonic-Chip-enabled 25 Tb/s optical superchannel using cyclic spectra,” in *European Conference on Optical Communication (ECOC)*, Gothenburg, Sweden (2017).

- L. Zhuang, C. Zhu, B. Corcoran, **Z. Geng**, B. Song and A. Lowery, “On-Chip Optical Sampling using an Integrated SOA-based Nonlinear Optical Loop Mirror,” in European Conference on Optical Communication (ECOC), Dusseldorf, Germany (2016).
- Y. Xie, L. Zhuang, R. Broeke, Q. Wang, B. Song, **Z. Geng**, and A. J. Lowery, “Compact 4×5 Gb/s Silicon-on-Insulator OFDM Transmitter,” in Optical Networking and Communication Conference (OFC), Los Angeles, America, pp. W2A.9 (2017).

Journal papers to be submitted:

- **Z. Geng**, D. Kong, V. Rozental, A. Lowery and B. Corcoran, “Optical pre-sampling enhanced direct-detection of the Nyquist signal in a bandwidth limited receiver.”
- **Z. Geng**, D. Kong, B. Corcoran, P. Guan, F. D. Ros, E. P. d. Silva, L. K. Oxenløwe, A. J. Lowery, “All-optical OFDM demultiplexing with optical Fourier transform and matched sampling.”
- **Z. Geng**, B. Corcoran, D. Kong, B. Foo and A. Lowery, “Optical sampling with noise bandwidth suppression.”

Chapter 2

Optical signal processing fundamentals

Linear optics	Nonlinear optics
Optical properties of materials are <i>not</i> dependent of intensity	Optical properties of materials are dependent of intensity
Light can <i>not</i> control light	Light can control light
The principle of superposition applies	The principle of superposition does <i>not</i> apply
The central wavelength of light does <i>not</i> change	The central wavelength of light may change

Fig. 2.1 Differences between linear and nonlinear optics.

Optical signal processing exploits diverse linear and nonlinear physical phenomena in optical devices. The differences between linear and nonlinear optics is shown in Fig. 2.1. In nonlinear optics, the optical properties of materials are dependent upon the intensity of light. Consequently, light can control light by changing the physical properties of the matter. The wavelength of light may change due to nonlinear interactions. The principle of superposition does not apply in nonlinear optics. In terms of linear optics, the optical properties of materials are independent of the intensity of light. Thus light cannot control light.

Examples of optical signal processing using nonlinear optics are supercontinuum (SC) generation [66–68], time-division demultiplexing [69–74], optical phase conjugation (OPC) [75], optical signal regeneration [76–79], wavelength conversion [80, 81], analog-to-digital conversion [82], optical sampling [83, 84], parametric amplification [85] and logic gating [86, 87].

Optical signal processing based on linear optics includes dispersion compensation [88], optical add-drop multiplexing [89] and passive optical filtering [90]. Most photonic integrated circuits (PIC) are based on linear optics. The applications of the PICs include Fourier transforms [91], wave shaping [92, 93], filtering [94, 95], switching [96–100], quantum processing [101, 102] and networking [103–105].

Assume in a lossless and dispersionless medium, the polarization $\vec{P}(t)$ of a material depends only upon the instantaneous electric field $\vec{E}(t)$ strength of the applied light. The relationship between the polarization and the electric field is

$$\vec{P}(t) = \xi_0 \left[\chi^{(1)} \vec{E}(t) + \chi^{(2)} \vec{E}^2(t) + \chi^{(3)} \vec{E}^3(t) + \dots \right] \quad (2.1)$$

where ξ_0 is the permittivity of vacuum. In the case of linear optics, only the term $\vec{P}(t) = \xi_0 \chi^{(1)} \vec{E}(t)$ is significant. The induced polarization is linearly proportional to the electric field, where the constant of proportionality $\chi^{(1)}$ is called linear susceptibility. Higher order susceptibilities exist in nonlinear optics. $\chi^{(2)}$ and $\chi^{(3)}$ are second- and third-order nonlinear optical susceptibilities respectively. The second-order nonlinear optical interaction does not occur in materials with inversion symmetry or in centrosymmetric materials. In contrast, the third-order nonlinear susceptibility exists in both of centrosymmetric and noncentrosymmetric materials [106].

2.1 OSP based on nonlinear optics

Nonlinear optics comprises a substantial portion of optical signal processing. Thanks to the fast response of nonlinearities in optical devices, large volumes of data can be processed with femtosecond response times, giving a terahertz bandwidth [50–52]. As depicted in Fig. 2.2, second-order susceptibility $\chi^{(2)}$ can support three-wave mixing such as sum-frequency generation (SFG), difference-frequency generation (DFG), and second-harmonic generation (SHG) [107–109]. Third-order susceptibility $\chi^{(3)}$ results in Kerr effects such as four-wave mixing (FWM), cross-phase modulation (XPM) and self-phase modulation (SPM) [110]. These nonlinear processes happen in optical media such as highly nonlinear fibers (HNLF) [111], silicon waveguides [112, 113], chalcogenide waveguides [114, 115], periodically poled lithium niobate (PPLN) waveguides [108], and photonic crystals [116].

The cascaded SHG and DFG effects in a PPLN waveguide are used for optical sampling in Chapter 4 and WDM aggregation in Chapter 5. The FWM effect in a HNLF is employed for optical sampling in Chapter 4 and time-lenses in Chapter 6. The combined effects of XPM and dispersion in a dispersion compensating fiber (DCF) are utilized for optical integration

in Chapter 4. The combined effects of SPM and dispersion in a HNLF are used to achieve large linear chirp in Chapter 6.

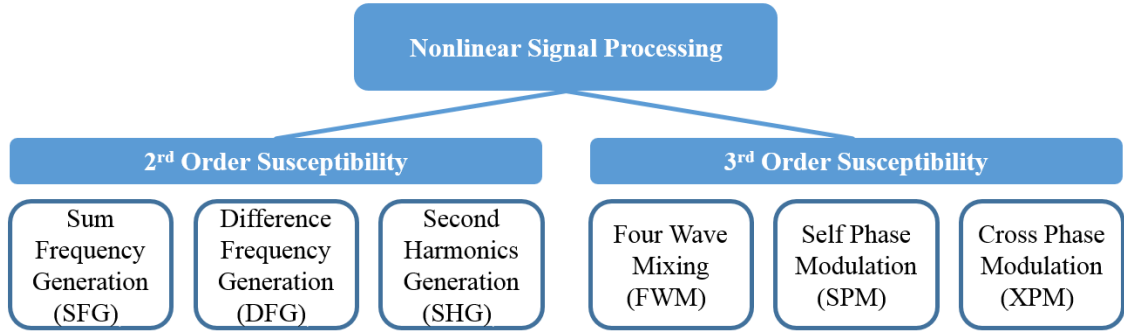


Fig. 2.2 Nonlinear optical signal processing.

2.1.1 Second-order susceptibility

When the incident light of a nonlinear medium has a single frequency component at angular frequency ω [106]

$$\vec{E}(t) = E e^{-i\omega t} + c.c. \quad (2.2)$$

The second-order nonlinear polarization created in the medium is [106]

$$\vec{P}^{(2)}(t) = \xi_0 \left[2\chi^{(2)} E E^* + \chi^{(2)} E^2 e^{-2i\omega t} + c.c. \right] \quad (2.3)$$

The first term in Eq. 2.3 contributes to the generation of a static electric field and this process is known as optical rectification (OR). The second term in Eq. 2.3 describes the generation of radiation at frequency 2ω , that is, second-harmonic generation. In this quantum-mechanical process, two photons vanish at frequency ω to create a new photon at frequency 2ω . Under proper conditions, the second-harmonic generation efficiency can be close to 100% [106]. When the incident light of the nonlinear medium has two distinct frequency components [106]

$$\vec{E}(t) = E_1 e^{-i\omega_1 t} + E_2 e^{-i\omega_2 t} + c.c. \quad (2.4)$$

The second-order nonlinear polarization is of the form [106]

$$\begin{aligned} \vec{P}^{(2)}(t) = & \xi_0 \chi^{(2)} \left[E_1^2 e^{-2i\omega_1 t} + E_2^2 e^{-2i\omega_2 t} + 2E_1 E_2 e^{-i(\omega_1 + \omega_2)t} + 2E_1 E_2^* e^{-i(\omega_1 - \omega_2)t} + c.c. \right] \\ & + 2\xi_0 \chi^{(2)} [E_1 E_1^* + E_2 E_2^*] \end{aligned} \quad (2.5)$$

The first and second terms in Eq. 2.5 represent second-harmonics at $2\omega_1$ and $2\omega_2$ respectively. The third term refers to sum-frequency generation at $\omega_1 + \omega_2$. The fourth term refers to difference-frequency generation (DFG) at $\omega_1 - \omega_2$ [117]. The complex amplitudes of the frequency components in Eq. 2.5 are given by [106]:

$$\begin{aligned} P(2\omega_1) &= \xi_0 \chi^{(2)} E_1^2 & (SHG), \\ P(2\omega_2) &= \xi_0 \chi^{(2)} E_2^2 & (SHG), \\ P(\omega_1 + \omega_2) &= 2\xi_0 \chi^{(2)} E_1 E_2 & (SFG), \\ P(\omega_1 - \omega_2) &= 2\xi_0 \chi^{(2)} E_1 E_2^* & (DFG), \\ P(0) &= 2\xi_0 \chi^{(2)} (E_1 E_1^* + E_2 E_2^*) & (OR). \end{aligned} \quad (2.6)$$

For optical telecommunications, the cascaded SHG and DFG of a signal at ω_s and a high power pump at ω_p are used to generate a new frequency component, called the idler, at $\omega_i = 2\omega_p - \omega_s$. The power of the idler is approximated as $P_i = (\eta L^2 P_p / 2)^2 P_s$, where P_p , P_s and P_i are the pump, signal and idler powers, respectively, L is the propagation length, and η is the normalized efficiency of the $\chi^{(2)}$ waveguide [118].

Actually, only one or several of the above mentioned products would appear in a nonlinear crystal, depending on a phase matching condition $\Delta k = 0$ [119, 106], where Δk describes wave-vector mismatch. If the phase matching condition $\Delta k = 0$ is fulfilled, the amplitude of the mixing products increases linearly with the interaction distance, and consequently the intensity builds up quadratically with the interaction distance. However, in a dispersive medium, where the group velocity V_g of a wave depends on its frequency, the group velocity mismatch limits the spectral range in which phase matching is achieved. The phase-matching bandwidth is inversely proportional to the length of the nonlinear crystal and the temporal walk-off from group velocity mismatch ($GVM = 1/V_{g1} - 1/V_{g2}$) among two frequencies [120]. For example, the SHG phase-matching bandwidth of a light at 1550-nm is limited by the large GVM between lights at 1550 nm and 775 nm.

Quasi-phase matching can take place when normal phase matching cannot be implemented [121–123]. Figure 2.3 shows the comparison between no phase matching and quasi-phase matching using periodic poling. With phase mismatch in a homogeneous non-

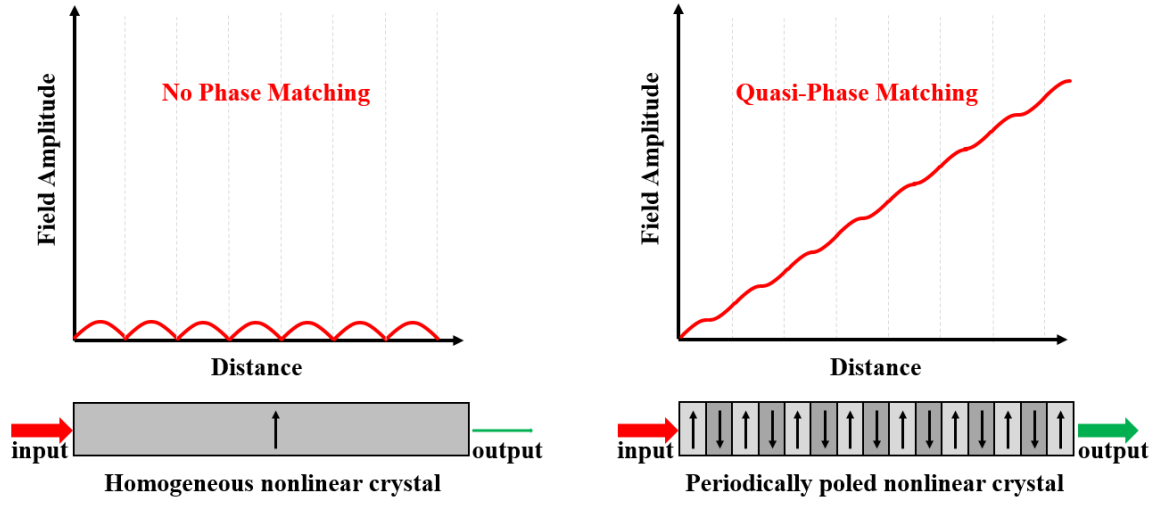


Fig. 2.3 The field amplitude of the generated wave in a nonlinear optical interaction based on second-order susceptibility at different distances under no phase matching (left) and quasi-phase matching (right) conditions. Adapted from [106].

linear crystal, the generated photons interfere constructively and destructively, limiting the maximal field amplitude of generated photons. In contrast, by flipping the orientation of the crystalline axes with proper periodicity, the generated photons will predominantly interfere constructively. The field amplitude of generated photons will grow as the light propagates through the periodically poled nonlinear crystal.

Periodically poled lithium niobate (PPLN) is a nonlinear crystal with periodic polling for quasi-phase matching [124]. To produce a PPLN, the orientation of the electric dipole in the lithium niobate ions are periodically inverted by large (22 kV/mm) electric fields applied by evenly spaced electrodes [125]. After applying the electric fields for a few milliseconds, the periodic polling is permanently imprinted into the lithium niobate crystal. To utilize the PPLN, the polarization of the incident light must be aligned with the dipole moment of the crystal. A polarisation mismatch would result in severely reduced conversion efficiency. In addition, the temperature of the crystal should be in the range of 100°C - 200°C to minimize the photorefractive effect [126]. The inappropriate temperature may lead to the damage to the crystal or the distortion to the optical beam. Doping of crystals with Mg can reduce or remove the temperature requirement. The quasi-phase matching (QPM) frequency can be slightly tuned by changing the temperature. The temperature requirement makes it difficult to integrate with multiple functions.

Due to merits like low crosstalk, high bandwidth and high conversion efficiency, PPLN devices have been used for dispersion compensation [127], wavelength conversion [128], time slot interchange [129], etc.

2.1.2 Third-order susceptibility

The refractive index of a medium is defined as the speed of light in vacuum over the phase velocity of light in the medium. If there is a single wavelength light in the nonlinear medium, the refractive index of the medium can be written as [106]

$$n = n_0 + n_2 I \quad (2.7)$$

where: I is the intensity of the plane wave, n_0 is the linear refractive index, which is related to the first order susceptibility $\chi^{(1)}$, n_2 is the nonlinear refractive index, namely the Kerr coefficient, which is related to $\chi^{(3)}$. For silica fibers, n_2 is around $2.35 \times 10^{-20} \text{ m}^2/\text{W}$ [130]. The dependence of the refractive index on the intensity of light is called the nonlinear Kerr effect. Phenomenon like SPM, XPM and FWM are based on the Kerr effect.

If only group velocity dispersion and third-order susceptibility are taken in account, a nonlinear Schrödinger equation (NLSE) can be [131]

$$i \frac{\partial U}{\partial z} - \frac{1}{2} \beta_2 \frac{\partial^2 U}{\partial \tau^2} + \gamma |U|^2 U = 0 \quad (2.8)$$

where: U is the normalized amplitude of the optical electric field, β_2 is the group velocity dispersion (GVD) parameter, τ and z represent time and distance respectively, γ is the nonlinear coefficient of the medium, given by $\gamma = \omega n_2 / (c A_{eff})$, where A_{eff} is the effective core area, c is the speed of light, and ω is the angular velocity of the incident light.

The effect of dispersion is pulse broadening and chirp, whereas the effect of nonlinearity is the phase modulation of the plane wave due to its own power variation. This phenomenon is called self-phase modulation. The general solution for the field amplitude $U(L, \tau)$ at time τ and fiber length L in the SPM process is [132]

$$U(L, \tau) = U(0, \tau) \exp [i \gamma L_{eff} P(0, \tau)] \quad (2.9)$$

where $P(0, \tau) = |U(0, \tau)|^2$ is the pulse power. The effective length L_{eff} includes the effect of attenuation and it is given by [133]

$$L_{eff} = \frac{1 - e^{-\alpha L}}{\alpha} \quad (2.10)$$

where α is the fiber loss coefficient, in Nepers per meter (Nepers/m). The loss coefficient α can be obtained by measuring the input P_{in} and output power P_{out} over the fiber length L [134].

$$\alpha = \frac{1}{L} \ln\left(\frac{P_{in}}{P_{out}}\right) \quad (2.11)$$

If the attenuation α_{dB} is expressed in dB/m. The fiber loss can be calculated as [134]

$$\alpha_{dB} = \frac{1}{L} \times 10 \log_{10}\left(\frac{P_{in}}{P_{out}}\right) \quad (2.12)$$

Therefore the conversion between α (Nepers/m) and α_{dB} (dB/m) is [134]

$$\frac{\alpha_{dB}}{\alpha} = \frac{10 \log_{10}\left(\frac{P_{in}}{P_{out}}\right)}{\ln\left(\frac{P_{in}}{P_{out}}\right)} = 10 \log(e) = 4.343 \quad (2.13)$$

If the fiber is short, the effective length L_{eff} is approximately equal to its length. If the fiber is very long, the effective length L_{eff} approaches a maximum value of $1/\alpha$. According to Eq. 2.9, the SPM-induced phase shift $\phi_{NL}(L, \tau)$ is [135]

$$\phi_{NL}(L, \tau) = \gamma L_{eff} P(0, \tau) \quad (2.14)$$

Thus the SPM-induced frequency shift $\Delta\omega_{SPM}$ is [135]

$$\Delta\omega_{SPM} = -\gamma L_{eff} \frac{\partial P}{\partial \tau} \quad (2.15)$$

According to Eq. 2.15, the SPM process introduces frequency chirp. At the leading edge of a pulse, where the power increases, the SPM-induced frequency shift is negative. In other words, the leading edge of the pulse is red-shifted by the SPM effect. Meanwhile, the trailing edge of the pulses is blue-shifted by the SPM effect. Chirp is the fact that frequency changes with time ($chirp = df/dt$). In the SPM process, the spectrum of the incident light is broadened due to chirp, while the temporal profile of the pulses remains the same. The broadening effect is related to the rate of power variation. Therefore, a high symbol-rate signal is more affected by SPM than low rate signals.

Considering the effect of dispersion only, in the normal dispersion regime ($\beta_2 > 0$), the instantaneous frequency of a pulse linearly increases with time. The leading edge of the optical pulse is red-shifted, whereas the trailing edge is blue-shifted. Thus the SPM effect and normal dispersion will work in the same direction and aggravate temporal broadening of

the pulses, leading to a further reduction of the system capacity. However, in an anomalous dispersion regime ($\beta_2 < 0$), GVD and SPM counter act with each other, resulting in a compression of pulses. Thus a nonlinear medium with anomalous dispersion can be used for short pulse generation [136, 137] and optical solitons generation [138, 139].

If there are multiple signals at different wavelengths in the nonlinear medium, the power of one signal will apply a phase modulation to all the other signals. This phenomenon is called cross-phase modulation (XPM). The XPM-induced frequency shift ($\Delta\omega_{XPM1}$) to the signal at frequency ω_1 by the power variation of the signal at frequency ω_2 is [135]

$$\Delta\omega_{XPM1} = -2\gamma L_{eff} \frac{\partial P_2}{\partial \tau} \quad (2.16)$$

where P_2 is the instantaneous power of the signal at frequency ω_2 .

FWM refers to a parametric process in which four waves interact with each other due to the third-order susceptibility of nonlinear materials, giving rise to signals at new frequencies. For the simplicity of numerical deduction, assume there are only two optical fields at frequency ω_1 and ω_2 in the nonlinear medium and only the third-order nonlinearity is taken into account, the differential wave equation is written as [135]

$$\omega_{FWM} = \omega_i + \omega_j - \omega_k \quad (2.17)$$

The FWM process is also present if there are only two incident waves; when $\omega_i = \omega_j$, it is called degenerate FWM. Under certain circumstances, FWM and SPM/XPM are explaining the same phenomenon. When $\omega_{FWM} = \omega_i = \omega_j = \omega_k$, SPM occurs. When $\omega_{FWM} = \omega_j$, $\omega_i = \omega_k$ but $\omega_i \neq \omega_j$, XPM occurs. The number of FWM products from N original channels is [135]

$$M_{FWM} = \frac{1}{2}N^2(N-1) \quad (2.18)$$

If the incident waves are evenly spaced, the new frequency products may coincide with the original frequencies or with each other.

Assume three original waves at frequencies ω_i , ω_j and ω_k interact in the fiber to generate a new wave at ω_{FWM} , the power of the generated wave at fiber length L can be approximated by [140]

$$P_{FWM}(L) = (\gamma D_F L_{eff})^2 P_i P_j P_k \eta e^{-\alpha L} \quad (2.19)$$

where: α is the fiber attenuation coefficient, γ is the nonlinear parameter, $D_F = 1$ for the degenerate FWM, otherwise $D_F = 2$. P_i , P_j and P_k are the power of the original waves at ω_i , ω_j and ω_k respectively. η is the FWM efficiency, given by [141]

$$\eta = \frac{\alpha^2}{\alpha^2 + \Delta k^2} \left[1 + \frac{4e^{-\alpha L} \sin^2(\Delta k L / 2)}{(1 - e^{-\alpha L})^2} \right] \quad (2.20)$$

where Δk is phase mismatch among the four waves, given by

$$\Delta k = \beta_{FWM} + \beta_k - \beta_i - \beta_j \quad (2.21)$$

$\beta_{i,j,k,FWM}$ are propagation constants of each tone. A smaller Δk means better phase matching. In order to achieve a high FWM efficiency, the waves should be placed close to the zero-dispersion wavelength (ZDW) of the fiber. To reduce the FWM effect, increasing channel spacing or dispersion of the fiber are two options.

2.2 OSP based on linear optics

Causal, time-invariant, and linear signal processing filters are called linear shift-invariant (LSI) filters. There are a multitude of methods to create optical filters with various properties that fall into the LSI category. In this thesis, optical filters based on PIC waveguide structures are used in Chapters 3 and 5. LSI filters include finite impulse response (FIR) filters and infinite impulse response (IIR) filters. FIR filters can be based on Mach-Zehnder interferometers (MZI) [142–145], which are composed of optical delay lines, optical couplers and optical splitters. IIR filters can be implemented with ring resonators (RR) [146–149].

2.2.1 FIR filters based on Mach-Zehnder interferometers

A FIR filter has a finite impulse response to a finite input. Analog FIR filters can be implemented using tapped delay lines (TDL). The transfer function of one tapped delay line can be expressed as

$$H(z) = bz^{-P} \quad (2.22)$$

where b is the scaling factor of the signal. The time delay is a multiple of the unit delay T [150], given by $T \times p$.

Multiple tapped delay lines in parallel can be used to scale and delay the input signal $x(n)$ by different amounts in order to simulate multiple echoes of $x(n)$ [151], so that the output

$y(n)$ of the delay lines is given by

$$y(n) = b_0x(n) + b_1x(n-1) + b_2x(n-2) + \dots + b_Mx(n-M) = \sum_{i=0}^M b_ix(n-i) \quad (2.23)$$

The transfer function therefore is

$$H(z) = b_0 + b_1z^{-1} + b_2z^{-2} + \dots + b_Mz^{-M} = \sum_{i=0}^M b_iz^{-i} \quad (2.24)$$

The transfer function in Eq. 2.24 represents a FIR filter [152, 153]. The filter response is periodic with a free spectral range (FSR) of $1/T$ [150]. The output $y(n)$ only depends on the current and past inputs such as $x(n)$, $x(n-1)$.

The splitting, combining and delaying of the optical signal forms a FIR response. The splitting and combining functions can be achieved by an optical coupler with a coupling ratio κ . The structure of the optical coupler is shown in Fig. 2.4. The transmission coefficient for the cross-port is given by $-js = -j\sqrt{\kappa}$ and the transmission coefficient for the through-port is given by $c = \sqrt{1-\kappa}$.

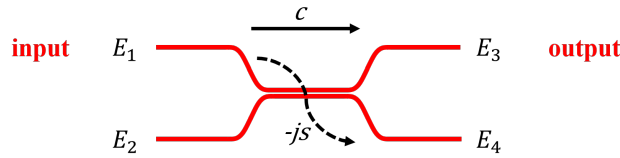


Fig. 2.4 Waveguide layout of a coupler.

The relationship between the inputs E_1 , E_2 and the outputs E_3 , E_4 is given by

$$\begin{bmatrix} E_3 \\ E_4 \end{bmatrix} = \begin{bmatrix} c & -js \\ -js & c \end{bmatrix} \begin{bmatrix} E_1 \\ E_2 \end{bmatrix} \quad (2.25)$$

A MZI is a fundamental building block of optical planar waveguide filters. As shown in Fig. 2.5, a MZI consists of two couplers with coupling ratios κ_1 , κ_2 and a delay line.

If the lengths of the two arms are identical, the MZI can be used as a variable coupler, whose coupling ratio is tuned by the relative phases of the two arms. In Fig. 2.5, the two arms have different lengths. The filter function arises from the interference of the two waves that are delayed relative to each other. When the two optical waves recombine, they may interfere constructively or destructively depending on their relative phases. In order to achieve interference, the optical waves must be coherent and they should have the same polarization

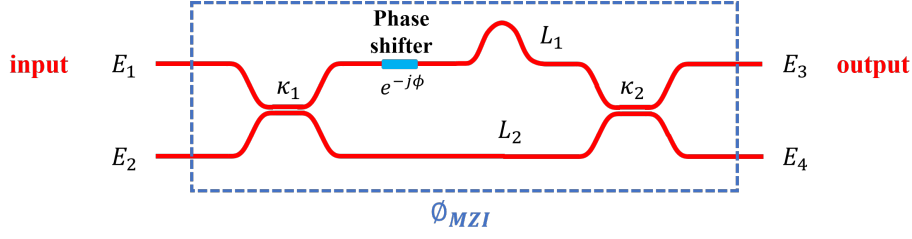


Fig. 2.5 Waveguide layout of an asymmetric MZI.

and the same frequency. The transfer matrix of the MZI is given by [154]

$$\begin{aligned} \phi_{MZI} &= \gamma \begin{bmatrix} c_2 & -js_2 \\ -js_2 & c_2 \end{bmatrix} \begin{bmatrix} e^{-j\phi}z^{-1} & 0 \\ 0 & 1 \end{bmatrix} \begin{bmatrix} c_1 & -js_1 \\ -js_1 & c_1 \end{bmatrix} \\ &= \gamma \begin{bmatrix} c_1c_2e^{-j\phi}z^{-1} - s_1s_2 & -j(s_1c_2e^{-j\phi}z^{-1} + c_1s_2) \\ -j(c_1s_2e^{-j\phi}z^{-1} + s_1c_2) & -s_1s_2e^{-j\phi}z^{-1} + c_1c_2 \end{bmatrix} \end{aligned} \quad (2.26)$$

where γ is the propagation loss in the MZI. The phase shifter introduces a ϕ phase shift. The unit delay T of this MZI is decided by the difference between the path lengths of the two arms, $\Delta L = L_1 - L_2$.

If a FIR filter with multiple taps is desired, cascading multiple MZIs is a solution [155]. Different delays are inserted in different stages to achieve the transfer function shown in Eq. 2.24. The delays should be integer multiples of the unit delay T .

2.2.2 IIR filters based on ring resonators

Different from FIR filters, IIR filters have infinite impulse responses. Since there is feedback in IIR filters, IIR filters are known as recursive filters. The numerical relationship between an input $x(n)$ and an output $y(n)$ of an IIR filter is given by

$$y(n) = \frac{1}{a_0} \left(\sum_{i=0}^M b_i x(n-i) - \sum_{i=1}^N a_i y(n-i) \right) \quad (2.27)$$

where b_i is the scaling factor of the input $x(n-i)$ and a_i is the scaling factor of the output $y(n-i)$, i is a positive integer.

The general transfer function of an IIR filter is written as

$$H(z) = \frac{\sum_{i=0}^M b_i z^{-i}}{\sum_{i=0}^N a_i z^{-i}} \quad (2.28)$$

The IIR filter function can be implemented with ring resonators [156], fiber Bragg gratings [157], and thin film dielectric stacks [158]. Among those, only ring resonators are related to the original work in this thesis. As shown in Fig. 2.6, a feedback path is achieved by looping the delay line back on itself.

The transfer functions for Ports 1 to 2 and Ports 1 to 3 of the ring resonator are given by [154]

$$H_{12}(z) = \frac{c - \gamma e^{-j\phi} z^{-1}}{1 - c\gamma e^{-j\phi} z^{-1}} \quad (2.29)$$

$$H_{13}(z) = \frac{-js}{1 - c\gamma e^{-j\phi} z^{-1}} \quad (2.30)$$

where ϕ is the phase of the phase shifter. The coupling intensity for the throughput path is $c = \sqrt{1 - \kappa}$ and for the cross path is $-js = -j\sqrt{\kappa}$. The round trip loss of the ring is given by $\gamma = 10^{-\alpha L/20}$, where γ is the average ring loss per unit length, L is the ring circumference. The intensity transfer function is written as [154]

$$|H_{12}(z)|^2 = \frac{c^2 + \gamma^2 - 2c\gamma \cos(\pi\Delta\nu)}{1 + (\gamma c)^2 - 2c\gamma \cos(\pi\Delta\nu)} \quad (2.31)$$

where $\Delta\nu$ is the full-width resonance bandwidth defined at half-power points of $|H_{13}(z)|^2$ [154]. For a lossless ring resonator, $\gamma = 1$. In this case, an all-pass filter with constant magnitude response and tailored phase response can be achieved [159]. This approach can be useful for dispersion compensation [160, 161].

A more complex case to have two couplers with a ring resonator, as shown in Fig. 2.7. The unit delay is given by the circumference of the ring resonator L .

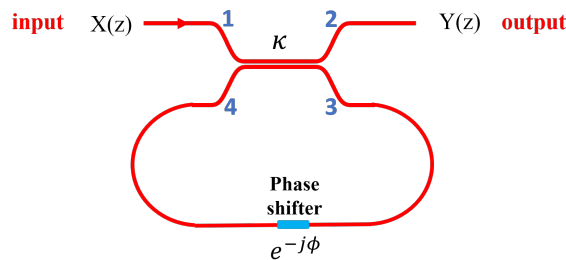


Fig. 2.6 Waveguide structure of a ring resonator with one coupler.

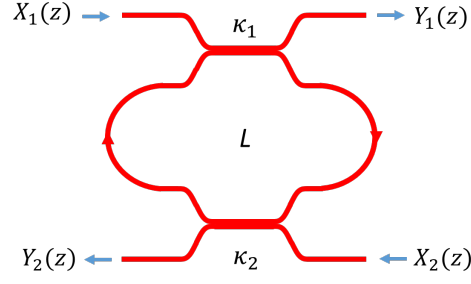


Fig. 2.7 Waveguide structure of a ring resonator with two couplers.

The transfer function between the output $Y_2(z)$ and the input $X_1(z)$ or the output $Y_1(z)$ and the input $X_2(z)$ is written as [154]

$$H_{21} = H_{12} = \frac{Y_2(z)}{X_1(z)} = \frac{-\sqrt{\kappa_1 \kappa_2 \gamma z^{-1}}}{1 - c_1 c_2 \gamma z^{-1}} \quad (2.32)$$

where $\gamma = 10^{-\alpha L/20}$. γ , c_1 and c_2 are always less than unity, which means that the filter is always stable. If a gain is introduced in the ring resonator, it may become a laser. For stability, the pole location is within a circle of radius γ in the Z -plane. Phase shifters can be introduced into the ring resonator to move the pole to anywhere in this circle. Reducing the coupling ratio and the ring loss can move the pole closer the unit circle in the Z -plane, thus the response of the ring resonator features a narrower passband and a larger stopband rejection. If there is no loss, the waveguide in Fig. 2.7 is a lossless filter.

The transfer function between the output $Y_1(z)$ and the input $X_1(z)$ is given by [154]

$$H_{11} = \frac{Y_1(z)}{X_1(z)} = \frac{c_1 - c_2 \gamma z^{-1}}{1 - c_1 c_2 \gamma z^{-1}} \quad (2.33)$$

The transfer function between the output $Y_2(z)$ and the input $X_2(z)$ is given by [154]

$$H_{22} = \frac{Y_2(z)}{X_2(z)} = \frac{c_2 - c_1 \gamma z^{-1}}{1 - c_1 c_2 \gamma z^{-1}} \quad (2.34)$$

By cascading multiple ring resonators different functions can be achieved [162]. In addition, the ring resonators and MZIs can be combined to form an interleaver with a sharp roll-off [163], which will be explained in Chapter 5.

In conclusion, the fundamental physical basics of OSP functions have been reviewed to provide a framework for subsequent chapters investigating the applications of OSP. In the next chapter, optical frequency comb are introduced, as these form a key tool for the OSP applications in this thesis.

Chapter 3

Frequency Comb Generation and Manipulation

This chapter is about frequency comb generation and manipulation. In terms of frequency comb generation, our target is to develop a workable frequency comb generation method for our laboratory, rather than proposing a novel method. Frequency combs are indispensable for my experiments, building a reliable phase-locked frequency comb source is necessary for the following experiments in Chapters 4-6.

There are a number of devices that can be used for the frequency comb generation, such as: soliton-assisted time-lenses [164], directly modulated lasers [165], electro-absorption modulators (EAM) [166], semiconductor mode-locked lasers [167], cascaded intensity modulators (IM) and phase modulators (PM) [168–170].

To begin with, some of the methods are briefly discussed and classified in this chapter. Considering the feasibility, stability and equipment availability, flat-top frequency comb generation using cascaded intensity and phase modulators [171] is preferable for implementation in our laboratory. The principle, simulations and experiments of electro-optic frequency comb generation are presented in Section 3.2. In Section 3.4, a novel photonic integrated circuit (PIC) implementation of an optical clock multiplier is reported [60]. The idea is verified by an experiment of clock rate multiplication, i.e. from 2.5 Gpulses/s to 10 Gpulses/s and from 10 Gpulses/s to 50 Gpulses/s.

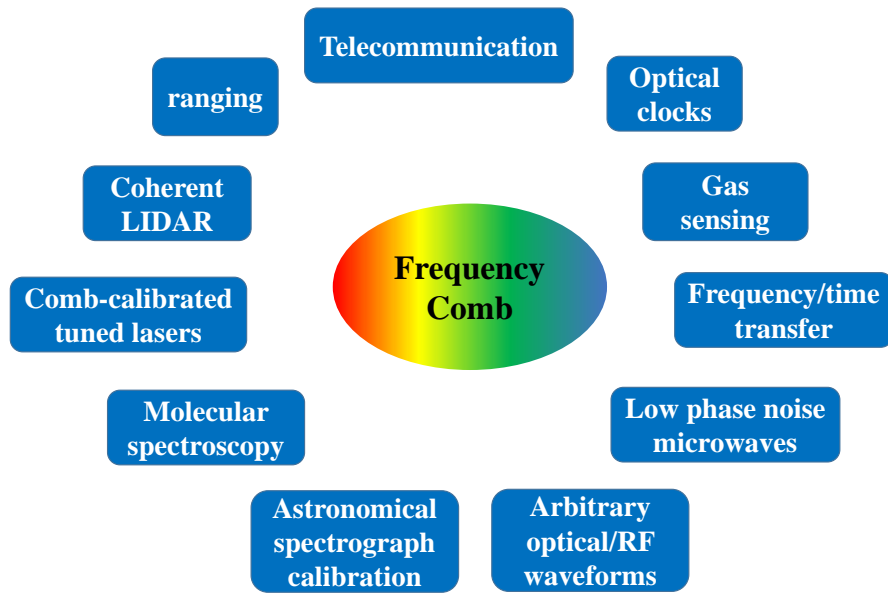


Fig. 3.1 Applications of frequency combs.

3.1 Prior art in frequency comb generation

An optical frequency comb is composed of equally spaced spectral lines with fixed-phase relationship across the entire band. Correspondingly, it is a regular short-pulse train in the time domain. As shown in Fig. 3.1, optical frequency combs are widely used in various fields of industry and research including telecommunications, medical diagnosis, topography, airborne observatory, aerospace and material science [173–182]. As a "frequency ruler", optical frequency combs are applicable to high precision measurement of optical clocks [183, 184], microwave frequency references [185], spectroscopy [186–188], and astrophysical spectrometer calibration. Other applications include arbitrary optical waveform generation [189, 190], coherent light detection and ranging (LIDAR) [191], sensing [192], and telecommunications [193, 194].

The desired characteristic of an optical frequency comb depends on the target application [195]. Each frequency comb generation method gives a distinct feature. For example, a Ti:sapphire laser enables the generation of short pulses of less than 10-fs duration [196]. Passively mode-locked miniature lasers [197] and harmonically mode-locked fiber lasers are able to generate high repetition-rate frequency combs. Especially, higher than 1-THz repetition rates can be achieved with distributed-Bragg-reflector (DBR) laser diodes [198]. A passively mode-locked thin-disk laser can emit a peak output power of 80 W in femtosecond pulses. [199].

In telecommunications, arrays of independent lasers are limited by the drift of the emission wavelengths and guard bands. Optical frequency combs have excellent phase coherence and stability, and high signal-to-noise ratios (SNR). The tunability of bandwidth, central frequencies and repetition rates of the optical frequency combs are desirable for optical communications. Greater than 1-Tbps coherent optical transmission has been demonstrated with frequency combs generated by schemes such as: gain-switched comb source (GSCS) [200], Kerr frequency comb [201], silicon-organic hybrid (SOH) modulator [202], cascaded LiNbO₃ modulators [203], cascaded phase modulators (PM) in a recirculating frequency shifter (RFS) [204], parametric comb [205], and a mode-locked laser (MLL) followed by a highly nonlinear fiber (HNLF) [206, 207]. There are limitations of these methods. For example, frequency combs based on electro-optic modulators are limited by the achievable modulation depth. A Kerr comb [3] has a line spacing fixed to the free spectral range (FSR) of the resonator and large line-to-line power variations. Comb generation and broadening based on a MLL followed by a HNLF [208] requires high power pumps and a large interaction length.

Most of the above-mentioned methods are based on mode-locking [209, 210]. The concept of mode-locking was proposed in 1964 by Willis [209]. Methods of mode-locking are shown in Fig. 3.2. The mode-locking of a frequency comb source can be verified with the comparison to a well-established mode-locked laser comb [211] or the measurement of the radio frequency (RF) spectrum of a mode locking state [212]. A multi-channel synchronous phase and frequency recorder are required for the comparison. Then, the phase alignment can be confirmed with the auto-correlation of the tested comb, and an equally spaced short pulse train is expected.

A mode-locked laser contains either an active element, such as an optical modulator driven by an external RF oscillator, or a nonlinear passive element, such as a saturable absorber. These two cases correspond to the two major mode-locking categories, which are active mode-locking and passive mode-locking [213].

3.1.1 Actively mode-locked lasers

Active mode-locking involves periodic modulation of resonator losses, gains, or the phase of the pulses, with an external RF oscillator. The modulators can be an electro-optic modulator, an acousto-optic modulator, a semiconductor electroabsorption modulator, a Mach-Zehnder integrated modulator, or a gain element. Active mode-locking is divided into three major categories: amplitude modulation (AM) mode-locking, frequency modulation (FM) mode-locking and synchronous mode-locking.

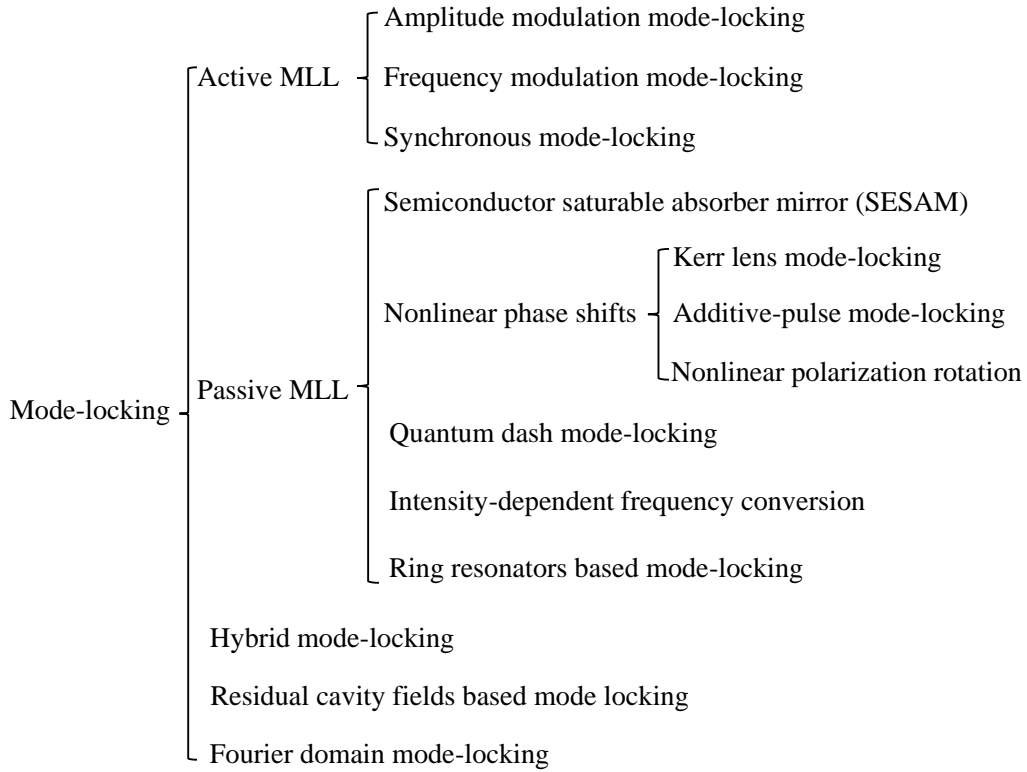


Fig. 3.2 Techniques for phase coherent frequency comb generation.

Synchronous mode-locking requires a precise match between the round-trip time of the resonator and the period of the modulator driving waveform [214]. Also, there may be timing jitter due to the mismatch. Thus synchronous mode-locking has not been widely adopted.

Amplitude modulation mode-locking requires a gain medium and a modulator in a resonator [215]. The resonator loss is altered by the modulator driven by a periodic sinusoid RF signal. Parts of the optical wave that are temporally aligned with the high resonator loss keep decreasing in power during each round trip. Thus the optical pulses become narrower until the pulse shortening effects and other pulse broadening effects cancel out.

Frequency modulation mode-locking involves periodic phase modulation [215]. It normally results in chirped optical pulses, thus it requires dispersion compensation. Frequency modulation mode-locking is based on the Pockels effect in electro-optic phase modulators or the acousto-optic effect in acousto-optic modulators.

The mode-locking using electro-optic phase modulators [216] was chosen for implementation in our laboratory. The generated optical pulses are synchronised to an electronic driving signal, which facilitates synchronization cross the whole system. In Sections 3.1.5 and 3.2, comb generation based on electro-optic modulators will be discussed in detail.

3.1.2 Passively mode-locked lasers

Passive mode-locking [217–220] does not require a signal external to the laser. Commonly, it is based on a saturable absorber. In a passively mode-locked laser, a pulse circulates in the resonator with a constant round-trip time. When the pulse passes through the saturable absorber, its peak saturates the absorption due to high optical power. Thus the loss due to the saturable absorber is equal to the gain from the gain medium at the peak, while the leading and trailing edges of the pulse are attenuated by the saturable absorber. The saturable absorber keeps reducing the pulse width until it reaches a steady state. Every time the pulse reaches the output coupler mirror, a pulse is emitted.

There are a variety of saturable absorbers, including absorbers based on ring resonators, nonlinear phase shifts, quantum dot, intensity-dependent frequency conversion, semiconductor saturable absorber mirror (SESAM).

Some of the above-mentioned devices are not suitable for optical communications. For example, Ti:Sa [221] or Er-fiber lasers [222] offer an octave-spanning bandwidth spectrum, but they operate below 10-GHz repetition rate.

Lasers based on SESAM or micro-ring resonators can reach a repetition rate of 10-GHz or higher, so they are applicable to optical communication systems.

3.1.3 ERGO pulse generating laser

A commercial ERGO pulse generating laser can deliver stable picosecond pulses [223]. It is a passively mode-locked Er-glass micro-laser based on SESAM and fundamental mode-locking. Its fundamental mode-locking, which means the laser cavity has only one pulse in it, leads to excellent amplitude and phase stability. The generated pulse width is 1-2 ps, and the timing jitter is less than 100 fs. The pulse generator delivers 10, 12.5, or 25-GHz repetition rate. The operation band is 1545 nm to 1560 nm, covering the majority of C-band for optical communications [223].

The ERGO pulse generating laser can be used in optical communications experiments in research laboratories. Its merits include self-starting, stable operation over a long period, high extinction ratios, high repetition rates, low jitter and low chirp. However, it is expensive and its repetition rate is fixed once produced. Furthermore, the saturable absorber degrades over time.

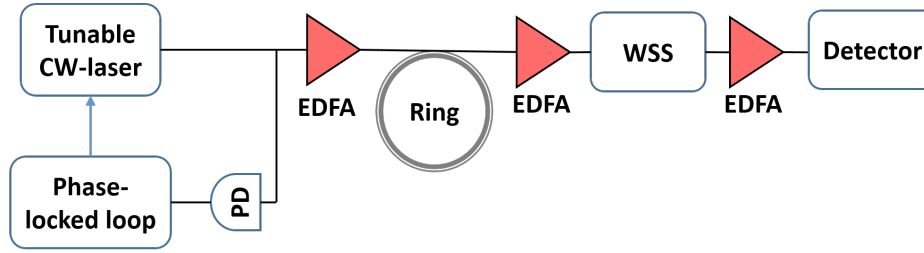


Fig. 3.3 Frequency comb generation with a monolithic micro-ring resonator.

3.1.4 Microring resonator based frequency comb generation

In recent years, chip-scale frequency combs have attracted considerable research interest [202, 200, 224]. Here are two examples of microring resonator-based frequency comb generation.

Pascal [211] has reported a microresonator-based optical frequency-comb generation with outstanding stability and noise suppression. Phase-stable optical frequency combs are generated, but with non-deterministic phase relationships among individual comb modes. As shown in Fig. 3.3, a tunable laser generates microcombs, which are then amplified and coupled into a whispering-gallery-mode of a fused silica micro-resonator with 25.6-GHz mode spacing and a quality factor, $Q = 1.85 \times 10^8$ [225]. Once the laser is tuned into the cavity resonance, the resonator is locked to the laser thermally, and generates bunched comb but with mutual offsets among different bunches. The self-injection-locking of microcombs induced by overlapping of the bunches results in a broadband offset-free frequency comb [211]. The overlap can be changed by the detuning of the pump laser frequency with respect to the microresonator mode. The phase and amplitude of each individual microcomb mode can be finely tuned by a liquid-crystal-based programmable wavelength-selective switch (WSS), to obtain a flat and phase-aligned frequency comb. The generated frequency comb has a 25.6-GHz repetition rate, 290-fs pulse width, and more than 100-dB signal-to-noise ratio [211]. The frequency comb can remain stable for more than two days, despite temperature changes and frequency drifts [211]. However, the phase relationships between individual comb modes are non-deterministic and need to be aligned by programming a WSS.

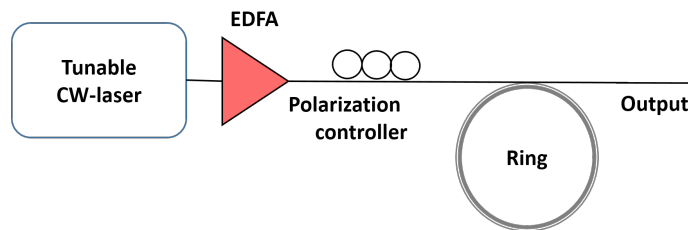


Fig. 3.4 Frequency combs generation using dissipative Kerr solitons in a microresonator.

In Pablo's work [226], 50-Tbps transmission was demonstrated using a microresonator-based soliton frequency comb. In this work, neither a phase-locked loop nor a WSS was required. The Dissipative Kerr Solitons (DKS) comb is generated via Kerr-nonlinear four-photon interactions in the Si_3N_4 microresonator. An amplified CW is pumped into the microresonator at about 35-dBm input power. At the output of the microresonator, a notch filter suppresses residual pump power to match the other carriers. The generated Kerr frequency comb has a line spacing of 95.8 GHz, a 3-dB bandwidth of more than 6 THz, a linewidth of less than 100 kHz and about 40-dB OSNR. These features support applications in optical wavelength-division multiplexing (WDM) systems. However, a precise wavelength tuning at a resolution of 1 pm is required to achieve the single-soliton state. The stability of the comb is related to the balance between dispersion, Kerr non-linearity, nonlinear parametric gain and cavity loss. The repetition rate of the frequency comb is rigidly defined by the optical resonator.

3.1.5 Optoelectronic frequency comb generation

When a continuous-wave (CW) light is modulated by electro-optic modulators driven by an external radio-frequency (RF) sinusoidal oscillator, the sinusoidal phase modulation (PM) at a frequency f generates frequency sidebands at multiples of f about the CW lasing frequency. All of the frequency sidebands generated by optoelectronic modulation will be locked to the RF clock, thus the frequency sidebands are phase locked. To achieve a chirp-free frequency comb, dispersion compensation is required.

The bandwidths of the optical frequency combs are limited by the achievable modulation depth. A number of resonant schemes have been reported to increase the modulation depth. For example, the Fabry-Perot modulator is composed of an electro-optic modulator inside a Fabry-Perot cavity [216]. The frequency comb is actively stabilized by locking the input laser to the cavity resonance. The generated frequency comb features terahertz bandwidth and sub-10 fs timing jitter. However, there are rigid requirements for the Fabry-Perot based comb generator to work. Firstly, the frequency of the RF oscillator that drives the electro-optic modulator must match precisely the free spectral range of the cavity. Secondly, the input CW laser should be precisely tuned to one of the optical resonances [195]. Therefore, to use this resonant scheme, feedback mechanisms are required to compensate for the environmental instabilities like temperature change. The long-term stability is questionable. In practice, the modulation depth of a frequency comb can be increased by increasing the RF driving voltage or cascading multiple phase modulators.

The optical frequency comb based on optoelectronic modulation is locked to an RF signal, which facilitates synchronization of the optical comb with other electronic devices. Also, the

repetition rate and the central frequency of the generated frequency comb are independently tunable. The devices required to build an optoelectronic frequency comb might be available in most optical communication laboratories. The comb frequency spacing is determined by the frequency of the RF sinusoidal signal and limited by the bandwidth of the optoelectronic modulators. Although some polymer modulators can reach a 110-GHz bandwidth [227], most commercial electro-optic modulators can only provide a bandwidth of less than 40 GHz.

3.2 Comb generation simulations and experiments

For telecommunications, the desired features of optical frequency combs are: high stability, flat-top spectrum, chirp-free, high optical signal-to-noise ratio (OSNR) (i.e. 40-dB OSNR), tunable repetition rate from 10- to 50-GHz, tunable central frequency, and phase locking to an external RF clock.

After considering the above-mentioned requirements and the equipment in our laboratory, different experimental designs have been tried. In the end, the steps described in Dou's paper were followed [171] to generate 10-GHz repetition rate, flat-top frequency combs of 90-GHz bandwidth in the experiment and 300-GHz bandwidth in the simulation, which are described in Section 3.2.2. In this scheme, there is a CW laser followed by an intensity modulator and a phase modulator, both driven by sinusoid RF signals. The phase modulator is the main contributor to the spectral broadening, and the properly biased intensity modulator shapes the spectrum to have a flat-top.

Note that no new frequency comb generation method is presented here. This section is included because building a stable phase-locked frequency comb was part of my PhD study and the content may be useful for people who want to build a frequency comb for optical communications.

3.2.1 Principle of comb generation with a phase modulation

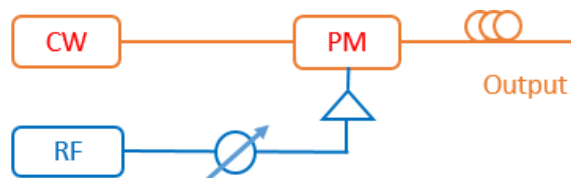


Fig. 3.5 Simulation setup of pulse compression with phase modulation and dispersion.

Figure 3.5 shows the setup of short pulse generation based on phase modulation. The CW light is chirped periodically by the phase modulator driven by a 10 GHz sinusoidal RF signal. To achieve an optical comb with a broad bandwidth, a large modulation index, $\Delta\phi_p = \pi V/V_\pi$, is required. Therefore, electro-optic modulators with a low V_π parameter and the ability to sustain high RF input power are preferable. A large bandwidth can also be achieved by connecting several phase modulators in tandem, with their phases properly aligned. Then, the chirped CW is compressed by a dispersive medium to obtain a short pulse train [228].

The numerical relation between the chirp rate K and the optimal dispersive fiber length L is given by [229]

$$K = \frac{\Delta\omega}{\Delta t} = \frac{1}{\beta_2 L} \quad (3.1)$$

where: K is the chirp rate, the product of $\beta_2 L$ is the accumulated dispersion over the fiber length L , c is the speed of light, D is the chromatic dispersion, f_0 is the centre frequency of the optical CW source.

The phase shift produced by the phase modulator driven by a sinusoidal RF signal of ω_{RF} angular frequency is

$$\phi(t) = \phi_p \cos(\omega_{RF} t) \quad (3.2)$$

where $\phi_p = \pi \frac{V}{V_\pi}$ is the peak phase deviation, i.e. modulation index. The half-wave switching voltage V_π is the voltage that induces a π phase shift in the electro-optic modulator. In the phase modulator, the parts around extrema of the sinusoid RF signal approximately give quadratic phase modulation. By isolating the quadratic part from Taylor expansion of the phase shift, the phase shift is written as [230]

$$\phi(t) = \phi_p \left[1 - \frac{(\omega_{RF} t)^2}{2} \right] \quad (3.3)$$

The chirp rate of the phase modulator is $K = \phi_p \omega_{RF}^2$. Combined with Eq. 3.1, the optimal dispersive fiber length for pulse compression is [164]

$$L = \frac{1}{\beta_2 \omega_{RF}^2 \phi_p} \quad (3.4)$$

The output of the dispersive fiber has a bandwidth Δf related to the modulation frequency f_{RF} and peak phase variation ϕ_p [231]. The pulse width is inversely proportional to the optical signal bandwidth at the output of the electro-optic phase modulator.

3.2.2 Flat top frequency comb generation - simulation

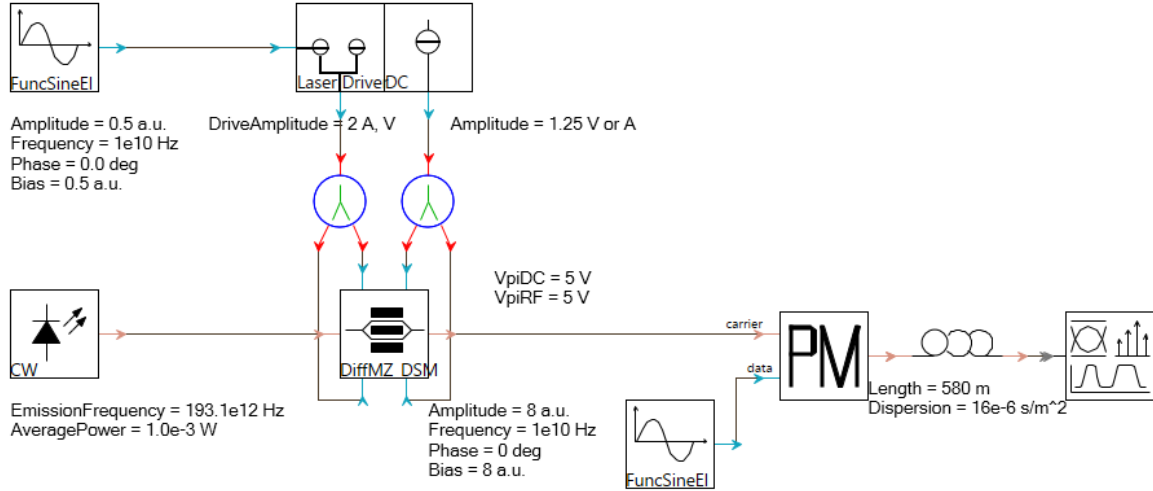


Fig. 3.6 Schematic of optical frequency comb generation and pulse compression from VPItransmissionMaker™

Optical frequency combs generated by sinusoidal phase modulation have uneven spectra. The unevenness can be balanced out using an intensity modulator (IM) [171]. The bias and the driving voltage of the intensity modulator are crucial to the flatness of the final spectrum. Also, the phase shifts between all the RF driving signals should be zero or very close to zero. The bandwidth of the final frequency comb is directly related to the driving voltage of the phase modulator.

In the simulation, a CW laser is modulated by a dual-drive MZM followed by a phase modulator, both driven by a single 10-GHz sinusoidal RF source, as shown in Fig. 3.6. The dual-drive MZM is used as an intensity modulator by applying 180°-out-of-phase signals to its inputs. The DC bias of the MZM is $0.25 \times V_\pi$, and the amplitude of the driving signal is $0.4 \times V_\pi$, where $V_\pi = 5$ V is the voltage for π phase shift. To generate about 30 comb carriers with a small power variation, the driving voltage of the PM should be 8 times of the voltage for a π phase shift at 10 GHz. A dispersive fiber with dispersion = 16×10^{-6} s/m² and length = 500 m compresses the pulses. According to Fig. 3.7, the output spectrum of the PM has about 30 comb lines with 1.5-dB peak-to-peak power variation at 10-GHz spacing.

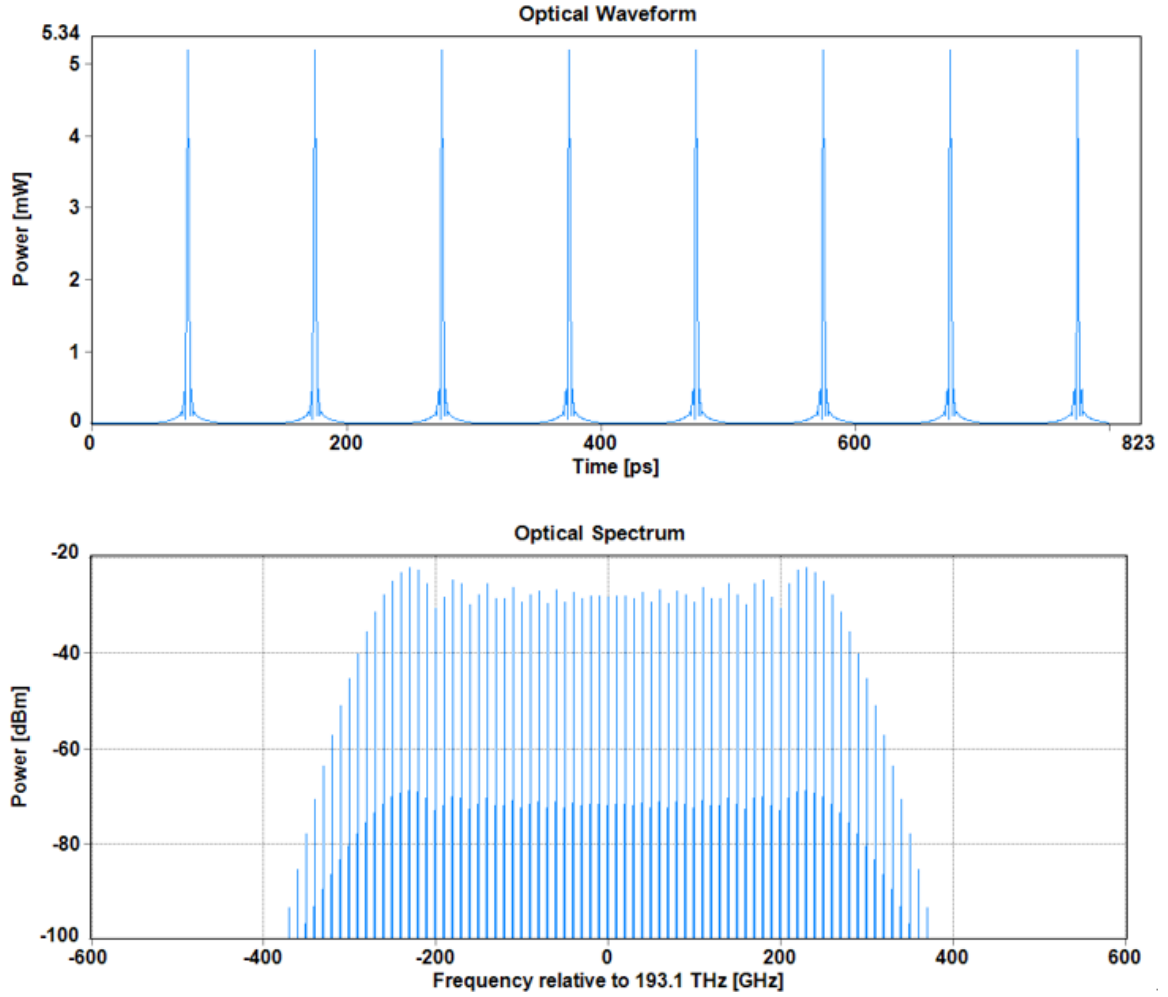


Fig. 3.7 Simulated optical waveform and spectrum of compressed pulses with VPItransmissionMakerTM

3.2.3 Flat-top frequency comb generation - experiment

The same procedure as described in Section 3.2.2 was used to perform the experiment. In the experiment, the DC bias of IM is 0.77 V, and the driving sinusoid amplitude is 0.8 V peak-to-peak. The intensity modulator is COVEGA Mach-10 zero-chirp IM. The driving RF power of the PM is 29 dBm. The phase modulator is COVEGA LN058 low V_π modulator. The resultant spectrum is a frequency comb composed by 9 carriers with 10-GHz spacing, as shown in Fig. 3.10. The number of comb lines was increased from 9 to 15 by adding a second PM. The auto-correlation of the generated pulse are shown in Section 3.3.2.

3.3 Short pulse characterization

3.3.1 Autocorrelation measurement methods

9 coherent frequency comb lines with 10-GHz spacing and almost equal power with less than 2-dB variations were generated by the experiment in Section 3.2.3. The 90-GHz bandwidth of the frequency comb is larger than most of the commercial oscilloscope's bandwidths (e.g. 63 GHz). In order to estimate the width of the short pulses, an optical autocorrelator is needed. The commercial autocorrelator has the structure shown in Fig. 3.8. The pulse to be measured is split into two and delayed one with respect to the other, and overlapping them in a second-harmonic-generation (SHG) crystal. The second harmonic of the signal

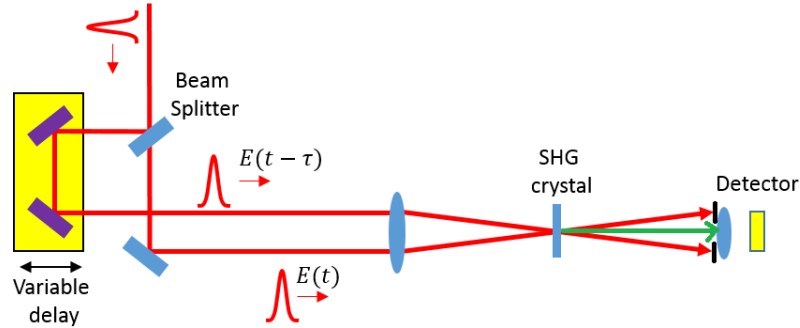


Fig. 3.8 Layout of an intensity autocorrelator using second-harmonic generation.

will be produced at twice the frequency of input light in the SHG crystal when the pulses from the two paths overlap. The intensity of the SHG signal is proportional to the product of the intensities of the two input signals $I(t)I(t - \tau)$. The photodetector integrates because its response is usually much slower than the short pulse width. The intensity autocorrelation is given by

$$A(\tau) = \int_{-\infty}^{\infty} I(t)I(t - \tau)dt \quad (3.5)$$

The delay τ is scanned through by horizontally moving the two mirrors on the left. However, the method requires precise alignment of the mirrors and the SHG crystal. As a result, another method, shown in Fig. 3.9, was used to measure the pulses using interference.

The principal of this interference method is similar to the above mentioned SHG method, giving an output proportional to the value calculated in Eq. 3.5. A 50/50 coupler and a balance photo-detector act as the replacement of the SHG and the detector in the SHG method.

In the interference method, the pulse to be measured is split into two separate paths by the 50/50 coupler. In one path, the pulse is delayed by time τ relative to the other path. The

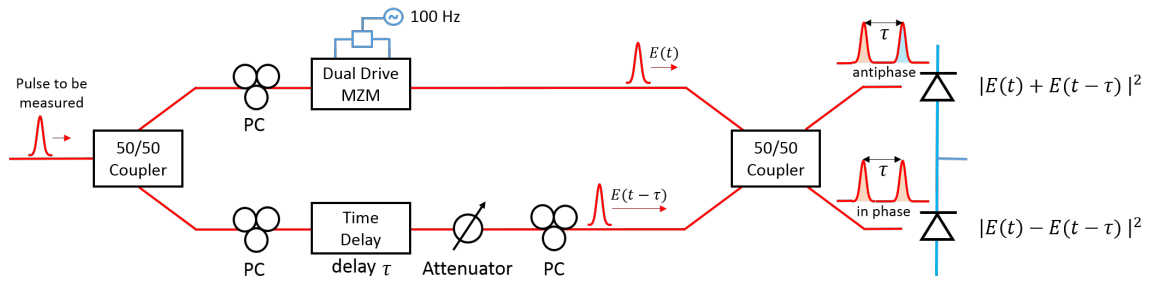


Fig. 3.9 Experimental setup for the autocorrelation.

delay time τ is swept with constant step and the sweep range should be long enough to reveal the width of the measured pulse. This optical delay line in Fig. 3.9 has the same function as the variable delay in Fig. 3.8. The optical field of one optical pulse and its delayed version are represented as $E(t)$ and $E(t - \tau)$ respectively.

The attenuator and the polarization controllers (PCs) are used to make the pulses on both paths have the same power and polarization. Between the two 50/50 couplers, the optical phases of the two paths are randomly and independently changing, thus a phase modulation is required to scan through all the possible phases to achieve the 90° relative phase of $E(t)$ and $E(t - \tau)$. In Fig. 3.9, the pulse in one arm is phase modulated by a dual-drive MZM driven by a 100-Hz sinusoid RF source.

When the pulses from the two paths recombine in the second 50/50 coupler, the output of the coupler depends on the relative phase and relative time delay of the two incoming pulses. When the time delay τ is large, the two pulses separated by delay τ are not overlapped. Both photodiodes generate the same pulse, and the subtraction results in complete cancellation. When the time delay τ is small, the two pulses are partially overlapped. If the relative phase of the two incoming pulses $E(t)$ and $E(t - \tau)$ is 90° , the two pulses on the coupler's output upper arm are antiphase (180° relative phase) and the overlapping part is cancelled out $E(t) - E(t - \tau)$. The two pulses on the lower arm are in phase (0° relative phase), so the overlapping parts add up $E(t) + E(t - \tau)$.

The output of the photo-detector is high-rate short pulses with low-rate sinusoid envelope. The sinusoid envelope is caused by the slowly varying phase differences of the signal on the two arms. The maxima of the measured peak-to-peak voltage is recorded for each time delay. A MATLAB program can be used to step through the time delay and record the corresponding voltage value. As such, the autocorrelation of the optical short pulses can be achieved.

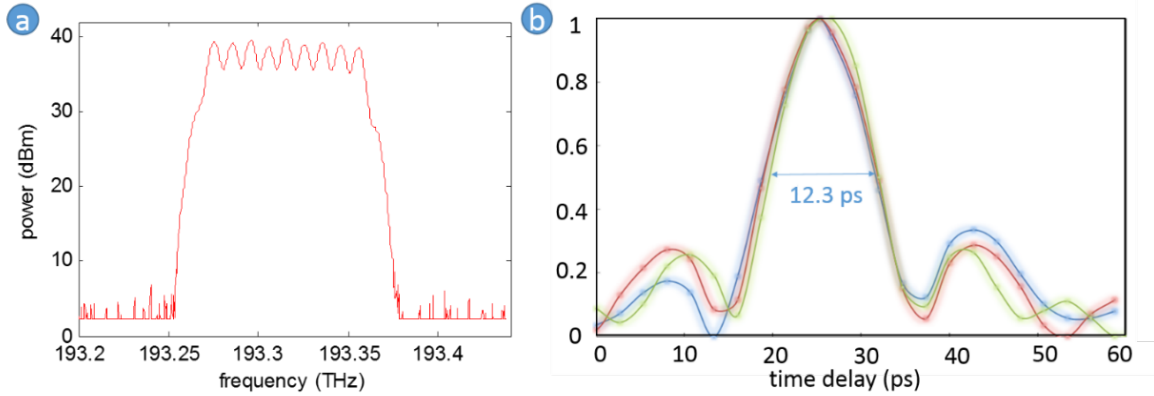


Fig. 3.10 (a) The spectrum and (b) the autocorrelation of a flat top frequency comb (short pulses) with a 90-GHz bandwidth and a 10-GHz comb spacing.

3.3.2 Autocorrelation measurement of experimental results

Figure 3.10 shows the frequency comb with 10-GHz spacing and corresponding autocorrelation of the pulse intensity. The spectrum is rectangular, that means the temporal waveform should be sinc. The bandwidth of experimentally generated frequency comb is 90 GHz, thus the expected pulse width is 11.1 ps. The autocorrelation of a sinc pulse is itself, so the measured sinc pulse width is 12.3 ps, as shown in Fig. 3.10. A flat top frequency comb with 150-GHz bandwidth and 10-GHz spacing was also generated. The expected pulse width is 6.7 ps, and the measured pulse width is 7.5 ps, as shown in Fig. 3.11.

The measurement results are close enough to our expectation that we are confident in the coherence of the generated pulses, and so of their usefulness in the experiments to follow in this thesis. The measured deviation from expected values is probably due to several factors. Firstly, the flat comb is generated by filtering Gaussian spectrum with programmable optical filter, which has a spectral resolution of 10 GHz. The spectral resolution is equal to the comb spacing, so the output spectrum may not have the expected rectangular shape. The temporal pulses may not be ideally sinc shaped. Secondly, the polarization of the time delay in the auto-correlator may change due to physical perturbations to the setup, especially when tuning the time delay by hand. Thirdly, the auto-correlator should be built by fibers with zero dispersion, but it is not available in the laboratory. SMF28 was used instead. Therefore, the measured autocorrelation is an approximation of the actual autocorrelation. Finally the resolution of the device shown in Fig. 3.9 is limited by the path length difference after the final 50/50 coupler to each of the PDs.

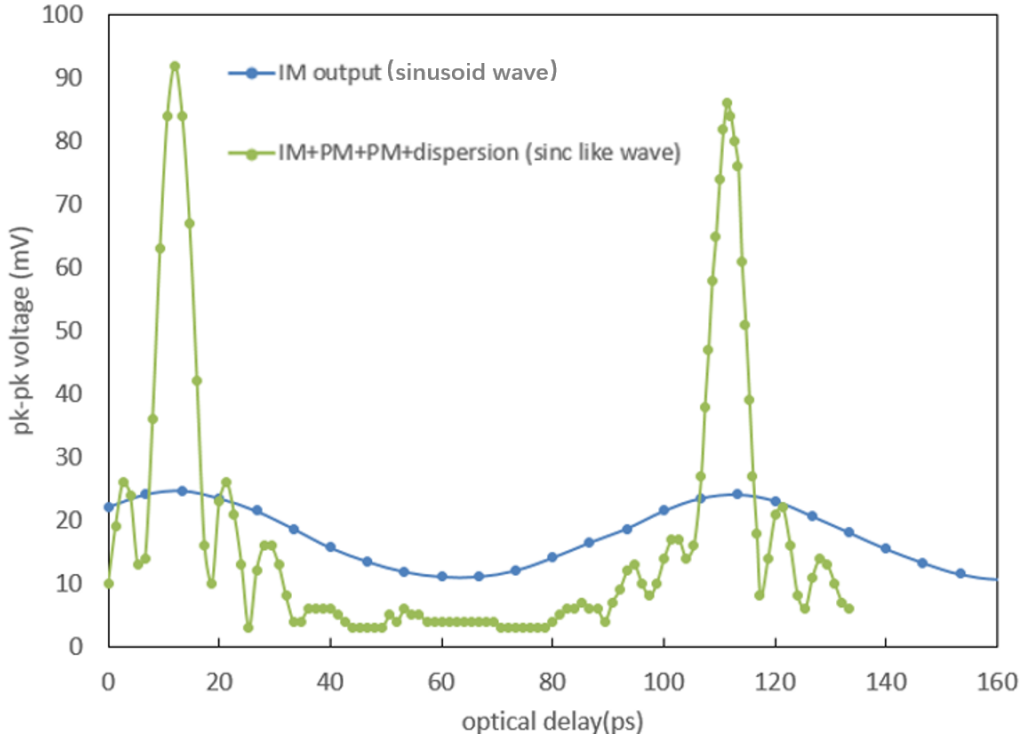


Fig. 3.11 The measured autocorrelation of a short pulse train with a 150-GHz bandwidth and a 10-GHz spacing (green), and the autocorrelation of a 10-GHz sinusoid wave (blue).

3.4 Comb repetition rate manipulation

The content in this section was published in Optics Express [60].

In the previous section, the methods to generate frequency combs were discussed. Since some of the optical frequency comb generation methods do not support tunable repetition rates or the tuning range is limited. A novel method to manipulate the repetition rate of the frequency comb was proposed. The photonic chip in this section was designed by Leimeng Zhuang and fabricated by LioniX.

3.4.1 Motivation for comb repetition rate manipulation

Introducing control of the repetition rate of an optical clock signal will greatly benefit optical frequency comb applications in terms of system flexibility and potential for wide-spread deployment. When applied to optical sampling in communication systems, for example, sampling rate adaptability is a useful technique for variable symbol rates in next generation elastic optical communication networks [23]. For LIDAR systems, the optical clock rate variability allows for optimum detection of objects at different distances or with different reflections [232].

Conventionally, an optical clock signal with a frequency comb spectrum can be generated using a fiber-based resonant cavity [233] or a serial cascade of multiple electro-optic modulators [231]. From a practical perspective, on-chip implementation of optical clock sources is highly desired as it provides an ultimately stable and compact solution [53, 234]. However, it is difficult to incorporate comb spacing variation, i.e. clock rate variation, in such sources due to the fixed device structures. An effective solution for this drawback is to use external optical comb filters. In principle, spatial light modulators are a straightforward approach to synthesize arbitrary filter shapes [235]. However, this approach requires a combination of free-space optical devices, which typically have a spectral resolution about 10 GHz [236] and need feedback control.

As an alternative approach, interferometric filters implemented in photonic integrated circuits (PICs) open a path for practical solutions. PIC-based filters not only enjoy the general advantages inherent to the PIC technologies [237–242, 25] such as small size, low weight, low power consumption (small SWaP), ultimate stability and control precision, and a strong potential for low-cost volume fabrication, but also offer great design flexibility and the possibility to be incorporated in programmable signal processors [105, 243]. However, such filters conventionally suffer from a tradeoff between the key performance metrics such as operational bandwidth, circuit complexity, insertion loss, and the chip size. In particular, the feature of sub-GHz frequency selectivity requires significant waveguide path lengths, e.g. in the order of a centimetre or longer [154]. In fact, this requirement severely affects PICs using high-index-contrast waveguides such as silicon materials [237–241] and III-V semiconductors [242, 25], which are being widely investigated in both academia and industry because of their intrinsic superiority in device compactness and function diversity over their low-index-contrast counterparts. Typically, filters using such waveguides are more susceptible to fabrication imperfections that affect the waveguide geometry and uniformity [244], causing degradation in key performance metrics, i.e. higher waveguide loss and reduced operational bandwidth. In addition, waveguide materials with high nonlinearity and dispersion such as silicon on insulator [237] and indium phosphide [242] may give rise to significant phase errors between the waveguide paths, particularly with long waveguides, which limits the filter performance.

A new PIC implementation of an optical clock multiplier is reported. This chip was designed by Leimeng Zhuang and fabricated by LioniX. It comprises a novel topology of a ring-resonator-assisted asymmetric Mach-Zehnder interferometer (A-MZI) incorporated in a Sagnac loop, providing a reconfigurable comb filter with sub-GHz frequency selectivity and low complexity. A proof-of-concept device is fabricated in a stoichiometric $\text{Si}_3\text{N}_4/\text{SiO}_2$ waveguide, featuring low loss, small size, and large bandwidth. As additional features, this

circuit topology provides a promising solution for optical comb filters that have significantly lower requirement for control precision than conventional ring resonator-based filters [245–248] and have a 2-orders-of-magnitude advantage in size when compared with tapped-delay-line filters [249, 250].

3.4.2 Design principle

Table 3.1 Circuit parameters for the filter

	κ_1	κ_2	ϕ_0^*	ϕ_n
No ring	0	0	$\in [0, \pi]$	$\phi_0 + \pi$
1 ring	0.78	0	$\in [0, \pi]$	$\phi_0 + \pi$
2 rings	0.89	0.35	$\in [0, \pi]$	$\phi_0 + \pi$

* $\phi_0 \in [0, \pi]$ allows a tuning range of the filter-passband center frequency equal to the passband interval.

Figure 3.12 (a) shows the filter's topology. The A-MZI has identical ring resonators attached to both of its arms, and has Port 3 and 4 interconnected forming a Sagnac loop. The coupling between the ring resonators and the A-MZI is implemented using 2-by-2 tunable couplers [105, 243]. As an important part of the filter reconfigurability, each ring resonator can be completely decoupled from the A-MZI when its coupling coefficient is set to zero. In effect, this enables the synthesis of a variety of filter transfer functions, by simply choosing a different number of ring resonators. The Sagnac loop in the filter serves as a mirror, which reflects an input lightwave (e.g. from Port 1) so that it passes the A-MZI twice in opposite directions. To derive the filter transfer function, an equivalent lattice-structured circuit topology can be used as shown in Fig. 3.12 (b). In this topology, the filter reduces to a 1-dimensional network of two identical 2-by-2-port sections, i.e. two A-MZIs with one being a vertically inverted version of the other, which can be described using a transfer matrix [154]. The A-MZIs have an arm-length difference equal to half of the ring resonator's roundtrip length, the time delay and corresponding spectral period of which define the unit delay, $\Delta\tau$, (minimum delay difference between the optical paths) and the free spectral range (FSR) of the A-MZI, Δf_{FSR} , respectively. The transfer matrix of an A-MZI, in the case that it stands alone, is given by

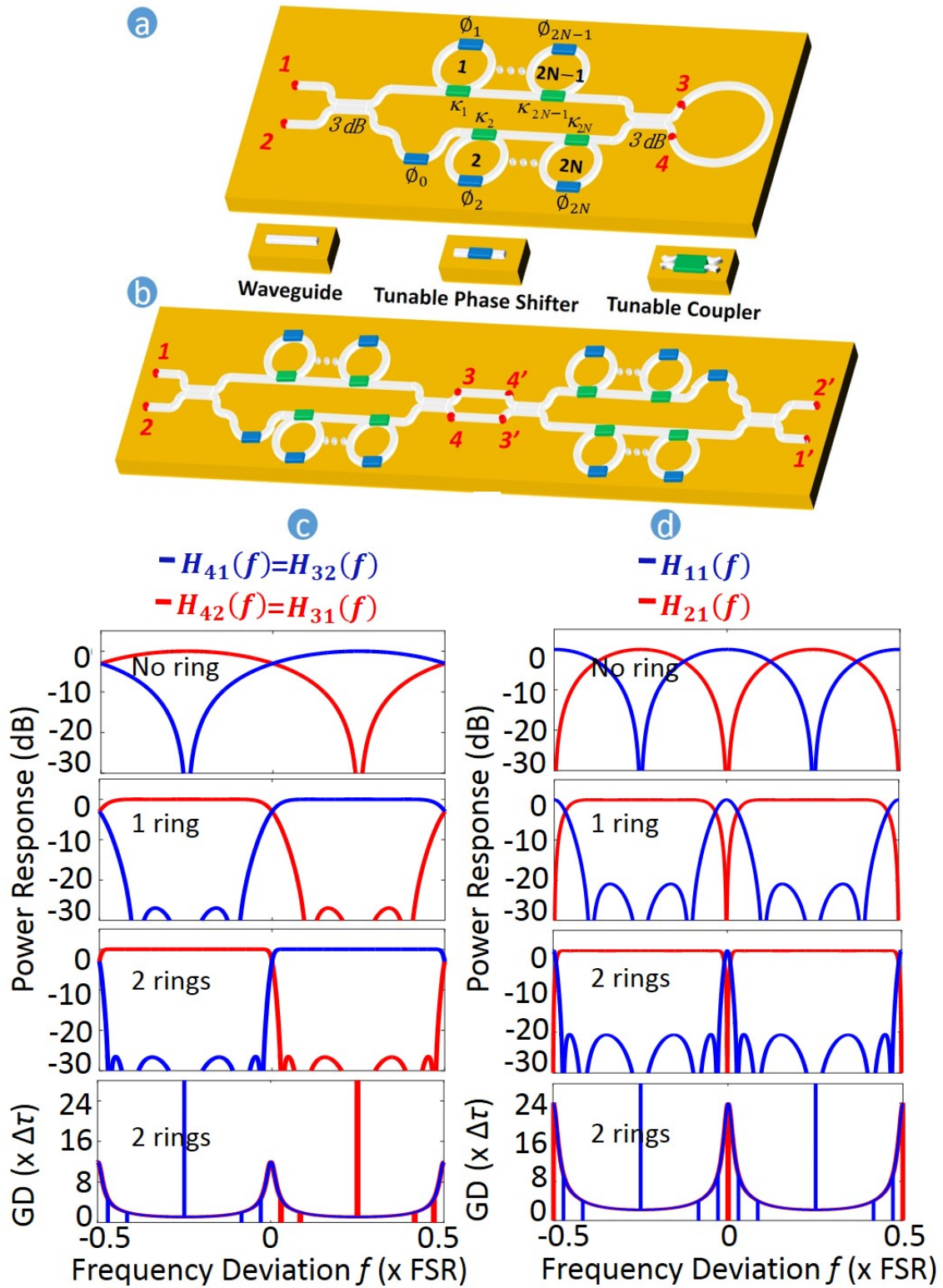


Fig. 3.12 (a) A schematic of the novel filter topology, (b) an equivalent lattice-structured circuit, (c) an illustration of the interleaving Chebyshev Type II filter shapes and group delays (GDs) of an A-MZI, (d) corresponding filter shapes and GDs at the outputs of the novel filter topology in (a).

$$\begin{aligned}
\begin{bmatrix} H_{31}(f) & H_{41}(f) \\ H_{32}(f) & H_{42}(f) \end{bmatrix} &= \begin{bmatrix} H_{1'3'}(f) & H_{1'4'}(f) \\ H_{2'3'}(f) & H_{2'4'}(f) \end{bmatrix} \\
&= \eta \begin{bmatrix} \frac{\sqrt{2}}{2} & -j\frac{\sqrt{2}}{2} \\ -j\frac{\sqrt{2}}{2} & \frac{\sqrt{2}}{2} \end{bmatrix} \begin{bmatrix} \prod_{n=1,3,5,\dots}^{2N+1} R_n(f) & 0 \\ 0 & D(f) \prod_{n=2,4,6,\dots}^{2N} R_n(f) \end{bmatrix} \begin{bmatrix} \frac{\sqrt{2}}{2} & -j\frac{\sqrt{2}}{2} \\ -j\frac{\sqrt{2}}{2} & \frac{\sqrt{2}}{2} \end{bmatrix} \quad (3.6)
\end{aligned}$$

with

$$D(f) = t e^{-j2\pi f / \Delta f_{FSR}} e^{-j\Phi_0} \quad (3.7)$$

$$R_n(f) = \frac{\sqrt{1 - \kappa_n} - t^2 e^{-j4\pi f / \Delta f_{FSR}} e^{-j\Phi_n}}{1 - \sqrt{1 - \kappa_n} - t^2 e^{-j4\pi f / \Delta f_{FSR}} e^{-j\Phi_n}} \quad (3.8)$$

in which $D(f)$ and $R(f)$ describe the inter-arm delay line and ring resonator, respectively, with t the amplitude factor determined by the waveguide loss of a unit delay length, ϕ_n the tunable phase shift, κ_n the power coupling coefficient, and η a complex coefficient describing the overall insertion loss and phase shift of the A-MZI. Importantly, such an A-MZI is able to synthesize a spectrally interleaved pair of Chebyshev Type II filters featuring equal-ripple stopbands [154] at the two complementary outputs. Figure 3.12 (c) demonstrates such filter shapes for three cases where different number of ring resonators are coupled to the A-MZI. The corresponding filter coefficients are shown in Table 3.1. Based on this, the overall transfer matrix of the entire lattice-structured network is given by

$$\begin{aligned}
\begin{bmatrix} H_{2'1}(f) & H_{2'2}(f) \\ H_{1'1}(f) & H_{1'2}(f) \end{bmatrix} &= \begin{bmatrix} H_{31}(f) & H_{32}(f) \\ H_{41}(f) & H_{42}(f) \end{bmatrix} \begin{bmatrix} H_{2'4'}(f) & H_{2'3'}(f) \\ H_{1'4'}(f) & H_{1'3'}(f) \end{bmatrix} \\
&= \begin{bmatrix} H_{31}(f)H_{2'4'}(f) + H_{32}(f)H_{1'4'}(f) & H_{31}(f)H_{2'3'}(f) + H_{32}(f)H_{1'3'}(f) \\ H_{41}(f)H_{2'4'}(f) + H_{42}(f)H_{1'4'}(f) & H_{41}(f)H_{2'3'}(f) + H_{42}(f)H_{1'3'}(f) \end{bmatrix} \quad (3.9)
\end{aligned}$$

Then, by combining the above equations, the transfer matrix of the novel filter topology in Fig. 3.12 (a) results to be

$$\begin{aligned} \begin{bmatrix} H_{11}(f) \\ H_{21}(f) \end{bmatrix} &= \begin{bmatrix} H_{22}(f) \\ H_{12}(f) \end{bmatrix} \\ &= \begin{bmatrix} 2H_{31}(f)H_{41}(f) \\ H_{31}(f)H_{42}(f) + H_{41}(f)H_{32}(f) \end{bmatrix} \end{aligned} \quad (3.10)$$

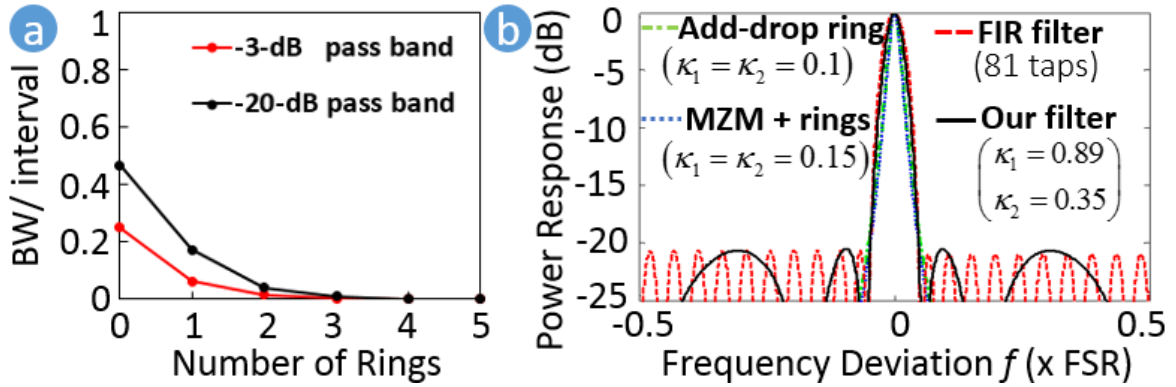


Fig. 3.13 (a) Calculations of filter passband bandwidth relative to interval as a function of the number of ring resonators. (b) Passband comparison between different filter designs, i.e. a tapped-delay-line (FIR) filter with 81 taps, a serial cascade of two add-drop ring resonators, and a serial cascade of two RAMZIs.

Figure 3.12 (d) demonstrates the filter shapes of $H_{11}(f)$ and $H_{21}(f)$, which are a complementary pair. In association with the spectral periodicity of the device, $H_{11}(f)$ provides a narrow-passband optical comb filter with reconfigurable bandwidth. The spectral passbands and similar-shaped group delays repeat themselves at a frequency interval (spectral period) equal to half of the A-MZI's FSR. This is because for $H_{11}(f)$ an input lightwave will sequentially pass two interleaving filter shapes of the A-MZI where the passband overlapping occurs at an interval of half FSR (Fig. 3.12 (c)). Regarding this filter property, Fig. 3.13 (a) shows the filter passband bandwidths relative to the interval as a function of the number of ring resonators. From a practical viewpoint, using two ring resonators provides both excellent frequency selectivity and a low circuit complexity (a low number of building blocks such as delay lines, couplers, and tuning elements). Figure 3.13 (b) shows the implementation advantages over several conventional filter topologies. For comparison, similar passband characteristics will require 81 taps for a tapped-delay-line filter. Such a large number of taps (delay lines) would require a 2-orders-of-magnitude larger chip area and tens of times longer waveguides. As a result, the fabrication of such a filter will be more prone to severe issues of

wafer uniformity and waveguide loss that lead to poor filter performance or total functional failure. Alternatively, conventional ring resonator-based topologies such as add-drop rings [245, 246] and ring resonator-assisted Mach-Zehnder interferometers (RAMZIs) [247, 248] feature similar circuit complexity. However, these will require the ring resonators to operate with much higher quality factors (shown by much lower κ in Fig. 3.13 (b)) to provide comparable filter passband characteristics. As a result, the filter performance and stability of the ring resonator is more sensitive to ambient disturbances and therefore will require more precise control during operation.

3.4.3 Device description

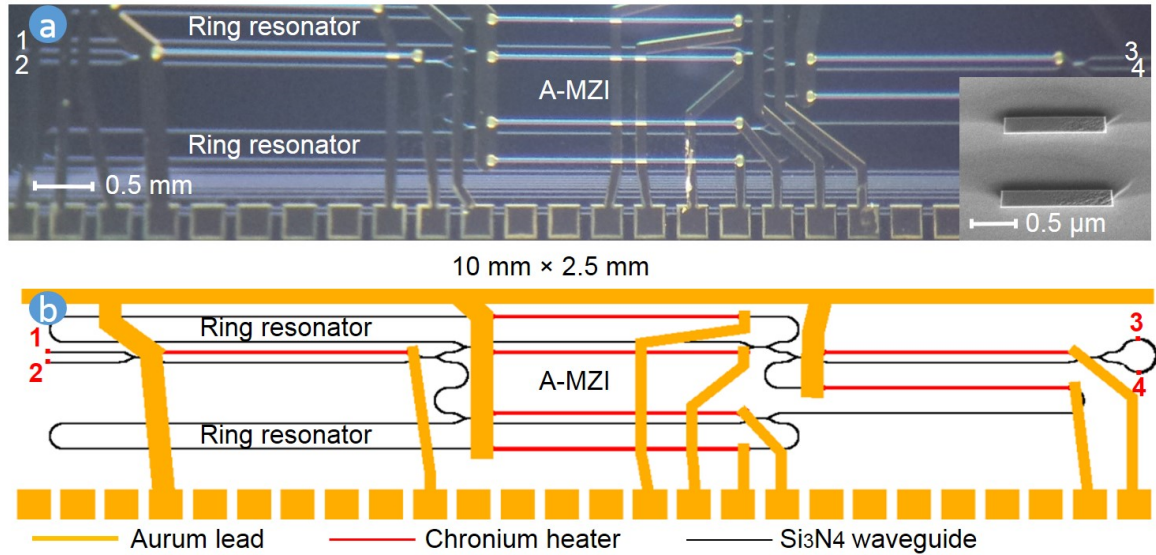


Fig. 3.14 (a) A photomicrograph of a fabricated chip. Inset: a scanning electron microscope (SEM) photograph of the waveguide cross-section. (b) The chip mask layout design.

Recent advances in PIC technology has demonstrated a $\text{Si}_3\text{N}_4/\text{SiO}_2$ waveguide platform (TriPleXTM, proprietary to Lionix B.V., The Netherlands) [241, 247] that provides a low waveguide propagation loss of lower than 0.1 dB/cm at a bend radius of 70 μm or larger, and a low wavelength dispersion at 1550 nm. Using this waveguide, a proof-of-concept filter was fabricated for the experimental verification. A microphotograph is shown in Fig. 3.14 (a). As shown in the inset of Fig. 3.14 (a), the waveguide consists of two strips of Si_3N_4 with a thickness of 170 nm, spaced vertically by 500 nm and surrounded by SiO_2 . This waveguide geometry increases the effective index of the optical mode compared to a single strip geometry, which results in higher mode confinement and lower bend losses.

The top strip has a width of $1.2\ \mu\text{m}$ and the sidewall angle of the waveguide is between 80° and 82° due to the etching process, which only supports a single mode at $1550\ \text{nm}$ and is optimized for coupling of TE polarization. The waveguide has a group index of 1.72 and wavelength dependency of $2 \times 10^{-5}/\text{nm}$, respectively. The fabricated filter uses a bend radius of $125\ \mu\text{m}$ to guarantee a low waveguide propagation loss and employs a circuit topology with two ring resonators (one on each arm of the A-MZI) corresponding to a chip size of $10 \times 2.5\text{mm}^2$ as shown in Fig. 3.14 (b). The circumference of the ring resonators and the MZI inter-arm delay difference are designed to be $1.4\ \text{cm}$ and $0.7\ \text{cm}$, respectively, resulting in an FSR of $12.5\ \text{GHz}$ for the ring resonator and an FSR of $25\ \text{GHz}$ for the A-MZI. The phase shifters are implemented thermo-optically using electrical resistor-based heaters placed on top of the waveguide; the tunable couplers are implemented using MZI couplers with phase shifters in its arms [105, 243]. The heaters have a size of $2000 \times 20\ \mu\text{m}^2$ for easy fabrication and alignment with waveguides, a tuning speed in the order of milliseconds, and an optical phase shifting efficiency of $\pi/250\ \text{mW}$. In this chip, an average power consumption of about $125\ \text{mW/heater}$ is used to compensate the initial circuit parameter offsets and to set the parameters to the target values. An effective measure to reduce the thermo-crosstalk is taken by etching trenches on both sides of the waveguide sections with heaters on top. This suppresses the crosstalk in terms of optical phase shift to less than 5% for a waveguide spacing of $100\ \mu\text{m}$. The filter has a total insertion loss of $9\ \text{dB}$ when coupled using 1550-nm standard single-mode fibers at both ends, with a polarization-aligned input. This includes two times fiber-chip coupling loss about $4\ \text{dB/facet}$ (estimated using separate test waveguide structures) and on-chip loss of less than $1\ \text{dB}$ with assumption of possible excess loss of the couplers in the circuit. In principle, the fiber-chip coupling efficiency can be further improved by using an optimal taper design of the waveguide facet, which should reduce the coupling loss to about $1\ \text{dB/facet}$ [251].

3.4.4 Experiment and results

The filter shapes measured using an optical vector analyzer (Luna System OVA5000) are shown in Fig. 3.15 (a) to 3.15 (f). The tuning elements (filter coefficients) are controlled in accordance to the calculations in Fig. 3.12. Figure 3.15 (a) to 3.15 (b) show the measured filter shapes and group delays at Port 1 and Port 2, for which the input light was applied to Port 1 via a circulator (AFW Technologies) and both ring resonators were coupled to the A-MZI. The two filter shapes manifest to be a complementary pair, demonstrating the capability of providing both narrow-bandpass and notch filtering functions. For the comb filter application in this work, the narrow-passband filter shape at Port 1 is investigated further. The passbands and similar-shaped group delays repeat themselves at a frequency

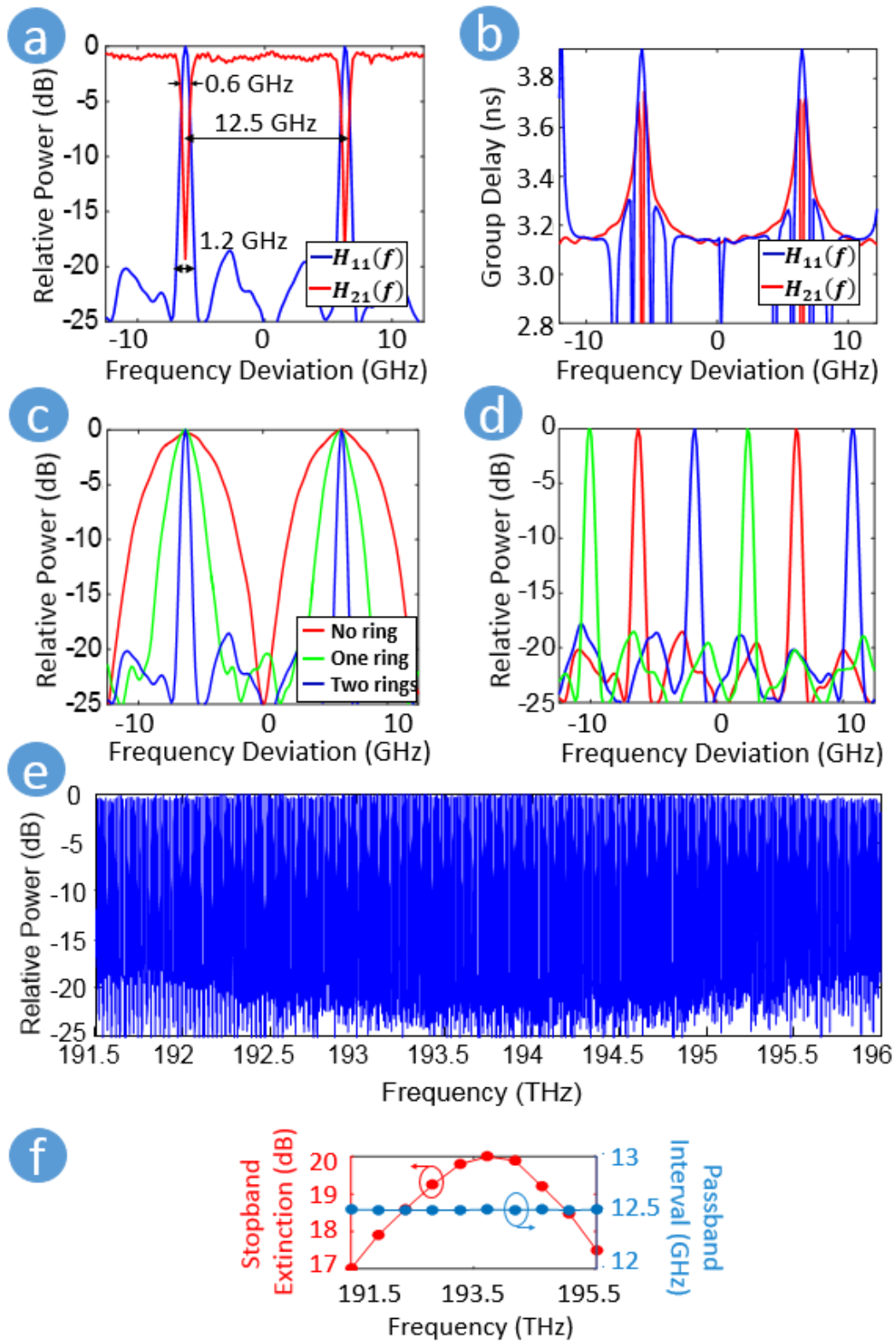


Fig. 3.15 Measured filter shapes demonstrating: (a-b) the capability of providing both narrow-passband and notch filtering functions, (c) the ability to select the pass-band-width, (d) the tuning of the passband's center frequency, (e) The full C-band coverage of the fabricated chip. The responses are normalized to their maximum values. (f) Stopband extinction and passband interval versus wavelength.

Table 3.2 Overview of several representative comb filters

Ref.	Components	Material	BW (GHz)	FSR (GHz)	Finesse	>20dB Ext.	Loss (dB/cm)	RC	NTE
[252]	RR	SOI	1	50	50	Yes	0.5	Yes	5
[248]	MZI, RR	SOI	0.8	16.5	20.6	Yes	3	Yes	10
[253]	MZI	SOI	1.536	13.5	8.8	No	3	Yes	10
[254]	RR	SOI	2.625	25	9.5	No	6	No	N.A.
[249]	MZI, RR	SOI	3.5	25	7.1	No	6	Yes	7
[94]	MZI, RR	SOI	0.4	10	25	Yes	0.4	Yes	26
[255]	MZI, RR	InGaAsP/InP	3	20	6.7	Yes	5.5	Yes	6
[256]	MZI, RR, SOA	InGaAsP/InP	3.9	26.5	6.8	Yes	N.A.	Yes	21
[257]	MZI, RR, SOA	InGaAsP/InP	1.9	23.5	12.4	Yes	N.A.	Yes	29
This work	MZI, RR	Si ₃ N ₄ /SiO ₂	0.6	12.5	20.8	Yes	0.1	Yes	5

RR: ring resonator, MZI: Mach-Zehnder interferometer, SOA: semiconductor optical amplifier, RC: reconfigurability, NTE: number of tuning elements, Ext: Extinction, BW is 3-dB bandwidth.

interval of 12.5 GHz. The passband shape features a -3-dB bandwidth of 0.6 GHz and a -20-dB bandwidth of 1.2 GHz, which are far narrower than previous demonstrations of similar filter shapes that had FSRs in the order of tens of GHz [247, 248, 251–254, 94, 255, 256]. An overview of several representative comb filters is shown in Table 3.2. Figure 3.15 (c) shows the filter shapes obtained when no ring resonator, one ring resonator or both ring resonators were coupled to the A-MZI. This result clearly shows that the bandwidth of the filter is adjustable. Figure 3.15 (d) shows the full-range tuning of the center frequency of the filter passbands. This tuning was performed by applying coordinated phase shifts (Table 3.1) to all phase shifters in the filter simultaneously. The results in Fig. 3.15 (c) and 3.15 (d) demonstrate the reconfigurability of the filter. As another important metric of the filter performance, Fig. 3.15 (e) shows a filter shape measurement with a frequency span of 4.5 THz, i.e. ranging from 191.5 THz to 196 THz. Figure 3.15 (f) shows a nearly constant passband interval of 12.5 GHz and a fluctuation of stopband power extinction of about 3 dB over the complete range. This large bandwidth is accredited to the accurate design, low wavelength dispersion, and excellent waveguide uniformity of the fabricated chip.

As an application example, a comb filter was used as an external optical clock multiplier. In this experiment, first, an optical clock signal at 1550 nm with a fixed repetition rate of 2.5 Gpulse/s was used as the input to Port 1. The input has a 3-dB bandwidth of about 50 GHz and a pulse width of about 10 ps. Figure 3.16 (a) shows the measurements of this pulsed signal in both the frequency (top) and time domains (bottom), where a frequency spacing of 2.5 GHz was measured between the frequency comb lines, associated with a pulse time interval of 400 ps. The filter was configured with two ring resonators coupled to the A-MZI to provide the narrow passband filter shape as shown in Fig. 3.16 (a). Moreover, the filter

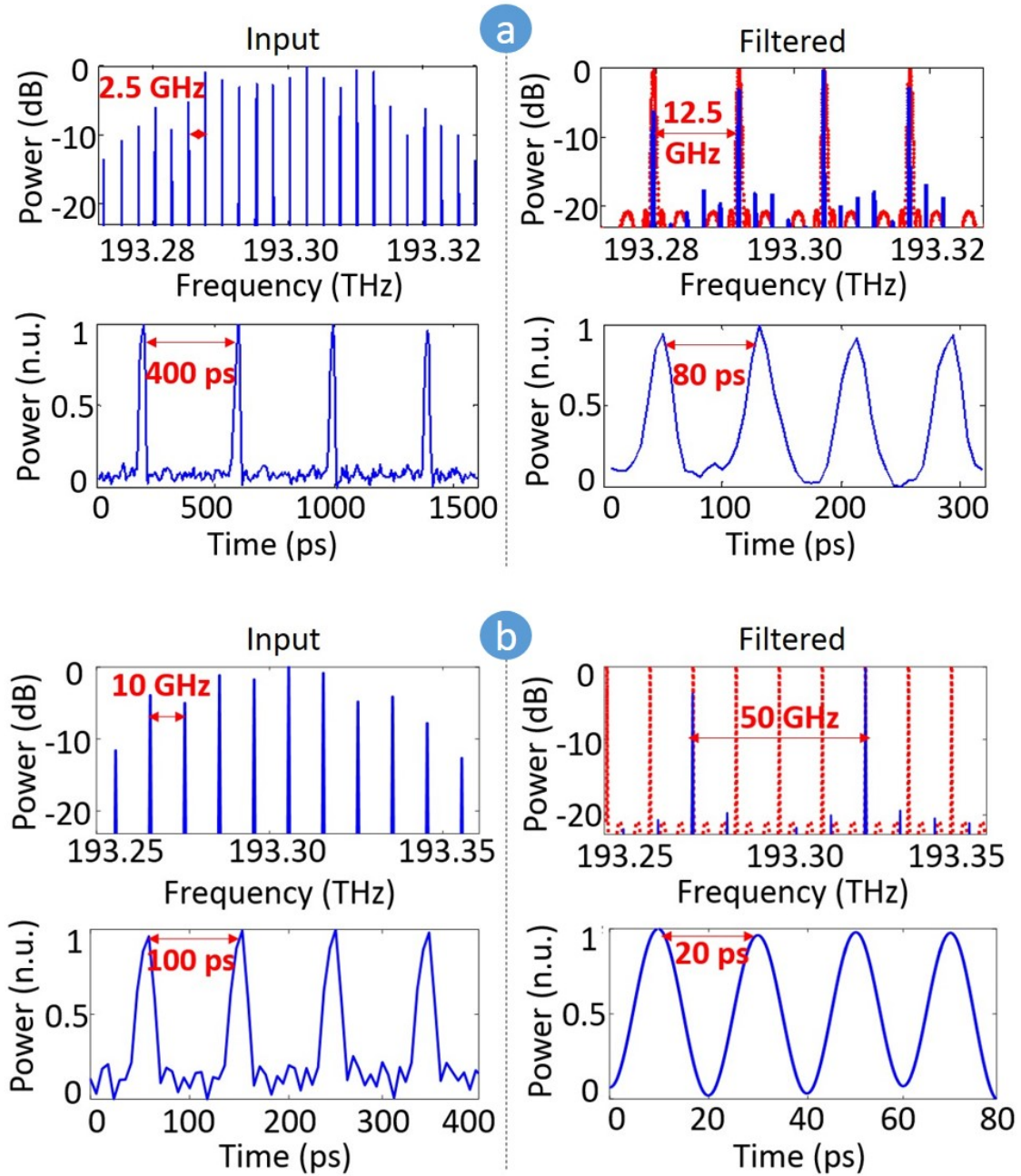


Fig. 3.16 Demonstration of five-fold repetition rate multiplication of periodically pulsed optical signals: (a) from 2.5 Gpulse/s to 12.5 Gpulse/s, (b) from 10 Gpulse/s to 50 Gpulse/s. The signal spectra were measured using a high-resolution optical spectrum analyzer (Agilent 8164B) and the waveforms were measured using a 50-GHz real-time oscilloscope (Agilent DSO-X 95004Q).

has its passbands frequency-aligned to the comb lines such that each passband allows only one in every five comb lines to pass the filter, while suppressing the other four comb lines that are out of the passbands. In effect, the filter performed a sharp spectral selection of frequency comb lines at a frequency spacing of 12.5 GHz, which in the time domain modifies the time interval of the pulses to 80 ps, or equivalently a repetition rate of 12.5 Gpulse/s. Next, another optical clock signal was applied to the filter input, which has a repetition rate of 10 Gpulse/s and a comb spacing of 10 GHz as shown in Fig. 3.16 (b). Likewise, the frequency alignment between the filter passbands and comb lines allows the filter to select one in every five comb lines due to their frequency spacing difference. This filtering results in an output with a comb spacing of 50 GHz, equivalent to a time domain pulse interval of 20 ps and a repetition rate of 50 Gpulse/s. In our case, however, the bandwidth limitation of the input signal in our laboratory setup allows for only two comb lines in the output, and therefore reduces the output waveform to a Sine shape. This experiment verifies that the critical filter shape of our design enables high-resolution spectral shaping, with a successful demonstration of five-fold repetition rate multiplication of periodically pulsed optical signals, i.e. from 2.5 Gpulse/s to 12.5 Gpulse/s and from 10 Gpulse/s to 50 Gpulse/s.

3.5 Conclusion

As this thesis focuses on OSP applications using optical frequency combs, these applications rely on having a useful frequency comb source. Methods for optical frequency comb generation, characterization and manipulation are included in this chapter.

Different optical frequency comb generation methods have their pros and cons. For example, frequency comb generation using a SESAM can operate stably over a long time and it has a tunable central frequency. But it only supports one repetition rate and the SESAM ages over time. The method using electro-optic modulators was chosen for building a coherent frequency comb source with a flat spectrum in the laboratory. A 150-GHz bandwidth comb with 10-GHz spacing was obtained. Using this method, both of the comb source and the coded signal can be synchronized by the same sinusoidal RF source. By changing the frequency of the sinusoidal signal, the repetition rate of the frequency comb can be changed. The coherence of this comb source was verified by coherent communications experiments, and it can work stably over more than one day.

There are some considerations of comb generation using electro-optic modulators. The maximal repetition rate is limited by the bandwidth of the electro-optics modulators. Although modulators with higher bandwidths have been reported [258], most the electro-optic modulators have bandwidths less than 100 GHz. The number of frequency comb lines is

determined by the maximum output power of the RF amplifier, the maximum sustainable input voltage of the modulator, and the voltage for a π phase shift of the modulator. For comb generation, RF amplifiers with high output powers (i.e. 29 dBm) and wide bandwidths (i.e. 18-40 GHz) are desired. However, most RF amplifiers only have one of these two features. Unlike SESAM mode-locked lasers [259], the electro-optics comb generation cannot plug-and-play. The driving voltages and bias voltages of the modulators need to be carefully tuned. The timing and polarizations of the light entering the modulators should be aligned. The length of the dispersive fiber for dispersion compensation need to be altered if the frequency of the RF driving sinusoid signal is changed. Once the devices are switched on and off, most parts of the system need to be tuned again.

Currently, some research groups are working towards on-chip frequency comb generation for telecommunications. For example, a 50 Tbit/s transmission was demonstrated using a soliton frequency comb generated in microresonators [226]. A mode-locked dark-pulse Kerr comb from microresonators has recently been reported with the demonstration of a 4 Tbit/s transmission [260]. These frequency combs based on microresonators cover broad bandwidths. However, they need active stabilization as solitons rely on the balance between nonlinearity, dispersion and temperature [261, 262]. Furthermore, a frequency comb with a small bandwidth can be broadened in highly nonlinear devices, such as highly nonlinear fibers with anomalous dispersion [263] and aluminium-gallium-arsenide-on-insulator (AlGaAsOI) nanowaveguides [264].

In the frequency comb manipulation section, a PIC was used as a comb filter for optical clock multiplication. A number of highly desirable features, such as sub-GHz selectivity, reconfigurability, low loss, small size, and large bandwidth, were combined in a single chip. The nearly constant filter passband interval across a bandwidth of 4.5 THz verifies the low dispersion of the waveguide. The comb filter shows a sub-GHz frequency selectivity, i.e. a very narrow passband with a -3-dB bandwidth of 0.6 GHz and a -20-dB bandwidth of 1.2 GHz at a passband interval of 12.5 GHz. This selectivity enables comb line selection with an order-of-magnitude higher spectral resolution compared with commercial optical filters based on free-space optics [235, 236]. For further improvements in the speed of reconfiguration and power efficiency, the tuning elements can be optimized by heat confinement in the waveguide or by employing other kinds of tuning mechanisms, such as stress-optic modulators [257].

This comb filter was verified in clock rate multiplication applications, i.e. from 2.5 Gpulses/s to 10 Gpulses/s and from 10 Gpulses/s to 50 Gpulses/s. A frequency comb was generated by means of a CW laser and external electro-optical modulators, where the frequency alignment with the filter were performed by either tuning the CW laser frequency or on-chip reconfiguring filter passband central frequency (using heaters or adjusting the overall

chip temperature). The experiment used typical open-loop control, showing good stability of both comb source and filter spectral characteristics. However, keeping the frequency comb and filter in a frequency-locked status would be required for many applications. With this regard, improvement of two aspects can be considered: one is to increase the system robustness by having all optical functions monolithically integrated in one chip and packaged with good shielding from ambient disturbances [241]; the second is to develop a closed-loop control of the comb and filter frequencies.

Chapter 4

Optical sampling based on frequency combs

In the previous chapter, the applications and methods to generate frequency combs were discussed. One of the major applications of frequency combs is optical sampling.

In this chapter, the concept of optical sampling and different methods to perform optical sampling are included. Optical sampling can be implemented with nonlinear optical fibers, semiconductor devices, crystals or waveguides [265]. In an optical fiber, the nonlinear effects such as four wave mixing (FWM) [266] and cross-phase modulation (XPM) [267] enable optical sampling. In addition, nonlinear optical loop mirror (NOLM) [268, 269] can be used for optical sampling. Optical sampling can also be performed in semiconductor devices such as semiconductor optical amplifiers (SOA) [270], ultrafast nonlinear interferometers (UNI) [271], and electroabsorption modulators (EAM) [272]. In terms of crystals [273] and waveguides such as periodically poled lithium niobate (PPLN) [274, 275], the nonlinear effects for optical sampling are second-harmonic generation (SHG), sum-frequency generation (SFG) and difference-frequency generation (DFG) [276, 277]. Among the above mentioned platforms, PPLNs, HNLFs and NOLMs are used in this thesis. The operation principle of NOLMs is explained in Section 4.2 and optical sampling based on FWM is discussed in Section 4.3.

Sections 4.4 and 4.5 are original. Section 4.4 shows optical sampling can be used to improve the performance of electronic devices Nyquist-shaped signal detection [61]. Section 4.5 presents a novel optical sampling method with noise suppression [62], while most of optical sampling does not reduce noise.

4.1 Overview on optical sampling

In ADCs, there are electronic samplers. The ultimate available bandwidth of electronic sampling is limited by the bandwidth of the photodiode (PD), the bandwidth of the transimpedance amplifier (TIA), and the electronic sampling system [278, 279]. In laboratory work, digital sampling oscilloscopes perform the sampling. In 2007, the bandwidth of the DSO produced by Tektronix was 20-GHz using digital boosting. In 2014, the world's fastest DSO is from LeCroy with a 100-GHz bandwidth and 240-GSa/s sampling rate, using a frequency interleaving technology. In OFC 2018's postdeadline session, Chen's work was performed with a 256-GSa/s DSO from Keysight [2]. These numbers show that the advance of DSOs' sampling rate has slowed down.

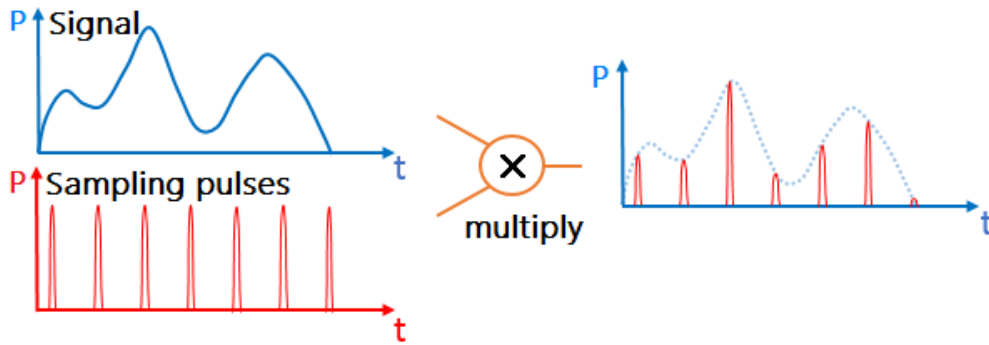


Fig. 4.1 Illustration of optical sampling by short pulses.

Optical sampling is a promising technique to overcome the bottleneck of electronic samplers. As illustrated in Fig. 4.1, optical sampling is based on nonlinear interactions between the signal to be measured and short optical pulses. Short optical pulses open short temporal gates to the signal and block it the rest of the time. The mixing process can be approximated by multiplication of the optical intensities in numerical analysis. In optical sampling systems, the requirement for high electrical bandwidth is transferred to high optical bandwidths [127, 280, 276, 281–283], which can provide a dramatic shift from 100's of GHz bandwidths to terahertz bandwidths.

Temporal resolution is the full-width at half-maximum (FWHM) width of the impulse response of the sampling system [265, 284]. Compared with the 3.9-ps resolution of the 256-GSa/s DSO [2], optical sampling can reach much finer time resolutions of less than 50 fs [285, 286].

If the signal under test is repetitive, asynchronous optical sampling [287] can be used to resolve the envelope of the signal. The frequency of the short sampling pulses is offset by a small amount to the repetition rate of the signal, such that the samples are slowly walking across the studied repetitive waveform [288, 285]. Then, the signal waveform can be

reconstructed by a computer after optical to electronic conversion, resulting time-magnified version of an ultrahigh-speed optical pulse signal.

If the measured signal is random, optical sampling with a low-repetition-rate train of short optical pulses enables detection of high-speed optical signals by time-interleaved demultiplexing. Linear optical sampling (LOS) supports both of intensity modulation formats and complex modulation formats [289, 283]. LOS enables the display of eye-diagrams, constellations diagrams and the calculated error vector magnitude (EVM). To decode all the information carried by a high-speed optical signal, parallel optical sampling can separate a serial high-speed signal into several low-speed parallel signals. In other words, optical sampling time-division-demultiplexes the signal to a rate that can be accurately detected by PDs and DSOs.

Optical samplers have been demonstrated by optical nonlinear effects in various platforms including nonlinear crystals [273], highly nonlinear fibers [266], silicon nanowires [290], planar waveguides [291], and semiconductor optical amplifiers (SOA) [270]. The optical-nonlinearity-based sampling methods can be classified as χ^2 or χ^3 . The early work on single-shot all-optical sampling around 1970 [292] and equivalent-time all-optical sampling in the 1980s [293], utilizes χ^2 for sampling. χ^2 -based schemes rely on crystals such as Lithium Niobate and KTiOPO_4 (KTP). Periodically poled lithium niobate (PPLN) crystal has a relatively high conversion efficiency of sum-frequency generation and a better temporal resolution than schemes based on KTP [294]. The χ^3 optical-fiber-based optical sampling schemes originate from nonlinear Kerr effect, in which the refractive index in fiber is intensity dependent. Most χ^3 -based solutions use optical fiber with vanishingly small second-order nonlinearity but strong χ^3 for cross-phase modulation (XPM) and four-wave mixing (FWM).

Different optical sampling methods have their cons and pros. For example, the FWM process in highly nonlinear fiber preserves amplitude and phase information and it is transparent to modulation formats, but this approach has a low conversion efficiency and requires high powers. SOA-based optical samplers require low switching powers but suffer from slow gain recovery and ASE noise. Optical sampling using PPLN has less noise from the nonlinear mixing because there is no SPM or XPM, but PPLN only supports signal processing in one polarization.

4.2 Sagnac loops

The Sagnac loop [295, 296] was proposed in the 19th century. The Sagnac loop is a ring interferometer. A beam of light is split and the two beams are made to follow the same path but in opposite directions. To act as a ring, the trajectory must enclose an area. On return

to the point of entry, the two light beams are allowed to exit the ring together and undergo interference.

A nonlinear-optical loop mirror (NOLM) [268] is a kind of Sagnac loop with a nonlinear component within the ring. It can be used to demultiplex high-speed optical signals through optical sampling [297]. In this section, sagnac loop mirrors and NOLMs are simulated using VPItransmissionMaker™.

4.2.1 Linear loop mirrors

The fiber loop in Fig. 4.2 acts as a perfect mirror and all the power is reflected back along the input fiber [298]. The coupling ratio of the coupler must be 0.5. Assuming that light travels towards the coupler in Leg 1 and that the coupler couples half of the power into Leg 3 and the other half into Leg 4. Fifty percent of the input light travels clockwise around the loop and fifty percent travels anticlockwise. Light coupled across the coupler suffers a $\pi/2$ phase lag with respect to light travelling straight through. The transmitted intensity in Leg 2 is the sum of a clockwise field of arbitrary phase ϕ and an anti-clockwise field of relative phase $\phi - \pi$ both of equal amplitude. This results in a zero transmitted power in Leg 2 and all input light is reflected back along the input Leg 1.

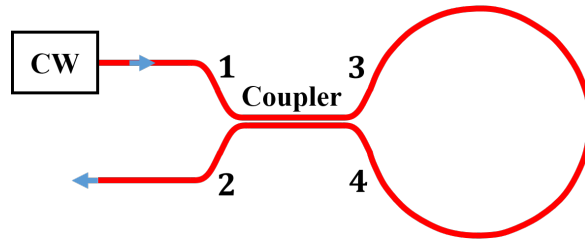


Fig. 4.2 Schematic of linear loop mirror.

4.2.2 Nonlinear-optical loop mirror

Figure 4.3 shows the schematic of a nonlinear optical loop mirror (NOLM), which has a highly nonlinear fiber (HNLF) in the loop [268]. The coupling ratio of a nonlinear optical loop mirror should be close to 0.5, but not equal to 0.5. The nonlinear effects are intensity dependent, so they are not identical for the two paths. If the input pulse duration is short compared to loop length, there is self-phase modulation (SPM) effect only. The phase shift acquired by a field E propagating a distance L under the influence of SPM is given by [268]

$$|E_{out}|^2 = |E_{in}|^2 \left(1 - 2\alpha(1 - \alpha) \left\{ 1 + \cos \left[(1 - 2\alpha) |E_{in}|^2 \times 2\pi n_2 L / \lambda \right] \right\} \right) \quad (4.1)$$

where: α is coupling ratio, n_2 is nonlinear Kerr coefficient, λ is the wavelength of the optical signal.

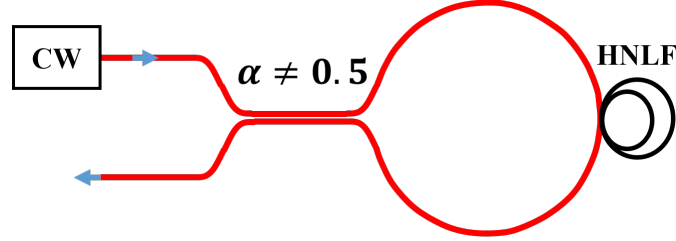


Fig. 4.3 Schematic of Nonlinear Optical Loop Mirror.

If the pulse duration is long compared with loop delay, both SPM and XPM should be taken into account. The nonlinear refractive indexes seen by the pulses in the two opposite directions are [268]

$$n_R = n_2 \left(|E_R|^2 + 2|E_L|^2 \right) \quad (4.2)$$

$$n_L = n_2 \left(2|E_R|^2 + |E_L|^2 \right) \quad (4.3)$$

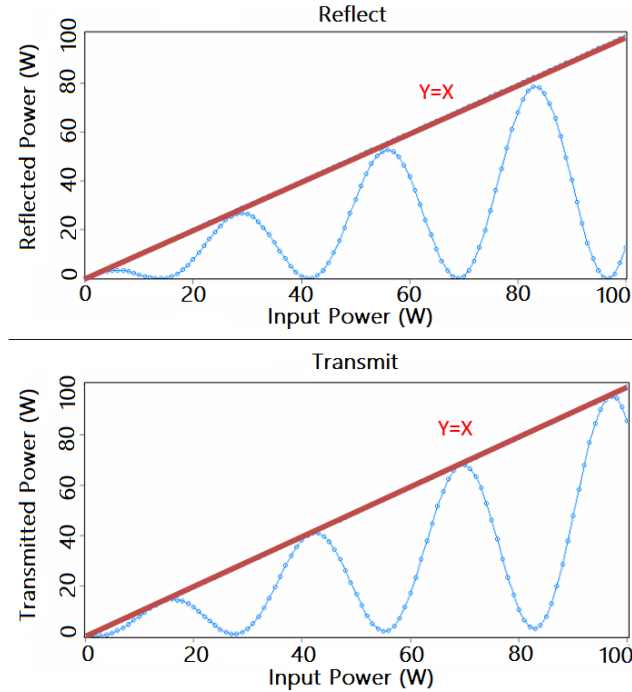


Fig. 4.4 Transfer function of nonlinear optical loop mirror without a control signal. Simulated with VPItransmissionMaker™

Since only the difference between n_R and n_L is important, Eq. 4.1 still can be used. The highly nonlinear fiber used in the simulation is 100-m long with $30 \times 10^{-20} \text{ m}^2/\text{W}$ nonlinear index and $30 \times 10^{-12} \text{ m}^2$ core area. Figure 4.4 illustrates the transfer function between the input optical power and the reflected or transmitted power. According to the figure, 100% of power emerges from transmit port whenever

$$\frac{n_2 2\pi |E|^2 L}{\lambda} = \frac{m\pi}{1 - 2\alpha} \quad (4.4)$$

for m odd. The minimum power appears for m even.

4.2.3 Nonlinear Sagnac interferometer with a control signal

As shown in Fig. 4.5, a control input can be added in the loop by attaching another coupler for the control pulse in the loop and set the coupling ratio of bi-directional coupler to be 0.5 [299]. This structure was used in the experiments presented in Chapter 4. When the control pulse width is narrow compared with loop delay and signal symbol duration, the clockwise signal copropagates with control pulse, and modulated by a control pulse, while the counterclockwise signal almost remains the same. The control-pulse induced phase shift on the co-propagating signal is normalized by the peak phase shift

$$\phi_{co}^{max} = \frac{4\pi n_2 I_0 L}{\lambda_s A_{eff}} \quad (4.5)$$

where: n_2 is nonlinear (Kerr) coefficient, λ_s is wavelength of input signal, I_0 is the peak power of the control pulse, L is the length of the nonlinear fiber, A_{eff} is the effective area of the nonlinear fiber.

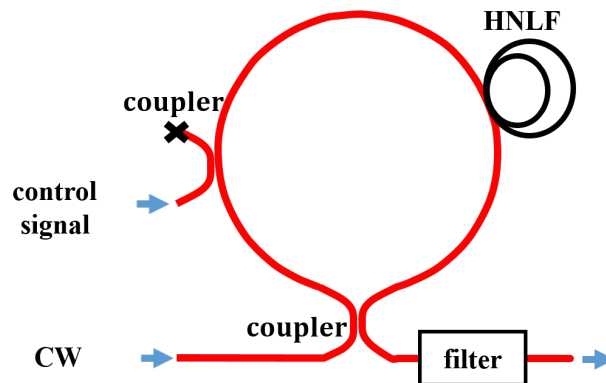


Fig. 4.5 Setup of a nonlinear sagnac interferometer with a control signal.

4.3 FWM sampling

FWM can be used for optical sampling through a nonlinear interaction between the signal and optical short pulses [266]. In the FWM sampling process, the generated idler pulses have a phase which is locked to the phase of the signal at the sampling event. This is the result of the phase matching requirement of the FWM process. Hence, the samples contain both the amplitudes and phases of the signal at the sampling events [300].

The interaction of pump pulses and signal in FWM process generates a sampling product (idler) at $\lambda_{idler} \approx 2\lambda_{pump} - \lambda_{signal}$. The idler power is characterised by power of signal P_s , power of sampling pulse P_c , non-linear coefficient γ , chromatic dispersion D , attenuation α , fiber effective length L_{eff} and FWM efficiency η [140].

$$P_{idler} = \gamma^2 P_s P_c^2 L_{eff}^2 \eta (D, \Delta\lambda) e^{-\alpha L} \quad (4.6)$$

The FWM efficiency η is high when the dispersion is lower and involved pump-signal spacing is small. The conversion efficiency η varies with wavelength [279]. Because the FWM sampling efficiency depends on the sampling pulse power squared, the temporal resolution of the optical sampler is slightly shorter than the initial sampling pulse width. The key factors to consider in an optical sampling gate design are:

- Nonlinearity (γ) 1/(W·km)
- Group-velocity dispersion (GVD) ps/km/nm
- Dispersion slope (S) ps/(km·nm²)
- Zero-dispersion wavelength (λ_0)
- Polarization-mode dispersion (PMD) ps/km
- Splice losses to standard fiber (L_s)
- Fiber effective length (L_{eff}) m

Polarizations and timing are important for FWM. Only signal power that has the same state of polarization as the sampling pulses will be sampled at any given time. The FWM process only occurs when the signal and the sampling pulses are temporally overlapped.

FWM is also related to the wavelengths of the signals. If the signal wavelength is moved further from the sampling pulse wavelength, the walk-off between them increases. Because of the walk-off, the signal and sampling pulse lose their overlapping along propagation. The phase-matching bandwidth is therefore inversely proportional to the walk-off [133].

In order to achieve a large operation bandwidth, the HNLF must be short enough for the negligible walk-off. Nonlinear fibers longer than 1 km can cause polarization fluctuations, signal-sampling pulse walk-off, attenuation and other instabilities [301]. Except for the limited phase-matching bandwidth, a long HNLF is prone to be affected by the environment

such as temperature and vibrations, which would result in timing jitters during the sampling process. There are trade-offs to be made in the system design. For example, a shorter HNLF for optical sampling is less affected by the ambient noise, but the reduction of fiber length results in the reduction of the idler's power.

4.4 Enhancing Nyquist-shaped signal detection bandwidth using optical pre-sampling

Optical pre-sampling to extend the effective receiver bandwidth is proposed here. The effect of optical pre-sampling on the direct-detection of Nyquist-shaped signals is investigated. In the simulation and proof-of-concept experiment, a 40-Gbaud Nyquist-shaped on-off-keying signal is optically sampled in a highly non-linear fiber at one-sample-per-symbol, then detected by a single photodiode. The electrical bandwidth limitation of the receiver is provided by an electrical filter. When the filter bandwidth is 11 GHz, optical pre-sampling improves the receiver sensitivity by 7.1 dB in the simulation. A sensitivity improvement of 4 dB with an 18-GHz bandwidth receiver was shown experimentally. Factors including sampling pulse width, receiver bandwidth, and sharpness of the electrical response of the receiver were further explored. This work shows that optoelectronic receivers can be enhanced to receive signals at baud rates beyond twice the receiver's bandwidth, providing a method to expand data carrying capacity in systems limited by the electronic bandwidth, including that of the photodiode. The work was presented in part at Optical Fiber Communications Conference and Exhibition (OFC), Los Angeles, CA, US, 2017 [61].

4.4.1 Motivation

Orthogonal multiplexing enables optical communication systems to efficiently occupy their available fiber bandwidth [302–304]. Sinc pulses generated by Nyquist shaping [305] can be orthogonally time-division multiplexed (OrthTDM) [304] to shape of each wavelength channel to a near rectangular spectrum, allowing wavelength division multiplexing without guard-bands [306–309]. Nyquist shaping can be performed in the electrical [310–312, 207] or optical domain. In terms of electrical Nyquist-shaping, accurately modulating a broadband electrical Nyquist signal onto an optical carrier requires a digital-to-analog converter (DAC) with a sufficiently high bandwidth and resolution (effective number of bits, ENOB). In addition, owing to the steep roll-off of Nyquist shaping, finite impulse response (FIR) filters with a large number of taps are required. The implementation of such FIR filters in digital signal processing (DSP) leads to increased computational effort and processing latency in the

transmitter. On the other hand, Nyquist signals can be generated optically by either filtering modulated signals [313, 308, 309, 163, 64, 314] or by modulating sinc-shaped optical pulses [304, 174, 315–317]. This reduces the requirements on DSP and DACs, while being able to operate over very high bandwidths [64]. This work focuses on direct-detection (DD) [304, 318–321] of Nyquist signals enhanced by optical pre-sampling [304]. When receiving a Nyquist-OTDM signal, or one channel of N-WDM, there is an inter-symbol-interference (ISI)-free sampling point in each symbol owing to time-domain orthogonality [304]. The ISI-free point is essential to direct detection of Nyquist shaped signals unless DSP is used. However, this orthogonality can be significantly degraded by electrical bandwidth limitations in the receiver, causing ISI. ISI caused by receiver bandwidth limitations can be reduced by optical pre-sampling.

Optical sampling is a well-known all-optical signal processing methodology and it has been used in various contexts to overcome bandwidth limitations during optoelectronic conversion [322, 293, 323–325]. Optical sampling at less than one sample-per-symbol, i.e., a sampling rate less than the signal's baud-rate, has been demonstrated for waveform measurement [293, 323], eye-diagram measurement [324], and in optical time-division multiplexing (OTDM) systems to demultiplex high-rate signals into low-rate tributaries [325]. However, sampling at less than the baud rate requires multiple parallel receivers to fully reconstruct data sequences. For example, coherently sampling a 100-Gbaud Nyquist OTDM signal with a 10-GHz repetition rate local oscillator requires 10 parallel coherent receivers. While most research is focused on optical sampling at less than one sample-per-symbol, this work focuses on the effect of optical sampling at one sample-per-symbol.

This work demonstrates mitigation of the receiver bandwidth limitations-induced ISI, through optical pre-sampling at one sample-per-symbol. This work focuses on optical sampling of an optically shaped N-OOK signal and make further analysis into factors such as the optical sampling pulse width and the sharpness of the magnitude response of the receiver. Note that this work is under the assumption that the receiver has an insufficient bandwidth for ISI-free direct-detection without equalization. Simulations show that optical pre-sampling can improve receiver sensitivity for N-OOK signal under a number of receiver bandwidths. In the proof-of-concept experiment, a 4×10 -Gbaud orthogonal time division multiplexing (OrthTDM) signal was used to emulate a 40-Gbaud N-OOK signal and show that optical sampling can improve the sensitivity of a band-limited 18-GHz receiver by 4 dB. In the simulation and experiment, the optical sampling is implemented through four-wave-mixing (FWM) process in a highly nonlinear fiber (HNLF). The sensitivities are measured at a 7% hard-decision forward-error correction (FEC) threshold. This work shows that optoelectronic

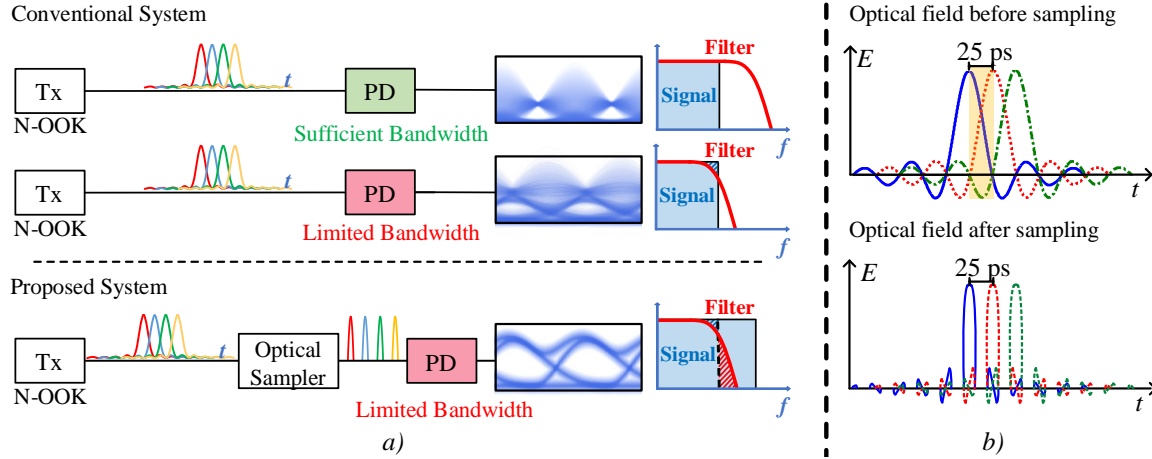


Fig. 4.6 (a) Principle of optical pre-sampling before bandwidth-limited receivers. (b) Optical field of optically shaped 40-Gbaud N-OOK before and after optical sampling.

receivers can be enhanced to receive signals at a symbol rate beyond twice the receiver bandwidth.

4.4.2 Operational principle

Figure 4.6 (a) shows three N-OOK detection systems with their eye diagrams and electrical spectra. With sufficient receiver bandwidth (upper system), there is a clear and short optimal sampling window for each symbol period, as observed in the eye diagram. If the receiver is bandwidth-limited (middle system), there is significant degradation due to the attenuation of the high frequency components, causing ISI. In the proposed system (bottom system), the degradation due to ISI is reduced by the optical pre-sampler. The optical sampling at one sample-per-symbol can be viewed in the frequency domain as a convolution of the signal spectrum and a frequency comb, leading to repeated frequency components and spectral "whitening" [326, 327]. As indicated in the bottom row of Fig. 4.6 (a), the repeated frequency components from the sampling operation allow for reshaping through filtering. In previous work [328, 329], the repeated frequency components have been shown to increase tolerance to band-limiting effects of optical filters in transmission links. This is conceptually similar to the effect of optical sampling and receiver electrical bandwidth limiting filters in this investigation.

Alternatively, this approach can be explained in the time domain. Figure 4.6 (b) shows the envelope of the optical field of an optically shaped 40-Gbaud N-OOK signal [304, 313] before and after optical sampling. The envelope has negative excursions, which are π phase shifts to the optical carrier. As each '1' data bit is a sinc pulse with long tails that change sign from bit-slot to bit-slot, the tails of adjacent 1-bits will partially destructively interfere (e.g. the

blue and red traces), whereas 1-bits separated by two bit slots have tails that constructively interfere (e.g. the blue and green traces in Fig. 4.6 (b)). Because the sines have long tails, many 1-bits will contribute to the total field at a given instant; but zero bits will not contribute as they are encoded as zero power. Thus the total field will depend on the pattern of data sent. Fortunately, if there is no bandwidth limitation, the zero-crossing points of all of the tails align with the peak of the wanted pulse; this is the sampling time that will give zero-ISI. However, if the receiver has insufficient bandwidth, the low-pass filter (LPF) distorts the symbols, causing a loss of orthogonality between adjacent symbols, and there will not be a sampling time that will give zero-ISI. Optical sampling (that is, sampling before the PD-induced bandwidth limitation) selects the peak of the desired data-bit's sinc, and suppresses the tails of the preceding and following sines away from the crossing points. Thus, there is very little energy left in the tails of the preceding and following sines, energy that would have caused ISI after band-limiting. This means that the electrical waveform becomes much less dependent on the data pattern, reducing the variances of the traces corresponding to the 1 and 0 bits.

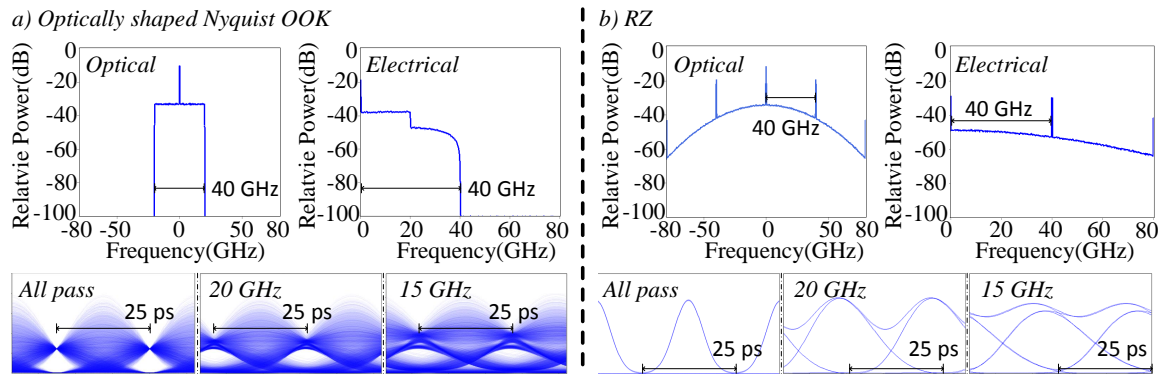


Fig. 4.7 Optical and electrical spectra and eye-diagrams of 40-Gbaud (a) optically shaped N-OOK and (b) RZ direct detection with no electrical band limitation, or with 20-GHz or 15-GHz 4th-order Bessel electrical low pass filter. The results are from a VPItransmissionMaker simulation without additional noise.

This simulation used Gaussian pulses, whose time-bandwidth product is 0.44, to sample N-OOK signals. When the optical sampling pulses are significantly narrower than the bit-period of the N-OOK signal, the N-OOK symbols are transformed into return-to-zero (RZ) symbols through optical sampling. If the sampling pulse width is equal to or less than $0.44 \times$ the symbol duration, the sampled signal is roughly RZ-shaped with some inter-symbol-interference from other symbols. In Fig. 4.7, optical spectra, electrical spectra and eye-diagrams of 40-Gbaud N-OOK and 40-Gbaud RZ signal are compared. The bandwidth-limiting is modelled by a 4th-order Bessel electrical low-pass filters. The 40-Gbaud double side-band (DSB) N-OOK signal has a 40-GHz optical bandwidth centered around a carrier. If

the electrical signal was solely due to the mixing of the carrier and the sidebands, a 20-GHz-wide electrical spectrum would be expected. However, additional frequency components are generated due to the square-law of photo-detection causing mixing of all of the tones within both sidebands, to give a 40-GHz-wide electrical spectrum. As shown in the eye diagrams of Fig. 4.7 (a), limiting the electrical bandwidth causes substantial ISI.

There are trade-offs in using N-OOK in DD systems. N-OOK signals have a well-confined optical spectrum, which is suitable for multiplexing, all-optical routing and elastic networks [308, 309]. However, as shown in Fig. 4.7 (a), N-OOK can be very sensitive to receiver bandwidth limitations, with the required electrical bandwidth exceeding the symbol rate for penalty-free reception. On the other hand, an RZ signal is less sensitive to limited receiver bandwidths, but an RZ signal occupies a much wider optical bandwidth during transmission, so should be more affected by fiber dispersion. In this way, Nyquist-shaped signals are preferred for transmission, and RZ signals are more desirable for detection. Optical pre-sampling before photodetection combines the merits of both of them.

4.4.3 Simulation setup

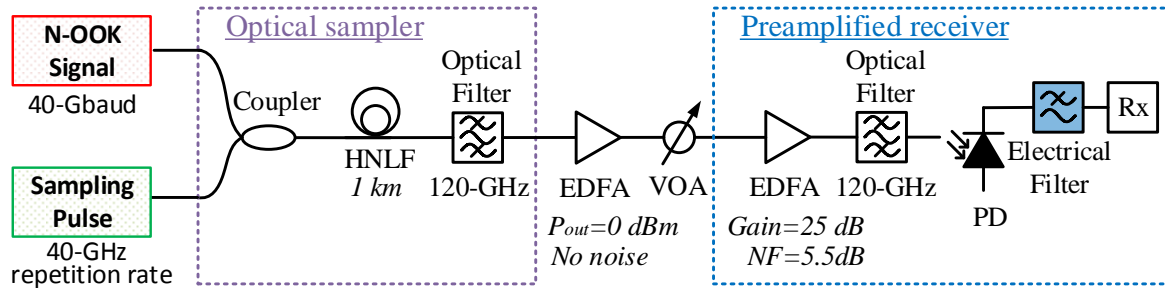


Fig. 4.8 Simulation Setup of receiver enhanced by optical pre-sampler. EDFA: erbium-doped fiber amplifier. VOA: variable optical attenuator. HNLF: highly nonlinear fiber.

Figure 4.8 shows the simulation setup for the optical pre-sampler. A 15th-order pseudorandom binary sequence (PRBS) of 2^{18} bits is simulated for each BER calculation. The N-OOK signal is generated by modulating a Gaussian-shaped ultra-short optical pulse train, whose repetition rate is 40 GHz, with a 40-Gbaud electrical non-return-to-zero (NRZ) signal, followed by a 40-GHz rectangular optical band-pass filter (BPF) [313]. A zero roll-off, 40-Gbaud N-OOK signal ("signal") centred at 1550.9 nm, is optically sampled by 3.67-ps width (120-GHz bandwidth), 40-GHz repetition rate short Gaussian pulses ("pump") centred at 1547 nm, in a HNLF to generate the optically sampled signal ("idler") at a new frequency through the FWM process. The sampling process was simulated with a HNLF to gain insight into the experiments. The HNLF is 1-km long with a 1547-nm zero-dispersion wavelength and 9.3

$W^{-1} \cdot \text{km}^{-1}$ non-linear coefficient. The conversion efficiency of the FWM is about -10 dB. The idler is extracted by a 120-GHz optical band pass filter, and amplified by an EDFA with 25-dB gain and 5.5-dB noise figure. The 3-dB bandwidth of the electrical low-pass filter (LPF) after the photodiode was switched between 11, 18, 19, 20, 22, 62 GHz to emulate receiver bandwidth limitations, as shown in Fig. 4.9. The performance of systems with a sharp brick-wall rectangular filter (implemented as a 30th-order Gaussian filter, red traces in Fig. 4.9) and a slow roll-off filter (4th-order Bessel filter, blue traces in Fig. 4.9) are compared. The brick-wall filter resembles a digitally-defined anti-aliasing filter used in some real-time digital oscilloscopes, while the Bessel filter is more typical of analog bandwidth limits (e.g. photodiode response). Note that the time-bandwidth product of the sampling pulses is 0.44, which is the transform limit for Gaussian pulses.

4.4.4 Simulation results

Figure 4.9 shows the simulated BER versus received optical power for signals and idlers under various electrical filter bandwidths. The Bessel filter (blue traces) and the rectangular filter (red traces) mentioned above are simulated. The solid lines represent signals without optical pre-sampling, and the dashed lines indicate idlers or optically sampled signals. When the receiver bandwidth is set by a 11-GHz Bessel filter, error-free operation below the 7%

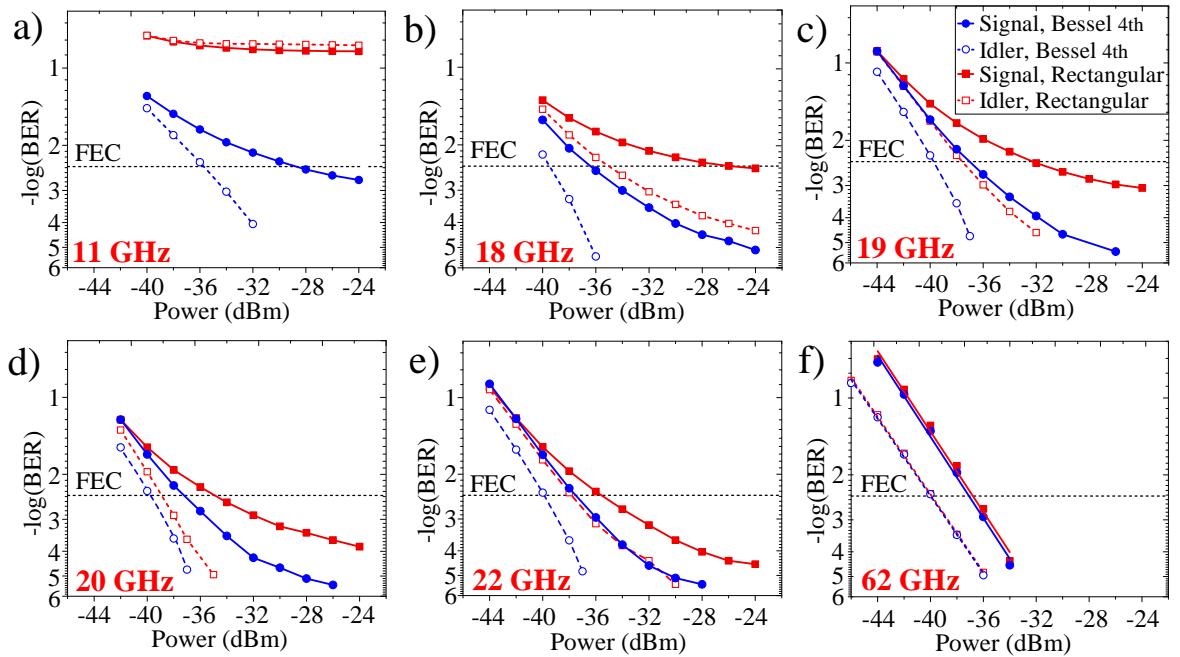


Fig. 4.9 Simulated BER versus received optical power plots for signals and idlers filtered by 4th order Bessel electrical filter (B.4th), and rectangular electrical filter (Rec.) after photo-detection.

hard-decision FEC threshold ($\text{BER} = 3.8 \times 10^{-3}$) can be achieved with optical sampling, providing 7.1-dB sensitivity improvement. When brick-wall electrical filtering is applied, optical sampling provides no improvement and error-rates are well above the FEC threshold. Figs. 4.9 (b)-(e) show the performance for filter bandwidths between 18-22 GHz. For the brick-wall filter, optical sampling improves sensitivity by 9, 5.5, 4.1 and 2.2 dB for 18, 19, 20 and 22 GHz bandwidth filters, respectively. For the Bessel filter, the improvements are 3.8, 3.3, 3.1 and 2.8 dB for the same filter bandwidths, respectively. In Fig. 4.9, the traces for 62-GHz receiver bandwidth follow the same tendency, but there is a 3.3-dB sensitivity improvement from optical sampling. This base line sensitivity improvement is attributed to the RZ shaping. Given the same average power, compared with the N-OOK signal, the low duty-cycle RZ signal has 3.3 times the peak power of "1" level.

Figure 4.10 (a) summarizes the sensitivity versus electrical filter bandwidth. The sampling pulse width is set to 3.67 ps, which corresponds to a 120-GHz pump bandwidth, and the electrical filter at the receiver is 4th-order Bessel filter. Comparing the two lines in Fig. 4.10 (a), the N-OOK signal has a higher slope. The N-OOK signal is more sensitive to receiver bandwidth. The optical pre-sampler improves the receiver sensitivity by 3.1 dB at 20-GHz electrical filter bandwidth, and 7.1 dB at 11-GHz bandwidth.

Figure 4.10 (b) plots BER versus pump bandwidth. The measurement is taken with an 18-GHz low-pass 4th-order Bessel filter at the receiver. According to Fig. 4.10 (b) optical sampling with 80-GHz pump bandwidth outperforms sampling with 120-GHz pump

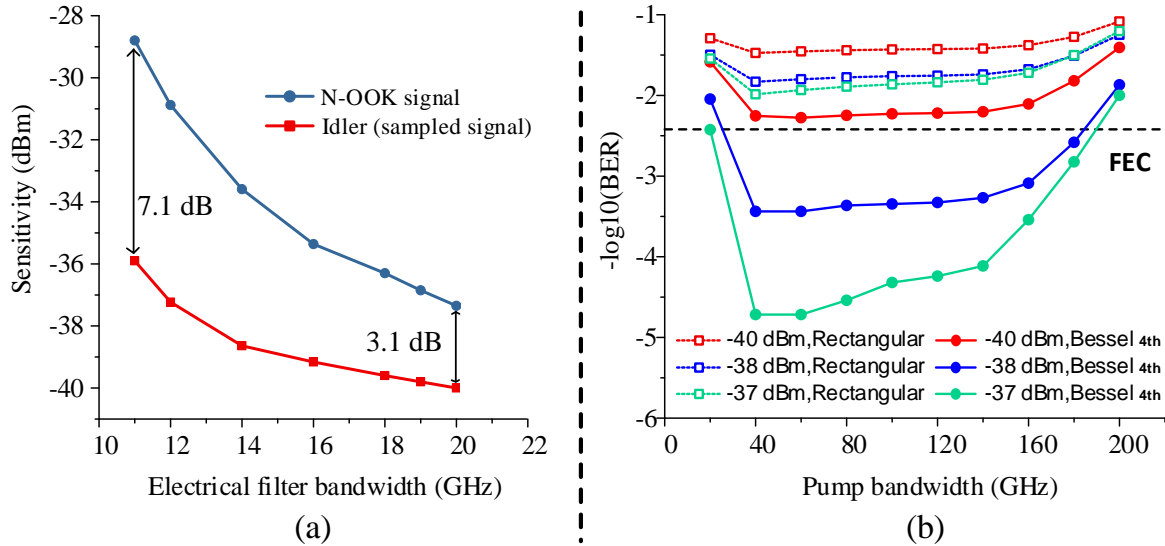


Fig. 4.10 (a) Sensitivity (received optical power at $\text{BER} = 3.8 \times 10^{-3}$) versus electrical filter bandwidth, with 120-GHz pump and 4th order Bessel electrical filter. (b) BER versus pump (sampling pulse) bandwidth, with 18-GHz low-pass 4th order Bessel electrical filter.

bandwidth, and this conclusion is consistent with the experimental results in the following section. When the pump bandwidth is less than 40 GHz, the sampling pulses with a repetition rate of 40 GHz start to overlap. Thus the optical sampling gate will not be completely off. When the pump bandwidth is larger than 120-GHz, due to the optical and electrical filters in the system, the received signal power before the PD is reduced. In addition, as the increase of pump bandwidth, the spectra of the pump and idler may be partially overlapped. Among the parameters swept in the simulation, 40-GHz and 60-GHz bandwidths give maximum performance.

4.4.5 Experimental setup

A proof-of-concept experiment was conducted to validate the simulation. Figure 4.11 shows the experimental setup of a 40-Gbaud Nyquist on-off keying (N-OOK) transmitter and a receiver with an optical pre-sampler, which is conceptually similar to the simulation. The 40-Gbaud N-OOK signal were sampled by short optical pulses with a 40-GHz repetition rate. The signal is emulated by time-division multiplexing of four 10-Gbaud N-OOK signals. An ERGO mode-locked laser, centered at 1555.5 nm, generates frequency comb lines with 10-GHz spacing and 1.4-ps optical pulses. The frequency comb is amplified by an erbium-doped fiber amplifier (EDFA) to 21.8 dBm and spectrally broadened through self-phase

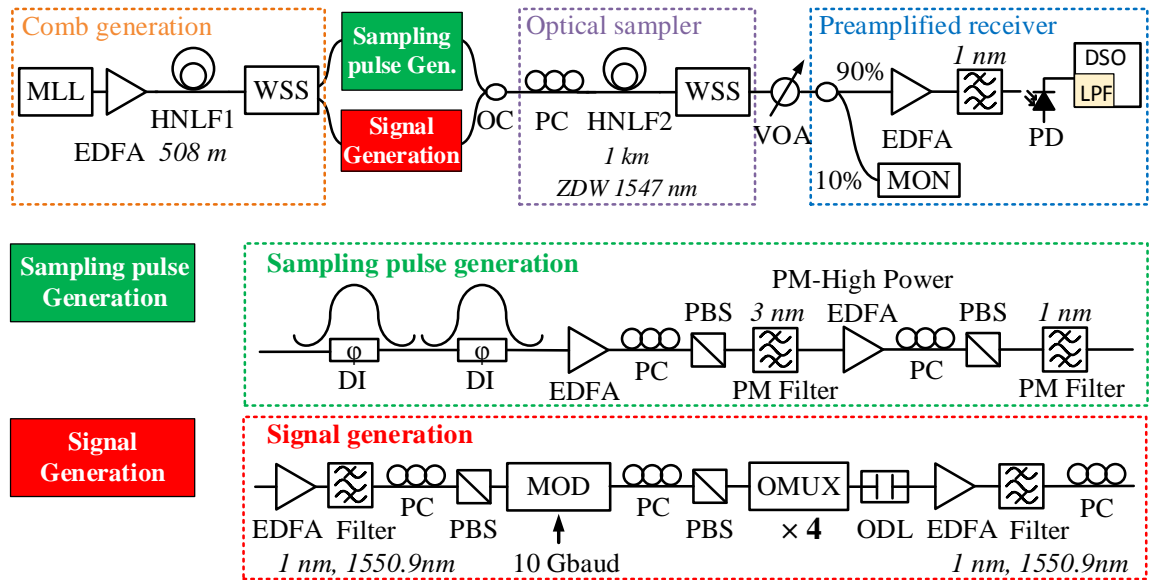


Fig. 4.11 Experimental setup of receiver enhanced by optical pre-sampling. MLL: mode-locked laser. MOD: modulator. WSS: wavelength selective switch. PC: polarization controller. PBS: polarization beam splitter. DI: delay line interferometer. OMUX: optical multiplexer. ODL: optical delay line. OC: optical coupler. MON: monitor. ZDW: zero dispersion wavelength. WDM: wave division multiplexing. PD: photodiode. DSO: digital sampling oscilloscope.

modulation (SPM) in a normally-dispersive highly nonlinear fiber (HNLF) (508 m length, -0.5 ps/nm/km dispersion @ 1550 nm, 0.016 ps/nm²/km dispersion slope @ 1550 nm, 11 W⁻¹·km⁻¹ non-linear coefficient). A wavelength selective switch (WSS) is used to shape the signal and the sampling pulses.

The sampling pulse train is generated by filtering the 10-GHz spacing comb lines with the WSS and two delay-line interferometers, and it is centered at 1547 nm with a 40-GHz repetition rate. The 40-Gbaud N-OOK signal is generated by intensity modulation of the frequency comb and time division multiplexing. The WSS-filtered frequency comb with 40-GHz bandwidth, 10-GHz frequency comb spacing, and 1550.9-nm centre frequency, is intensity modulated by a 10-Gbaud PRBS-15 signal, and then de-correlated and time division multiplexed by 4 times with a Pritel optical clock multiplier. The intensity modulator is biased at quadrature point and driven to maximize the extinction ratio. The time alignment between the signal and gating pulses is achieved by tuning the variable optical delay line. Note that since the Nyquist-shaping WSS has a 10-GHz granularity, there is a deviation in the Nyquist-shaping filter responses between the experiment and the simulation.

The optical sampler is a 1-km HNLF with 1547 nm zero dispersion wavelength (ZDW), and 0.074 ps/nm²/km dispersion slope at 1550 nm. The signal and pump powers at the input of the WDM coupler are 2.2 dBm and 15.5 dBm respectively. Polarization controllers are used to align the signal and pump polarizations for maximum FWM efficiency. A WSS extracts the idler by applying a Gaussian-shaped band-pass filter at 1543.1 nm with 120-GHz bandwidth.

In the pre-amplified receiver, a variable optical attenuator (VOA) sets the average power at the input of the pre-amplified receiver, and 10% of the power is monitored by a power meter. Before photodetection, a 1-nm optical BPF reduces out-of-band noise produced by the receiver EDFA pre-amplifier. The photodiode is a Finisar XPDV3120 70-GHz photodetector. In the digital sampling oscilloscope (DSO), the sampling rate is 160 GSa/s. The anti-alias filter, which is a 9-bit FIR digital low-pass filter built into the oscilloscope, is switched between 18, 19, 20, and 62 GHz (Fig. 4.13).

4.4.6 Experimental results

Figure 4.12 (a) shows the FWM spectra at the output of HNLF2 in blue. In the spectral domain, the idler carries the information of the signal with about -8 dB FWM conversion efficiency. The green and the red traces are the pump and signal before HNLF2. Comparing the three traces indicates the spectrum of the pump is broadened, and the signal's spectrum is shaped. The pump broadening effect is attributed to SPM in the HNLF, and signal shaping due to a combination of SPM and cross-phase modulation (XPM) from the pump. These

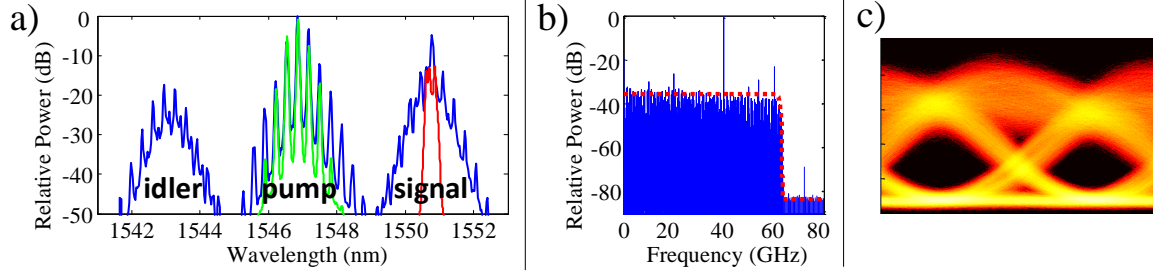


Fig. 4.12 (a) Red: spectrum of the signal before FWM process. Green: spectrum of the sampling frequency comb (pump) before FWM process. Blue: spectrum at the output of the HNLF2. (b) Electrical spectrum of the idler limited by 62-GHz electrical bandwidth. (c) Eyediagram of the 40-Gbaud N-OOK signal detected with 62-GHz electrical bandwidth receiver.

processes may introduce some distortion on the idler. Figure 4.12 (b) shows the electrical spectrum of the received idler limited by the 62-GHz LPF in the oscilloscope. According to the spectrum, this digital LPF has a sharp transition and a high extinction of 57 dB. The electrical spectrum fits well to a 0.02 roll-off raised-cosine filter response represented by a red dashed line. From the prior simulations, this brick-wall-like filter will have a strong effect on the received signal quality, dominating over the 70-GHz 3-dB bandwidth limit of the photodiode. Figure 4.12 (c) shows the eye-diagram of N-OOK signal at -31 dBm average power detected by a 62-GHz electrical bandwidth receiver, which has sufficient bandwidth to detect 40-Gbaud N-OOK signal.

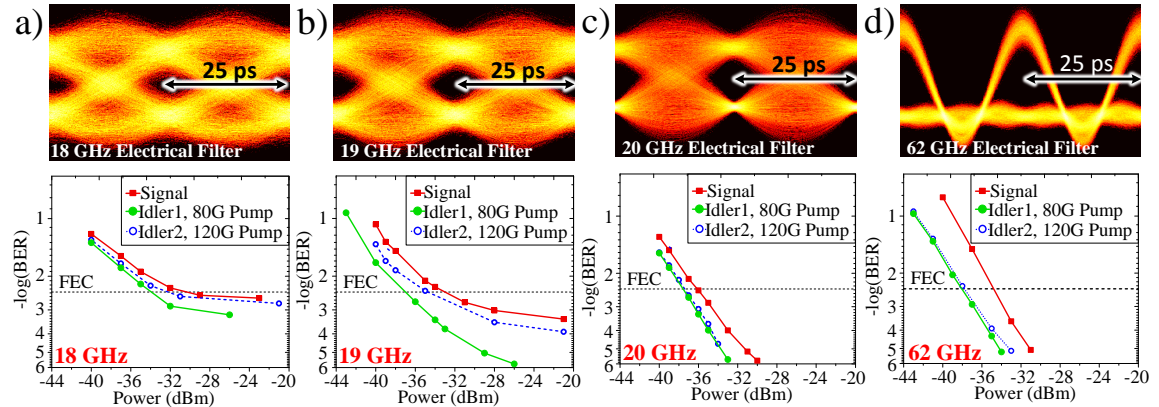


Fig. 4.13 Experimental eye-diagrams of signal optically sampled by a 80-GHz sampling pulse train (pump) at -36 dBm average power and BER versus received optical power curves for (a) 18-GHz (b) 19-GHz (c) 20-GHz (d) 62-GHz bandwidth-limited signal and idler.

Figure 4.13 shows BER versus received optical power, as well as eye diagrams for the received optically sampled idler at -36 dBm average power. Two separate curves were plotted for the idler, corresponding to Gaussian-shaped pumps with either 80- or 120-GHz bandwidths, which should ideally result in sampling pulses with 5.5-ps or 3.6-ps durations,

respectively. The performance with 18, 19, 20 and 62-GHz Bessel filters were applied in the oscilloscope. For the 18-GHz and 19-GHz filters, the 120-GHz bandwidth sampling pulse produces worse sensitivity than the 80-GHz wide pulse (Figs. 4.13 (a) & (b)), owing to the greater signal loss caused by the electrical and optical filters in the receiver.

For the 18- and 19-GHz bandwidth receiver filters, a sensitivity improvement of 4 dB was measured for pre-sampling. With the 20-GHz filter, this improvement drops to 2 dB. With a 62-GHz filter applied, the improvement from optical sampling increases to 3.8 dB. It is due to full conversion of the idler to an RZ signal (as illustrated by the eye diagram), alongside a large susceptibility of the signal to sampling timing jitter in the receiver due to the signal's pulse shape.

Both the simulation and the experiment show that for receiver bandwidths less than half the signal symbol rate, optical pre-sampling can improve sensitivity. The main contributor to the improvement is the N-OOK to RZ conversion, as indicated in the simulation, and a minor contributor could be the reduced noise-noise beating due to the noise being time-gated by optical sampling [330]. Comparing the simulation and the experiment, there are other factors besides the receiver bandwidth and the sampling pulses that define the receiver sensitivity. Most factors affect the BER results of signal and idler similarly, except for the optical Nyquist-shaping filter response. In the experiment, the WSS for optical Nyquist-shaping is set to 40-GHz rectangular BPF, but it has a granularity of 10 GHz. The resultant optical spectrum has a roll-off softer than the simulated ideal rectangular spectra. According to Nakazawa [304], the quasi-orthogonal property can be maintained in Nyquist pulses even when the roll-off is not zero, and the softer roll-off results in better tolerance to the bandwidth limitation. Therefore, compared with simulation, the N-OOK signal in the experiment has better sensitivities, leading to reduced sensitivity improvements in the experiment. Note that there are no equalization stages in either simulations or experiments, with the receiver acting only as a simple threshold comparator. It may be possible to improve system performance through the use of an equalizer, at the cost of some computational complexity and processing latency. For future mass production, the mode-locked laser and the HNLF in this work should be replaced with on-chip frequency combs [226] and on-chip optical sampling [331, 332].

In this work and the previous work [61], optical pre-sampling at one sample-per-symbol was used for direct-detection of both optically shaped and electrically shaped Nyquist signals. For further studies, it would be interesting to investigate the effect of optical sampling at one sample-per-symbol for coherent detection of Nyquist-shaped signals, considering that parallel optical sampling has been shown to be advantageous for coherent detection [333, 334]. Moreover, the proposed method may be applicable to WDM systems and other modulation formats.

This work has experimentally demonstrated that the quality of a direct-detected 40-Gbaud Nyquist OOK signal can be improved by optical pre-sampling in a band-limited system, where the receiver bandwidths are below the single-sided bandwidth of the optical signal. Proof-of-concept experiments using FWM in an HNLF show a receiver sensitivity improvement of 4 dB with an 18-GHz electrical bandwidth receiver, and the bandwidth limit is performed by a brick-wall anti-aliasing filter. Simulations show that with a 4th-order Bessel filter, it is possible for optical pre-sampling to improve receiver sensitivity of an 11-GHz bandwidth receiver by 7.1 dB.

4.4.7 Alternative implementation with a PPLN chip

This work was published in Optical Fiber Communications Conference and Exhibition (OFC), Los Angeles, CA, US, 2017 [61]. In this work an electrically shaped Nyquist on-off-keyed (N-OOK) signal was optically sampled in a PPLN chip.

Fig. 4.14 shows the experimental setup of a Nyquist-OOK system with an optical pre-sampler. The signal that is centered at 193.1 THz is modulated by 10-Gbaud Nyquist-OOK with a 215 bit long random data sequence. A variable optical delay line to temporally align the N-OOK signal with short sampling pulses. The sampling pulses are generated from a CW laser centered at 193.3 THz, whose output is intensity modulated and phase modulated by a 10-GHz sinusoidal RF source [335]. A wavelength selective switch compresses the sinusoid waveform by applying a quadratic phase shift across the spectrum.

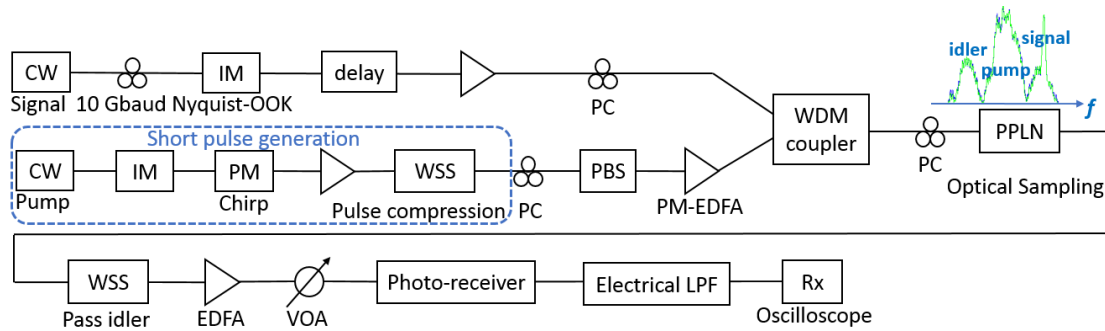


Fig. 4.14 N-OOK receiver with optical pre-sampling (a) experimental setup (b) simulation setup. CW: constant wave. IM: intensity modulator. PM: phase modulator. EDFA: erbium-doped fiber amplifier. PM-EDFA: polarization maintaining erbium-doped fiber amplifier. WSS: wavelength selective switch. PC: polarization controller. PBS: polarization beam splitter. VOA: variable optical attenuator. LPF: low pass filter. PD: photodiode.

The optical sampling gate is a 50-mm long periodically poled lithium niobate (PPLN) waveguide. In the PPLN chip, the optical short pulse train (commonly called ‘pump’) and the N-OOK signal generate the ‘idler’ at a new frequency by difference frequency generation

(DFG) [34]. The idler, in this case, is the desired optically sampled signal. Since the PPLN chip is polarization sensitive, polarization controllers are used to maximize the idler power. The WSS filter operates as a 170-GHz band-pass filter centered at 193.5 THz to extract the idler. The EDFA and attenuator control the average power at the photo-receiver to plot BER versus received average optical power. A 3.8-GHz photo-receiver is implemented using a 43-GHz photo-receiver followed by a 3.8-GHz electrical low-pass filter (LPF). The photodiode is a Finisar XPRV 2021(A), and the electrical filter is a Minicircuits VLF 3800+.

In the simulation, an ideal intensity modulator driven by short Gaussian pulses mimics the optical sampling gate. To simulate the experiment setup, the 10-Gbaud N-OOK signal is sampled by the intensity modulator, and becomes 12-ps OOK pulses. The electrical low-pass filter is modeled by a 4th-order Bessel filter with a 3.8-GHz bandwidth.

Figure 4.15 (a) compares the simulation results (dashed line) and experimental results (solid line). In each case, represented by different colors, the simulated and experimental results follow the same tendency. Therefore, the simulation provides a reasonable estimation of the experimental results.

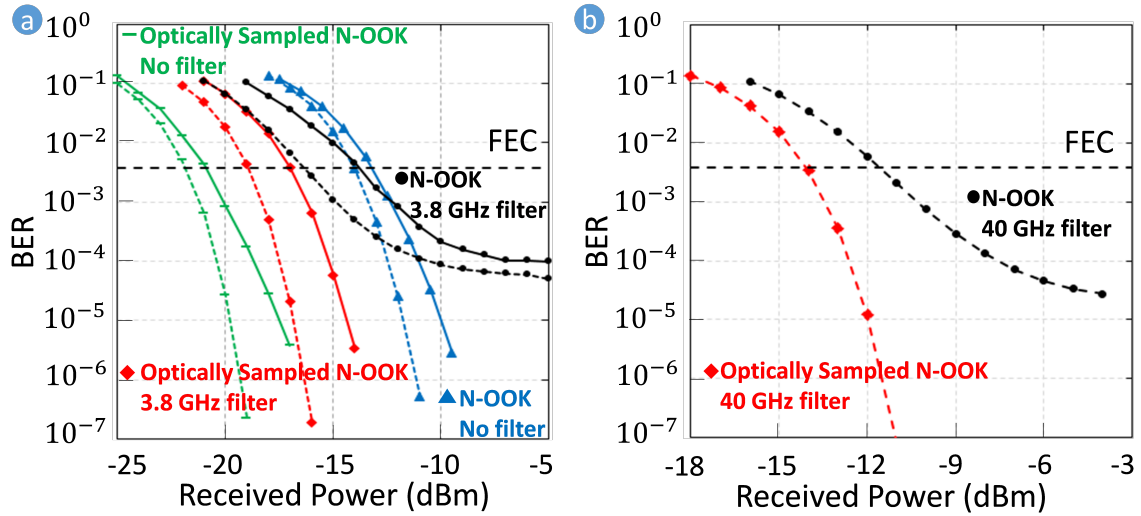


Fig. 4.15 (a) BER vs. Received Optical Power plot from experiments (solid line) and simulations (dashed line). (b) BER vs. Received Optical Power plot of 100 Gbaud N-OOK received by 40-GHz bandwidth photodiode simulation.

To show the degradation caused by the receiver's limited electrical bandwidth, the two systems without optical pre-samplers are first compared. The curve with 3.8-GHz electrical filter is slightly better than the one without filter when BER is less than 10^{-3} , since out-of-band noise is reduced. When the BER is close to 10^{-4} , the insufficient receiver bandwidth dominates, and there is little improvement in BER with further increases in optical power.

A comparison between the systems with and without optical sampling when both are bandlimited shows the advantage of optical sampling. Without optical pre-sampler, the BER hits an error floor at 10^{-4} . However, with an optical pre-sampler, the BER can be well below 10^{-7} . The experimental result shows that the optical power can be decreased by 4 dB, at $\text{BER}=3.8 \times 10^{-3}$, and by more than 9-dB for BERs less than 10^{-4} . The simulations confirm the advantage of the optical pre-sampler. Without a band-limiting filter applied to the receiver, the optically sampled signal also requires much less average received optical power (same peak power). This is to be expected when sampling a continuous signal with a discrete short optical pulse before reception.

Fig. 4.15 (b) shows the simulation results for a 100-Gbaud N-OOK systems and a 40-GHz photo-receiver. The N-OOK system without an optical sampler has an error floor at about 5×10^{-5} , while the system with optical sampling (1.2 ps pulses) can reach a BER less than 10^{-7} . The similarity between curves for the 10-Gbaud case and 100-Gbaud indicates the result is scalable to other frequencies, if the ratio between the signal and photoreceiver bandwidths is maintained. The difference results in different error floor for N-OOK received by band-limited photodiode.

In conclusion, it has been experimentally demonstrated that optical pre-sampling with short optical pulses helps to mitigate the electronic bandwidth limitations. A 4-dB sensitivity improvement was measured at the 7% hard FEC limit.

In these experiments, with a single sampling gate, there is no noticeable performance difference using a PPLN-based sampler over a HNLF-based sampler. However, the PPLN waveguide is a few centimeters long, as opposed to the 1-km long HNLF, and so can achieve the same functionality in a much smaller device.

4.5 Noise-bandwidth-reduced all-optical sampling based on a temporal integrator

A novel noise-bandwidth-reduced all-optical sampling method enabled by temporal integration is proposed in this section. The integration effectively provides a precise self-tracking optical filtering function, which improves the receiver sensitivity by up to 8 dB with a PAM4 signal.

The combined effect of walk-off and XPM between the signal and sampling pulses results in the integration of the signal during sampling, resulting in a rectangular sampling gate. The noise is averaged by this integration process. This work can be used to reduce noise and

so improve the signal-to-noise ratios (SNR) without optical-to-electrical-to-optical (OEO) conversion.

This work was published at the Conference on Lasers and Electro-Optics (CLEO), San Jose, CA, US, 2018 [62].

4.5.1 Motivation

When optical sampling [336, 325, 293, 324, 63, 61, 337] is used to sample a signal, it also samples noise, both in-band and out-of-band. Although conventional optical filters can be applied to reduce the out-of-band noise, the achievable minimum bandwidth is limited, and precise optical frequency alignment is needed. Optical sampling with a strong noise suppression capability is therefore desirable to improve the quality of the sampled signal. The cross-phase modulation (XPM) based temporal integrator proposed by Kong [338] is able to reject out-of-band noise. It has been used to improve the pulse fidelity from an all-optical digital-to-analog converter (DAC). In this work, the temporal integrator is extended to provide all-optical sampling with strong out-of-band noise suppression for a 1.25-Gbaud pulse amplitude modulation PAM-4 signal. The proposed sampling scheme is experimentally investigated under various optical signal-to-noise ratios (OSNRs) of the input signal. The proposed scheme is applied at the receiver side, enabling up to an 8-dB receiver sensitivity improvement over the case without the temporal integrator.

4.5.2 Operational principle

The temporal integrator is based on XPM with an appropriately designed walk-off between the probe and the pump [338]. The probe is a train of short optical pulses. The pump is the signal to be sampled. The probe is modulated by the integral of the signal's optical power over the designed walk-off duration. The phase modulation can be converted into amplitude modulation with an optical interferometer. Although it operates in the optical domain, this operation is a filtering function of the signal's power operating at the baseband. It also effectively self-tracking the optical carrier frequency. Assume in the loop, the group velocity dispersion (GVD) does not change the slowly-varying-envelope of the pump and the amplitude of the pump is a constant plus a non-deterministic random noise over the walk-off duration. By adapting Chiang's equations [339] into this application, the accumulated phase modulation from the slowly-varying-envelope of the pump to the probe pulses can be

approximated by [338]

$$\Delta\phi_{XPM} = -2\gamma L_{eff} \sqrt{\eta_{XPM}} \frac{\int_0^{T_w} P_{pump}(t) dt}{T_w} \quad (4.7)$$

where T_w is the walk-off duration, γ is the nonlinear coefficient of the medium, L_{eff} is the effective length, P_{pump} is the optical power of the pump, η_{XPM} is the cross-phase modulation efficiency given by [339]

$$\eta_{XPM} = \frac{\alpha^2}{\omega^2 d_{12}^2 + \alpha^2} \left[1 + \frac{4 \sin^2 \left(\frac{\omega d_{12} L}{2} \right) e^{-\alpha L}}{(1 - e^{-\alpha L})^2} \right] \quad (4.8)$$

where: ω is the frequency offset from the center of the pump's frequency, α is the attenuation coefficient of the fiber, L is the length of the fiber, d_{12} is the walk-off parameter defined as [339]

$$d_{12} = \int_{\lambda_{pump}}^{\lambda_{probe}} D(\lambda) d\lambda \quad (4.9)$$

where: D is the dispersion coefficient, λ_{pump} and λ_{probe} are the center wavelengths of the pump and probe respectively. When dispersion slope S is zero, d_{12} can be approximated by $d_{12} = D \times \Delta\lambda$, where $\Delta\lambda = \lambda_{probe} - \lambda_{pump}$.

If the fiber dispersion is zero, the cross-phase modulation efficiency η_{XPM} is independent of frequency. If the fiber is dispersive, the dispersion contributes to the base-band filtering effects of this temporal integrator. Equation 4.8 shows the low-frequency part of the pump induces stronger XPM to the probe pulse than the higher frequency part.

By re-arranging Eq. 4.8 with the attenuation α set close to zero, in a lossless fiber, $\sqrt{\eta_{XPM}}$ can be approximated by

$$\sqrt{\eta_{XPM}} = \text{sinc} \left(\frac{\omega d_{12} L}{2} \right) \quad (4.10)$$

By substituting the same parameters in Eq. 4.10 (lossy fiber) and Eq. 4.8 (lossless fiber), the effect of fiber loss α to the square-root of the cross-phase modulation efficiency $\sqrt{\eta_{XPM}}$ is shown in Fig. 4.16. The estimated attenuation (α) of the DCF in these experiments is 0.77 dB/km, which effects the nulls of the sinc function, but not the overall filtering effect used for noise suppression.

As shown in Fig. 4.17 (a), this noise-bandwidth-reduced all-optical sampling scheme can be realized with a nonlinear loop mirror (NOLM). If the pump is a 1.25-Gbaud PAM-4

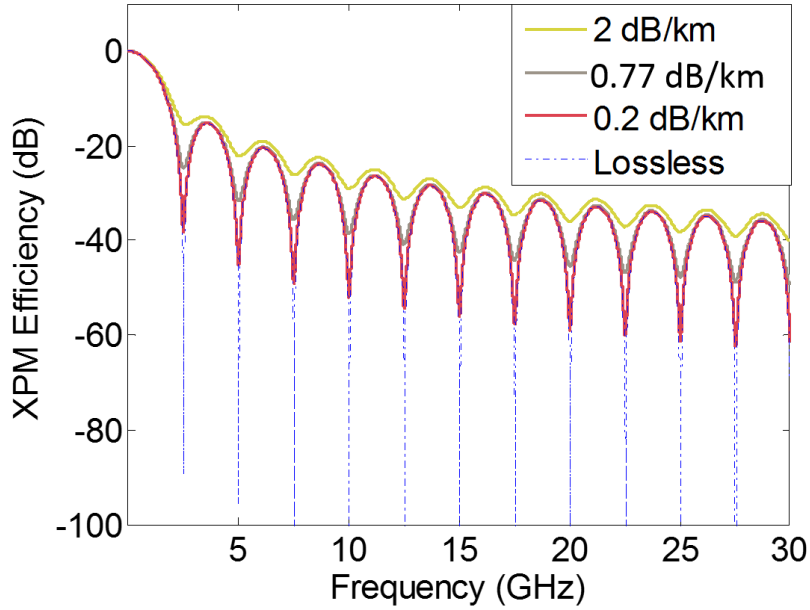


Fig. 4.16 Square-root of the cross-phase modulation efficiency $\sqrt{\eta_{XPM}}$ against the frequency offset to the centre frequency of the pump ω with fiber loss set to 2, 0.77, 0.2, 0 dB/km. (length $L=3$ km, dispersion $D= -107.412$ ps/km.nm, dispersion slope $S=0$, wavelength separation between the pump and the probe pulses $\Delta\lambda = 1.24$ nm).

signal, the maximum integration time should then be 800 ps. However, a walk-off of 400 ps was used to avoid the transitions of the pump pulses. If a 3.4-km DCF module with a dispersion of -107.4 ps/nm/km and a dispersion slope of -0.3567 ps/nm²/km (@1566 nm) is utilized as the nonlinear medium for XPM, the pump and the probe pulses are then allocated at 1551.385 nm and 1552.935 nm for the desired walk-off duration.

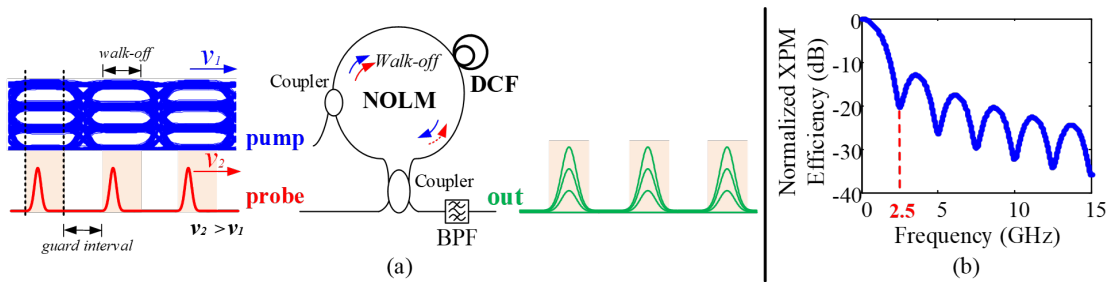


Fig. 4.17 (a) Principle of all-optical sampling based on a NOLM; (b) XPM efficiency at baud rate of 2.5 Gbaud. DCF: dispersion compensation fiber; BPF: band pass filter.

Fig. 4.17 (b) shows the XPM efficiency against the frequency offset from the center of the pump of a $\Delta\lambda$ of 1.154 nm. By introducing the 400 ps walk-off with respect to the probe pulses, a 2.5-GHz sinc-shaped filter is realized. Therefore, most of the out-of-band noise from the pump will be filtered out when performing the all-optical sampling.

4.5.3 Experimental setup

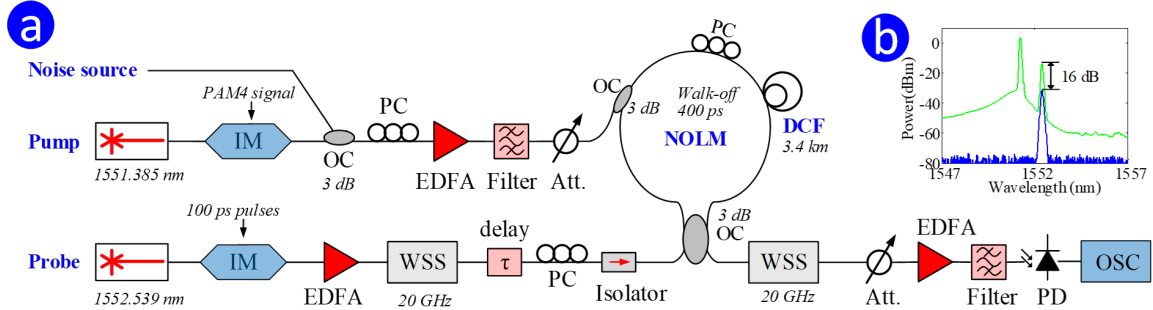


Fig. 4.18 (a) Experimental setup of all-optical temporal integrator for noise suppression of PAM 4 signal; OC: optical coupler; PC: polarization controller; EDFA: erbium doped fiber amplifier; Att.: attenuator; PD: photo-diode; OSC: oscilloscope. (b) Optical spectra of the output of NOLM with and without pump.

Fig. 4.18 (a) shows a proof-of-concept experiment setup for the all-optical sampling scheme. A continuous wave (CW) at 1551.385 nm is intensity-modulated with a 1.25-Gbaud non-return-to-zero (NRZ) PAM 4 signal as the pump. An optical noise source with 100-GHz bandwidth is adjusted by a variable optical attenuator (VOA) for appropriate power levels and then coupled with the pump for evaluating the performance under various optical signal-to-noise ratios (OSNRs). The pump is amplified and then filtered by a 100-GHz optical band pass filter (OBPF) before it is coupled into the NOLM. Another CW at 1552.539 nm is intensity-modulated into an optical pulse train with 100-ps pulse-width and 1.25-GHz repetition rate as the probe pulses. The probe pulses are then amplified and filtered by a 20-GHz Gaussian filter implemented by a wavelength-selective switch (WSS). An optical delay line is used to align the pump and the probe pulses. A 3.4-km DCF with the same parameters described in the principle section is inserted in the NOLM as the nonlinear medium. The probe pulses are phase-modulated by the pump in the NOLM with a designed 400-ps temporal integration and are then automatically phase-to-amplitude converted at the output port of the NOLM. The modulated probe pulses are then selected by a 20-GHz Gaussian filter. An optical preamplifier receiver, including an EDFA, a 100-GHz OBPF, and a 70-GHz photodiode, is used to detect the sampled signal. The EDFA with a 5.5-dB noise figure is set to a constant output power of 3 dBm. A real-time sampling oscilloscope with a sampling rate of 40 GSa/s is used. The anti-aliasing low-pass filter in the oscilloscope is set to 2 GHz and 10 GHz for performance comparison.

Fig. 4.18 (b) shows the optical spectra at the output of NOLM with and without the pump. The pump power at the input of NOLM is limited to 11.2 dBm (for NOLM “on” state) to avoid the stimulated Brillouin scattering (SBS), for a better signal quality. The measured difference between NOLM “on” and “off” states from the spectra is 16 dB.

4.5.4 Results and discussions

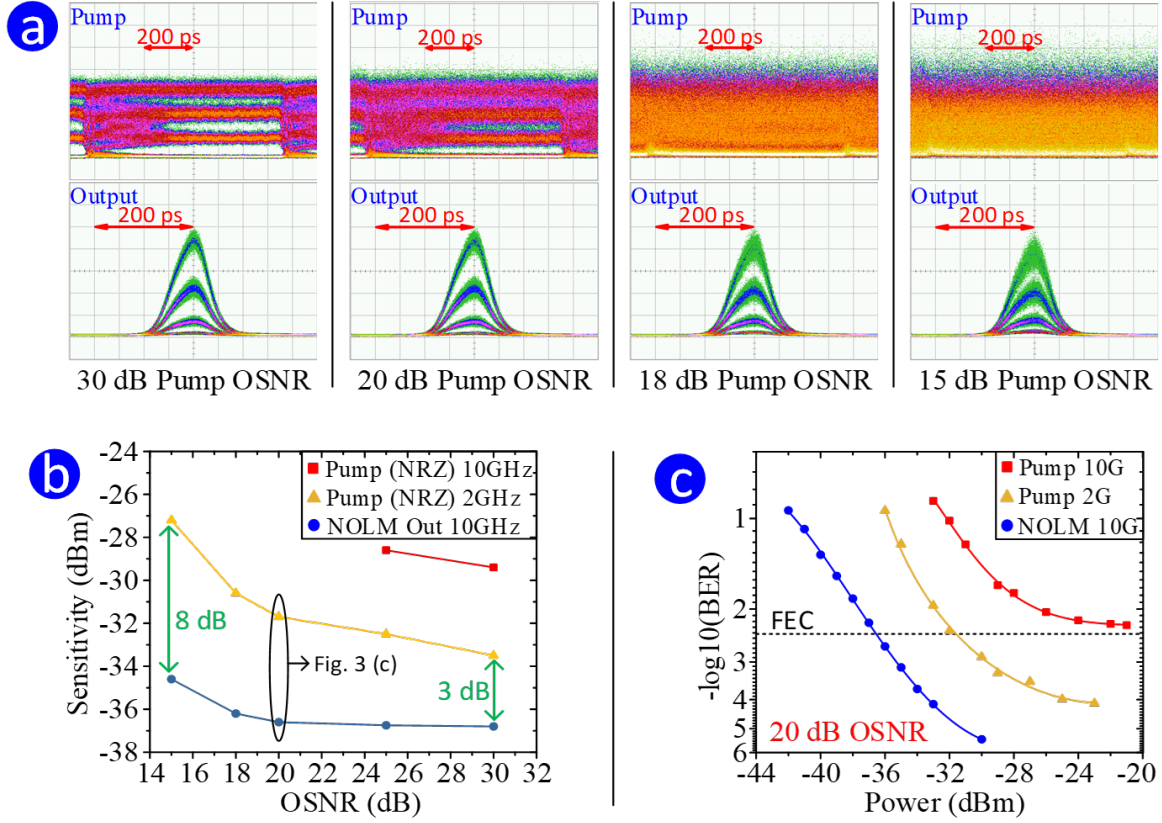


Fig. 4.19 (a) Eye diagrams of the pump with 10-GHz anti-aliasing filter and the output of NOLM with 10-GHz anti-aliasing filter under OSNRs of 30 dB, 20 dB, 18 dB and 15 dB. (b) Sensitivity versus OSNR plot (c) BER versus received optical power plot at 20-dB OSNR for pump with 10-GHz anti-aliasing filter, pump with 2-GHz anti-aliasing filter, and output of NOLM with 10-GHz anti-aliasing filter.

Figure 4.19 (a) shows eye-diagrams of the pump and NOLM outputs, with anti-aliasing filter set at 10-GHz. The 30-dB OSNR pump eye-diagram depicts there is about 400-ps portion in the transition of each 800-ps long symbol, so the temporal integrator is designed to integrate over the 400-ps middle portion of each symbol. The output of the NOLM is RZ PAM4 signal with about 90 ps width. The eye-diagrams of lower OSNRs show the dramatic noise suppression effect of the temporal integrator.

Figure 4.19 (b) shows sensitivity versus OSNR plots. The system performance of the pump with a 2-GHz (yellow), or a 10-GHz oscilloscope filter (red), and the output of the NOLM with 10-GHz filter (blue) are compared under different OSNRs. The 2-GHz and 10-GHz filters are implemented by a digitally defined anti-aliasing filter in the OSC. The 10-GHz anti-aliasing filter represents the case that the signal is received with considerable

out-of-band noise. The 2-GHz anti-aliasing filter eliminates noise, and it is used to compare with the proposed 2.5-GHz sinc-shaped filter. Note that the anti-aliasing filter can only be set to integer numbers. Compared with 10-GHz filtered pump, the proposed temporal integrator improves sensitivity by 7 and 8 dB at OSNRs of 30 and 25 dB. Compared with 2-GHz filtered pump, the proposed temporal integrator improves sensitivity by 3, 5 and 8 dB at OSNRs of 30, 25, and 15 dB. At OSNRs equal or less than 20 dB, the BERs of 10-GHz anti-aliasing filtered pump are all above 3.8×10^{-3} FEC limit, so there is no sensitivity for those points in Fig. 4.19 (b). Fig. 4.19 (c) shows received optical power versus BER at 20 dB OSNR. The BERs of the NOLM output can be much lower than 10^{-6} , while pump with 2-GHz filter tends to have an error floor at 4.5×10^{-4} .

The proposed temporal integrator is preferable, since it provides sinc-shaped filtering, and also very narrow filter passband. The pass bandwidth can be altered by changing the frequency separation between the probe pulses and pump or by replacing the DCF.

4.6 Conclusion

The focus of this chapter is optical sampling using optical frequency combs. Three devices for optical sampling and applications of optical sampling were presented. Simulations and experiments of optical sampling using Sagnac loops, PPLN, and highly nonlinear fibers are included in this chapter.

There are two original works in this chapter. The first one is to use optical sampling to pre-process a 10-Gbaud Nyquist-OOK optical signal so that the signal can be detected by a receiver with an electrical bandwidth less than half the symbol rate (i.e. 3.8-GHz). Optical sampling at the ISI-free point of a Nyquist signal avoids the stringent requirement on the orthogonality among the pulses in the receiver. Thus the optically sampled signal has more immunity to receiver bandwidth limitation compared to the original Nyquist signal. This investigation highlights the potential of optical sampling to improve the overall capacity of optical communication systems.

The second original idea was noise-bandwidth-reduced optical sampling using a temporal integrator. The proposed method overcomes the problem of large noise bandwidths in most sampling processes. The way to reduce noise bandwidth in electrical sampling is to add a digital filter after the sampling process. In the proposed optical sampling process, the integration effectively provides a precise self-tracking optical filtering function operating on baseband intensity. Taking the advantage of XPM and dispersion, the proposed temporal integrator acts as a baseband filter but is implemented in the optical domain. In the future, the noise-bandwidth-reduced sampler can be used to temporally compress and filter multiple low-

speed optical tributaries, so that the compressed tributaries can be time division multiplexed to form a high-speed signal.

There are two considerations of the OSP methods proposed in this chapter and also the following two chapters. Firstly, a clock recovery circuit [340] is required at the receiver to synchronize the optical sampling pulses and the signal. For this proof-of-concept investigation, an electrical cord was used to synchronize the device for sampling pulse generation and the device for signal generation. In a live communication system, a real-time analogue clock recovery system would be required, before the single-sample-per-symbol optical sampling stage. Secondly, the repetition rate of the sampling pulses should be matched to the symbol rate of the signal. Therefore, for flexibility, a comb source with a tunable repetition rate is required [341–343, 60]. For example, comb generation using electro-optics modulators described in Chapter 3 allows tuning of the repetition rate.

The optical samplers described in this chapter sample at one-sample-per-symbol, that means digital signal processing such as clock recovery and dispersion compensation cannot be implemented. The assumptions of the ideas in this chapter are the dispersion has been compensated and there is no significant signal distortion. To enable the digital signal recovery algorithms, optical sampling at two-samples-per-sample is required [344].

In summary, optical short pulses enable ultra-fast optical signal processing, overcoming the bandwidth limitation of electronics. By pre-processing a high-speed signal with short temporal gates, the required receiver's electrical bandwidth is significantly reduced. Optical short pulses enable signal processing over a wide bandwidth. Correspondingly, most optical sampling results in a high noise bandwidth. The sampling process can be improved by using the proposed integrator, which delivers an optically sampled output with a high signal bandwidth and a low noise bandwidth. In this chapter, optical sampling was used for single-carrier signal processing, but it can also be used for WDM signal processing. Each WDM channel can be treated as a single-carrier signal after extracted by an optical filter.

In this chapter, optical frequency combs act as short pulses for optical sampling. Optical sampling is usually used to resolve high-speed signals in the time domain. In the next Chapter, optical frequency combs act as carriers for WDM aggregation. Each optical frequency comb line is coded with different or the same information to enhance broadband signal processing or to resolve the frequency tracking and alignment problems in optical WDM systems. From this chapter to the next chapter, the research focus moves from time domain to spectral domain.

Chapter 5

Frequency combs for WDM aggregation

As dense wavelength-division-multiplexing (DWDM) is widely used in optical communication systems with add-drop multiplexers, it is essential to have each WDM channel precisely aligned to the WDM grid. In DWDM systems, there may be problems such as frequency offsets among types of equipment and frequency drifts of lasers.

Frequency combs enable the generated signal to have its spectrum defined by an optical filter. By sampling the signal with a frequency comb whose repetition rate is the same as the symbol rate of the signal, the frequency components of the signal are replicated over a wide bandwidth. Therefore, an optical filter can select any wavelength of the replicated spectra, and the output of the filter will carry the same information as the input signal, but its central wavelength and spectral shaping are re-defined by the optical filter.

Section 5.2 introduces the concept of WDM wavelength quantizer, which aligns signals with random frequency drifts to precise static frequencies. The key idea is to generate repeated spectra by optical sampling the signal with a frequency comb so that the redundant frequency components provide tolerance of the frequency misalignment between the signal and the WDM filter. Therefore, the new signal frequency redefined by the filter is independent of its initial frequency. This follows the work of Lowery et al.[327].

Section 5.3 presents a demonstration of full C-band Nyquist-WDM (NWDM) generation with an interleaver chip. This work shows not only the central frequency but also the envelope of the spectrum can be redefined by filters. An optical interleaver with repeated Nyquist-shaped amplitude responses enables optical Nyquist-shaping and multiplexing of WDM channels. To generate Nyquist superchannel, all the inputs of the interleaver should have flat spectra in their passing band. One way to achieve flat spectra is to modulate a signal onto a frequency comb.

5.1 Introduction

As passive-optical networks increase their penetration in the access networks [345], the interfaces between optical networks of different scales become important in overall network operation. Currently, aggregation of access network connections onto higher capacity networks is achieved through optical-electronic-optical (O-E-O) conversions. This provides for signal regeneration and wavelength conversion, to make the incoming signal compatible with the WDM grid on the high-capacity side.

There are several considerations of WDM aggregation using O-E-O conversion. The first concern is the latency in the O-E-O conversion process. Secondly, to process hundreds of WDM channels, requires hundreds of O-E-O converters and modulators. The third consideration is wavelength stability and accuracy.

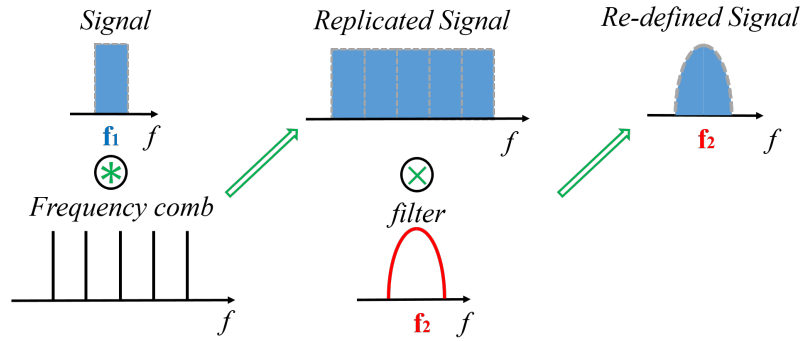


Fig. 5.1 Principle of filter defined spectra.

In a dense wavelength-division multiplexing (DWDM) system with narrow channel spacing, wavelength stability against environmental perturbations is essential. For example, for a 10-Gb/s transmission in a 25-GHz spacing WDM grid, the maximum allowable wavelength deviation recommended by ITU-T is 1.25 GHz [346]. This requirement is more stringent in an ultra-dense WDM system. However, the central wavelength for a laser can change with the environment, for example, temperature [347]. By packing a thermoelectric cooler with the laser, the temperature variation can be limited to 1°C [348]. Other techniques have been developed to stabilize lasers [349–351]. For instance, a frequency discriminator based on molecular gases enables the frequency stability to within 1 MHz [348]. In 2013, the typical linewidth of a commercial optical communication laser is 40 MHz [352]. In 2018, the commercial DWDM laser LS5000 from Thorlabs features 10-MHz linewidth. The problem of these lasers is, due to the high energy levels in the laser cavity, the end facets are degraded over time [353, 354], resulting in laser frequency drift. Another consideration is the accuracy of the laser wavelengths in regards to the ITU-T grid. Ideally, all the WDM

channels should be properly aligned to the ITU-T grid to avoid interferences and loss of information. However, the manufactured laser may not operate at the exact desired frequency or the reference frequencies of different devices are different. The frequency offset between a transmitter and a local oscillator can reach up to 5 GHz [355].

The above mentioned problems can be solved by all-optical WDM aggregation. As shown in Fig. 5.1, one-sample-per-symbol optical sampling convolves a signal and an optical frequency comb in the spectral domain, resulting a flat-top "white spectrum" with multiple copies of the signal [327]. When filtering the replicated signal, a new spectrum whose central frequency and spectral envelope are defined by the optical filter is generated. This method avoids O-E-O conversions and it makes the alignment to the ITU-T grid easier. More importantly, it is robust to the laser drift of the initial signal.

5.2 WDM wavelength quantizer

This section presents an original work called "WDM Wavelength Quantizer" published in Asia Communications and Photonics Conference (ACP), Wuhan, China, 2016 [63]. The periodically poled lithium niobate (PPLN) waveguide is provided by Dr. Andreas Boes at RMIT University.

A WDM wavelength quantizer is an all-optical frequency shifter that remaps signals with significant unknown frequency drifts onto precise static frequencies, as defined by channel multiplexing filters. A WDM quantizer can be useful for aggregating access networks into core networks.

As illustrated in Fig. 5.2(a), interfacing different networks, while keeping the signals in the optical domain, is problematic. At the access side, the user's optical interface is extremely cost sensitive, often requiring sacrifices in system performance. The frequency grid used for wavelength division multiplexing (WDM) is tightly specified, requiring frequency stabilization of the transmit lasers used in this system, while in access networks, lasers may run without temperature control or precise frequency tuning, resulting in significant drifts in optical frequency.

Optical sampling (Fig. 5.2(b)) followed by optical filtering with arbitrary center frequency can quantize a randomly drifting incoming optical signal to the desired WDM grid. This is in contrast to most wavelength conversion methods, which require known signal frequencies [356] or significant and controlled signal-carrier frequency offset [357].

In the experimental demonstration, the sampling is achieved by mixing a train of short optical pulses (a wide bandwidth comb in the spectral domain) with a narrowband signal. The resulting broad-band signal can be filtered to match a WDM grid with a small (<1 dB)

performance penalty. The experimental demonstration includes 10-Gbps on-off keyed (OOK) signals, sampled in a periodically poled lithium niobate waveguide.

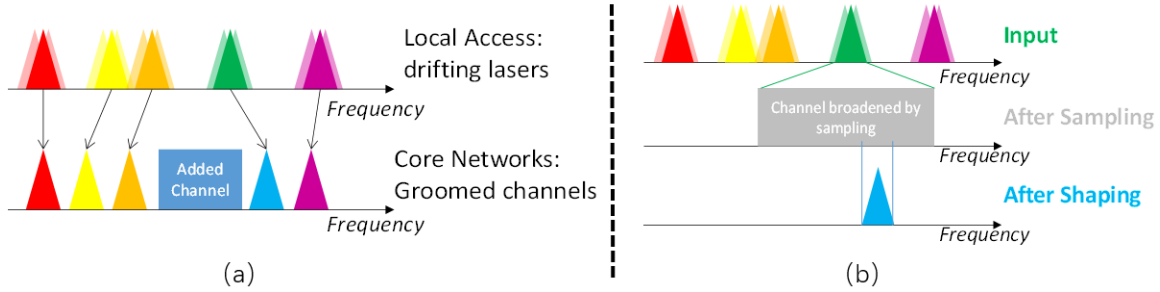


Fig. 5.2 (a) Grooming Access wavelengths onto a Core network. (b) All-optical grooming by sampling and shaping.

5.2.1 Principle of optical arbitrary frequency shifting

As illustrated in Fig. 5.2(b), the mixing of the short optical pulses and the signal results in a “white” spectrum [327], when the baud rate of the signal is the same as repetition rate of the sampling. This white spectrum can then be optically filtered (or pulse shaped) to generate a signal at the desired frequency. In the last part, it has been shown that commercial wavelength-selective switches are able to reshape modulated pulses to provide almost any signalling format, such as optical OFDM and Nyquist-WDM [326, 358].

In this work, the “white” spectrum can be optically filtered anywhere within its spectral extent, regardless of center frequencies of the comb lines associated with the short optical pulses, to generate a new signal at the desired optical frequency. As such, if the signal laser is drifting, the optical channel filter (provided by a wavelength selective switch for instance) can ensure that the desired center frequency has been filtered out. Furthermore, the resulting center frequency can be changed by simply changing the optical channel filter.

5.2.2 Experimental setup and results

The experimental setup (Fig. 5.3) consists of an optical pulse source, on-off keyed transmitter, optical sampler, channel filter, and direct-detection receiver. The pulse source operates at 193.3 THz, with pulses generated from a CW wave followed by intensity (IM) and phase (PM) modulators driven by a 10-GHz sinusoid [335]. The phase modulator is driven via a 29-dBm RF amplifier, and provides the majority of the spectral broadening. A wavelength selective switch (WSS) compresses the pulses by applying a quadratic spectral phase filter and flattens the spectrum through line by line attenuation [359], producing a 90-GHz wide,

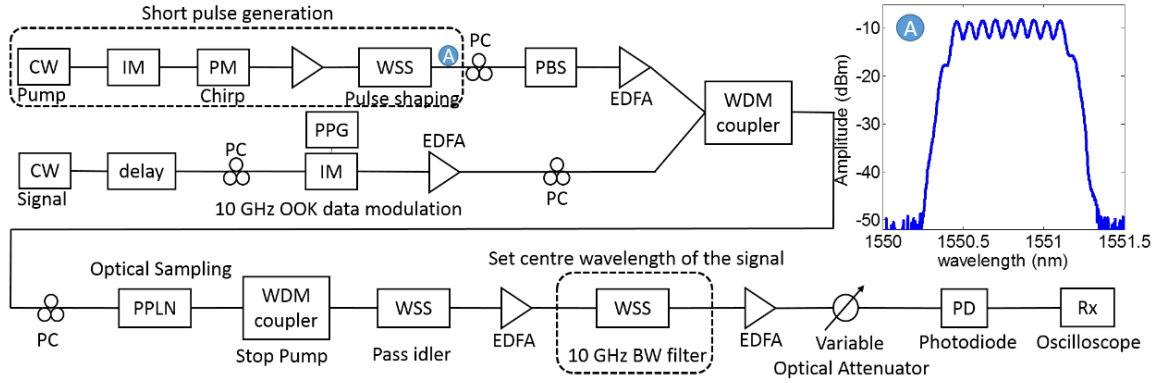


Fig. 5.3 Experimental setup. EDFA: Erbium doped fiber amplifier. PPG: Pulse pattern generator. PBS: Polarization beam splitter.

flat-top spectrum (inset, Fig. 5.3). The pulse average power is amplified to 1.45 W and combined with the signal with a WDM coupler, which additionally filters the pulses with a 100-GHz bandpass filter. The transmitter provides a signal centered at 193.1 THz, that is NRZ-OOK modulated with a $2^{15} - 1$ binary PRBS sequence at 10 Gbaud, and is delayed by variable optical delay line to temporally align the signal with pump sampling pulses. The optical sampler is a 50-mm long PPLN waveguide, where difference frequency generation (DFG) allows the generation of a phase-conjugate sampled signal at a different wavelength [360, 275, 34], commonly called the idler. The polarization controllers (PCs) are used to align the polarizations of the signal and pump to maximize the output idler power. Fig. 5.4 is the spectrum of the PPLN output. After the PPLN chip, the high-power pump is attenuated by a WDM coupler, which acts as a band-stop filter. A WSS filter with 170-GHz bandwidth and 193.5-THz center frequency is then used to select the sampled signal (or 'idler') as the output from the sampler.

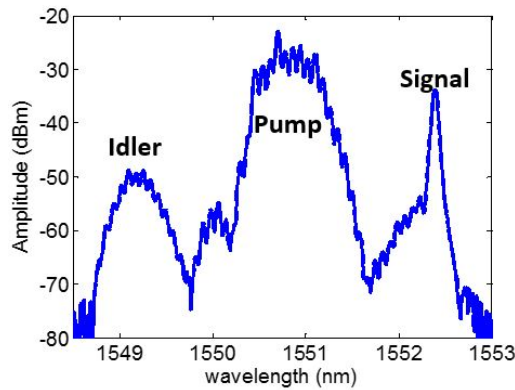


Fig. 5.4 C-band spectrum at the output of PPLN chip.

The sampled signal is amplified, then filtered with a 10-GHz bandwidth ‘channel’ filter. The filter’s center frequency is changed to simulate the frequency drifting effect of the signal laser. This is equivalent to the transmit laser’s frequency drift, as the conversion efficiency of the chip is flat over the 10-GHz tuning range used, owing to the THz-wide phase matching bandwidth for DFG in the PPLN chip [34].

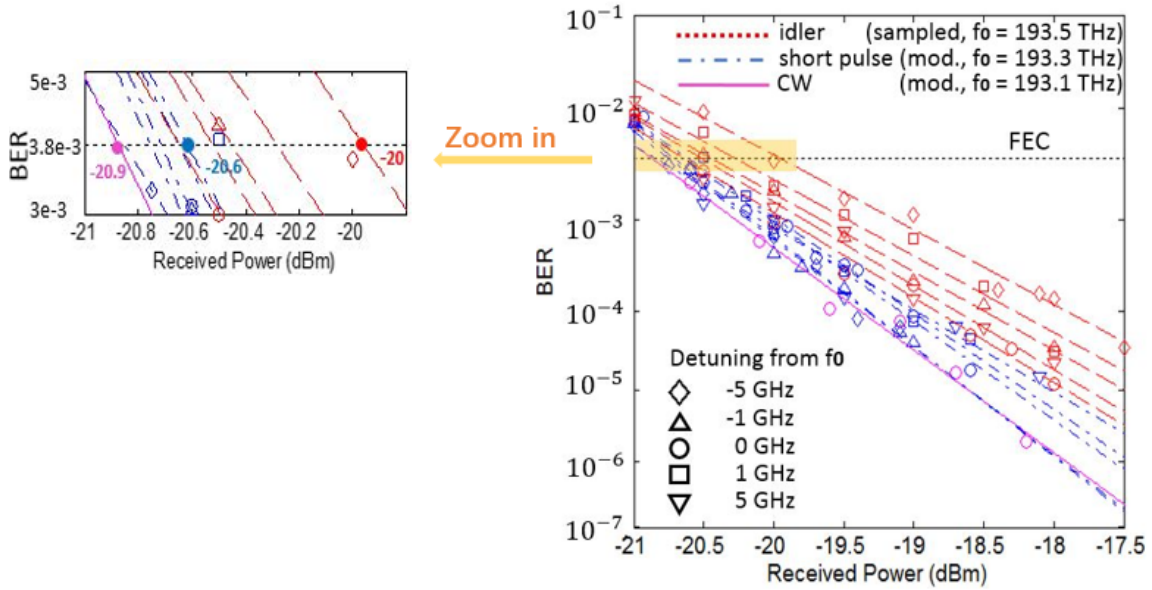


Fig. 5.5 BER vs. Received Power for modulated CW, modulated short pulse and idler. The zoom-in figure shows the maximum required received power for modulated pulse (blue) and sampled (red) signal, relative to the CW reference (pink).

The receiver comprises a 40-GHz bandwidth photo-receiver with an internal trans-impedance amplifier (Finisar XPRV2021A), with the output digitized by a 40-GSa/s, 16-GHz bandwidth real-time oscilloscope. The received waveforms are stored and analyzed offline for error counting. The received power level is controlled via a variable optical attenuator. The bit-error ratio (BER) is plotted against received power in Fig. 5.5, for various central frequencies. In this experiment, assuming that the system will be running with a 7% overhead forward error correction code (FEC) to bring a pre-FEC measured bit-error rate down from 3.8×10^{-3} to an error-free level of 1×10^{-15} . As such, the receiver’s sensitivity is defined as the received power at a $\text{BER} = 3.8 \times 10^{-3}$. The measured performance of the modulated continuous wave (CW) signal is passed directly into the receiver as a ‘back-to-back’ benchmark (magenta circles Fig. 5.5). This gives a receiver sensitivity of -20.9 dBm.

The curves for the idler filtered at various center frequencies by a 10-GHz bandwidth channel filter are shown in red in Fig. 5.5. The receiver sensitivity varies between -20.7 and -20 dBm, corresponding to a performance penalty compared with the modulated CW wave of

between 0.2 and 0.9 dB. In order to investigate the penalty introduced by the mixing process in the PPLN chip, the pump is modulated in the same manner as the case of a CW input, then filtered by 10-GHz bandwidth filter (blue traces in Fig. 5.5). For the modulated pump, the receiver sensitivities are -20.8 to -20.6 dBm, corresponding to penalties of 0.1 to 0.3 dB. The average sensitivities of the filtered idlers and modulated pump are -20.4 dBm and -20.7 dBm, respectively. The additional 0.3-dB sensitivity penalty may be due to spectral shaping of the idler away from the ideal white spectrum, or through noise introduced by the amplifiers before and after the PPLN. The spread in BER curves of idlers (± 0.4 dB in sensitivity) further points to spectral shaping as a prime cause of penalty, as the modulated pump spread is much less (± 0.1 dB sensitivity spread). Figure 5.6 shows the sensitivities of the converted signal when the incoming signal wavelength drifts from -20 to 30 GHz. The implementation penalty of this method is 0.5 dB on average. The maximum variation of the sensitivities is 0.9 dB.

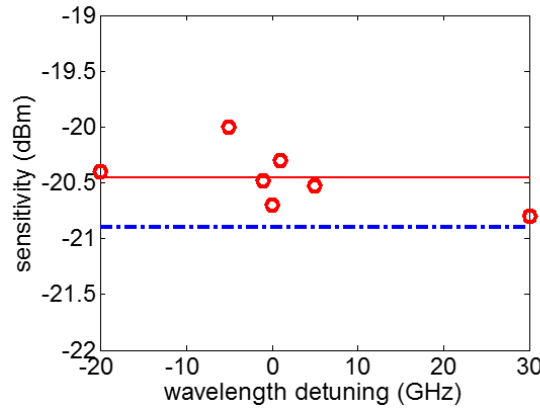


Fig. 5.6 Sensitivity vs. wavelength detuning of the incoming signal.

The sampler used for this function must be synchronized to the clock of the incoming signal. This can be achieved in synchronous systems, or through a clock recovery/synchronization stage [361], at the expense of some electronic control. By using a chip-based nonlinear device, this system has the potential to be a compact addition to racks. With higher conversion efficiency sampling [362], the amplifiers used in this set-up may be avoided.

5.3 Full C-band Nyquist-WDM Generation

This section presents an original work called "Full C-band Nyquist-WDM interleaver chip" published in Optical Fiber Communications Conference and Exhibition (OFC), Los Angeles, CA, US, 2017 [64].

Optical filters are crucial to the spectral shaping of the re-defined signal. As the demands on capacity at the metro and long-haul continue to increase, higher precision components are required to optimize overall system capacity. To generate Nyquist wavelength division multiplexing (N-WDM) signal, it requires optical filters with sharp passband-stopband transitions [163, 363]. Optical filters can be implemented with tapped delay lines and ring resonators. Goh *et al.* reported an on-chip Nyquist-filtering multiplexer with tapped delay lines, in which the maximum delay line length is 56 times of the circuit unit delay [250]. Wang *et al.* reported a ring-resonator based interleaver with simpler circuitry and smaller size, with a pass-band width of 100-GHz [364]. For NWDM generation, a narrower pass-band (i.e. 12.5-GHz) is desired, necessitating tighter fabrication tolerances due to the longer waveguide delays. A demonstration of full C-band Nyquist-WDM generation using an interleaver chip is described in this chapter. This is the same chip that was exploited for clock rate multiplication in Chapter 3, in a different configuration.

In this work, full C-band coverage of a Nyquist-filtering interleaver for super-channel multiplexing has been experimentally demonstrated. The work shows N-WDM super-channel multiplexing with zero guard-band, 12.5-GHz spacing, and a Q fluctuation <0.3-dB across the C-band.

This experiment is implemented with a ring-resonator-assisted Mach-Zehnder interferometer (RAMZI) interleaver on a $\text{Si}_3\text{N}_4/\text{SiO}_2$ platform, which features full C-band coverage (1530 nm-1565 nm), small size (1.2 mm \times 0.4 mm), sub-GHz spectral resolution, and a 0.08 RRC roll-off transition-band. Previously it has been shown that a PIC using a RAMZI can be used to shape and de-interleave N-WDM channels, with narrow or zero-guard bands, and nearly-flat pass-bands [365].

Full C-band coverage is always challenging to achieve due to the wavelength dependence of the material. For the first time, full C-band coverage of the RAMZI based Nyquist-filtering WDM multiplexer is experimentally demonstrated. The maximum Q variation over the C-band is less than 0.3-dB at the 7% hard FEC limit (@ BER= 3.8×10^{-3}). The presented RAMZI interleaver is an important building block for C-band N-WDM super-channel transmitters that are integrated on a photonic chip.

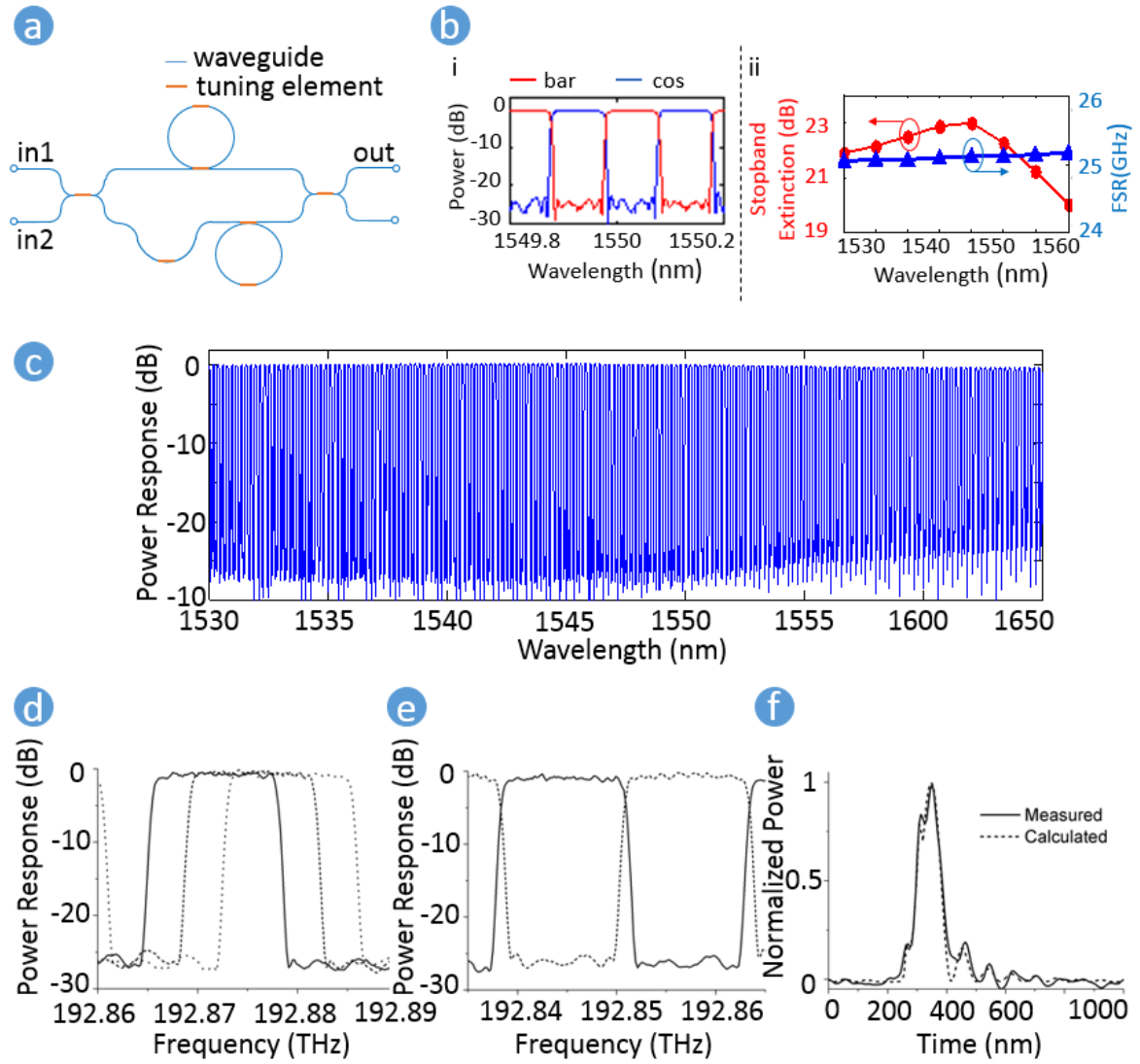


Fig. 5.7 (a) Chip topology; (b) i. power response of bar and cross; ii. FSR and stop-band extinction; (c) Full C-band response; (d) Demonstration of tuning; (e) demonstration of swapping; (f) Power envelope of the impulse response of the circuit.

5.3.1 Device characterization

Figure 5.7(a) shows the topology of the RAMZI interleaver, which comprises an asymmetric Mach-Zehnder interferometer (MZI) with one ring resonator coupled to each arm. The tuning elements can adjust optical phase or coupling ratios to obtain a flat-top filter response [105]. The response of the interleaver depends on whether the signals pass horizontally through it (e.g. from top port to top port), which is called the "bar" response, or diagonally across it (the "cross" response).

Figure 5.7(b) plots the stopband extinction measured at eight frequencies. The stopband extinction is larger than 20 dB at all points across the C-band. Figure 5.7(b) also plots the free spectral range (FSR) variation across the C-band. The variation is less than 120 MHz, measured with 19 MHz wavelength accuracy. Figure 5.7(c) plots the bar response over the entire C-band, measured with an optical vector analyzer (Luna System OVA5000).

Figures 5.7(d) and 5.7(e) demonstrate the programmability of the interleaver circuit. In Fig. 5.7(d), the phases of the two ring resonators and phase of the asymmetric MZI were tuned. This shows the passband's central frequency can be tuned without changing its shape, which is a useful function for flexible channel allocation in N-WDM. In Fig. 5.7(e), the passbands and stopbands swap positions, simply by introducing a phase change of π to one arm of the MZI.

Figure 5.7(f) is the power-envelope of the impulse response of the interleaver. It shows a deviation from a sinc-shaped response that would be required for a true Nyquist-WDM signals. This is because the ring-resonators have decaying responses, it is difficult to synthesize an overall response that is more symmetrical in time (in addition to the usual considerations of non-causality with sinc-shaped signals). This means the interleaver may introduce inter-symbol interference.

The filter has a total insertion loss of 9 dB, which is dominated by the fiber-chip coupling losses of 4 dB/facet. However, in principle, the coupling loss can be reduced to 1 dB/facet by waveguide facet optimization [366].

5.3.2 Experimental system

Figure 5.8 shows the experiment to test the performance of the RAMZI as an interleaver/shaper in a multi-channel system. Seven QPSK or OOK channels are generated at a 12.5-GHz spacing, using seven tunable lasers coupled through two modulators, to give three odd and four even channels. This number is sufficient to assess the inter-channel interference due to close neighbors. The tunable lasers were tuned across the C-band. The QPSK channels were spectrally shaped by the interleaver to approximate to N-WDM channels [163]. The output

signal of the interleaver was loaded with white noise (amplified spontaneous emission) then band-pass filtered with a Finisar WaveShaper to select one channel. The receiver was either a single photoreceiver (Finisar XPRV2021A) with a 40-GHz bandwidth for the OOK eye diagrams, or a coherent receiver (U^2T). The oscilloscope was a Keysight DSO-X 95004Q with a 50-GHz bandwidth and 160-GSamples/s rate.

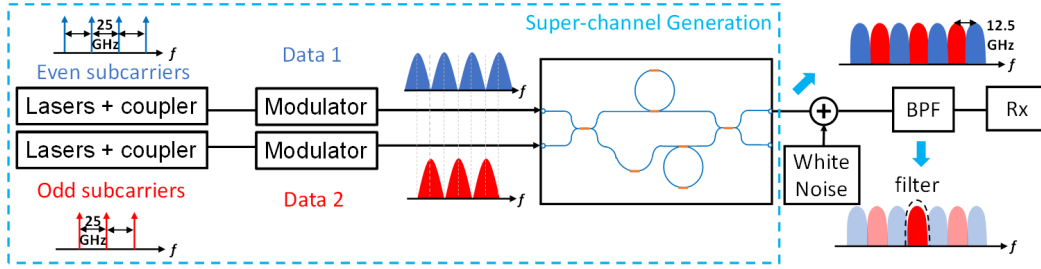


Fig. 5.8 Experimental setup of N-WDM generation using RAMZI Nyquist interleaver; CMZM: complex I/Q modulator.

5.3.3 Results and discussion

Figure 5.9(a) shows the eye-diagrams of OOK signals at four different baud-rates. Both the 5-Gbaud and 7.5-Gbaud cases show clear open eyes, which indicate little distortion. In the 10-Gbaud case, the eye-diagram shows some ringing causing broadening of the 0-1-0 transitions, possibly originating from the 120-ps separation of the main peak and the second peak of the impulse response (Fig. 5.9(e)). The 12.5-Gbaud signal has significant eye closure, possibly because it excites the 12.5-GHz resonances of the ring resonators.

Figures 5.9(b) and 5.9(c) demonstrate the uniformity cross C-band. Figure 5.9(b) plots the quality factors of the on-chip interleaved N-WDM QPSK signal measured over the full C-band, with OSNR = 25 dB (12.5-GHz resolution bandwidth). Since the chip was optimized at 1550 nm by adjusting the heaters, the maximum quality factor ($Q = 16.5$ dB) is observed at 1550 nm. The quality factor degrades away from this wavelength due to a reduced stopband extinction, as was shown in Fig. 5.7(c)—the lowest Q (15.2 dB) occurs at 1565 nm. The difference in quality factors between the best-case and the worst-case wavelengths is 1.3 dB. Figure 5.9(c) plots QPSK quality factor versus OSNR for central wavelengths of 1530, 1550 and 1565 nm, which are the best and the worst wavelengths in Fig. 5.9(b). The Q factors differ by 0.3 dB at the error-free threshold for 7% forward-error-correction (FEC) ($Q = 8.53$ dB).

In Fig. 5.9(d), the center frequency of the single-channel 12.5-Gbaud QPSK signal has been detuned away from the center of the filter passband. For frequency deviations less than

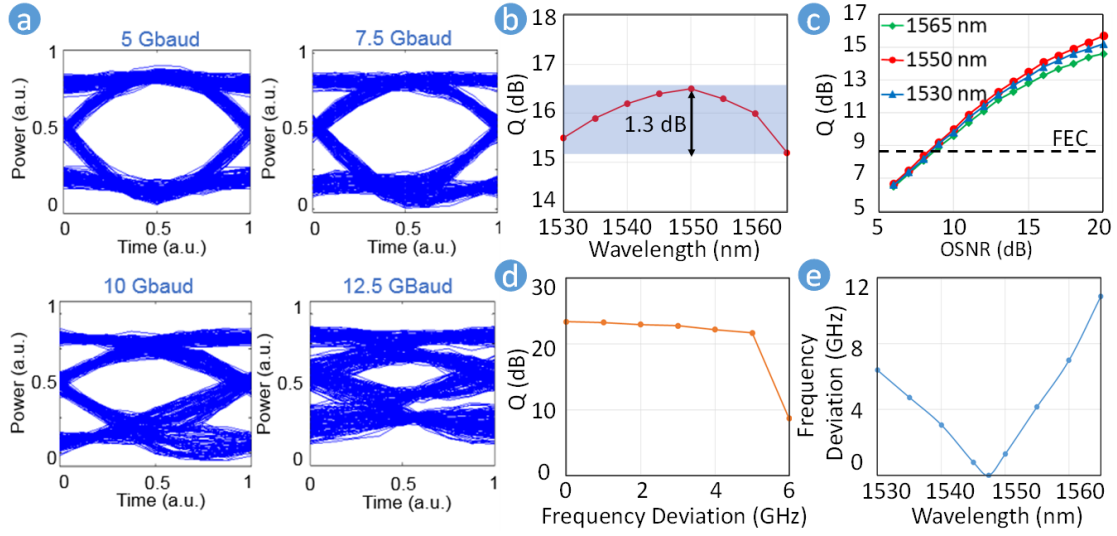


Fig. 5.9 (a) Eye-diagrams of OOK signals filtered by RAMZI; (b) Quality factor of QPSK signal at different wavelengths over the C-band; (c) Q vs. OSNR for QPSK signals centered at 1530 nm, 1550 nm, and 1565 nm; (d) Q degradation due to frequency misalignment; (e) Frequency deviation of the central frequencies compared with a 50-GHz grid.

5-GHz, the data can be decoded with less than a 1.7-dB penalty. If the deviation is larger than 6.25 GHz (half of the passband-width), the signal cannot be recovered.

The FSR of the chip is 25.1-GHz, so there will be an accumulated frequency deviation from the chip's grid and the 50-GHz PTC grid over the C-band. As shown in Fig. 5.9(e), when the chip is aligned at 1547.4 nm, a 10.9-GHz frequency deviation is measured at 1565 nm. Frequency errors can be reduced by optimizing the filter design.

5.4 Conclusions

In this chapter, frequency combs are used for the enhancement of WDM aggregation. Two original works are included in this chapter. The first one is the WDM wavelength quantizer. The information of the signal is copied and converted to a number of different evenly spaced frequencies by convolving with the frequency comb in the spectral domain. By applying an optical filter to the converted spectrum, the new wavelength and the new spectral envelope can be defined by this optical filter. The proposed scheme provides a solution to laser drifting problem when connecting access networks to core networks. This idea was demonstrated through an experiment, where a 10 Gbps OOK signal was decoded with <1dB power penalty, while the incoming frequency drifted over 50-GHz range. The advantage of this method is its robustness to incoming frequency drifts, low latency and transparency to modulation formats. Theoretically, the WDM wavelength quantizer can work for multiple incoming signals at separated wavelengths, which may be experimentally demonstrated in the future.

There are also aspects that need to be considered when using this WDM quantizer. Firstly, the PPLN used for wavelength conversion only support one polarization [118]. Polarization diversity techniques are required for a signal with different information on two polarizations. Secondly, the filter only takes a small portion of the copied spectrum. That means, most of the optical power is wasted. To solve this issue, the bandwidth of the copied spectrum can be reduced to just slightly larger than the laser drift range, thus reducing the power loss.

Another work is full C-band Nyquist-WDM generation. The reported chip overcomes conventional challenges, which include having broad-band coverage, small size, sub-GHz spectral resolution, tenability, and sharp transition simultaneously. Full C-band coverage is essential for building highly compact, low-cost and high-speed optical communication systems. For the first time, full C-band coverage of the RAMZI based Nyquist filtering WDM multiplexer is experimentally demonstrated. Each subcarrier is a 12.5-Gbaud QPSK signal. The chip was optimized at 1550 nm by adjusting the heaters where the maximum quality factor $Q = 16.5$ dB was observed. The maximum Q variation over the C-band is less than 0.3-dB at the 7% hard FEC limit. The future work can be the integration of a frequency comb source and the RAMZI interleaver on a single chip to achieve a chip-scale WDM transmitter [343, 367].

There are several considerations that effect the performance of this PIC in our Nyquist shaping application. The dispersion at the edges of the filter effect the pulse shape, and so limit the rate of the signals that can be successfully shaped for IM/DD systems. Note that in coherent systems, this dispersion can be compensated for in DSP [363]. Moreover, as the interleaver has a 3dB cross-over for adjacent channels, there can be significant inter-channel interference that can reduce performance. As shown in this chapter and in Corcoran,

Geng et al. [314], using a frequency comb with a spacing smaller than the FSR of the photonic interleaver can provide signals that are robust effects at the filter edges, as well as misalignment to the filter (similar to the operation principle of the WDM quantizer).

In summary, optical signal processing can be used to improve WDM aggregation in two aspects. The first one is broad operation bandwidth, which enables simultaneous signal processing of numerous WDM channels, while DSP can only process each WDM channel separately. The second is frequency alignment and tracking. The optical WDM quantizer enables frequency tracking of 50 GHz, which is far beyond the reach of frequency tracking using electronic methods [368–372]. The WDM quantizer can also be used to avoid the frequency misalignment caused by the difference in the frequency references of the WDM filter and the signal. Therefore, compared with electronic-only signal processing, OSP-aided systems provide wider operation bandwidth, wider frequency tracking bandwidth and better alignment ability.

These demonstrations, as with the optical sampling applications shown in Chapter 4, demonstrate that a stable, repetition rate tunable comb source is desirable for frequency-comb-based OSP.

This chapter is about OSP operations on WDM channels that are not spectrally overlapped. In the next chapter, OSP is used to process orthogonal frequency-division multiplexed (OFDM) signals, which have overlapped spectra among WDM channels. All the WDM channels of an OFDM signal are processed as one block in the time-lenses described in the next chapter.

Chapter 6

Time-lenses in optical communication systems

Time-lenses [230] are based on the space-time duality of light [373, 374]. They enable optical Fourier Transforms (OFT) and signal scaling in both temporal and spectral domains. Time-lenses are composed of linear chirp and dispersion elements. In order to efficiently process broad optical bandwidths, nonlinear optical effects such as four wave mixing (FWM) are often used to provide the key chirping step needed in time-lens systems. Ideally a linearly chirped control pulse will transfer its chirp to the target signal, which when combined with group velocity dispersion in an optical fiber, can produce the desired time-lens function. The generation of the control pulse (i.e. frequency comb in the spectral domain) has been discussed in Chapter 3.

Practically, time-lens based systems are limited by the achievable pulse shapes for the control pulse, higher-order nonlinear mixing and higher-order chromatic dispersion contributions which can introduce distortions to the time-lens function. Ultimately, these effects degrade the processed signal. While these degradations have been investigated in terms of the manipulation of Gaussian pulses [375], their impact on signals carrying optical data has not been well explored. Section 6.2 investigates these degradations and the design constraints in optical communication systems [65]. Meanwhile, a novel time-lens based system to compress OFDM symbols, and then time-division multiplex them was proposed. It is inspired by time-lens based pulse compression for short pulse generation [228, 376].

Section 6.3 investigates the use of temporal compression to time-division multiplex spectrally efficient optical orthogonal frequency division multiplexed (OFDM) [16-18] signals to provide a 1 Tb/s superchannel. The experiment shows that there is no significant penalty from inter-symbol interference among channels when demultiplexing OFDM with the proposed method.

6.1 Introduction

Time-lenses were proposed in 1989 by Brian Kolner [230]. As shown in Fig. 6.1, a time-lens is a temporal analogue to a physical lens, where chromatic dispersion and temporal chirp provide a mathematically identical effect on an optical waveform in the time domain to the effect of physical lens on an optical wavefront in space. In a physical lens system, the wavefront diffracts and so that it is spatially dispersed as it travels, while the lens provides a phase change on the wavefront that is dependent on position, generating a spatial chirp. In a time-lens system, diffraction is emulated by chromatic dispersion, spreading a temporal waveform out in time. The spatial chirp as generated by the physical lens is substituted for a temporal chirp. A time-lens can be constructed using two dispersive elements, such as dispersive optical fiber, and a device to impart a linear temporal chirp.

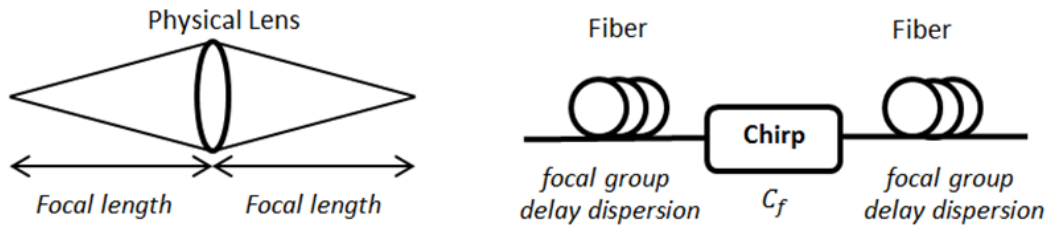


Fig. 6.1 Analogue between physical lens and time-lens. Input and Output dispersions act as free-space diffraction. Temporal chirp plays the role of spatial chirp.

The ‘focal length’ of a time-lens is defined by the chirp applied to the optical waveform [377]. In order for this lens system to focus, the temporal waveform needs to undergo an equivalent dispersion, such that the applied chirp (C_f [Hz/s]) is inversely proportional to the accumulated dispersion ($\beta_2 L_f$), with the focal group delay dispersion defined as $\phi_f = 1/(2\pi C_f) = \beta_2 L_f$ (where β_2 is the group-velocity dispersion parameter of the dispersive fiber, and L_f is the length of that fiber) [378].

As with physical lenses, a time-lens can be used for a multitude of applications. A time-lens can produce an output temporal waveform which is the time-domain Fourier transform of the input waveform. The Fourier transform property has been used for applications such as DWDM-to-OTDM conversion [379], ultrafast optical oscilloscope [380, 378], generation of arbitrary optical waveforms [381, 382] and optical OFDM generation [383]. Other combinations of time-lenses enable temporal or spectral scaling, which has provided ultrafast waveform compression [384] and spectral magnification [385–387, 229].

Time-lenses are also of interest to the manipulation of optical signals in communication systems due to their ability to scale and exchange the temporal and spectral information of optical waveforms. There are demonstrations of the conversion of time-to-wavelength





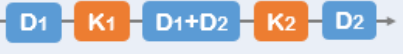
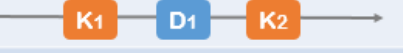

Complete OFT		
Configurations	Conditions	Input & Output Relations
	$K_2 = K_1$ $D_1 \times K_1 = 1$	$\Delta t_{out} = (1/K_1) \Delta \omega_{in}$ $\Delta \omega_{out} = K_1 \Delta t_{in}$
	$D_2 = D_1$ $D_1 \times K_1 = 1$	$\Delta t_{out} = (1/K_1) \Delta \omega_{in}$ $\Delta \omega_{out} = K_1 \Delta t_{in}$
"Partial" OFT		
Configurations	Conditions	Input & Output Relations
Time-to-frequency Conversion 	$D_1 \times K_1 = 1$	$\Delta \omega_{out} = K_1 \Delta t_{in}$ Have residual dispersion
Frequency-to-time Conversion 	$D_1 \times K_1 = 1$	$\Delta t_{out} = (1/K_1) \Delta \omega_{in}$ Have residual chirp
Complete Scaling		
Configurations	Conditions	Input & Output Relations
	$D_1 \times K_1 = 1$ $D_2 \times K_2 = 1$	$\Delta t_{out} = (K_1/K_2) \Delta t_{in}$ $\Delta \omega_{out} = (K_2/K_1) \Delta \omega_{in}$
"Partial" Scaling		
Configurations	Conditions	Input & Output Relations
Spectral Scaling 	$1/K_1 + 1/K_2 = D_1$	$\Delta \omega_{out} = (K_2/K_1) \Delta \omega_{in}$ Have residual dispersion
Temporal Scaling 	$1/D_1 + 1/D_2 = K_1$	$\Delta t_{out} = (D_2/D_1) \Delta t_{in}$ Have residual chirp

Fig. 6.2 Different Time-lenses configurations. (D is accumulated dispersion of a fiber which is the 2nd order dispersion of the fiber times fiber length. K is chirp rate. $\Delta \omega$ is signal bandwidth times 2π , Δt is signal pulse width.)

division multiplexed signals [388], optical time-division demultiplexing [389], retiming and synchronization of optical signals [390], format conversion [391], mitigation of linear channel impairments [392], indicating the range of potential uses of these devices in communication systems. The ability to transform optical signals to and from a variety of multiplexing formats and baud rates is useful when considering interchanges in heterogeneous optical networks. The manipulation of spectrally efficient optical super-channels [327, 393] is of particular interest since this is difficult to do using traditional methods.

As shown in Fig. 6.2, different time-lens configurations are required for different functions. A complete OFT supports time-to-frequency and frequency-to-time conversion simultaneously [394, 395, 380, 396]. The output signal pulse width is the bandwidth of the input signal over the chirp rate of the time-lens, and the output signal bandwidth is the pulse width of the input signal times the chirp rate of the time-lens. The output of a complete OFT is chirp-free, hence this time-lens configuration can be used in the transmitter side of optical communication systems. There are two configurations for complete OFT. The D-K-D one requires a long guard interval, otherwise, the dispersion before the chirp broadens the signal beyond its time slot, causing signal degradations. The K-D-K one requires a short guard interval to avoid undesired chirp. If the temporal or spectral profile of the signal is of interest, "partial" OFT is opted. It only allows time-to-frequency conversion [397] or frequency-to-time conversion [398, 399]. A "partial" OFT requires fewer elements than the complete OFT, but there is a residual chirp or dispersion. Thus a "partial" OFT can be used in receivers rather than transmitters due to the residual chirp. Time-lenses can also be used to scale the temporal or the spectral profile of the signal, for example, spectral magnification [400, 385, 386, 401], temporal magnification [378, 402], and waveform compression [228, 376, 384]. A complete scaling time-lens is composed of two complete OFT time-lenses with different chirp rates. A spectral scaling time-lens is composed of a frequency-to-time conversion time-lens followed by a time-to-frequency conversion time-lens. If the order is switched, a temporal scaling time-lens is achieved.

The linear chirp stage of a time-lens is composed of a phase modulator (PM) or nonlinear optical effects like FWM. The PM driven by a quadratic RF signal applies a linear chirp to the signal. The nonlinear optical effects transfer the chirp from a linearly chirped control pulse to the target signal. The FWM-based time-lens allows a broad processing bandwidth and a large chirp rate, but it requires control pulse generation. Section 6.1.1 shows the principle of FWM-based time-lenses for complete OFT and complete scaling. In Section 6.1.2, the principle of spectral imaging time-lenses is presented.

6.1.1 Principle of complete OFT and complete-scaling time-lens

Space-time duality of time-lens stands for the parallel between paraxial diffraction of beams and dispersion of optical pulses, and the analog between a spatial lens and a quadratic phase modulation in time domain. Just as a spatial lens, a complete OFT time-lens can be used to obtain Fourier transform of a pulse. A complete scaling time-lens is a cascade of two complete OFT time-lenses, which performs two time-frequency conversions, resulting in temporal or spectral magnification or compression. The resolution and numerical aperture of the lens are highly related to the quadratic phase modulation stage. Compared with a phase modulator driven by sinusoidal waveform which has limited low aberration time fraction and limited maximum voltage, the broadband FWM in highly nonlinear waveguide provides better quadratic phase modulation with excellent maximum spectral width and record temporal length [378]. Figure 6.3 shows the structure of complete scaling imaging time-lens. The group delay dispersion (GDD) of the fiber is expressed as $\phi_{jk} = \beta_2^{jk} L_{jk}$, where β_2^{jk} is the group velocity dispersion (GVD) of the fiber, L_{jk} is the length of the fiber. The GDD results in quadratic phase filtering in the frequency domain, which can be written as a dispersion operator $G(\omega) = \exp(-i\omega^2 \phi/2)$. The dispersed pump and FWM process act as an optical quadratic phase modulator with operator $H(t) = \exp(it^2/\phi_p)$, where $\phi_p = L_p \beta_2$. L_p and β_2 are the length and GVD of the dispersive path where the pump propagates through before FWM interaction. The "focal length" of the complete OFT time-lens is defined as $\phi_f = -\phi_p/2$.

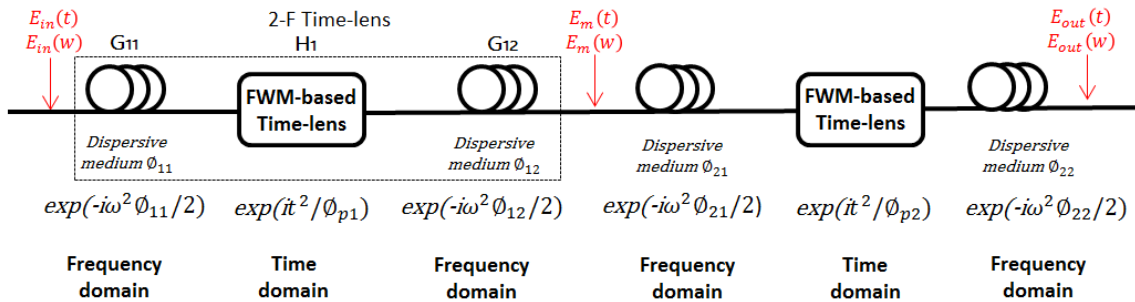


Fig. 6.3 Schematic of 4-F time-lens imaging system.

Since in the FWM process the idler field is proportional to the conjugate of the signal field $E_{idler1}(t) \propto E_{p1}^2(t)E_{in}^*(t)$, this corresponds to conjugation and reversal in spectrum domain. The idler (Idler1) field after the first complete OFT time-lens is [381]

$$E_m(t) = F^{-1} \{ [(E_{in}^*(-\omega) G_{11}^*(-\omega)) \otimes F(H_1(t))] G_{12}(\omega) \} \quad (6.1)$$

When the pump dispersion is twice the input signal dispersion $\phi_{p1} = 2\phi_{11}$. The spectral profile at the output of the first dispersion and the first FWM process matches the intensity profile of the input signal, but with residual chirp. The residual chirp is compensated by the second dispersive element $\phi_{12} = -\phi_{11}$. The negative sign is due to the conjugation of the signal in the FWM. The time-to-frequency conversion factor of the complete OFT system is

$$\frac{\Delta\omega_m}{\Delta t_{in}} = \left| \frac{1}{\phi_{f1}} \right| \quad (6.2)$$

where $\Delta\omega_m$ is the full-width at half-maximum (FWHM) of Idler1 spectrum $E_m(\omega)$ and Δt_{in} is FWHM of input signal field $E_{in}(t)$. Similarly, in terms of frequency-to-time conversion, the ratio between the FWHM of Idler1 field and the FWHM input signal spectrum is $|\phi_{f1}|$. However, this complete OFT time-lens operation generates an output whose spectrum is proportional to the conjugation of the temporal input signal.

In the complete scaling system, expect for the focal length ϕ_{f2} , the second complete OFT time-lens is identical to the first complete OFT time-lens. Two FWM processes lead to two conjugation operations, so the conjugation can be cancelled out. The relation between the input and output of the complete scaling time-lens can be written as

$$E_{out}(t) = E_{in} \times K \quad (6.3)$$

As shown in Eq. 6.3, the complete scaling time-lens provides scaling in both time and spectrum domain. The conversion factor is given by $K = \phi_{f1}/\phi_{f2} = \phi_{p1}/\phi_{p2}$.

6.1.2 Principle of spectral imaging time-lens

Figure 6.4 shows the structure of a spectral magnification/compression system based on time-lenses. In a time-lens, a quadratic phase modulator is designed to impart linear frequency chirp $A_{in} \exp(j/2C_1 t^2)$, where C_1 [Hz/s] is chirp rate. When travelling through the dispersive fiber, the chirped waveform will be compressed or expanded. The group delay dispersion (GDD) of the fiber is expressed as $\phi_1 = \beta_2 L_1$, where β_2 is the group velocity dispersion (GVD) of the fiber, L_1 is the length of the fiber. The GDD results in quadratic phase filtering $\exp(j/2\phi_1 \omega^2)$, in frequency domain.

The optical field after a time-lens is given by the convolution of optical fields of chirp and dispersion. When $C_1 = 1/\phi_1$, The waveform at the output of the system has an intensity profile that matches the spectral profile of the input of the system $A_m(t) \propto H_{in}(\omega = tC_1)$, with the scale factor $t = \omega/C_1$, where $H_{in}(\omega)$ is Fourier Transform of input signal $A_{in}(t)$. The resulting spectral envelope of convolving $A_m(t)$ with optical fields of the second dispersive

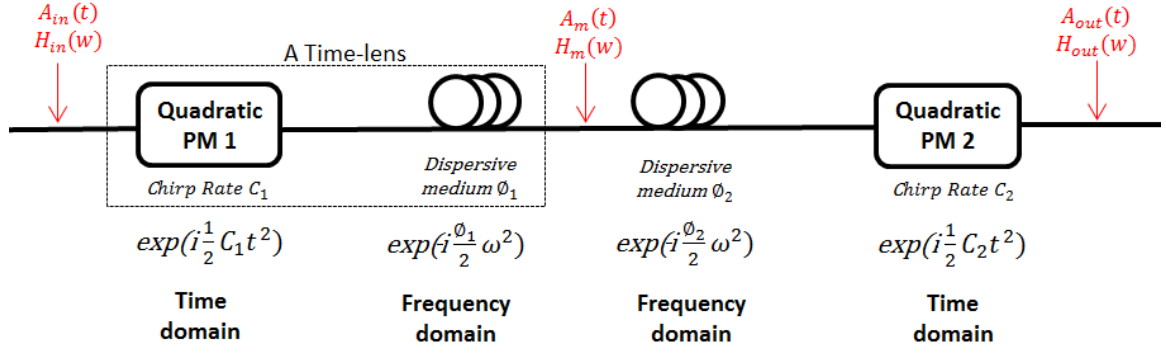


Fig. 6.4 Schematic of two time-lens spectral imaging system.

medium and quadratic phase modulation is [385]

$$H_{out}(\omega) = \frac{2\pi}{\sqrt{K}} \exp\left(j\frac{\phi}{2K}\omega^2\right) \times \int A_{in}(t) \exp\left(j\frac{1}{2}t^2\right) \left(C_1 - \frac{1}{\phi} - \frac{1}{\phi^2(C_2 - 1/\phi)}\right) \exp\left(j\frac{\omega}{K}t\right) dt \quad (6.4)$$

where $\phi = \phi_1 + \phi_2$, $K = 1 - \phi C_2$. When $\phi = 1/C_1 + 1/C_2$, the output spectrum is scaled version of input spectrum

$$|H_{out}(\omega)|^2 = \frac{1}{|K|} \left| H_{in}\left(\frac{\omega}{K}\right) \right|^2 \quad (6.5)$$

The quadratic phase modulation can be implemented via FWM [170]. In the FWM process, the idler has its phase determined by the phases of the signal and pump. Therefore the output signal bandwidth is K times of input signal bandwidth, where K can also be written as $-C_2/C_1$. This spectral imaging property enables OFDM signal decoding with band pass filter.

In this way, the phase modulation is applied using linearly chirped pump, where the pump has periodic linear chirp and flat spectrum. Thus the quadratic phase modulation operator can be replaced by $\exp(jt^2/\beta_2^{pump}L^{pump})$ [389]. The operation condition changes from above mentioned $\phi = 1/C_1 + 1/C_2$ to $\phi_{p2} - \phi_{p1} = 2\phi$, where $\phi_{p1} = \beta_2^{pump1}L^{pump1}$ and $\phi_{p2} = \beta_2^{pump2}L^{pump2}$ are the group delay dispersion of the pump pulses for the first and second quadratic phase modulation. The spectral magnification factor is $K = -\phi_{p1}/\phi_{p2}$.

6.2 Time-lenses for time-division multiplexing (TDM) of optical OFDM channels

This original work called "Time-lenses for time-division multiplexing of optical OFDM channels" was published in Optics Express [65].

Time-lenses provide a promising platform for novel, broadband optical signal processing. However, in order to minimize system penalties, design constraints must be adequately taken into account. The impact of third-order-dispersion and nonlinear distortion on the performance of time-lens-based communication systems for the first time are investigated in this section. Here, a novel application of time-lenses — temporal compression and time-division multiplexing of optical OFDM channels is proposed, to provide a 1 Tb/s superchannel. Time-lens system performance degradations are investigated in the proposed system and the results are applicable to all four wave mixing based time-lens systems. This work can help to optimize time-lens based communication systems.

The a time-lens based system which combines low-symbol rate OFDM tributaries into a higher baud rate channel provides a test case to probe the limitations of time-lenses for all-optical signal processing. This investigation provides the first thorough performance characterization of the impact of non-ideal time-lens system parameters on optical data, in terms of the widely used digital communication metric of signal quality factor (Q). The system can provide close to ideal performance using selected off-the-shelf components.

Through numerical modelling of a practically achievable, four-wave mixing (FWM) based time-lens system, and isolating and quantifying the impact of higher-order nonlinear and dispersive distortions on the processed data symbols, and it is found that the performance of the time-lens-based sub-system is primarily limited by distortions to signal chirping from the dispersion slope in highly nonlinear fiber.

6.2.1 Time-lens based symbol compression for TDM

The dispersion required for a time-lens can be imposed by dispersive fiber, and the linear temporal chirp is commonly achieved by mixing the input waveform with a linearly chirped optical pulse via FWM in highly nonlinear fiber. As FWM is produced via the ultrafast Kerr effect, its response time is in the order of femtoseconds. Moreover, highly nonlinear fibers can be engineered to allow for phase matching over large bandwidths. As such, FWM-based time-lenses can support real-time and broadband optical signal processing.

The time-lens system numerically derived in [403] provides scaling in both temporal and spectral domain. This system will be called a "time-lens pair" in this work. As shown in Fig.

6.5, a time-lens pair is composed of two time-lenses. By using different chirp rates in the two time-lenses, the temporal pulse and power spectra of the input signal can be compressed or magnified, analogous to a spatial system using two lenses with different focal lengths. ϕ_{f1} and ϕ_{f2} are the focal group delay dispersions of the first and second time-lens, respectively. The output waveform of the time-lens pair is scaled replica of the input waveform, with the scaling factor is given by $K = \phi_{f1}/\phi_{f2}$. This configuration is used as it provides Fourier transform-limited compression of the incoming waveform, such that the product of the symbol duration ($\Delta\tau$) and spectral widths (Δf) of the incoming signal remains at a single value (i.e. $\Delta_{in} \times \Delta f_{in} = \Delta_{out} \times \Delta f_{out}$). This property is not provided by the ‘spectral imaging’ type time-lens [385, 386].

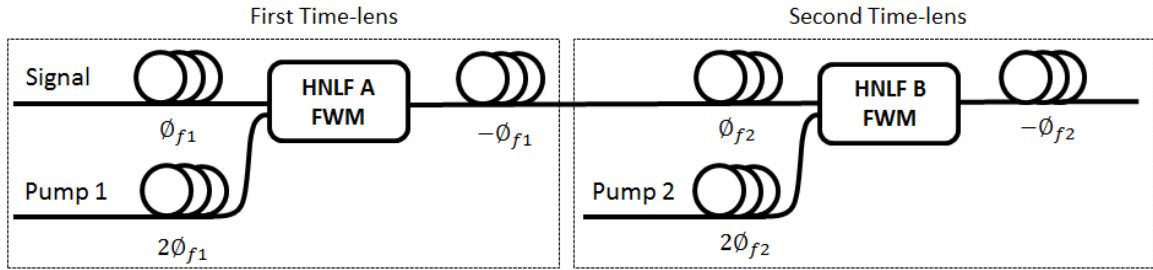


Fig. 6.5 Schematic of a time-lens imaging system. The first time-lens converts OFDM to Nyquist-OTDM, and the second time-lens converts the signal to spectrally magnified OFDM.

This work proposes a novel application of a time-lens pair, using temporal compression and aggregation of OFDM symbols to provide optical time-division multiplexing (OTDM) of OFDM symbols. Figure 6.6 shows the principle. The compression block in Fig. 6.6, refers to the time-lens pair shown in Fig. 6.5. Stream A and Stream B are two OFDM channels; each symbol within each channel is compressed in time by a pair of time-lenses. Stream B is delayed by half of the bit period.

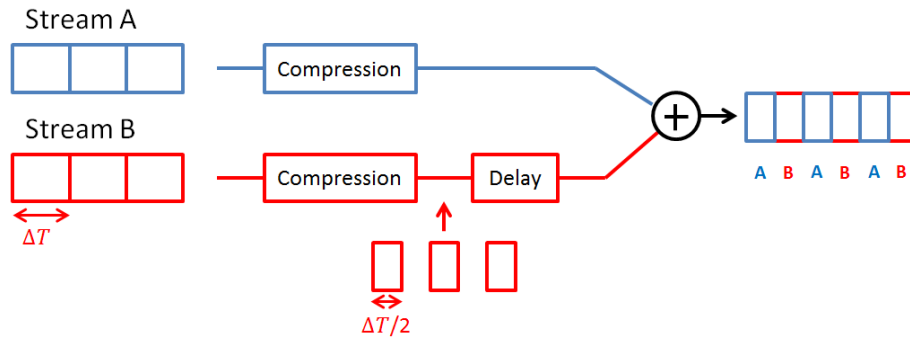


Fig. 6.6 Schematic of Time Division Multiplexing of time-lens compressed OFDM streams. Two OFDM channels are separately compressed by time-lenses and then time-interleaved.

The compression creates gaps in the waveforms of each channel, allowing the channels to be time interleaved. In this way, several channels of OFDM symbols could be combined into a single data stream. The number of channels that can be time-division multiplexed is limited by the compression ratio of two time-lenses. In our simulations, five OFDM channels are combined into one data stream to investigate time-lens based OTDM of OFDM. This is a complex system, which requires synchronized inputs and pumps over 10 time-lens pairs. The bandwidth requirements for this system do, however, make it suitable for the investigation of penalties that arise from non-idealities present in practically achievable time-lens systems.

6.2.2 Time-lens design guidelines

The performance of the time-lens pair is affected by some constraints. The time-lens pair is constrained by a limited temporal ‘record window’, a limited spectral capture range, aberrations from third-order dispersion (TOD) and practical limits on the chirping ‘pump’ pulse shape.

In the FWM process, the signal would be chirped only in the time slots in which a pump pulse is present [380]. This leads to a limited temporal record window, defined by the temporal duration of the chirping pump pulse, and can be approximated by

$$t_{record} = 4\pi\phi_f\Delta f_{pump} \quad (6.6)$$

where Δf_{pump} is the bandwidth of the pump used to impart chirp on the input optical waveform. To work within this limitation, the input OFDM symbol length should be shorter than the record window of the first time-lens. In addition, the chirp rate of the first time-lens should be properly chosen to make the time-domain symbol length of the first time-lens output smaller than the record window of the second time-lens. The output signal time-domain symbol length of first time-lens is given by input signal bandwidth divided by the chirp rate C_1 , where $C_1 = 1/(2\pi\phi_{f1})$.

Related to the record window is a limitation on the input spectral bandwidth that is able to be processed by the time-lens pair [400]. If the above mentioned record window condition is fulfilled, the maximum possible bandwidth of the input spectrum that can be processed by time-lens is given by

$$\Delta f_{in} = \left| \frac{C_1}{C_2} 2\Delta f_{pump2} \right| = \left| \frac{\phi_{f2}}{\phi_{f1}} 2\Delta f_{pump2} \right| \quad (6.7)$$

where Δf_{pump2} is the pump bandwidth of the second time-lens [378]. The process in the first time-lens is a frequency-to-time conversion and the process in the second time-lens is a time-

to-frequency conversion. Since the record window of the second time-lens $4\pi\phi_{f2}\Delta f_{pump2}$ is finite, the frequency components converted from the temporal waveform at the input of the second time-lens are limited in bandwidth. The input and output of the first time-lens follow the relationship $\Delta f_{in} = \Delta t_{out1}/2\pi\phi_{f1}$, where Δf_{in} is the full-width at half-maximum (FWHM) of the input signal's spectrum and Δt_{out1} is FWHM of the output of the first time-lens. This then leads to the restriction given by Eq. 6.7. When a time-lens is used to process signals with wide bandwidths - as is the case with the sinc 'tails' of an OFDM spectrum - the frequency components far from the center frequency of the signal will be lost. In order to keep enough frequency information to prevent significant signal distortion, the bandwidth of Pump 2 must exceed a minimum value.

From the analysis above, a broader pump bandwidth implies a longer record window and a wider maximum spectral range. However, if the bandwidth of the pump is excessively large, third-order dispersion can distort the FWM nonlinear mixing process, limiting the maximum useful pump bandwidth. It was previously stated that for Gaussian pulse inputs to a time-lens, perturbations (or aberrations) to the output signal due to third-order dispersion can be ignored if the dispersion effects of β_2 greatly outweigh those of β_3 [375].

Ideally, the pump pulses should be rectangular and the chirp of the pump should be linear; however, in practical systems the pump pulses will have gradual rising and falling edges. The edges of pump pulses often have non-linear chirp and will have reduced power compared with the predominantly flat, constant power, linearly chirped, middle part. As such, any part of the signal that overlaps with pump edges will experience severe spectral and temporal distortion [404]. The distortion from these edges will lead to reduced symbol compression, and so to inter-symbol-interference when time division multiplexing the compressed pulses. Thus, maximizing the overlap between the signal and the flat-top middle of the pump is important when optimizing a time-lens system.

The pump pulses' edges pose problems if the time-lens is to operate continuously in the time domain. To avoid this problem, the repetition rate of the pump is set to half of the baud rate of the signal, with the signal temporally interleaved to create two parallel streams of odd and even symbols. The odd and even symbols are then processed separately in two time-lens pairs. This allows the signal to be aligned to the middle of the pump pulse to mix only with the flat, linearly chirped part of the pump pulse.

Further complications arise from symbol temporal broadening due to the focal group delay dispersion fiber placed before the first FWM stage. The amount of broadening is dependent upon the length of the dispersive fiber, and is inversely proportional to the chirp rate of the first time-lens. Thus a lower chirp rate means more temporal symbol broadening

in Fiber 1. This then limits the minimum bandwidth that the pump pulses can take, providing a lower bound, in contrast to the upper bound defined by third order dispersion.

By observing the limitations outlined above, it is often possible to tailor a time-lens systems to the required signal processing application. However, in some cases these sources of distortion can be a fundamental limiting factor.

6.2.3 Numerical simulations and results

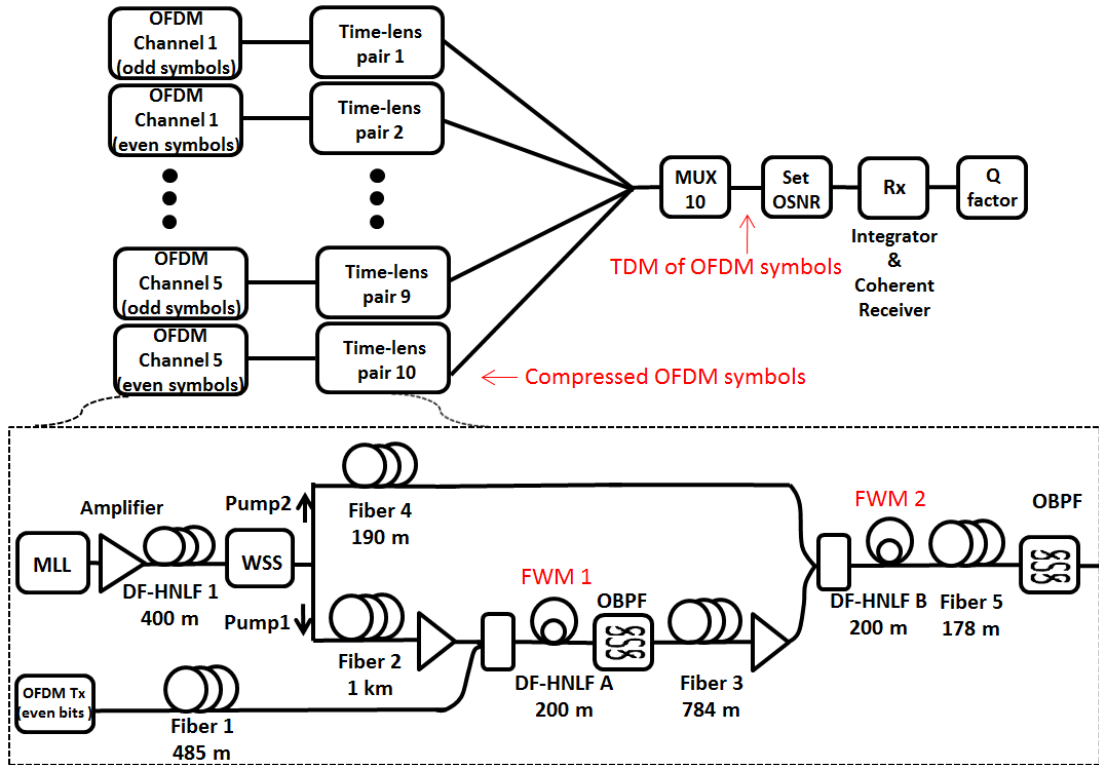


Fig. 6.7 Simulation setup of time division multiplexing five 5-subcarrier OFDM tributaries with quadrature phase-shift keying (QPSK).

VPItransmissionMakerTM was used to simulate a five tributary system, as shown in Fig. 6.7. At the transmitter, there are five OFDM channels, all with a center wavelength of 1552.5 nm (193.1 THz). As mentioned in Section 6.2.2, each channel is temporally interleaved into odd and even symbol tributaries. Each OFDM channel has five 20 Gbaud QPSK subcarriers with a 20-GHz subcarrier spacing, providing a line rate of 200 Gb/s per channel. The aggregate line rate of these channels is then 1 Tb/s.

Linearly chirped pump pulses are generated from short Gaussian pulses via self-phase modulation and dispersion. The mode-locked laser (MLL) produces 1.5-ps wide Gaussian

pulses at 10 Gpulses/s centered at 1534.2 nm (195.4 THz). The Gaussian pulses are amplified to 0.2-W average power, and then spectrally broadened in dispersion flattened highly nonlinear fiber (DF-HNLF 1). The amplified spontaneous emission (ASE) noise of amplifiers is set to zero in the simulation. Third-order dispersion in all the fibers is set to zero at this stage. The effect of TOD will be discussed in the next section. DF-HNLF 1 is 400-m long with a dispersion of -1.2 ps/nm/km and a nonlinear index of $10 \text{ W}^{-1}\text{km}^{-1}$. After DF-HNLF 1, a wavelength selective switch (WSS) is simulated as implementing two 5th-order Gaussian optical filters to produce two pumps with flat top spectra. The Gaussian filter bandwidth for Pump 1 is 360 GHz and is 1.3 THz for Pump 2. Pump 1 is linearly chirped using 1-km of dispersion compensating fiber (DCF) (Fiber 2) with -30 ps/nm/km dispersion, while Pump 2 is chirped in a 190-m DCF (Fiber 4). This produces a chirp rate of 9.2×10^{21} Hz/s in the first (DF-HNLF A) and 4.6×10^{22} Hz/s in second (DF-HNLF B) signal chirping stages. Note that the ratio of the applied chirps is 5, so the time-lens pair provides a factor 5 spectral magnification and temporal compression.

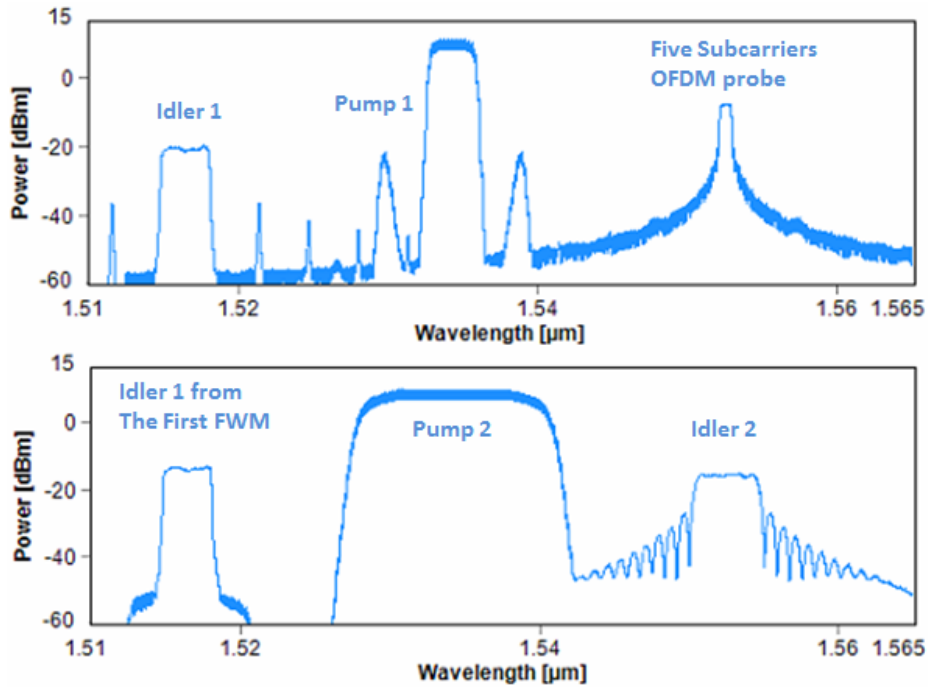


Fig. 6.8 (Top) optical spectra after the first time-lens; (Bottom) optical spectra after the second time-lens.

The even (or odd) symbols of one OFDM channel are dispersed in 485-m DCF (Fiber 1) with -30 ps/nm/km dispersion. Due to the FWM process in 200-m highly nonlinear fiber (DF-HNLF A), the chirped pulse and the input signal mix to produce an idler (Idler 1) that is strongly chirped. To reduce pump-signal walk-off in highly nonlinear fiber, high pump

power and short fiber length are used. An optical band pass filter filters out the idler (Idler 1) generated due to FWM process in DF-HNLF A. Idler 1 is linearly chirped and has the same intensity waveform as the input OFDM symbols. After propagation in 784 m of single mode fiber (SMF - Fiber 3), Idler 1 is combined with Pump 2 in DF-HNLF B to produce a highly chirped idler (Idler 2). Idler 2 is dispersed in a 178 m of SMF (Fiber 5) and compressed OFDM symbols are generated. Both the DF-HNLFs have a nonlinear index $= 10 \text{ W}^{-1} \text{ km}^{-1}$, are 200-m long and have a zero dispersion centered at 1534 nm. The average powers of Pump 1 and Pump 2 are set to 23 dBm and 28 dBm respectively. In this case, signal output power is equal to the signal input power (i.e. 0 dBm), and the input signal data quality can be preserved. Figure 6.8 shows the optical spectra after the two FWM processes. All of the five OFDM channels processed as described above simultaneously. The delays assigned to the 10 compressed OFDM symbol trains are 0 ps, 10 ps, 20 ps etc. Figure 6.9 shows that the original symbols are compressed after the ten parallel time-lens pairs and time division multiplexed.

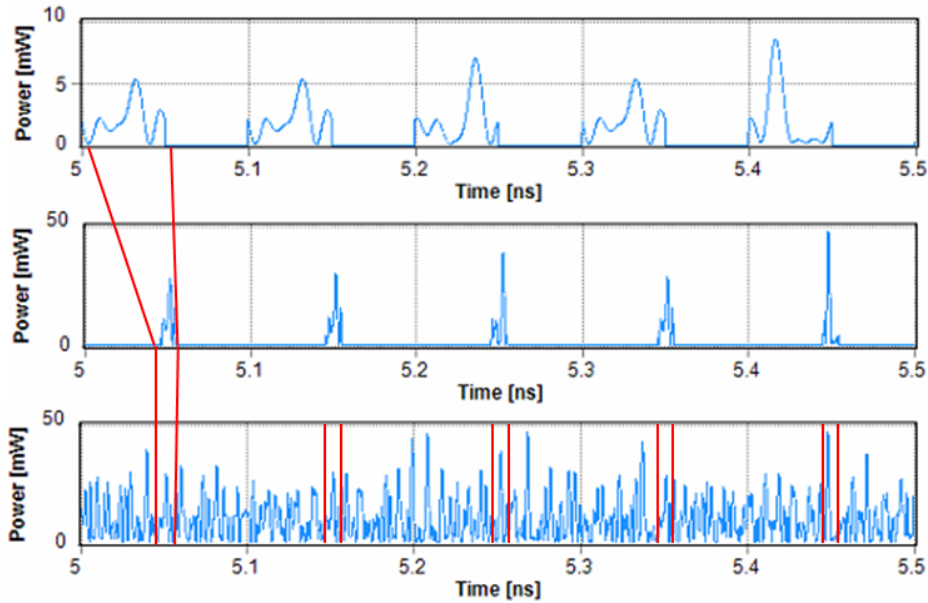


Fig. 6.9 (Top) Waveform of original signal; (Middle) Waveform of signal compressed by time-lenses; (Bottom) Waveform of the time division multiplexed five OFDM channels.

Each subcarrier is demultiplexed using a sinc filter with a sinc frequency response (a rectangular time response). To receive the QPSK modulated signal, a coherent receiver is used here to detect the amplitude and phase of the signal. The five channels are selected by sampling in their corresponding time slots.

A typical received signal is shown in Fig. 6.10. There are five eyes every 50 ps, which indicate that the five OFDM channels have been time division multiplexed successfully. Each

of the five eyes corresponds to one OFDM channel. By sampling at corresponding position, each channel's information can be decoded.

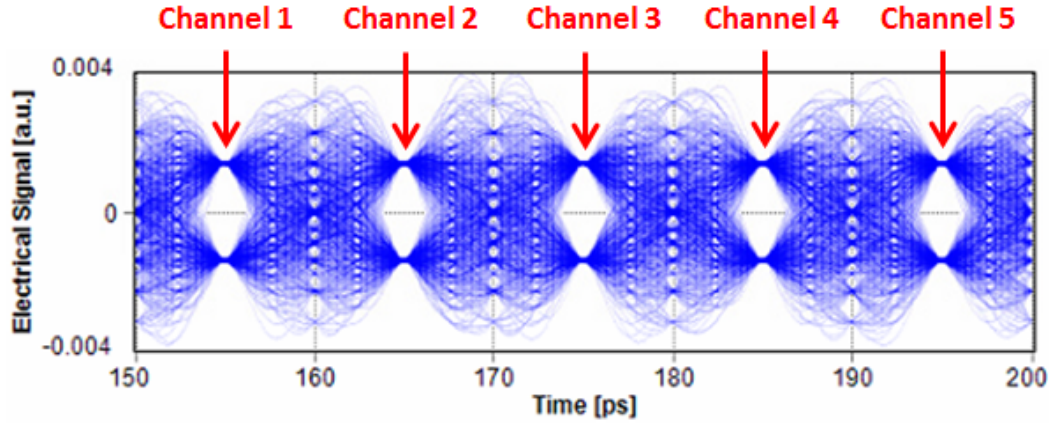


Fig. 6.10 Eye diagram of an OFDM subcarrier at receiver on I phase.

Figure 6.11 shows the signal quality, Q , versus the optical signal-to-noise ratio (OSNR) of 5-channel OTDM OFDM signal and the associated theoretical upper bound to performance [405]. In Fig. 6.11, the comparison between the OFDM signals composed by 5 compressed OFDM channels and the theoretical upper bound indicates the simulated time-lens system performance is close to ideal. When the optical signal-to-noise ratio (OSNR) is 40 dB, the Q -factor degradations for all the subcarriers are less than 0.5 dB.

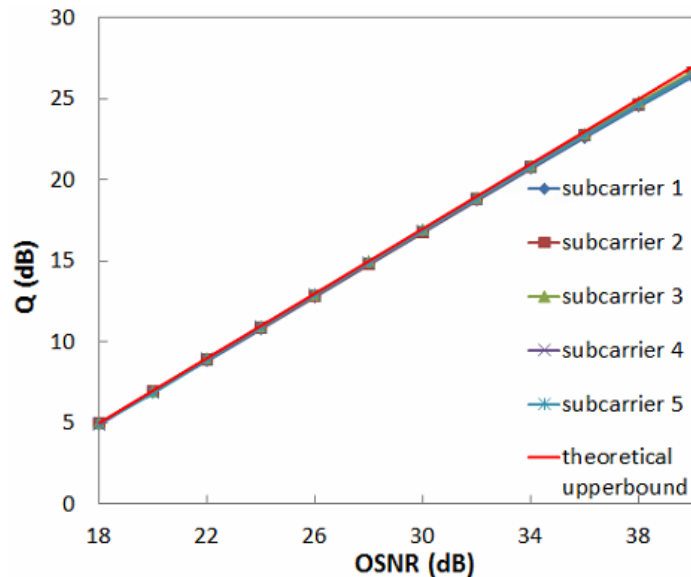


Fig. 6.11 Q vs. OSNR of TDM of 5 time-lenses compressed OFDM channels.

6.2.4 System penalty analysis - Nonlinear effects

The results in Section 6.2.3 are for a system with close to ideal operating conditions. Some of the parameters that may limit the system performance will be investigated in this section. Nonlinear distortion and third order dispersion are the major sources of aberration in the time-lens pair in the simulation.

In the DF-HNLF A and DF-HNLF B, the signal is highly chirped by mixing with the linearly chirped pumps. However nonlinear effects also cause aberrations in time-lens. Self-phase modulation (SPM) changes the phase of pumps and broadens the spectrum of pumps. Cross-phase modulation (XPM) causes unwanted mixing between pump, signal and idler. FWM within the pump pulse is caused by temporal overlapping of sequential pump pulses and generates undesired frequency components. FWM among the five OFDM subcarriers also generates unwanted nonlinear mixing terms.

To investigate the effect of nonlinear distortion, the effects of other distortion sources should be minimized. Therefore the third-order dispersion and power amplifier noise are set to zero in our simulation. As shown in Fig. 6.11, if the power of signal and pump and highly nonlinear fiber length are properly chosen, close to ideal performance can be achieved.

The effects of signal power, Idler 1 power, Pump 1 power and Pump 2 power are explored. For simplicity, only the results of center subcarrier (193.1 THz) are shown in Fig. 6.12. The default values are: signal average power = 0 dBm, Pump 1 average power = 23 dBm, Pump 2 average power = 28 dBm. Only one of the three powers is changed at any one time, while other two powers are set to default values. The signal under test is the same as in Section 6.2.3.

Figure 6.12 (a) suggests that lower signal input power should be used in this system, to avoid nonlinear distortion. However, in order to get a certain output power, the input power should exceed a certain level, otherwise an amplifier should be used at the end of time-lens pair and amplifier noise will add to the signal. In Fig. 6.12 (b), the performance trend, when varying the power of Idler 1 at the input to the second time-lens, has the similar effect to varying signal power at the input of the first time-lens, because Idler 1 is the “signal” in the second four wave mixing process. When the signal power and Pump 1 power are set to default values, the Idler 1’s power is -6.5 dBm.

Figures 6.12 (c) and 6.12 (d) show how the received signal quality and power varies with changing of pump power. In order to minimize the penalty due to power loss in the first time-lens (and hence noise from a required amplifier stage), 0 dBm output power is desired and so Pump 1 power is set to 23 dBm in our simulation. This provides only moderate distortion due to nonlinear cross-talk in the first time-lens. In Fig. 6.12 (d), the Q-factor is roughly constant for Pump 2 average powers lower than 30 dBm, dropping dramatically for

higher pump powers. Therefore, the output power of Pump 2 should be kept below 30 dBm. Conveniently, an average Pump 2 power of 28 dBm provides 0 dB conversion efficiency in the second time-lens, so an overall 0 dB conversion efficiency over the time-lens pair is possible without incurring significant nonlinear penalty.

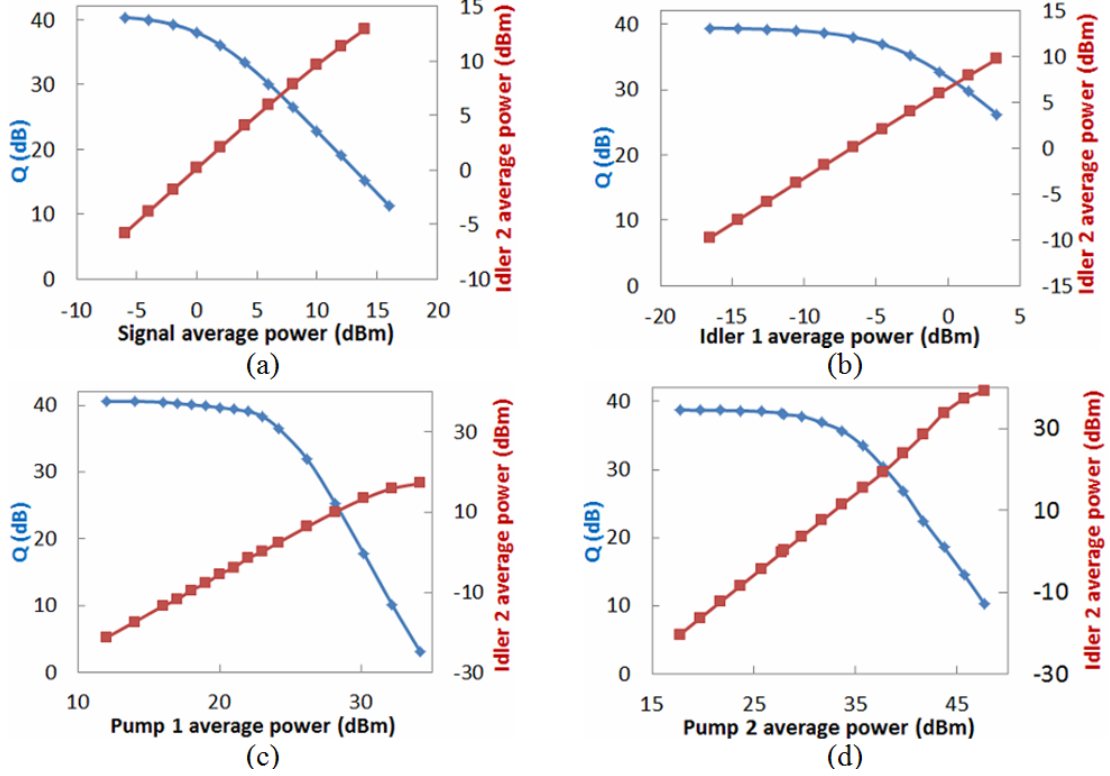


Fig. 6.12 Q factor vs. system parameters (a) Q factor vs. signal average power. (b) Q factor vs. Idler 1 power. (c) Q factor vs. Pump 1 average power. (d) Q factor vs. Pump 2 average power. Red represents Idler 2 average power. Blue represents Q factor.

To identify the source of the degradation due to unwanted nonlinear interactions as shown in Fig. 6.12, the optical spectra at the output of DF-HNLF A (left column) and DF-HNLF B (right column) are shown in Fig. 6.13. In this figure, the average powers of the two pump pulses and the signals at the input of the two separate time-lenses are varied. Figures 6.13(a) and 6.13(b) show the output spectra in the case of a signal power that is too high. Figures 6.13(c-f) are for Pump 1's power being too high. Figures 6.13(g) and 6.13(h) are for Pump 2 power's power being too high.

In Figs. 6.13(a) and 6.13(b), the signal power input to DF-HNLF A is 16 dBm, Pump 1 is 23 dBm and Pump 2 is 28 dBm. In this case, when the signal (right) and Pump 1 (middle) powers are similar, the top of the Pump 1 spectrum at DF-HNLF A output is no longer flat. When combined with the Idler 2 output power trend in Fig. 6.12(a), the penalty from increasing signal is not due to pump depletion, but is due to nonlinear mixing distorting

both the original signal and the pump. In Fig. 6.13(b), the spectrum of Idler 2 (right) is not typical of an OFDM signal, indicating significant distortion. Therefore, as shown in Fig. 6.12(a), the input signal power should well below the pump power to avoid unwanted nonlinear interactions.

As shown in Figs. 6.13(c) and 6.13(d), when Pump 1 is set to 33 dBm, the power of Idler 1 at the input of second time-lens (i.e. into DF-HNLF B) is high (13.5 dBm average power). This is well into the nonlinear distortion regime of Fig. 6.12(b), and as such, the output spectra of DF-HNLF B shown in Figs. 6.13(b) (high signal input) and 6.13(d) (high Pump 1 input) shows distortion of Pump 2 spectrum.

The operating condition for Figs. 6.13(e) and 6.13(f) is similar to Figs. 6.13(c) and 6.13(d), except that Idler 1 is attenuated by 14 dB (to -0.5 dBm average power) before the FWM process in DF-HNLF B. A clear OFDM spectrum can be seen in Fig. 6.13(f) and the quality factor of the received signal is 29 dB. Compared with Fig. 6.13(f), the degradation in Fig. 6.13(d) is primarily due to nonlinear distortion from having a too high Idler 1 power at the input to DF-HNLF 2, as opposed to resulting from nonlinear chirp due to the distorted Pump 1 pulse.

In Figs. 6.13(g) and 6.13(h), the average power of Pump 2 is increased to 40 dBm. As shown in Fig. 6.13(h), this results in a spectral broadening of Pump 2, which we infer to cause a nonlinear chirp on Idler 2, resulting in a degraded output signal. However, there is no drastic perturbation to the spectrum of Idler 2, even though the signal quality factor falls to 26 dB. Comparing Figs. 6.13(g) and 6.13(h), we note that the input Idler 1 seems to undergo parametric amplification.

Figure 6.13(g) shows the spectrum out of DF-HNLF A when the powers of signal and Pump 1 are properly chosen to minimize nonlinear distortion (i.e. 0 dBm and 23 dBm respectively). Notably, there are two spurious frequency components generated, appearing as frequency ‘spikes’ around Pump 1. The spikes are caused by the temporal overlap of pump pulses. Ideally, the pump pulses would not overlap, however in order to generate a constant chirp over the symbol duration after the signal undergoes focal dispersion, the leading and falling edges of the pumps do slightly overlap. Because of the way that the pump pulses are chirped, the leading edge corresponds to the lowest frequency components of the pump and the tailing edge corresponds to the highest frequency components of the pump. The two spikes are the FWM products of the two spectral edges of the pump. The distance between the left spike and the left edge is equal to the bandwidth of Pump 1, which holds for the right edge and spike. As shown in Figs. 6.13(c) and 6.13(e), when the power of Pump 1 is large, not only do the two spikes closest to Pump 1 become larger, more spikes appear around Pump 1 due to higher-order FWM. If the spikes overlap with desired signal spectrally, the

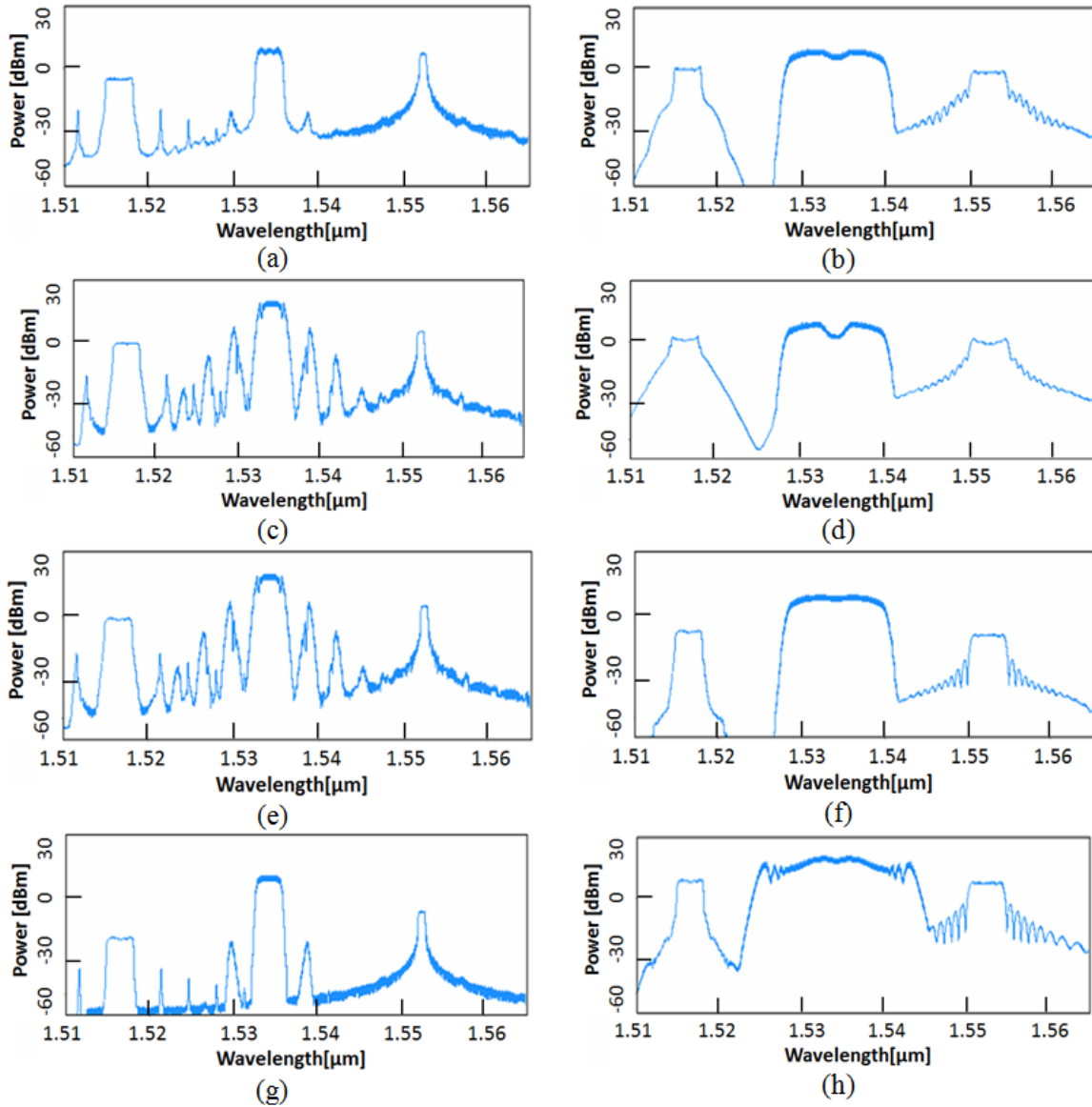


Fig. 6.13 Spectra at output of DF-HNL F A (left) and DF-HNL F B (right) under the conditions (a) and (b): 16-dBm signal power, 23-dBm Pump 1 power, 28-dBm Pump 2 power; (c) and (d): 0-dBm signal power, 33-dBm Pump 1 power, 28-dBm Pump 2 power; (e) and (f): 0-dBm signal power, 33-dBm Pump 1 power, 28-dBm Pump 2 power, with Idler 1 attenuated by 14 dB; (g) and (h): 0-dBm signal power, 23-dBm Pump 1 power, and 40-dBm Pump 2 power.

received data will be distorted. There is no spike close to Pump 2 because its bandwidth is tailored to avoid temporal pulse overlap.

6.2.5 Third-order dispersion

Third-order dispersion must be taken into consideration when broad pump bandwidth is used. The dispersion slopes of Fiber 3 and Fiber 5 are set to $0.092 \text{ ps/nm}^2/\text{km}$, as for standard SMFs, while the dispersion slopes of DF-HNLF A and DF-HNLF B are set to $0.006 \text{ ps/nm}^2/\text{km}$. From Fig. 6.14, the dispersion slope causes some performance penalty, degrading Q by about 4 dB at high OSNRs (40 dB). This trend is almost unchanged if the dispersion slope is eliminated in the SMF and DCF sections of the time-lens pair, indicating that the slope of the DF-HNLF is the major cause of the degradation shown in Fig. 6.14.

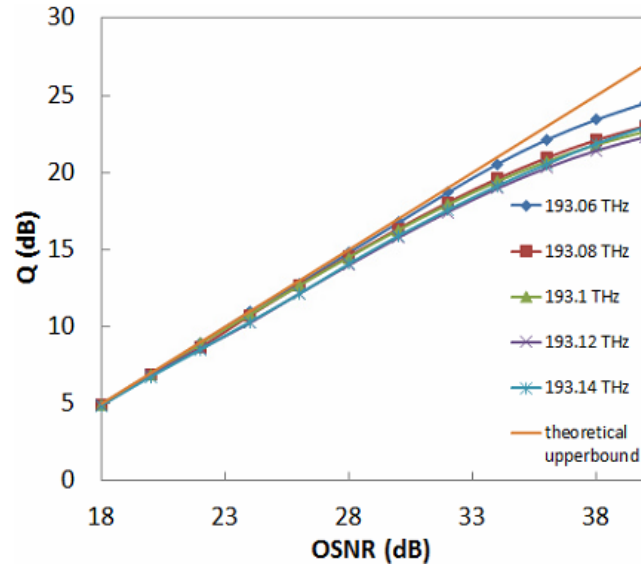


Fig. 6.14 Q vs. OSNR of 5-channel TDM of OFDM channels. The dispersion slopes of Fiber 3 and Fiber 5 are set to $0.092 \text{ ps/nm}^2/\text{km}$, and the dispersion slope of DF-HNLF A and DF-HNLF B are set to $0.006 \text{ ps/nm}^2/\text{km}$

As described in [375], third-order dispersion in the FWM chirp operation will lead to both temporal and spectral distortion because of imperfect mixing in the HNLFs. These distortions manifest as an asymmetric output idler spectrum, a timing shift and center frequency shift. In the dispersive fiber, third-order dispersion only affects the signal in the temporal domain. Third-order dispersion results in temporal pulse asymmetry and blurred tail on one side of each pulse. This asymmetry in the time domain can be transferred to the spectral domain if the signal is to be subsequently processed in a time-lens; however, this seems to have only a minor effect on the system, compared with the distortions caused by TOD in DF-HNLFs A and B.

Figure 6.15 shows the spectra of the signal (Idler 2) at the output of a time-lens pair when DF-HNLF A has dispersion slope of $0.006 \text{ ps/nm}^2/\text{km}$ and the dispersion slope of DF-HNLF B is zero (left), and conversely, where DF-HNLF B has dispersion slope of $0.006 \text{ ps/nm}^2/\text{km}$ and DF-HNLF A has zero slope (right). A more severe asymmetry effect can be observed in Fig. 6.15(b), because the bandwidth of Pump 2 is five times broader than Pump 1, and so will be more heavily affected by third-order dispersion. From Fig. 6.15, the frequency shift caused by third order dispersion is dominated by the first time-lens, and the asymmetry effect from TOD is dominated by the second time-lens.

The timing shift due to TOD in the time-lens pair results in an output frequency shift. The temporal shift generated in the first time-lens is converted to frequency shift in the second time-lens through time-to-frequency conversion, and it is multiplied by the conversion factor (i.e. the chirp rate of the second time-lens). For example, with a chirp rate of the second time-lens $4.6 \times 10^{22} \text{ Hz/s}$, a dispersion slope in DF-HNLF A of $0.01 \text{ ps/nm}^2/\text{km}$ results in a center frequency shift of 10 GHz. Delaying Pump 2 in order to temporally align the Idler 1 symbols and Pump 2 pulses can solve this issue. As such, the timing shift effect at the output of time-lens pair has a negligible impact compared with spectral shift and asymmetry.

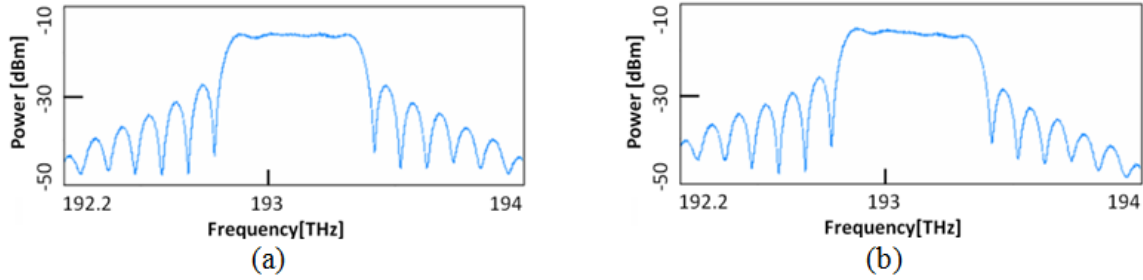


Fig. 6.15 Spectra of time-lens pair output in case of (a) dispersion slope of DF-HNLF A is $0.006 \text{ ps/nm}^2/\text{km}$, other dispersion slopes are set to zero. (b) dispersion slope of DF-HNLF B is $0.006 \text{ ps/nm}^2/\text{km}$, other dispersion slopes are set to zero.

6.3 All-optical OFDM demultiplexing with OFT and sinc sampling

This work proposes a novel all-optical OFDM demultiplexing scheme with a time-lens optical Fourier transform (OFT) and sinc sampling. This transforms the challenge of optical demultiplexing from matched filtering in the frequency domain, to sinc sampling in the time domain. Compared with OFDM demultiplexing with a matched filter, the proposed method replaces specialized optical filters with commercially available equipment and avoids

precise frequency alignment. A proof of concept experiment was performed with 160-Gbaud AO-OFDM QPSK signal and OFDM demultiplexing without penalty from ICI.

All-optical orthogonal frequency-division multiplexing (AO-OFDM) enables ultra-high speed optical communication with high spectral efficiency. Broad-band AO-OFDM can be generated by multiplexing several sinc-shaped subcarriers orthogonally [327]. However, the reception of such broad-band, tightly spaced signals can be challenging. Theoretically, an OFDM signal can be decoded with a digital fast Fourier transform (FFT), but the maximum capacity is limited by the electrical bandwidths of coherent receivers, the bandwidths of analog-to-digital converters (ADC) and speed of digital signal processing (DSP) [406]. By contrast, all-optical OFDM demultiplexers can detect ultra-high speed, broad-band OFDM signals [407, 91, 206, 408–410, 386]. In general, AO-OFDM de-multiplexers perform an optical discrete Fourier transform (DFT), which acts as a matched filter [407, 91]. All-optical de-multiplexers based on cascaded optical delay interferometers (ODI) [206], arrayed-waveguide gratings (AWG) [408], passive planar hybrids [409], and multimode interference (MMI) [410] have been reported. However, these optical DFT implementations require phase stabilization, and the optical circuits required can be complex. Furthermore, significant inter-channel interference (ICI) may be introduced by imperfect matched filtering, which in photonic integrated circuits can arise naturally from manufacturing variability [411].

Nyquist optical time-division multiplexing (N-OTDM) has similar spectral efficiencies to AO-OFDM, but in contrast, temporal sinc sampling of N-OTDM signals has been proven to be effective in eliminating inter-symbol-interference (ISI) [412, 413]. Optical sampling is a well-known approach used for demultiplexing optical time-division multiplexed (OTDM) signals [412–415]. Optical sampling of N-OTDM signals using pulses with a sinc-shape in the time domain, as opposed to a Gaussian profile, has been shown to have advantages in terms of sampling pulse bandwidth and time domain orthogonality [412–415].

This work proposes a novel ICI-free AO-OFDM de-multiplexing method with a time-lens-based optical Fourier transform (OFT) [416, 394] and temporal sinc sampling. This is the first work to demultiplex OFDM signals using temporal sinc sampling, instead of spectral matched filtering.

6.3.1 Principle

Figure 6.16 shows the principle of the proposed ICI-free AO-OFDM receiver. Here, the AO-OFDM signal is first Fourier transformed to the N-OTDM signal by a time-lens. Instead of performing a complete OFT with dispersion-chirp-dispersion (D-K-D) structure, a frequency-to-time mapping time-lens with a chirp-dispersion (K-D) structure was used, to avoid pulse broadening before the chirp stage. The chirp can be applied to the signal by electro-optic

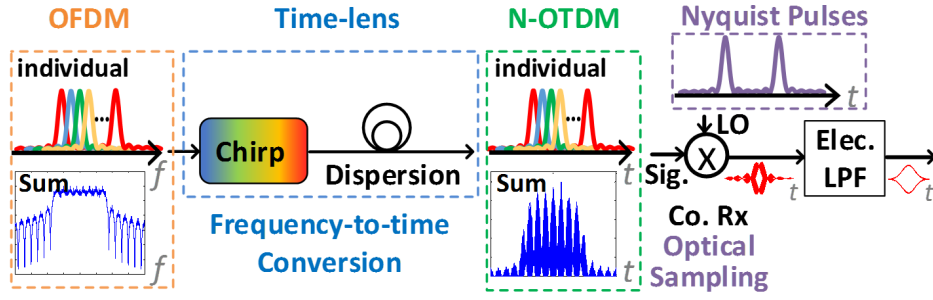


Fig. 6.16 The principle of ICI-free AO-OFDM receiver.

modulation or by four-wave mixing (FWM) with a chirped pulse train. FWM was chosen for its large operation bandwidth. The dispersive element can be a standard single-mode fiber (S-SMF) or a dispersion compensating fiber, and its accumulated dispersion is $D = \beta_2 \times L$, where L is the length of the fiber, β_2 is the group-velocity dispersion parameter of the fiber. To achieve an OFT with a time-lens, the chirp rate (K) needs to equal to the inverse of the accumulated dispersion (D), that is $K = 1/D$. Take a 160-Gbaud AO-OFDM signal with sixteen 10-Gbaud subcarriers as an example. The 16 OFDM subcarriers are transformed into 16 channels of N-OTDM all at once. Suppose the spacing between adjacent OFDM subcarriers (Δf) is 20 GHz, which means there are 50% guard intervals (GI). The guard intervals ensure the data to be fully covered by the time aperture of the chirp stage. Actually the designed guard interval can be reduced to improve spectral efficiency (SE). 50% guard interval was chosen to achieve a margin for the possible misalignment between the signal and the pump. The temporal spacing between neighboring channels of the transformed N-OTDM signal (Δt) should be less than 6.25 ps to avoid overlap. Suppose Δt is designed to be 5 ps, and a S-SMF is used. The dispersion needed can be calculated as

$$D_{data} = D = -\frac{\Delta t}{2\pi\Delta f} = -\frac{5 \text{ ps}}{2\pi \times 20 \text{ GHz}} \approx -39.8 \text{ ps}^2 \quad (6.8)$$

Then the chirp required for the time lens to implement an OFT is

$$K = \frac{1}{D} = \frac{1}{-39.8 \text{ ps}^2} \approx -0.0251 \text{ ps}^{-2} \quad (6.9)$$

To achieve the desired chirp rate, a short repetitive pulse train firstly propagates through a fiber with an accumulated dispersion of D_{pump} . The output of the fiber should be pulses with rectangular envelopes and linear chirp. Then, the chirp is transferred to a new frequency component (called “idler”), generated by the FWM between the chirped pulses (called

“pump”) and the signal. To cover all the subcarriers of OFDM signal, the pump width is

$$\Delta T_{pump} = 100 \text{ ps} \times (100\% - 10\%) = 90 \text{ ps} \quad (6.10)$$

The accumulated dispersion experienced by the pump is

$$D_{pump} = -2D = 79.6 \text{ ps}^2 \quad (6.11)$$

Therefore, the bandwidth of the pump is

$$\Delta f_{pump} = \frac{\Delta T_{pump}}{2\pi D_{pump}} = \frac{90 \text{ ps}}{2\pi \times 79.6 \text{ ps}^2} \approx 180 \text{ GHz} \quad (6.12)$$

After the OFDM to N-OTDM conversion, the ICI of OFDM signal is mapped to the ISI of N-OTDM signal. Sampling a N-OTDM signal with temporally sinc pulses suppresses ISI [412, 415]. The sinc pulses are generated by applying a rectangular band-pass filter (BPF) to a flat-top 640-GHz wide frequency comb. In the time domain, there is a π phase shift between neighboring side lobes of the sinc pulse, and the π phase shift results in large chirp on most of the subcarriers of the N-OTDM signal [415]. Therefore, the frequency components of the subcarrier to be de-multiplexed remain the same, while all the other subcarriers are red shifted or blue shifted. If a band-pass filter centred at the signal’s frequency is applied, the chirped sub-carriers are dramatically suppressed. With the same sampling pulse width, the sinc sampling using sinc pulses results in much less ISI than the case of optical sampling with Gaussian pulses [415]. Plus, for pulses with the same duration, Nyquist pulses have less spectral bandwidth than Gaussian pulses.

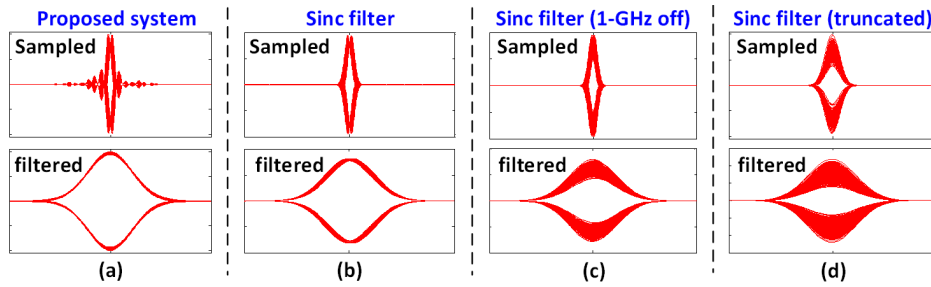


Fig. 6.17 Simulated electrical eye-diagrams of AO-OFDM demultiplexing with MATLAB. The AO-OFDM signal is composed of eight 10-Gbaud BPSK subcarriers. In the receiver, the signal is optically sampled in a coherent receiver (the upper row), then filtered by a 20-GHz electrical Gaussian filter (the lower row). (a) In our proposed system, the OFDM converted N-OTDM signal is optically sampled by a sinc pulse train. (b) AO-OFDM demultiplexing with sinc matched filter then optical sampling with a Gaussian pulse train. (c) The central frequencies of the sinc filter and the signal are 1-GHz off. (d) The matched filter is truncated to one side-lobe either side.

OFDM demultiplexing based on optical matched sinc filters requires precise matching between the signal and the filter in terms of amplitude, phase and central frequency [406, 408, 417]. Figure 6.17 shows simulated electrical eye-diagrams of AO-OFDM demultiplexing with our proposed method and matched sinc filters. In our proposed system, the OFDM signal is converted into an N-OTDM signal, optically sampled by sinc pulses (Fig. 6.17a, upper) then passed through a low-pass filter (Fig. 6.17a, lower). The eye-diagram shows our proposed method is ICI-free in principle. Figure 6.17b shows a similarly good performance with a matched sinc filter followed by optical sampling. However, if the filter is misaligned by 1 GHz or the filter is truncated to a single side-lobe on each side, there is significant interference, as shown in Fig. 6.17 (c) and 6.17 (d). This illustrates the challenge of providing both precise frequency alignment and pulse shaping when relying on optical filtering for OFDM demultiplexing. Particularly, Fig. 6.17 (d) indicates that an amplitude or phase mismatch in the side-lobes of the demultiplexing filter can result in considerable signal degradation, which provides significant challenges for filter implementation, particularly on integrate platforms [411]. Our method moves the problem from frequency alignment to timing synchronization, which can be solved by tuning a variable delay line.

6.3.2 Experimental setup

Figure 6.18 shows the experimental setup of 160-Gbaud AO-OFDM generation and reception. The experiment is based on the parameters calculated above. Frequency comb lines with 10-GHz spacing are generated by the mode-locked laser (MLL), and then broadened in a 400-m dispersion-flattened highly non-linear fiber (DF-HNLF). The broadened comb is filtered at three different central wavelengths and diverted to three output ports by a wavelength selective switch (WSS1).

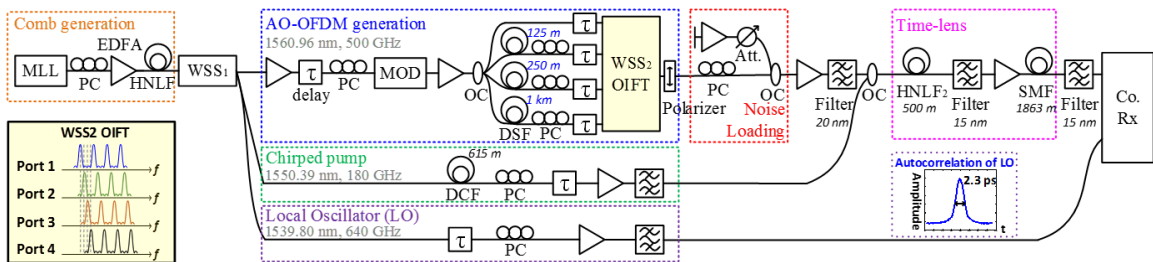


Fig. 6.18 Experimental setup of time-lens and optical sampling based AO-OFDM de-multiplexing.

In the AO-OFDM generation sub-system, a rectangular band-pass filter with 1560.96-nm central wavelength and 500-GHz pass bandwidth is set at Port 1 of WSS1. Output 1 is time aligned and polarization aligned to the IQ-modulator by a time delay and a polarization controller (PC). The output of the IQ-modulator is a 10-Gbaud single polarization QPSK

optical signal with 500-GHz bandwidth and flat-top spectra, and it is equally separated into four paths. The signals in the four paths are de-correlated by dispersion shifted fibers (DSF) of 0 m, 125 m, 250 m and 1 km. The polarization and timing of the four paths are aligned by tuning time delays and polarization controllers. WSS2 performs an optical inverse Fourier transform (OIFT) by applying filters with sinc-shaped magnitude responses and π phase shifts between adjacent side lobes [327]. The bandwidth of each OFDM subcarrier and the subcarrier frequency spacing are designed to be 20 GHz to generate a 50% guard interval between OFDM symbols. Using a 20-GHz bandwidth also avoids filter distortions away from the ideal sinc shape due to the 10-GHz optical transfer function of the WSS. A 1×4 port WSS is used to form OFDM with 16 subcarriers. Therefore, a filter passing 4 subcarriers separated by 80 GHz is designed for each input port, and the filter is shifted by 20 GHz between every two adjacent ports. The generated AO-OFDM signal is 160-Gbaud QPSK OFDM signal with 320-GHz bandwidth. The noise generated by an EDFA is coupled to the AO-OFDM signal to measure system performance.

At the chirped pump generation stage, the band-pass filter at Port 2 of WSS1 is centered at 1550.39 nm with 180-GHz bandwidth. The 615-m dispersion compensation fiber (DCF) chirps the pump and broaden the pump pulses in the time domain. The time delay and polarization controller align the pump and the signal to optimize the FWM process. A high power Erbium-doped fiber amplifier (EDFA) is followed by a cascaded 1560-nm low-pass filter (LPF) and a 1570-nm high-pass filter (HPF) filter.

The bandwidth of the local oscillator (LO) is 640 GHz [415]. The full width half maximum (FWHM) of the LO measured by the auto-correlator is 2.3 ps, which corresponds to a 1.6-ps pulse width. The central frequency of LO is 1539.8 nm, which is equal to the central frequency of FWM-generated N-OTDM signal. The subcarrier to be demultiplexed is selected by tuning the time delay of LO.

At the time-lens stage, the signal power and the pump power coupled into HNLF2 are -2.5 dBm and 20.5 dBm respectively. The OFDM signal and the chirped pump generate a new frequency component (idler) at 1539.8 nm by FWM in HNLF2. The idler is extracted by a band-pass filter, and dispersed by an 1863-m standard SMF.

The signal and the LO powers at the input of the coherent receiver are 4.5 dBm and 0.5 dBm respectively. The band limitation of the coherent receiver acts as a low-pass filter, which eliminates interference from other subcarriers. Common DSP algorithms, including Gram-Schmidt orthogonalization, equalization based on constant modulus algorithm (CMA), 4th-power based frequency offset compensation, and phase estimation, have been utilized to recover the demultiplexed channel.

6.3.3 Results and discussions

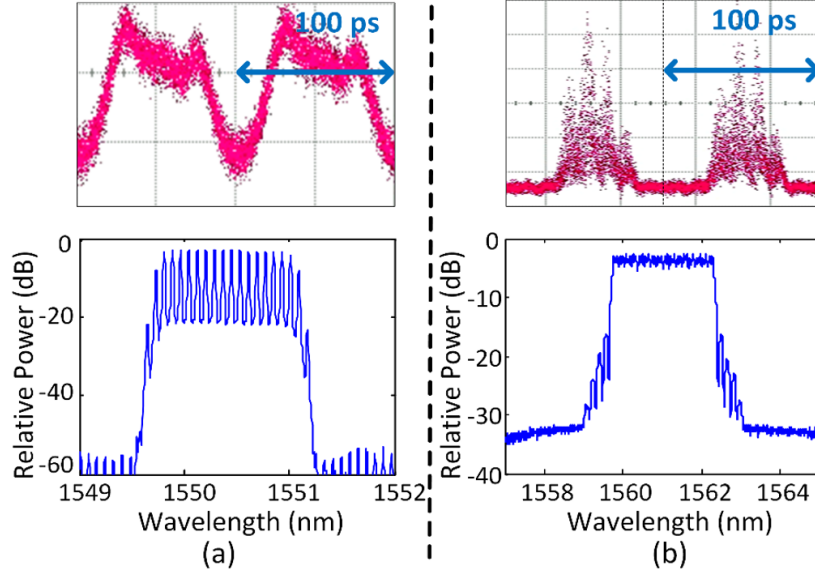


Fig. 6.19 Eye-diagrams and spectra of (a) chirped pump and (b) AO-OFDM signal.

Figure 6.19 shows the eye-diagrams and spectra of the chirped pump and the AO-OFDM signal. The eye-diagram is detected by a 40-GHz photo-detector and an equivalent-time sampling oscilloscope. According to Fig. 6.19 (a), the pump pulses have fluctuations in amplitude resulting differences in the converted N-OTDM signal quality. The bandwidth of the pump is only 180 GHz, which makes it hard to meet the Fraunhofer requirement [418]. From the eye-diagram in Fig. 6.19 (b), the AO-OFDM signal has guard intervals, so that the signal does not temporally overlap with the rising and falling edges of the chirped pump in the FWM process. In Fig. 6.19 (b), the spectrum of an AO-OFDM signal with a flat top and several sidelobes on each side. The AO-OFDM signal and the chirped pump generate an idler at 1539.8 nm through FWM process with -7 dB conversion efficiency.

Figure 6.20 (a) shows the bit error rates (BER) of all the 16 demultiplexed AO-OFDM channels at 38-dB OSNR. Assuming that the system will be running with a 7% overhead forward error correction code (FEC) to bring a pre-FEC measured bit-error rate down from 3.8×10^{-3} to an error-free level of 1×10^{-15} . The minimum reliable measured BER is 1.6×10^{-6} , based on the measuring an average of 10 errors. Channels 7, 9, 11, 13, and 15 were below this threshold in the experiment, thus their BERs are not shown in Fig. 6.20 (a). The maximum measured BER is 4.5×10^{-5} . In general, Channels 1 to 6 are worse than the other channels. There are multiple potential causes for the performance difference. Firstly, Channels 1 to 6 are relatively far away from the pump, they may be degraded due to phase mismatch in the FWM process. Secondly, the signal is chirped by FWM, which multiplies

the signal waveform and the pump waveform in the time domain. Ideally, the pump should have flat-top waveform and linear chirp, so that the signal is linearly chirped but with its waveform maintained. In this experiment, the power fluctuations on the pump may distort the time-lens operation. The difference among channels are also shown in Fig. 6.20 (b), where the BERs of Channels 1, 7, 8 and 16 are plot against OSNRs. The OSNRs are measured from the spectra at the output of the noise loading coupler. The maximum OSNR variation is 2.8 dB at $\text{BER} = 3.8 \times 10^{-3}$.

To investigate the ISI from the close-spaced neighboring channels, the performance of AO-OFDM with 16×10 Gbaud channels, and coarse WDM with 4×10 Gbaud channels, is compared in Fig. 6.20 (b). In the experimental set-up, these two different signals are generated by changing the filter profiles in WSS2 [236]. In the coarse WDM case, Ports 2 to 4 of WSS2 are blocked, and Port 1 is retained. At FEC limit, the OSNR difference between AO-OFDM and WDM is 6 dB. In theory, this four times capacity difference results in 6-dB difference in the required OSNR. As there is no correlation between penalty and whether a channel is at the edge of the OFDM spectrum (lower ICI) or near the middle (higher ICI), this indicates that there is no penalty due to the cross-talk from neighboring channels.

The implementation penalty is investigated by comparing the experimental results with the calculated theoretical upper bounds [405]. Fig. 6.20 (b) shows a penalty of 3.4 dB for both the 40-Gbaud coarse WDM and the 160-Gbaud AO-OFDM at $\text{BER} = 3.8 \times 10^{-3}$. The penalty of the AO-OFDM increases to 6 dB at $\text{BER} = 1 \times 10^{-4}$, indicating an error floor. The

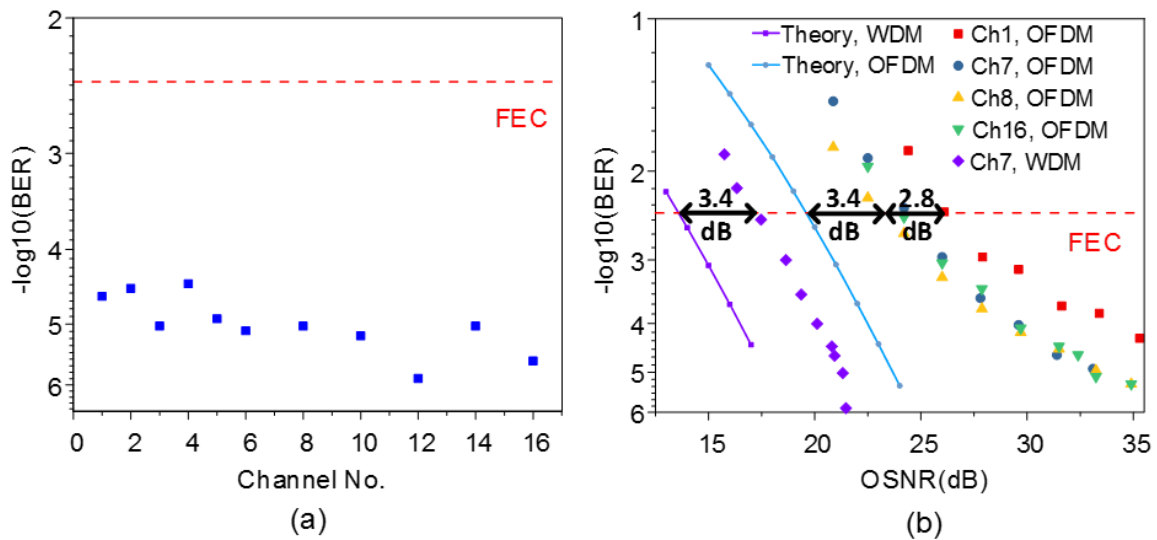


Fig. 6.20 (a) The performances of the 16 subcarriers at 40-dB OSNR. (b) BER versus OSNR plot of the 160-Gbaud OFDM signal and the 40-Gbaud coarse WDM signal.

error floor for the AO-OFDM could be due to a number of factors, related to imperfections in the time-lens [419] or imperfect definition and crosstalk of sub-carrier shaping through WSS2 [420, 421].

6.4 Conclusion

This chapter shows the principle of different time-lens configurations and investigated the degradations of time-lens based systems. Two original works are included. They are time-lens based time-division multiplexing of OFDM symbols and OFDM demultiplexing with a time-lens and optical sinc sampling.

In the time-division multiplexing of OFDM symbols work, through simulation, 1 Tb/s signal was generate by time division multiplexing five temporally compressed 200-Gbps OFDM signals. The compression is achieved by using two time-lens-based Fourier transforms with different chirp rates. In this work, the impact of third-order-dispersion and nonlinear distortion on the performance of time-lens based communication systems was investigated for the first time, using metrics known to communications engineers. The penalties shown in this system stress the need for careful engineering of generic time-lens systems for optical signal processing. Penalties in time-lens systems are often notable, generally resulting in error floors [388, 383, 386].

To avoid error floors due to third-order dispersion in the highly nonlinear fiber, slope vales of $<0.006 \text{ ps/nm}^2/\text{km}$ are required for pump bandwidths approaching or in excess of 1.3-THz. These bandwidths are required when the product of processing signal input bandwidths and spectral magnification factor is greater than 2.6 THz. If significantly lower pump bandwidths are allowed, more conventional HNLFs may be used.

To avoid error floors from nonlinear distortion, signal powers should be at least 20 dB below the pump power. Note that this is well below the pump saturation level of the parametric mixer. The nonlinear mixing stages should be engineered to ensure that TOD is low, and it may be desirable to utilize fiber Bragg gratings or spectral phase filters (such as LCOS based devices) to impart focal group delay dispersion without third-order aberrations.

In the second work of this chapter, a novel AO-OFDM de-multiplexing method based on time-lenses and sinc optical sampling was proposed, with an experimental demonstration of 320-Gbps AO-OFDM demultiplexing. This method avoids the problems of AWG-based OFDM demultiplexers like manufacturing variability. More importantly, this method overcomes the bandwidth limitations of electronic receivers.

However, there are some challenges for applying time-lenses to future communication systems, especially the instability of time-lenses. Each time-lens includes a FWM process

and the FWM process requires proper polarization and timing of the signal and short pulses. However, the fibers in the time-lenses are affected by the temperature and air flow of the environment, which would affect the timing and polarization. For the correct timing, the short pulses should be phase locked with the signal by an electric cord or a phase recovery circuit. In addition, the accumulated dispersion of the dispersive fibers have to be very close to the reciprocal of the chirp rate. However, there are always some variations in the fiber production process. Different fiber lengths need to be tried in order to achieve the right accumulated dispersion. One possible solution is to integrate the whole time-lens on a photonic chip and package it with good shielding from ambient disturbances. Tuning elements should be designed in the chip to alter the accumulated dispersions, so that the numerical conditions of time-lenses can be fulfilled. Since time-lenses need guard intervals, another future work for time-lens based system is to minimize the required guard interval by improving the control pulse shaping technique.

In conclusion, time-lenses can enable ultra-fast Fourier transforms, providing higher operation bandwidth and lower latency than electronic-only signal processing. Compared with using multiple parallel optical-electrical-optical stages to process high-speed OFDM signals, time-lenses are more efficient [422]. As some optical signal processing functions, such as optical sampling [337] and phase regeneration [423], only operate on a single wavelength. Time-lenses enable optical signal processing of WDM signals by converting them to TDM signals. For example, Guan [424] proposed a scalable WDM phase regeneration in a single phase-sensitive amplifier through optical time lenses. If the instability problem of time-lenses can be solved by future research, time-lens-based systems can be very useful for ultra-high-speed signal processing in optical communication systems.

Chapter 7

Conclusion

7.1 Achievements and future work

This research has aimed to improve optical communication systems by enhancing or replacing some of the digital signal processing functions with frequency comb-based optical signal processing. Seven original comb-based OSP applications were proposed in this thesis, ranging from single-carrier signal processing to WDM signal processing, from IMDD systems to coherent systems, from transmitter side to receiver side. By taking advantage of the phase coherence and high bandwidth coverage of frequency combs, these OSP-aided systems overcame some limitations of electronics-only signal processing, such as computational latency of high-capacity data, bandwidth limitation of electronic interferences, bandwidth limitation of frequency tracking, frequency mismatch to the WDM grid. By combining OSP with DSP, ultra-high-speed signal processing of broadband WDM signals can be achieved.

The seven original ideas were reported in Chapters 3-6, including a method to change the repetition rate of a frequency comb and six novel applications of frequency combs in the telecommunication systems. These applications were categorized into-optical sampling, WDM aggregation and timelenses. The original ideas reported in this thesis are:

- Optical clock multiplier (Sec. 3.4)
- Optical pre-sampler for Nyquist signal detection in a bandwidth limited receiver (Sec. 4.4.7)
- Optical sampling with noise bandwidth suppression (Sec. 4.5)
- Optical wavelength quantizer (Sec. 5.2)
- Full C-band N-WDM generation on a photonic chip (Sec. 5.3)
- Time-lenses for compression and time division multiplexing of OFDM symbols (Sec. 6.2)
- AO-OFDM demultiplexing based on timelenses and sinc sampling (Sec. 6.3)

The details of the major achievements and future work of these seven original ideas are:

- **Optical clock multiplier**

- ◇ An on-chip comb filter with periodic narrow passbands was proposed for optical clock multiplication.
- ◇ This filter is among the narrowest optical filters and the filter shape enables comb line selection with an order-of-magnitude higher spectral resolution compared with commercial optical filters based on space optics [235, 236].
- ◇ A five-times clock rate multiplication was verified experimentally using this filter.
- ◇ In the future, the robustness of the system can be increased by having all optical functions monolithically integrated into one chip and packaged with good shielding from ambient disturbances.
- ◇ This work was published. Z. Geng, Y. Xie, M. Burla, C. G. H. Roeloffzen, M. Hoekman, L. Zhuang, A. J. Lowery, “Photonic integrated circuit implementation of a sub-GHz-selectivity frequency comb filter for optical clock multiplication,” *Opt. Express* 25 (22), 27635-27645 (2018).

- **Optical pre-sampler for Nyquist signal detection in a bandwidth limited receiver**

- ◇ This work shows that optoelectronic receivers can be enhanced to receive Nyquist signals at a baud rate beyond twice the receiver bandwidth, providing a method to expand data carrying capacity in systems limited by the electronic bandwidth.
- ◇ The simulation shows that a 40-GHz electrical bandwidth receiver can be used to detect a 100-Gbaud Nyquist-OOK signal.
- ◇ The experiment shows a receiver sensitivity improvement of 4 dB through optical pre-sampling, when detecting a 40-Gbps Nyquist-OOK signal with an 18-GHz electrical bandwidth receiver.
- ◇ This work was published. Z. Geng, B. Corcoran, A. Boes, A. Mitchell, L. Zhuang, Y. Xie and A. J. Lowery, “Mitigation of Electrical Bandwidth Limitations using Optical Pre-Sampling,” in *Optical Networking and Communication Conference (OFC)*, Los Angeles, U.S., pp. Tu2I.4 (2017).

- **Optical sampling with noise bandwidth suppression**

- ◇ Most optical sampling with short pulses results in a large noise bandwidth. However, the proposed optical sampling has an integration stage, which provides a precise self-tracking optical sinc-shaped filter to reduce noise bandwidth.
- ◇ The experiment shows the receiver sensitivity improvements of 3 to 8 dB with a 10-Gbaud PAM4 signal at 30 to 14 OSNRs.

- ◇ In future work, the noise-resistant sampler can be used to temporally compress and filter multiple low-speed optical tributaries, so that the compressed tributaries can be time division multiplexed to form a high-speed signal.
- ◇ The integration process may be further optimized to achieve a matched baseband filter in the optical domain. A full noise analysis would be useful to identify the ultimate performance of this system.
- ◇ This work was published. Z. Geng, B. Corcoran, D. Kong, B. Foo and A. Lowery, “Noise Suppression based on All-optical Temporal Integrator,” in CLEO: Science and Innovations, pp. SM1C.2 (2018).

• Optical wavelength quantizer

- ◇ The proposed scheme provides a solution to laser drifting when connecting access networks to core networks, and allows the output frequency to be defined by a filter.
- ◇ Frequency re-quantizing a 10 Gbps OOK signal to a fixed frequency with the incoming frequency drifts from -20 to 30 GHz.
- ◇ In future work, other modulation formats would be used in the experimental demonstration. Simultaneous processing of multiple signals is possible.
- ◇ This work was published. Z. Geng, C. Zhu, B. Corcoran, A. Boes, A. Mitchell, J. Hart, and A. Lowery, “WDM Wavelength Quantizer,” in Asia Communications and Photonics Conference (ACP), Wuhan, China, pp. AF3B.2 (2016).

• Full C-band N-WDM generation on a photonic chip

- ◇ Full C-band coverage is always challenging to achieve due to the wavelength dependence of the material. For the first time, full C-band coverage of the RAMZI based Nyquist-filtering WDM multiplexer is experimentally demonstrated.
- ◇ The experiment shows N-WDM super-channel multiplexing with zero guard-band, 12.5-GHz spacing, and a Q fluctuation <0.3-dB across C-band.
- ◇ The RAMZI interleaver shows the possibility of fabricating chip-scale N-WDM multiplexer.
- ◇ This work was published. Z. Geng, L. Zhuang, B. Corcoran, B. Foo, and A. J. Lowery, “Full C-band Nyquist-WDM Interleaver Chip,” in Optical Networking and Communication Conference (OFC), Los Angeles, America, pp. M2J.6 (2017).

• Time-lenses for compression and time division multiplexing of OFDM symbols

- ◇ Temporal compression and time-division multiplexing of optical OFDM channels was proposed, to provide a 1 Tb/s by the compression of 5×200 Gb/s channels.

- ◇ For the first time, the impact of third-order-dispersion and nonlinear distortion on the performance of time-lens based communication systems are investigated.
- ◇ This work gives designers an indication of which equipment to select and the optimum design of time-lens based systems.
- ◇ This work was published. Z. Geng, B. Corcoran, C. Zhu, and A. Lowery, "Time-lenses for time-division multiplexing of optical OFDM channels," *Opt. Express* 23, 29788-29801 (2015).

- **AO-OFDM demultiplexing based on timelenses and sinc sampling**

- ◇ This work enables the detection of ultra-high speed OFDM signal.
- ◇ The demultiplexing of a 320-Gbps AO-OFDM signal without significant ICI was experimentally demonstrated.
- ◇ The future work for time-lens based system is to minimize the required guard interval by improving the control pulse shaping technique.
- ◇ This work will be submitted as a journal paper. Z. Geng, D. Kong, B. Corcoran, P. Guan, F. D. Ros, E. P. d. Silva, L. K. Oxenløwe, A. J. Lowery, "All-optical OFDM demultiplexing with optical Fourier transform and sinc sampling,"

In conclusion, a combination of simulations and experimental work has illustrated that optical signal processing is a promising technique to process high-data-rate signals. It is possible to build an ultra-high-speed optical communication system with the techniques proposed in this thesis. For example, in the transmitter, broadband optical frequency comb can be used as carriers to generate hundreds of WDM channels with equal frequency spacing. With the on-chip full C-band interleaver, the WDM channels are Nyquist shaped and multiplexed. The WDM signal can be converted to a TDM signal by a time-lens. Optical sampling enables the detection of the high-speed single-carrier optical signal with low-speed ADCs. A conclusion picture of the original work is shown in Fig. 7.1.

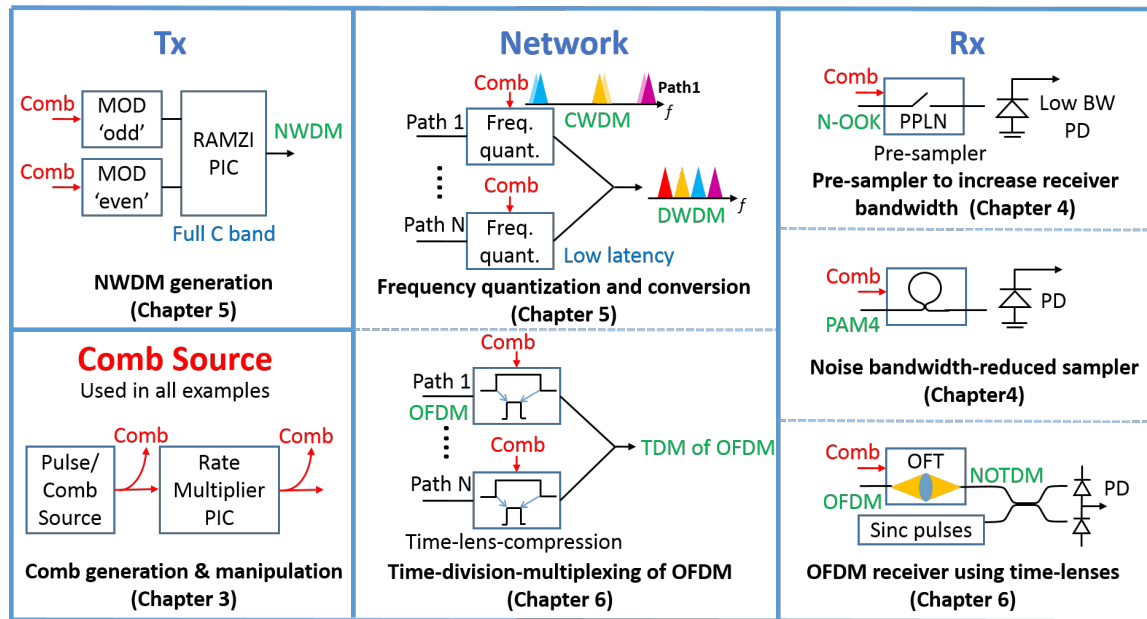


Fig. 7.1 Applications of the work explored in this thesis.

There are four major advantages of all-optical signal processing:

- **High bandwidth**

Most of the commercial O-E-O conversion devices have bandwidths less than 100 GHz, while the available bandwidth for optical communication in a fiber is more than 10 THz. The response times of nonlinear optical processes are in the order of femtosecond, corresponding to a terahertz bandwidth. With proper design and fabrication, passive optical filters on PICs can also operate over terahertz bandwidth. Chapters 3 and 5 show a PIC for processing optical signals over THz of bandwidth.

- **Low latency**

In a WDM system without OSP, key operations like wavelength conversion, switching and regeneration require optical-to-electrical-to-optical (O-E-O) conversion. The conversion process introduces latency to the optical communications systems. Instead of processing the data bit-by-bit using electrical circuits, OSP avoids O-E-O conversion by keeping all the operations in the optical domain. OSP uses the physical effects of the optical devices to process optical signals. Chapter 4 showed a method to overcome limitations in the bandwidth of O-E-O conversion and a low-latency, line-rate method for matching signal wavelengths to defined WDM channels. Chapter 6 demonstrates both multiplexing and demultiplexing of optical OFDM signals, again operating at the line-rate with low-latency.

- **Transparent to modulation formats**

Most all-optical signal processing methods work for various modulation formats. The change of the modulation formats of the incoming signal does not require the OSP part to be changed correspondingly. For example, Shu's group demonstrated SBS-enhanced FWM for polarization division multiplexed signals in coherent communication systems [425]. The FWM process preserves the amplitude, phase and polarization information of the incoming signal. While modulation format independent operations are not always explicitly demonstrated in the work presented in this thesis, most of the applications mentioned are modulation format independent.

- **Five processing dimensions**

In optical communications, the information can be encoded on five dimensions to increase the transmission capacity. They are amplitude, phase, wavelength, polarization and space. OSP can be used to process optical signals in all of these five dimensions, leading to large processing capacity. Here, we process optical intensity in Chapter 4, wavelength in Chapter 5 and use frequency-time symmetry in Chapter 6.

However, for OSP to be useful in practical systems, there are a number of challenges that need to be overcome:

- **Requirements on phase locking and synchronization**

As the relative phase of the two free-running lasers is constantly changing, most OSP experiments are performed using a single optical source or using a RF clock to phase lock different parts of the experimental setup. Therefore, it can be challenging for some OSP applications in the field; for example, to aggregate several low-order modulation signals from different data centers to a high-order modulation signal [56]. While this point is important in assessing the application of OSP to communication systems, this thesis avoids devices and sub-systems that rely on optical phase locking. Timing synchronization is however crucial to a number of the demonstrations presented in this thesis. For example, in Chapter 4, if the clock of the sampling pulse and the signal are not synchronized, there will be an ever-increasing walk-off between the signal and the sampling pulse. As a result, the output of the optical sampling cannot be decoded.

This clock mismatch problem can be solved by using a clock recovery circuit, and high-speed clock recovery is needed to transition our demonstrations toward real-world systems applications. High-speed analogue signal processing circuits are less common in systems applications since the advent of ubiquitous high-speed DSP in optical communication systems. However, if the advantages of OSP begin to outweigh the extra complexity of high-speed analogue circuitry (e.g. enhancing effective receiver bandwidths well beyond O-E device

limits), the applications explored in this thesis may become feasible in a communications context.

• **Instability**

A great portion of the all-optical signal processing is sensitive to polarization and temperature. For example, the response of an on-chip filter made by Si_3N_4 can be tuned by heaters. With proper packaging and use of materials that are less sensitive to the environmental perturbations, these effects can be reduced, and closed-loop control can assist further. Changes to the communication system (e.g. by adding a wavelength quantizer) can also address issues of frequency misalignment, and perhaps frequency combs could be used as frequency references for closed-loop control in the future. Moreover, for non-linear OSP, the FWM process only works when the polarization and timing of the signal and pump are properly aligned. PPLN chips are sensitive to the polarization of the incoming signal. As such, polarization diverse approaches are needed, for which PICs might be a good candidate.

• **Stable, tunable frequency combs**

While there has been significant research into frequency combs, the performance and flexibility required to support OSP applications in optical communications are demanding. This thesis identified the need for a coherent comb that is broadly repetition rate tunable and able to be locked to the timing of an incoming signal at will. This represents a challenge for future work.

7.2 Recent advances in the OSP enabling technologies

Although there are hundreds and thousands of different OSP applications in optical communications, the key enabling technologies of OSP such as nonlinear optics and photonic integrated circuits pave the way for the commercialization of OSP-based optical communication in the future [112]. Low power consumption, dense integration, high bandwidth and great flexibility [426, 105] are desired features of future OSP.

Systems-on-a-chip has reached new heights with publications in Nature and Science. In 2018, dense integration of photonics with silicon nanoelectronics [427] and multidimensional quantum entanglement with large-scale integrated optics [428] are reported. The inclusion of systems-on-a-chip for analogue functions such as clock recovery and closed-loop PIC control could prove a crucial enabler for the communications system applications highlighted in this thesis.

In terms of nonlinear optics, high conversion efficiency and large operation bandwidth are two desired features. Moss's group reported sub-picosecond wavelength conversion via four-wave mixing in a 45-cm long high index doped silica spiral waveguide with a

signal to idler conversion efficiency of + 16.5 dB over 100 nm [429]. Pu reported a 3-mm long dispersion-engineered AlGaAs nano-waveguide for 750 nm ultra-broad wavelength conversion [430]. A wavelength conversion of a 1.28-Tbaud signal was experimentally demonstrated.

On-chip frequency comb generation is a promising technique for broadband WDM transmission and OSP. It replaces hundreds of CW lasers with a single frequency comb source. Also, the optical frequency comb source can be integrated with other functions on photonic chips. In recent years, on-chip Kerr frequency comb generation in ring resonators has attracted extensive research interests [431, 3, 432]. However, the repetition rates of the frequency combs are fixed by the radius of the ring resonators. In 2018, Nagarjun [343] reported on-chip frequency comb generation in C-band with continuously tunable repetition rates from 7.5- to 12.5-GHz, but only 8 comb lines were generated. This low bandwidth frequency comb can be broadened in a highly nonlinear photonic chip. For example, in Hao's paper [264], a coherent optical frequency comb with 44-nm bandwidth was generated by broadening a 3-nm bandwidth comb a non-resonant aluminium-gallium-arsenide-on-insulator (AlGaAsOI) nanowaveguide, whose nonlinear parameter is $660 \text{ W}^{-1}\text{m}^{-1}$. This 44-nm frequency comb was used to demonstrate a 661 Tbit/s space-division multiplexed WDM transmission. As this work highlights, the requirements for such combs are continuously tunable repetition rate, broadband coherent comb lines at required wavelengths, and precise control of pulse timing. With the rapid pace development of new frequency comb technologies, such devices may be available in the near future, and would help enable transition of the work presented in this thesis into real-world applications.

With the advance of the above-mentioned techniques, more and more optical signal processing functions would emerge in commercial ultra-high-speed optical communication systems to enhance or replace electronics-only signal processing.

References

- [1] F. A. Kish, “The past, present, and future of photonic integrated circuits in optical communications,” in “Device Research Conference (DRC),” pp. 23–24.
- [2] X. Chen, S. Chandrasekhar, G. Raybon, S. Olsson, J. Cho, A. Adamiecki, and P. Winzer, “Generation and Intradyne Detection of Single-Wavelength 1.61-Tb/s Using an All-Electronic Digital Band Interleaved Transmitter,” in “Optical Fiber Communication Conference,” (Optical Society of America, 2018), pp. Th4C–1.
- [3] P. Del’Haye, A. Schliesser, O. Arcizet, T. Wilken, R. Holzwarth, and T. J. Kippenberg, “Optical frequency comb generation from a monolithic microresonator,” *Nature* **450**, 1214 (2007).
- [4] J. D. Marconi, M. L. Abbade, C. M. Serpa-Imbett, and E. A. Fagotto, “Ultra-broadband two-pump optical parametric amplifier in tellurite waveguides with engineered dispersion,” *Optics Express* **25**, 4268–4283 (2017).
- [5] F. Idachaba, D. U. Ike, and O. Hope, “Future trends in fiber optics communication,” in “Proc. of the World Congress on Engineering,” (2014), pp. 2–4.
- [6] K. Kao and G. A. Hockham, “Dielectric-fibre surface waveguides for optical frequencies,” in “Proc. Institution of Electrical Engineers,” , vol. 113 (IET, 1966), vol. 113, pp. 1151–1158.
- [7] E. Desurvire, *Erbium-doped fiber amplifiers: principles and applications*, vol. 19 (Wiley New York, 1994).
- [8] O. E. DeLange, “Wide-band optical communication systems: Part II—Frequency-division multiplexing,” *Proc. IEEE* **58**, 1683–1690 (1970).
- [9] C. A. Brackett, “Dense wavelength division multiplexing networks: Principles and applications,” *IEEE J. Sel. Areas in Communications* **8**, 948–964 (1990).
- [10] A. Chraplyvy, A. Gnauck, R. Tkach, J. Zyskind, J. Sulhoff, A. Lucero, Y. Sun, R. Jopson, F. Forghieri, R. Derosier *et al.*, “1-Tb/s transmission experiment,” *IEEE Photon. Technol. Lett.* **8**, 1264–1266 (1996).
- [11] S. J. Savory, “Digital coherent optical receivers: Algorithms and subsystems,” *IEEE J. Sel. Topics in Quantum Electron.* **16**, 1164–1179 (2010).
- [12] S. J. Savory, “Digital filters for coherent optical receivers,” *Opt. Express* **16**, 804–817 (2008).

- [13] X. Li, X. Chen, G. Goldfarb, E. Mateo, I. Kim, F. Yaman, and G. Li, "Electronic post-compensation of WDM transmission impairments using coherent detection and digital signal processing," *Opt. Express* **16**, 880–888 (2008).
- [14] E. M. Ip and J. M. Kahn, "Fiber impairment compensation using coherent detection and digital signal processing," *J. Light. Technol.* **28**, 502–519 (2010).
- [15] A. Sano, T. Kobayashi, S. Yamanaka, A. Matsuura, H. Kawakami, Y. Miyamoto, K. Ishihara, and H. Masuda, "102.3-Tb/s (224×548 -Gb/s) C-and extended L-band all-Raman transmission over 240 km using PDM-64QAM single carrier FDM with digital pilot tone," in "Optical Fiber Communication Conference and National Fiber Optic Engineers Conference (OFC/NFOEC)," (IEEE, 2012), pp. 1–3.
- [16] D. Richardson, J. Fini, and L. Nelson, "Space-division multiplexing in optical fibres," *Nat. Photon.* **7**, 354 (2013).
- [17] B. Puttnam, R. Luís, W. Klaus, J. Sakaguchi, J.-M. D. Mendinueta, Y. Awaji, N. Wada, Y. Tamura, T. Hayashi, M. Hirano *et al.*, "2.15 Pb/s transmission using a 22 core homogeneous single-mode multi-core fiber and wideband optical comb," in "European Conference on Optical Communication (ECOC)," (IEEE, 2015), pp. 1–3.
- [18] Y. Amma, Y. Sasaki, K. Takenaga, S. Matsuo, J. Tu, K. Saitoh, M. Koshiba, T. Morioka, and Y. Miyamoto, "High-density multicore fiber with heterogeneous core arrangement," in "Optical Fiber Communications Conference and Exhibition (OFC)," (IEEE, 2015), pp. 1–3.
- [19] T. Hayashi, Y. Tamura, T. Hasegawa, and T. Taru, "Record-low spatial mode dispersion and ultra-low loss coupled multi-core fiber for ultra-long-haul transmission," *J. Light. Technol.* **35**, 450–457 (2017).
- [20] N. K. Fontaine, R. Ryf, H. Chen, A. V. Benitez, J. A. Lopez, R. A. Correa, B. Guan, B. Ercan, R. P. Scott, S. B. Yoo *et al.*, "30 \times 30 MIMO transmission over 15 spatial modes," in "Optical Fiber Communications Conference and Exhibition (OFC)," (IEEE, 2015), pp. 1–3.
- [21] S. Matsuo, K. Takenaga, Y. Sasaki, Y. Amma, S. Saito, K. Saitoh, T. Matsui, K. Nakajima, T. Mizuno, H. Takara *et al.*, "High-spatial-multiplicity multicore fibers for future dense space-division-multiplexing systems," *J. Light. Technol.* **34**, 1464–1475 (2016).
- [22] D. Soma, Y. Wakayama, S. Beppu, S. Sumita, T. Tsuritani, T. Hayashi, T. Nagashima, M. Suzuki, M. Yoshida, K. Kasai, M. Nakazawa, H. Takahashi, K. Igarashi, I. Morita, and M. Suzuki, "10.16-Peta-B/s Dense SDM/WDM Transmission Over 6-Mode 19-Core Fiber Across the C+L Band," *J. Light. Technol.* **36**, 1362–1368 (2018).
- [23] O. Gerstel, M. Jinno, A. Lord, and S. B. Yoo, "Elastic optical networking: A new dawn for the optical layer?" *IEEE Communications Magazine* **50** (2012).
- [24] S. J. McNab, N. Moll, and Y. A. Vlasov, "Ultra-low loss photonic integrated circuit with membrane-type photonic crystal waveguides," *Opt. Express* **11**, 2927–2939 (2003).

- [25] L. A. Coldren, S. W. Corzine, and M. L. Mashanovitch, *Diode lasers and photonic integrated circuits*, vol. 218 (John Wiley & Sons, 2012).
- [26] C. Laperle and M. O'Sullivan, "Advances in high-speed DACs, ADCs, and DSP for optical coherent transceivers," *J. Light. Technol.* **32**, 629–643 (2014).
- [27] J. L. Jewell, J. Harbison, A. Scherer, Y. Lee, and L. Florez, "Vertical-cavity surface-emitting lasers: design, growth, fabrication, characterization," *IEEE J. Quantum Electron.* **27**, 1332–1346 (1991).
- [28] C. W. Wilmsen, H. Temkin, and L. A. Coldren, "Vertical-cavity surface-emitting lasers," *Vertical-Cavity Surface-Emitting Lasers* p. 474 (1999).
- [29] R. G. Plumb, "Distributed feedback laser," (1989). US Patent 4,813,054.
- [30] H. Kogelnik and C. Shank, "Coupled-wave theory of distributed feedback lasers," *J. Appl. Phys.* **43**, 2327–2335 (1972).
- [31] E. L. Wooten, K. M. Kiss, A. Yi-Yan, E. J. Murphy, D. A. Lafaw, P. F. Hallemeier, D. Maack, D. V. Attanasio, D. J. Fritz, G. J. McBrien *et al.*, "A review of lithium niobate modulators for fiber-optic communications systems," *IEEE J. Sel. Top. Quantum Electron.* **6**, 69–82 (2000).
- [32] H. J. Lee, "Optic repeater system for extending coverage," (2002). US Patent 6,496,290.
- [33] S. M. Park and C. Toumazou, "Low noise current-mode CMOS transimpedance amplifier for giga-bit optical communication," in "Proc. IEEE Intl. Symposium Circuits and Systems," .
- [34] A. E. Willner, S. Khaleghi, M. R. Chitgarha, and O. F. Yilmaz, "All-optical signal processing," *J. Light. Technol.* **32**, 660–680 (2014).
- [35] R. Pyndiah, A. Picart, and A. Glavieux, "Performance of block turbo coded 16-QAM and 64-QAM modulations," in "Global Telecommunications Conference," , vol. 2 (IEEE, 1995), vol. 2, pp. 1039–1043.
- [36] R. v. Nee and R. Prasad, *OFDM for wireless multimedia communications* (Artech House, Inc., 2000).
- [37] G. Bosco, V. Curri, A. Carena, P. Poggiolini, and F. Forghieri, "On the performance of Nyquist-WDM terabit superchannels based on PM-BPSK, PM-QPSK, PM-8QAM or PM-16QAM subcarriers," *J. Light. Technol.* **29**, 53–61 (2011).
- [38] S. J. Savory, G. Gavioli, R. I. Killey, and P. Bayvel, "Electronic compensation of chromatic dispersion using a digital coherent receiver," *Opt. Express* **15**, 2120–2126 (2007).
- [39] E. Ip and J. M. Kahn, "Digital equalization of chromatic dispersion and polarization mode dispersion," *J. Light. Technol.* **25**, 2033–2043 (2007).
- [40] E. Ip and J. M. Kahn, "Compensation of dispersion and nonlinear impairments using digital backpropagation," *J. Light. Technol.* **26**, 3416–3425 (2008).

- [41] M. I. Yousefi and F. R. Kschischang, "Information transmission using the nonlinear Fourier transform, Part I: Mathematical tools," *IEEE Trans. Info. Theory* **60**, 4312–4328 (2014).
- [42] T. Fehenberger, G. Böcherer, A. Alvarado, and N. Hanik, "LDPC coded modulation with probabilistic shaping for optical fiber systems," in "Optical Fiber Communication Conference (OFC)," (Optical Society of America, 2015), pp. Th2A–23.
- [43] A. Mecozzi, C. Antonelli, and M. Shtaif, "Kramers–Kronig coherent receiver," *Optica* **3**, 1220–1227 (2016).
- [44] H. Huang, G. Milione, M. P. Lavery, G. Xie, Y. Ren, Y. Cao, N. Ahmed, T. A. Nguyen, D. A. Nolan, M.-J. Li *et al.*, "Mode division multiplexing using an orbital angular momentum mode sorter and MIMO-DSP over a graded-index few-mode optical fibre," *Scientific Reports* **5**, 14931 (2015).
- [45] M. Horowitz, "1.1 computing's energy problem (and what we can do about it)," in "IEEE Intel. Solid-State Circuits Conference," (IEEE, 2014), pp. 10–14.
- [46] W. Huang, K. Rajamani, M. R. Stan, and K. Skadron, "Scaling with design constraints: Predicting the future of big chips," *IEEE Micro* **31**, 16–29 (2011).
- [47] J. A. H. Victor V. Zhirnov, Ralph K. Cavin and G. I. Bourianoff, "Limits to Binary Logic Switch Scaling-A Gedanken Model," *Proc. IEEE* **91** (2003).
- [48] H. N. Khan, D. A. Hounshell, and E. R. Fuchs, "Science and research policy at the end of Moore's law," *Nat. Electro.* **1**, 14 (2018).
- [49] A. Shacham, K. Bergman, and L. P. Carloni, "Photonic networks-on-chip for future generations of chip multiprocessors," *IEEE Trans. on Computers* **57**, 1246–1260 (2008).
- [50] A. McClelland, V. Fomenko, and E. Borguet, "Ultrafast Time-Evolution of the Non-linear Susceptibility of Hot Carriers at the Ge (111)- GeO₂ Interface As Probed by SHG," *J. Physical Chemistry B* **108**, 3789–3793 (2004).
- [51] J. Shah, "Ultrafast luminescence spectroscopy using sum frequency generation," *IEEE J. Quantum Electron.* **24**, 276–288 (1988).
- [52] A. Owyong, R. Hellwarth, and N. George, "Intensity-induced changes in optical polarizations in glasses," *Physical Review B* **5**, 628 (1972).
- [53] J. S. Levy, A. Gondarenko, M. A. Foster, A. C. Turner-Foster, A. L. Gaeta, and M. Lipson, "CMOS-compatible multiple-wavelength oscillator for on-chip optical interconnects," *Nat. Photon.* **4**, 37 (2010).
- [54] A. Pospischil, M. Humer, M. M. Furchi, D. Bachmann, R. Guider, T. Fromherz, and T. Mueller, "CMOS-compatible graphene photodetector covering all optical communication bands," *Nat. Photon.* **7**, 892 (2013).
- [55] T. Sakamoto, T. Yamamoto, K. Kurokawa, and S. Tomita, "DWDM transmission in O-band over 24 km PCF using optical frequency comb based multicarrier source," *Electron. Lett.* **45**, 850–851 (2009).

- [56] A. Fallahpour, M. Ziyadi, A. Mohajerin-Ariaei, A. Kordts, M. Karpov, M. Pfeiffer, C. Bao, P. Liao, Y. Cao, A. Almain *et al.*, “Experimental generation of a 64-QAM by optically aggregating three independent QPSK channels using nonlinear wave mixing of multiple Kerr Comb lines,” in “CLEO: Applications and Technology,” (Optical Society of America, 2017), pp. JTh2A–59.
- [57] G.-W. Lu, T. Bo, T. Sakamoto, N. Yamamoto, and C. C.-K. Chan, “Flexible and scalable wavelength multicast of coherent optical OFDM with tolerance against pump phase-noise using reconfigurable coherent multi-carrier pumping,” *Opt. Express* **24**, 22573–22580 (2016).
- [58] A. Lorences-Riesgo, M. Mazur, T. A. Eriksson, P. A. Andrekson, and M. Karlsson, “Self-homodyne 24×32 -QAM superchannel receiver enabled by all-optical comb regeneration using brillouin amplification,” *Opt. Express* **24**, 29714–29723 (2016).
- [59] Y. Cao, A. Almain, M. Ziyadi, A. Mohajerin-Ariaei, C. Bao, P. Liao, F. Alishahi, A. Fallahpour, Y. Akasaka, C. Langrock *et al.*, “Reconfigurable channel slicing and stitching for an optical signal to enable fragmented bandwidth allocation using non-linear wave mixing and an optical frequency comb,” *J. Light. Technol.* **36**, 440–446 (2018).
- [60] Z. Geng, Y. Xie, L. Zhuang, M. Burla, M. Hoekman, C. G. Roeloffzen, and A. J. Lowery, “Photonic integrated circuit implementation of a sub-GHz-selectivity frequency comb filter for optical clock multiplication,” *Opt. Express* **25**, 27635–27645 (2017).
- [61] Z. Geng, B. Corcoran, A. Boes, A. Mitchell, L. Zhuang, Y. Xie, and A. J. Lowery, “Mitigation of electrical bandwidth limitations using optical pre-sampling,” in “Optical Fiber Communications Conference and Exhibition (OFC),” (IEEE, 2017), pp. 1–3.
- [62] Z. Geng, B. Corcoran, D. Kong, and A. J. Lowery, “Noise-resistant all-optical sampling based on a temporal integrator,” in “CLEO laser science to photonic applications,” (IEEE, 2018), pp. 1–3.
- [63] Z. Geng, C. Zhu, B. Corcoran, A. Boes, A. Mitchell, J. Hart, and A. Lowery, “WDM Wavelength Quantizer,” in “Asia Communications and Photonics Conference (ACP),” (Optical Society of America, 2016), pp. AF3B–2.
- [64] Z. Geng, L. Zhuang, B. Corcoran, B. Foo, and A. J. Lowery, “Full C-band Nyquist-WDM interleaver chip,” in “Optical Fiber Communications Conference and Exhibition (OFC),” (IEEE, 2017), pp. 1–3.
- [65] Z. Geng, B. Corcoran, C. Zhu, and A. J. Lowery, “Time-lenses for time-division multiplexing of optical OFDM channels,” *Opt. Express* **23**, 29788–29801 (2015).
- [66] J. M. Dudley, G. Genty, and S. Coen, “Supercontinuum generation in photonic crystal fiber,” *Rev. Modern Phys.* **78**, 1135 (2006).
- [67] A. Husakou and J. Herrmann, “Supercontinuum generation of higher-order solitons by fission in photonic crystal fibers,” *Phys. Rev. Lett.* **87**, 203901 (2001).

- [68] M. Settle, R. Engelen, M. Salib, A. Michaeli, L. Kuipers, and T. Krauss, "Flatband slow light in photonic crystals featuring spatial pulse compression and terahertz bandwidth," *Opt. Express* **15**, 219–226 (2007).
- [69] S. Kawanishi, H. Takara, T. Morioka, O. Kamatani, and M. Saruwatari, "200 Gbit/s, 100 km time-division-multiplexed optical transmission using supercontinuum pulses with prescaled PLL timing extraction and all-optical demultiplexing," *Electron. Lett.* **31**, 816–817 (1995).
- [70] B.-E. Olsson and D. J. Blumenthal, "All-optical demultiplexing using fiber cross-phase modulation (XPM) and optical filtering," *IEEE Photon. Technol. Lett.* **13**, 875–877 (2001).
- [71] H. Sotobayashi, C. Sawaguchi, Y. Koyamada, and W. Chujo, "Ultrafast walk-off-free nonlinear optical loop mirror by a simplified configuration for 320-Gbit/s time-division multiplexing signal demultiplexing," *Opt. Lett.* **27**, 1555–1557 (2002).
- [72] J. Li, B.-E. Olsson, M. Karlsson, and P. A. Andrekson, "OTDM demultiplexer based on XPM-induced wavelength shifting in highly nonlinear fiber," in "Optical Fiber Communication Conference," (Optical Society of America, 2003), p. TuH6.
- [73] Y. Fukuchi, T. Sakamoto, K. Taira, and K. Kikuchi, "All-optical time-division demultiplexing of 160 Gbit/s signal using cascaded second-order nonlinear effect in quasi-phase matched LiNbO₃/sub 3/waveguide device," *Electron. Lett.* **39**, 789–790 (2003).
- [74] E. Tangdiongga, Y. Liu, H. De Waardt, G. Khoe, A. Koonen, H. Dorren, X. Shu, and I. Bennion, "All-optical demultiplexing of 640 to 40 Gbits/s using filtered chirp of a semiconductor optical amplifier," *Opt. Lett.* **32**, 835–837 (2007).
- [75] R. A. Fisher, *Optical phase conjugation* (Academic Press, 2012).
- [76] K. Croussore, C. Kim, and G. Li, "All-optical regeneration of differential phase-shift keying signals based on phase-sensitive amplification," *Opt. Lett.* **29**, 2357–2359 (2004).
- [77] V. G. Ta'eed, M. Shokooh-Saremi, L. Fu, I. C. Littler, D. J. Moss, M. Rochette, B. J. Eggleton, Y. Ruan, and B. Luther-Davies, "Self-phase modulation-based integrated optical regeneration in chalcogenide waveguides," *IEEE J. Sel. Top. Quantum Electron.* **12**, 360–370 (2006).
- [78] F. Parmigiani, S. Asimakis, N. Sugimoto, F. Koizumi, P. Petropoulos, and D. J. Richardson, "2R regenerator based on a 2-m-long highly nonlinear bismuth oxide fiber," *Opt. Express* **14**, 5038–5044 (2006).
- [79] P. Mamyshev, "All-optical data regeneration based on self-phase modulation effect," in "Optical Communication, 1998. 24th European Conference on," , vol. 1 (IEEE, 1998), vol. 1, pp. 475–476.
- [80] K. Inoue and H. Toba, "Wavelength conversion experiment using fiber four-wave mixing," *IEEE Photon. Technol. Lett.* **4**, 69–72 (1992).

- [81] B.-E. Olsson, P. Ohlen, L. Rau, and D. J. Blumenthal, "A simple and robust 40-Gb/s wavelength converter using fiber cross-phase modulation and optical filtering," *IEEE Photon. Technol. Lett.* **12**, 846–848 (2000).
- [82] K. Ikeda, J. M. Abdul, S. Namiki, and K.-i. Kitayama, "Optical quantizing and coding for ultrafast A/D conversion using nonlinear fiber-optic switches based on Sagnac interferometer," *Opt. Express* **13**, 4296–4302 (2005).
- [83] B. C. Thomsen, L. P. Barry, J. M. Dudley, and J. D. Harvey, "Ultra-sensitive all-optical sampling at 1.5/spl mu/m using waveguide two-photon absorption," *Electron. Lett.* **35**, 1483–1484 (1999).
- [84] H. Furukawa, H. Takakura, and K. Kuroda, "A novel optical device with wide-bandwidth wavelength conversion and an optical sampling experiment at 200 Gbit/s," *IEEE Trans. Instrumentation and Measurement* **50**, 801–807 (2001).
- [85] J. Hansryd, P. A. Andrekson, M. Westlund, J. Li, and P.-O. Hedekvist, "Fiber-based optical parametric amplifiers and their applications," *IEEE J. Sel. Top. Quantum Electron.* **8**, 506–520 (2002).
- [86] J.-Y. Kim, J.-M. Kang, T.-Y. Kim, and S.-K. Han, "All-optical multiple logic gates with XOR, NOR, OR, and NAND functions using parallel SOA-MZI structures: theory and experiment," *J. Light. Technol.* **24**, 3392 (2006).
- [87] A. Bogoni, L. Poti, R. Proietti, G. Meloni, F. Ponzini, and P. Ghelfi, "Regenerative and reconfigurable all-optical logic gates for ultra-fast applications," *Electron. Lett.* **41**, 435–436 (2005).
- [88] T. Birks, D. Mogilevtsev, J. Knight, and P. S. J. Russell, "Dispersion compensation using single-material fibers," *IEEE Photon. Tech. Lett.* **11**, 674–676 (1999).
- [89] K. Okamoto, K. Takiguchi, and Y. Ohmori, "16-channel optical add/drop multiplexer using silica-based arrayed-waveguide gratings," *Electron. Lett.* **31**, 723–724 (1995).
- [90] B. B. Dingel and M. Izutsu, "Multifunction optical filter with a Michelson–Gires–Tournois interferometer for wavelength-division-multiplexed network system applications," *Opt. Lett.* **23**, 1099–1101 (1998).
- [91] S. Shimizu, G. Cincotti, and N. Wada, "Demonstration and performance investigation of all-optical OFDM systems based on arrayed waveguide gratings," *Opt. Express* **20**, B525–B534 (2012).
- [92] W. Zhang and J. Yao, "Silicon-based integrated microwave photonics," *IEEE J. Quantum Electron.* **52**, 1–12 (2016).
- [93] E. J. Norberg, R. S. Guzzon, S. C. Nicholes, J. S. Parker, and L. A. Coldren, "Programmable photonic lattice filters in InGaAsP–InP," *IEEE Photon. Technol. Lett.* **22**, 109–111 (2010).
- [94] J. S. Fandiño, P. Muñoz, D. Doménech, and J. Capmany, "A monolithic integrated photonic microwave filter," *Nat. Photon.* **11**, 124 (2017).

- [95] L. Zhuang, “Flexible RF filter using a nonuniform SCISSOR,” *Opt. Lett.* **41**, 1118–1121 (2016).
- [96] W. R. Clements, P. C. Humphreys, B. J. Metcalf, W. S. Kolthammer, and I. A. Walsmley, “Optimal design for universal multiport interferometers,” *Optica* **3**, 1460–1465 (2016).
- [97] K. Suzuki, K. Tanizawa, S. Suda, H. Matsuura, T. Inoue, K. Ikeda, S. Namiki, and H. Kawashima, “Broadband silicon photonics 8×8 switch based on double-Mach-Zehnder element switches,” *Opt. Express* **25**, 7538–7546 (2017).
- [98] K. Tanizawa, K. Suzuki, M. Toyama, M. Ohtsuka, N. Yokoyama, K. Matsumaro, M. Seki, K. Koshino, T. Sugaya, S. Suda *et al.*, “Ultra-compact 32×32 strictly-non-blocking Si-wire optical switch with fan-out LGA interposer,” *Opt. Express* **23**, 17599–17606 (2015).
- [99] L. Lu, S. Zhao, L. Zhou, D. Li, Z. Li, M. Wang, X. Li, and J. Chen, “ 16×16 non-blocking silicon optical switch based on electro-optic Mach-Zehnder interferometers,” *Opt. Express* **24**, 9295–9307 (2016).
- [100] I. M. Soganci, T. Tanemura, K. A. Williams, N. Calabretta, T. de Vries, E. Smalbrugge, M. K. Smit, H. J. Dorren, and Y. Nakano, “Monolithically Integrated InP 1 16 Optical Switch With Wavelength-Insensitive Operation,” *IEEE Photon. Technol. Lett.* **22**, 143–145 (2010).
- [101] N. C. Harris, G. R. Steinbrecher, M. Prabhu, Y. Lahini, J. Mower, D. Bunandar, C. Chen, F. N. Wong, T. Baehr-Jones, M. Hochberg *et al.*, “Quantum transport simulations in a programmable nanophotonic processor,” *Nat. Photon.* **11**, 447 (2017).
- [102] J. Carolan, C. Harrold, C. Sparrow, E. Martín-López, N. J. Russell, J. W. Silverstone, P. J. Shadbolt, N. Matsuda, M. Oguma, M. Itoh *et al.*, “Universal linear optics,” *Science* **349**, 711–716 (2015).
- [103] D. Pérez, I. Gasulla, and J. Capmany, “Software-defined reconfigurable microwave photonics processor,” *Opt. Express* **23**, 14640–14654 (2015).
- [104] D. A. Miller, “Silicon photonics: Meshing optics with applications,” *Nat. Photon.* **11**, 403 (2017).
- [105] L. Zhuang, C. G. Roeloffzen, M. Hoekman, K. J. Boller, and A. J. Lowery, “Programmable photonic signal processor chip for radiofrequency applications,” *Optica* **2**, 854–859 (2015).
- [106] R. W. Boyd, *Nonlinear optics* (Academic press, 2003).
- [107] e. P. Franken, A. E. Hill, C. e. Peters, and G. Weinreich, “Generation of optical harmonics,” *Phys. Rev. Lett.* **7**, 118 (1961).
- [108] C. Langrock, S. Kumar, J. E. McGeehan, A. Willner, and M. Fejer, “All-optical signal processing using χ (2) nonlinearities in guided-wave devices,” *J. Light. Technol.* **24**, 2579 (2006).

- [109] A. Yariv and P. Yeh, *Optical waves in crystals*, vol. 5 (Wiley New York, 1984).
- [110] G. P. Agrawal, "Nonlinear fiber optics," in "Nonlinear Science at the Dawn of the 21st Century," (Springer, 2000), pp. 195–211.
- [111] S. Radic, "Parametric signal processing," *IEEE J. Sel. Top. Quantum Electron.* **18**, 670–680 (2012).
- [112] J. Leuthold, C. Koos, and W. Freude, "Nonlinear silicon photonics," *Nat. Photon.* **4**, 535 (2010).
- [113] M. A. Foster, A. C. Turner, R. Salem, M. Lipson, and A. L. Gaeta, "Broad-band continuous-wave parametric wavelength conversion in silicon nanowaveguides," *Opt. Express* **15**, 12949–12958 (2007).
- [114] C. Doerr, S. Chandrasekhar, P. Winzer, A. Chraplyvy, A. Gnauck, L. Stulz, R. Pafchek, and E. Burrows, "Simple multichannel optical equalizer mitigating intersymbol interference for 40-Gb/s nonreturn-to-zero signals," *J. Light. Technol.* **22**, 249–256 (2004).
- [115] K. Uchiyama, T. Morioka, M. Saruwatari, M. Asobe, and T. Ohara, "Error free all-optical demultiplexing using a chalcogenide glass fibre based nonlinear optical loop mirror," *Electron. Lett.* **32**, 1601–1602 (1996).
- [116] J. Knight and D. Skryabin, "Nonlinear waveguide optics and photonic crystal fibers," *Opt. Express* **15**, 15365–15376 (2007).
- [117] M. Bass, P. Franken, A. Hill, C. Peters, and G. Weinreich, "Optical mixing," *Phys. Rev. Lett.* **8**, 18 (1962).
- [118] S. Wabnitz and B. J. Eggleton, "All-optical signal processing," *Springer Series in Optical Sciences* **194** (2015).
- [119] R. Eckardt and J. Reintjes, "Phase matching limitations of high efficiency second harmonic generation," *IEEE J. Quantum Electron.* **20**, 1178–1187 (1984).
- [120] O. E. Martinez, "Achromatic phase matching for second harmonic generation of femtosecond pulses," *IEEE J. Quantum Electron.* **25**, 2464–2468 (1989).
- [121] A. Fiore, S. Janz, L. Delobel, P. Van der Meer, P. Bravetti, V. Berger, E. Rosencher, and J. Nagle, "Second-harmonic generation at $\lambda = 1.6 \mu\text{m}$ in AlGaAs/Al₂O₃ waveguides using birefringence phase matching," *App. Phys. Lett.* **72**, 2942–2944 (1998).
- [122] K. Mizuuchi, K. Yamamoto, M. Kato, and H. Sato, "Broadening of the phase-matching bandwidth in quasi-phase-matched second-harmonic generation," *IEEE J. Quantum Electron.* **30**, 1596–1604 (1994).
- [123] J. Armstrong, N. Bloembergen, J. Ducuing, and P. Pershan, "Interactions between light waves in a nonlinear dielectric," *Phys. Rev.* **127**, 1918 (1962).
- [124] R. Das, S. C. Kumar, G. Samanta, and M. Ebrahim-Zadeh, "Broadband, high-power, continuous-wave, mid-infrared source using extended phase-matching bandwidth in MgO: PPLN," *Opt. Lett.* **34**, 3836–3838 (2009).

- [125] J. Webjorn, V. Pruneri, P. S. J. Russell, J. Barr, and D. Hanna, "Quasi-phase-matched blue light generation in bulk lithium niobate, electrically poled via periodic liquid electrodes," *Electron. Lett.* **30**, 894–895 (1994).
- [126] A. Glass, D. Von der Linde, D. Auston, and T. Negran, "Excited state polarization, bulk photovoltaic effect and the photorefractive effect in electrically polarized media," *J. Electron. Mat.* **4**, 915–943 (1975).
- [127] M. Chou, I. Brener, G. Lenz, R. Scotti, E. Chaban, J. Shmulovich, D. Philen, S. Kosinski, K. Parameswaran, and M. Fejer, "Efficient wide-band and tunable midspan spectral inverter using cascaded nonlinearities in LiNbO₃ waveguides," *IEEE Photon. Technol. Lett.* **12**, 82–84 (2000).
- [128] G.-W. Lu, S. Shinada, H. Furukawa, N. Wada, T. Miyazaki, and H. Ito, "160-Gb/s all-optical phase-transparent wavelength conversion through cascaded SFG-DFG in a broadband linear-chirped PPLN waveguide," *Opt. Express* **18**, 6064–6070 (2010).
- [129] M. Cardakli, D. Gurkan, S. Havstad, A. Willner, K. Parameswaran, M. Fejer, and I. Brener, "Tunable all-optical time-slot-interchange and wavelength conversion using difference-frequency-generation and optical buffers," *IEEE Photon. Technol. Lett.* **14**, 200–202 (2002).
- [130] N. Broderick, T. Monro, P. Bennett, and D. Richardson, "Nonlinearity in holey optical fibers: measurement and future opportunities," *Opt. Lett.* **24**, 1395–1397 (1999).
- [131] T. Kato, "Nonlinear Schrödinger equations," in "Schrödinger operators," (Springer, 1989), pp. 218–263.
- [132] R. Stolen and C. Lin, "Self-phase-modulation in silica optical fibers," *Physical Review A* **17**, 1448 (1978).
- [133] S. P. Singh and N. Singh, "Nonlinear effects in optical fibers: Origin, management and applications," *Progress In Electromagnetics Research* **73**, 249–275 (2007).
- [134] R. Hui and M. O'Sullivan, *Fiber optic measurement techniques* (Academic Press, 2009).
- [135] M. F. Ferreira, *Nonlinear effects in optical fibers*, vol. 2 (John Wiley & Sons, 2011).
- [136] T. Inoue, J. Hiroishi, R. Miyabe, N. Kumano, M. Takahashi, M. Sakano, T. Yagi, and Y. Mimura, "Pulse compression techniques using highly nonlinear fibers," in "2007 Conference on Lasers and Electro-Optics (CLEO)," (2007), pp. 1–2.
- [137] J. K. Ranka, R. S. Windeler, and A. J. Stentz, "Visible continuum generation in air-silica microstructure optical fibers with anomalous dispersion at 800 nm," *Opt. Lett.* **25**, 25–27 (2000).
- [138] T. Herr, V. Brasch, J. D. Jost, C. Y. Wang, N. M. Kondratiev, M. L. Gorodetsky, and T. J. Kippenberg, "Temporal solitons in optical microresonators," *Nat. Photon.* **8**, 145 (2014).

- [139] K. Saha, “K. Saha, Y. Okawachi, B. Shim, JS Levy, R. Salem, AR Johnson, MA Foster, MRE Lamont, M. Lipson, and AL Gaeta, Opt. Express 21, 1335 (2013).” Opt. Express **21**, 1335 (2013).
- [140] F. Forghieri, R. Tkach, and A. Chraplyvy, “Fiber nonlinearities and their impact on transmission systems,” Optical Fiber Telecommunications IIIA **1** (1997).
- [141] N. Shibata, R. Braun, and R. Waarts, “Phase-mismatch dependence of efficiency of wave generation through four-wave mixing in a single-mode optical fiber,” IEEE J. Quantum Electron. **23**, 1205–1210 (1987).
- [142] P. Dong, L. Chen, and Y.-k. Chen, “High-speed low-voltage single-drive push-pull silicon Mach-Zehnder modulators,” Opt. Express **20**, 6163–6169 (2012).
- [143] W. M. Green, M. J. Rooks, L. Sekaric, and Y. A. Vlasov, “Ultra-compact, low RF power, 10 Gb/s silicon Mach-Zehnder modulator,” Opt. Express **15**, 17106–17113 (2007).
- [144] L. Liao, D. Samara-Rubio, M. Morse, A. Liu, D. Hodge, D. Rubin, U. D. Keil, and T. Franck, “High speed silicon Mach-Zehnder modulator,” Opt. Express **13**, 3129–3135 (2005).
- [145] X. Xiao, H. Xu, X. Li, Z. Li, T. Chu, Y. Yu, and J. Yu, “High-speed, low-loss silicon Mach-Zehnder modulators with doping optimization,” Opt. Express **21**, 4116–4125 (2013).
- [146] K. Oda, N. Takato, H. Toba, and K. Nosu, “A wide-band guided-wave periodic multi/demultiplexer with a ring resonator for optical FDM transmission systems,” J. Light. Technol. **6**, 1016–1023 (1988).
- [147] I. Wolff, “Microstrip bandpass filter using degenerate modes of a microstrip ring resonator,” Electron. Lett. **8**, 302–303 (1972).
- [148] A. Yariv, “Critical coupling and its control in optical waveguide-ring resonator systems,” IEEE Photon. Technol. Lett. **14**, 483–485 (2002).
- [149] M. Matsuo, H. Yabuki, and M. Makimoto, “Dual-mode stepped-impedance ring resonator for bandpass filter applications,” IEEE Trans. Micro. Theory and Tech. **49**, 1235–1240 (2001).
- [150] C. Madsen and J. H. Zhao, “Optical filter design and analysis: A signal processing approach,” Inc. US, New York (1999).
- [151] Y. Neuvo, D. Cheng-Yu, and S. Mitra, “Interpolated finite impulse response filters,” IEEE Trans. Acoustics, Speech, Signal Proc. **32**, 563–570 (1984).
- [152] B. Moslehi, J. W. Goodman, M. Tur, and H. J. Shaw, “Fiber-optic lattice signal processing,” Proc. IEEE **72**, 909–930 (1984).
- [153] K. P. Jackson, S. A. Newton, B. Moslehi, M. Tur, C. C. Cutler, J. W. Goodman, and H. Shaw, “Optical fiber delay-line signal processing,” IEEE Trans. Micro. Theory Tech. **33**, 193–210 (1985).

- [154] Z. MadsenCK, "Optical Filter Design and Analysis: A Signal Processing Approach," (1999).
- [155] K. Jinguji, N. Takato, Y. Hida, T. Kitoh, and M. Kawachi, "Two-port optical wavelength circuits composed of cascaded Mach-Zehnder interferometers with point-symmetrical configurations," *J. Light. Technol.* **14**, 2301–2310 (1996).
- [156] Z. Zhang, B. Dong, H. Li, F. Zhou, H. F. Zhang, and C. Sun, "Theoretical and experimental studies of distance dependent response of micro-ring resonator-based ultrasonic detectors for photoacoustic microscopy," *J. Appl. Phys.* **116**, 144501 (2014).
- [157] J. Ascorbe, J. M. Corres, I. del Villar, F. J. Arregui, and I. R. Matias, "Fabrication of Bragg Gratings on the End Facet of Standard Optical Fibers by Sputtering the Same Material," *J. Light. Technol.* **35**, 212–219 (2017).
- [158] C. M. Bledt, J. E. Melzer, and J. A. Harrington, "Theory and practical considerations of multilayer dielectric thin-film stacks in Ag-coated hollow waveguides," *Appl. Opt.* **53**, A70–A82 (2014).
- [159] B. M. Moslehi and H. J. Shaw, "Cascaded fiber optic lattice filter," (1988). US Patent 4,768,850.
- [160] C. Madsen and G. Lenz, "Optical all-pass filters for phase response design with applications for dispersion compensation," *IEEE Photon. Technol. Lett.* **10**, 994–996 (1998).
- [161] S. Dilwali and G. S. Pandian, "Pulse response of a fiber dispersion equalizing scheme based on an optical resonator," *IEEE Photon. Technol. Lett.* **4**, 942–944 (1992).
- [162] B. E. Little, S. T. Chu, H. A. Haus, J. Foresi, and J.-P. Laine, "Microring resonator channel dropping filters," *J. Light. Technol.* **15**, 998–1005 (1997).
- [163] L. Zhuang, C. Zhu, B. Corcoran, M. Burla, C. G. H. Roeloffzen, A. Leinse, J. Schröder, and A. J. Lowery, "Sub-GHz-resolution C-band Nyquist-filtering interleaver on a high-index-contrast photonic integrated circuit," *Opt. Express* **24**, 5715–5727 (2016).
- [164] M. Hanna, P.-A. Lacourt, S. Poinso, and J. M. Dudley, "Optical pulse generation using soliton-assisted time-lens compression," *Opt. Express* **13**, 1743–1748 (2005).
- [165] H. Hu, J. Yu, L. Zhang, A. Zhang, Y. Li, Y. Jiang, and E. Yang, "Pulse source based on directly modulated laser and phase modulator," *Opt. Express* **15**, 8931–8937 (2007).
- [166] K. Taira and K. Kikuchi, "Subpicosecond pulse generation using an electroabsorption modulator and a double-stage pulse compressor," *IEEE Photon. Technol. Lett.* **15**, 1288–1290 (2003).
- [167] C. Schubert, S. Ferber, M. Kroh, C. Schmidt-Langhorst, R. Ludwig, B. Huttl, R. Kaiser, and H. Weber, "40 GHz semiconductor mode-locked laser pulse source for 160 Gbit/s RZ-DPSK data transmission," in "European Conference on Optical Communication," , vol. 2 (IET, 2005), vol. 2, pp. 167–168.

- [168] J. Li and A. Berntson, "Subpicosecond 40 GHz pulse generation using simultaneous two-arm modulation of a Mach-Zehnder intensity modulator," in "European Conference on Optical Communication (ECOC)," (IEEE, 2008), pp. 1–2.
- [169] T. Otsuji, M. Yaita, T. Nagatsuma, and E. Sano, "10-80-Gb/s highly extinctive electrooptic pulse pattern generation," *IEEE J. Sel. Top. Quantum Electron.* **2**, 643–649 (1996).
- [170] R. Wu, V. Supradeepa, C. M. Long, D. E. Leaird, and A. M. Weiner, "Generation of very flat optical frequency combs from continuous-wave lasers using cascaded intensity and phase modulators driven by tailored radio frequency waveforms," *Opt. Lett.* **35**, 3234–3236 (2010).
- [171] Y. Dou, H. Zhang, and M. Yao, "Generation of flat optical-frequency comb using cascaded intensity and phase modulators," *IEEE Photon. Technol. Lett.* **24**, 727 (2012).
- [172] J. Ye and S. T. Cundiff, *Femtosecond optical frequency comb: principle, operation and applications* (Springer Science & Business Media, 2005).
- [173] N. R. Newbury, "Searching for applications with a fine-tooth comb," *Nat. Photon.* **5**, 186–188 (2011).
- [174] M. A. Soto, M. Alem, M. A. Shoaie, A. Vedadi, C.-S. Brès, L. Thévenaz, and T. Schneider, "Optical sinc-shaped Nyquist pulses of exceptional quality," *Nat. Commun.* **4**, 3898 (2013).
- [175] X. Yi, N. K. Fontaine, R. P. Scott, and S. B. Yoo, "Tb/s coherent optical OFDM systems enabled by optical frequency combs," *J. Light. Technol.* **28**, 2054–2061 (2010).
- [176] T. Bajraszewski, M. Wojtkowski, M. Szkulmowski, A. Szkulmowska, R. Huber, and A. Kowalczyk, "Improved spectral optical coherence tomography using optical frequency comb," *Opt. Express* **16**, 4163–4176 (2008).
- [177] C. She, J. Yu, H. Latifi, and R. Bills, "High-spectral-resolution fluorescence light detection and ranging for mesospheric sodium temperature measurements," *Appl. Opt.* **31**, 2095–2106 (1992).
- [178] A. G. Glenday, C.-H. Li, N. Langellier, G. Chang, L.-J. Chen, G. Furesz, A. A. Zibrov, F. Kärtner, D. F. Phillips, D. Sassellov *et al.*, "Operation of a broadband visible-wavelength astro-comb with a high-resolution astrophysical spectrograph," *Optica* **2**, 250–254 (2015).
- [179] D. F. Phillips, A. G. Glenday, C.-H. Li, C. Cramer, G. Furesz, G. Chang, A. J. Benedick, L.-J. Chen, F. X. Kärtner, S. Korzennik *et al.*, "Calibration of an astrophysical spectrograph below 1 m/s using a laser frequency comb," *Opt. Express* **20**, 13711–13726 (2012).
- [180] Q. Wu and X.-C. Zhang, "Free-space electro-optic sampling of terahertz beams," *Appl. Phys. Lett.* **67**, 3523–3525 (1995).

- [181] M. W. Graham, S.-F. Shi, D. C. Ralph, J. Park, and P. L. McEuen, “Photocurrent measurements of supercollision cooling in graphene,” *Nat. Phys.* **9**, 103 (2013).
- [182] N. Dudovich, D. Oron, and Y. Silberberg, “Single-pulse coherently controlled nonlinear Raman spectroscopy and microscopy,” *Nature* **418**, 512 (2002).
- [183] S. A. Diddams, T. Udem, J. Bergquist, E. Curtis, R. Drullinger, L. Hollberg, W. M. Itano, W. Lee, C. Oates, and K. Vogel, “An optical clock based on a single trapped $^{199}\text{Hg}^+$ ion,” *Science* **293**, 825–828 (2001).
- [184] T. Rosenband, D. Hume, P. Schmidt, C.-W. Chou, A. Brusch, L. Lorini, W. Oskay, R. E. Drullinger, T. M. Fortier, and J. Stalnaker, “Frequency ratio of Al^+ and Hg^+ single-ion optical clocks; metrology at the 17th decimal place,” *Science* **319**, 1808–1812 (2008).
- [185] T. M. Fortier, M. S. Kirchner, F. Quinlan, J. Taylor, J. Bergquist, T. Rosenband, N. Lemke, A. Ludlow, Y. Jiang, and C. Oates, “Generation of ultrastable microwaves via optical frequency division,” *Nat. Photon.* **5**, 425 (2011).
- [186] F. Keilmann, C. Gohle, and R. Holzwarth, “Time-domain mid-infrared frequency-comb spectrometer,” *Opt. Lett.* **29**, 1542–1544 (2004).
- [187] I. Coddington, W. C. Swann, and N. R. Newbury, “Coherent multiheterodyne spectroscopy using stabilized optical frequency combs,” *Phys. Rev. Lett.* **100**, 013902 (2008).
- [188] B. Bernhardt, A. Ozawa, P. Jacquet, M. Jacquety, Y. Kobayashi, T. Udem, R. Holzwarth, G. Guelachvili, T. W. Hänsch, and N. Picqué, “Cavity-enhanced dual-comb spectroscopy,” *Nat. Photon.* **4**, 55 (2010).
- [189] Z. Jiang, C.-B. Huang, D. E. Leaird, and A. M. Weiner, “Optical arbitrary waveform processing of more than 100 spectral comb lines,” *Nat. Photon.* **1**, 463 (2007).
- [190] F. Ferdous, H. Miao, D. E. Leaird, K. Srinivasan, J. Wang, L. Chen, L. T. Varghese, and A. M. Weiner, “Spectral line-by-line pulse shaping of on-chip microresonator frequency combs,” *Nat. Photon.* **5**, 770 (2011).
- [191] W. C. Swann and N. R. Newbury, “Frequency-resolved coherent lidar using a femtosecond fiber laser,” *Opt. Lett.* **31**, 826–828 (2006).
- [192] S. A. Diddams, L. Hollberg, and V. Mbele, “Molecular fingerprinting with the resolved modes of a femtosecond laser frequency comb,” *Nature* **445**, 627 (2007).
- [193] P. J. Delfyett, S. Gee, M.-T. Choi, H. Izadpanah, W. Lee, S. Ozharar, F. Quinlan, and T. Yilmaz, “Optical frequency combs from semiconductor lasers and applications in ultrawideband signal processing and communications,” *J. Light. Technol.* **24**, 2701 (2006).
- [194] J. S. Levy, A. Gondarenko, M. A. Foster, A. C. Turner-Foster, A. L. Gaeta, and M. Lipson, “CMOS-compatible multiple-wavelength oscillator for on-chip optical interconnects,” *Nat. Photon.* **4**, 37 (2010).

- [195] V. Torres and A. M. Weiner, “Optical frequency comb technology for ultra-broadband radio-frequency photonics,” *Laser Photonics Rev.* **8**, 368–393 (2014).
- [196] U. Morgner, F. X. Kartner, S.-H. Cho, Y. Chen, H. A. Haus, J. G. Fujimoto, E. P. Ippen, V. Scheuer, G. Angelow, and T. Tschudi, “Sub-two-cycle pulses from a Kerr-lens mode-locked Ti: sapphire laser,” *Opt. Lett.* **24**, 411–413 (1999).
- [197] A. E. Oehler, T. Sudmeyer, K. J. Weingarten, and U. Keller, “100 GHz passively mode-locked Er: Yb: glass laser at 1.5 μm with 1.6-ps pulses,” *Opt. Express* **16**, 21930–21935 (2008).
- [198] S. Arahira, Y. Matsui, and Y. Ogawa, “Mode-locking at very high repetition rates more than terahertz in passively mode-locked distributed-Bragg-reflector laser diodes,” *IEEE J. Quantum Electron.* **32**, 1211–1224 (1996).
- [199] F. Brunner, E. Innerhofer, S. V. Marchese, T. Sudmeyer, R. Paschotta, T. Usami, H. Ito, S. Kurimura, K. Kitamura, and G. Arisholm, “Powerful red-green-blue laser source pumped with a mode-locked thin disk laser,” *Opt. Lett.* **29**, 1921–1923 (2004).
- [200] J. Pfeifle, V. Vujicic, R. T. Watts, P. C. Schindler, C. Weimann, R. Zhou, W. Freude, L. P. Barry, and C. Koos, “Flexible terabit/s Nyquist-WDM super-channels using a gain-switched comb source,” *Opt. Express* **23**, 724–738 (2015).
- [201] J. Pfeifle, V. Brasch, M. Lauermann, Y. Yu, D. Wegner, T. Herr, K. Hartinger, P. Schindler, J. Li, D. Hillerkuss *et al.*, “Coherent terabit communications with microresonator Kerr frequency combs,” *Nat. Photon.* **8**, 375 (2014).
- [202] C. Weimann, P. Schindler, R. Palmer, S. Wolf, D. Bekele, D. Korn, J. Pfeifle, S. Koeber, R. Schmogrow, L. Alloatti *et al.*, “Silicon-organic hybrid (SOH) frequency comb sources for terabit/s data transmission,” *Opt. Express* **22**, 3629–3637 (2014).
- [203] X. Liu, S. Chandrasekhar, X. Chen, P. Winzer, Y. Pan, T. Taunay, B. Zhu, M. Fishteyn, M. Yan, J. Fini *et al.*, “1.12-Tb/s 32-QAM-OFDM superchannel with 8.6-b/s/Hz intrachannel spectral efficiency and space-division multiplexed transmission with 60-b/s/Hz aggregate spectral efficiency,” *Opt. Express* **19**, B958–B964 (2011).
- [204] J. Yu, Z. Dong, J. Zhang, X. Xiao, H.-C. Chien, and N. Chi, “Generation of coherent and frequency-locked multi-carriers using cascaded phase modulators for 10 Tb/s optical transmission system,” *J. Light. Technol.* **30**, 458–465 (2012).
- [205] V. Ataie, E. Temprana, L. Liu, Y. Myslivets, P. P. Kuo, N. Alic, and S. Radic, “Flex-grid compatible ultra wide frequency comb source for 31.8 Tb/s coherent transmission of 1520 UDWDM channels,” in “Optical Fiber Communication Conference,” (Optical Society of America, 2014), pp. Th5B–7.
- [206] D. Hillerkuss, R. Schmogrow, T. Schellinger, M. Jordan, M. Winter, G. Huber, T. Valaitis, R. Bonk, P. Kleinow, F. Frey *et al.*, “26 Tbit s⁻¹ line-rate super-channel transmission utilizing all-optical fast Fourier transform processing,” *Nat. Photon.* **5**, 364 (2011).

- [207] D. Hillerkuss, R. Schmogrow, M. Meyer, S. Wolf, M. Jordan, P. Kleinow, N. Lindenmann, P. C. Schindler, A. Melikyan, X. Yang *et al.*, “Single-laser 32.5 Tbit/s Nyquist WDM transmission,” *J. Opt. Commun. Netw.* **4**, 715–723 (2012).
- [208] T. Hori, J. Takayanagi, N. Nishizawa, and T. Goto, “Flatly broadened, wideband and low noise supercontinuum generation in highly nonlinear hybrid fiber,” *Opt. Express* **12**, 317–324 (2004).
- [209] W. E. Lamb Jr, “Theory of an optical maser,” *Phys. Rev.* **134**, A1429 (1964).
- [210] H. A. Haus, “Mode-locking of lasers,” *IEEE J. Sel. Top. Quantum Electron.* **6**, 1173–1185 (2000).
- [211] P. Del’Haye, K. Beha, S. B. Papp, and S. A. Diddams, “Self-injection locking and phase-locked states in microresonator-based optical frequency combs,” *Phys. Rev. Lett.* **112**, 043905 (2014).
- [212] H. Zhang, D. Tang, L. Zhao, Q. Bao, and K. Loh, “Large energy mode locking of an erbium-doped fiber laser with atomic layer graphene,” *Opt. Express* **17**, 17630–17635 (2009).
- [213] P. Delfyett, A. Dienes, J. Heritage, M. Hong, and Y. Chang, “Femtosecond hybrid mode-locked semiconductor laser and amplifier dynamics,” *Appl. Phys. B* **58**, 183–195 (1994).
- [214] S. Arahira and Y. Ogawa, “Synchronous mode-locking in passively mode-locked semiconductor laser diodes using optical short pulses repeated at subharmonics of the cavity round-trip frequency,” *IEEE Photon. Technol. Lett.* **8**, 191–193 (1996).
- [215] D. Kuizenga and A. Siegman, “FM and AM mode locking of the homogeneous laser-Part I: Theory,” *IEEE J. Quantum Electron.* **6**, 694–708 (1970).
- [216] E. Gordon and J. Rigden, “The Fabry-Perot Electrooptic Modulator,” *Bell Labs Tech. J.* **42**, 155–179 (1963).
- [217] C. Hönninger, R. Paschotta, F. Morier-Genoud, M. Moser, and U. Keller, “Q-switching stability limits of continuous-wave passive mode locking,” *JOSA B* **16**, 46–56 (1999).
- [218] E. Ippen, C. Shank, and A. Dienes, “Passive mode locking of the cw dye laser,” *Appl. Phys. Lett.* **21**, 348–350 (1972).
- [219] Y. Silberberg, P. Smith, D. Eilenberger, D. Miller, A. Gossard, and W. Wiegmann, “Passive mode locking of a semiconductor diode laser,” *Opt. Lett.* **9**, 507–509 (1984).
- [220] R. Fork, B. Greene, and C. V. Shank, “Generation of optical pulses shorter than 0.1 psec by colliding pulse mode locking,” *Appl. Phys. Lett.* **38**, 671–672 (1981).
- [221] D. J. Jones, S. A. Diddams, J. K. Ranka, A. Stentz, R. S. Windeler, J. L. Hall, and S. T. Cundiff, “Carrier-envelope phase control of femtosecond mode-locked lasers and direct optical frequency synthesis,” *Science* **288**, 635–639 (2000).

- [222] B. R. Washburn, S. A. Diddams, N. R. Newbury, J. W. Nicholson, M. F. Yan, and C. G. Jorgensen, "Phase-locked, erbium-fiber-laser-based frequency comb in the near infrared," *Opt. Lett.* **29**, 250–252 (2004).
- [223] B. Resan, A. Oehler, Z. Zhang, S. Kurmulis, K. Zhou, Q. Wang, M. Mangold, T. Suedmeyer, U. Keller, R. Hogg *et al.*, "10 GHz pulse repetition rate ERGO laser mode-locked by a 1550 nm InAs/GaAs quantum-dot SESAM," in "Quantum Electron. and Laser Science Conference," (Optical Society of America, 2012), pp. JTh2A–23.
- [224] J. N. Kemal, P. Marin-Palomo, K. Merghem, A. Guy, R. Brenot, F. Lelarge, A. Ramdane, S. Randel, W. Freude, C. Koos *et al.*, "32QAM WDM transmission using a quantum-dash passively mode-locked laser with resonant feedback," in "Optical Fiber Communication Conference," (Optical Society of America, 2017), pp. Th5C–3.
- [225] Y. K. Chembo, D. V. Strekalov, and N. Yu, "Spectrum and dynamics of optical frequency combs generated with monolithic whispering gallery mode resonators," *Phys. Rev. Lett.* **104**, 103902 (2010).
- [226] P. Marin-Palomo, J. N. Kemal, M. Karpov, A. Kordts, J. Pfeifle, M. H. Pfeiffer, P. Trocha, S. Wolf, V. Brasch, M. H. Anderson *et al.*, "Microresonator-based solitons for massively parallel coherent optical communications," *Nature* **546**, 274 (2017).
- [227] D. Chen, H. R. Fetterman, A. Chen, W. H. Steier, L. R. Dalton, W. Wang, and Y. Shi, "Demonstration of 110 GHz electro-optic polymer modulators," *Appl. Phys. Lett.* **70**, 3335–3337 (1997).
- [228] A. Godil, B. Auld, and D. Bloom, "Time-lens producing 1.9 ps optical pulses," *Appl. Phys. Lett.* **62**, 1047–1049 (1993).
- [229] P. Guan, K. M. Røge, M. Lillieholm, M. Galili, H. Hu, T. Morioka, and L. K. Oxenløwe, "Time lens-based optical Fourier transformation for all-optical signal processing of spectrally-efficient data," *J. Light. Technol.* **35**, 799–806 (2017).
- [230] B. H. Kolner and M. Nazarathy, "Temporal imaging with a time lens," *Opt. Lett.* **14**, 630–632 (1989).
- [231] H. Murata, A. Morimoto, T. Kobayashi, and S. Yamamoto, "Optical pulse generation by electrooptic-modulation method and its application to integrated ultrashort pulse generators," *IEEE J. Sel. Top. Quantum Electron.* **6**, 1325–1331 (2000).
- [232] T.-A. Liu, N. R. Newbury, and I. Coddington, "Sub-micron absolute distance measurements in sub-millisecond times with dual free-running femtosecond Er fiber-lasers," *Opt. Express* **19**, 18501–18509 (2011).
- [233] B. R. Washburn, S. A. Diddams, N. R. Newbury, J. W. Nicholson, M. F. Yan, and C. G. Jørgensen, "Phase-locked, erbium-fiber-laser-based frequency comb in the near infrared," *Opt. Lett.* **29**, 250–252 (2004).
- [234] H. Jung, C. Xiong, K. Y. Fong, X. Zhang, and H. X. Tang, "Optical frequency comb generation from aluminum nitride microring resonator," *Opt. Lett.* **38**, 2810–2813 (2013).

- [235] X.-L. Wang, J. Ding, W.-J. Ni, C.-S. Guo, and H.-T. Wang, "Generation of arbitrary vector beams with a spatial light modulator and a common path interferometric arrangement," *Opt. Lett.* **32**, 3549–3551 (2007).
- [236] J. Schröder, M. A. Roelens, L. B. Du, A. J. Lowery, S. Frisken, and B. J. Eggleton, "An optical FPGA: Reconfigurable simultaneous multi-output spectral pulse-shaping for linear optical processing," *Opt. Express* **21**, 690–697 (2013).
- [237] W. Bogaerts, D. Taillaert, B. Luyssaert, P. Dumon, J. Van Campenhout, P. Bienstman, D. Van Thourhout, R. Baets, V. Wiaux, and S. Beckx, "Basic structures for photonic integrated circuits in silicon-on-insulator," *Opt. Express* **12**, 1583–1591 (2004).
- [238] C. R. Doerr, "Silicon photonic integration in telecommunications," *Front. Phys.* **3**, 37 (2015).
- [239] M. J. Heck, J. F. Bauters, M. L. Davenport, J. K. Doylend, S. Jain, G. Kurczveil, S. Srinivasan, Y. Tang, and J. E. Bowers, "Hybrid silicon photonic integrated circuit technology," *IEEE J. Sel. Top. Quantum Electron.* **19**, 6100117–6100117 (2013).
- [240] C. G. Roeloffzen, L. Zhuang, C. Taddei, A. Leinse, R. G. Heideman, P. W. van Dijk, R. M. Oldenbeuving, D. A. Marpaung, M. Burla, and K.-J. Boller, "Silicon nitride microwave photonic circuits," *Opt. Express* **21**, 22937–22961 (2013).
- [241] K. Wörhoff, R. G. Heideman, A. Leinse, and M. Hoekman, "TriPleX: a versatile dielectric photonic platform," *Adv. Opt. Technol.* **4**, 189–207 (2015).
- [242] M. Smit, J. Van der Tol, and M. Hill, "Moore's law in photonics," *Laser Photon. Rev.* **6**, 1–13 (2012).
- [243] L. Zhuang, M. Hoekman, W. Beeker, A. Leinse, R. Heideman, P. Dijk, and C. Roeloffzen, "Novel low-loss waveguide delay lines using Vernier ring resonators for on-chip multi- λ microwave photonic signal processors," *Laser Photonics Rev.* **7**, 994–1002 (2013).
- [244] L. Chrostowski, X. Wang, J. Flueckiger, Y. Wu, Y. Wang, and S. T. Fard, "Impact of fabrication non-uniformity on chip-scale silicon photonic integrated circuits," in "Optical Fiber Communication Conference," (Optical Society of America, 2014), pp. Th2A–37.
- [245] O. Schwelb, "Transmission, group delay, and dispersion in single-ring optical resonators and add/drop filters-a tutorial overview," *J. Light. Technol.* **22**, 1380–1394 (2004).
- [246] F. Morichetti, C. Ferrari, A. Canciamilla, and A. Melloni, "The first decade of coupled resonator optical waveguides: bringing slow light to applications," *Laser Photonics Rev.* **6**, 74–96 (2012).
- [247] M. S. Rasras, D. M. Gill, S. S. Patel, K.-Y. Tu, Y.-K. Chen, A. E. White, A. T. Pomerene, D. N. Carothers, M. J. Grove, D. K. Sparacin *et al.*, "Demonstration of a fourth-order pole-zero optical filter integrated using CMOS processes," *J. Light. Technol.* **25**, 87–92 (2007).

- [248] P. Orlandi, F. Morichetti, M. J. Strain, M. Sorel, P. Bassi, and A. Melloni, “Photonic integrated filter with widely tunable bandwidth,” *J. Light. Technol.* **32**, 897–907 (2014).
- [249] R. Rudnick, A. Tolmachev, D. Sinefeld, O. Golani, S. Ben-Ezra, M. Nazarathy, and D. Marom, “Sub-banded/single-sub-carrier drop-demux and flexible spectral shaping with a fine resolution photonic processor,” in “European Conference on Optical Communication (ECOC),” (IEEE, 2014), pp. 1–3.
- [250] T. Goh, M. Itoh, H. Yamazaki, T. Saida, and T. Hashimoto, “Optical Nyquist-filtering multi/demultiplexer with PLC for 1-Tb/s class super-channel transceiver,” in “Optical Fiber Communication Conference,” (Optical Society of America, 2015), pp. Tu3A–5.
- [251] P. Dong, N.-N. Feng, D. Feng, W. Qian, H. Liang, D. C. Lee, B. Luff, T. Banwell, A. Agarwal, P. Toliver *et al.*, “GHz-bandwidth optical filters based on high-order silicon ring resonators,” *Opt. Express* **18**, 23784–23789 (2010).
- [252] H. Yu, M. Chen, P. Li, S. Yang, H. Chen, and S. Xie, “Silicon-on-insulator narrow-passband filter based on cascaded MZIs incorporating enhanced FSR for downconverting analog photonic links,” *Opt. Express* **21**, 6749–6755 (2013).
- [253] D.-X. Xu, A. Delâge, R. McKinnon, M. Vachon, R. Ma, J. Lapointe, A. Densmore, P. Cheben, S. Janz, and J. H. Schmid, “Archimedean spiral cavity ring resonators in silicon as ultra-compact optical comb filters,” *Opt. Express* **18**, 1937–1945 (2010).
- [254] S. Ibrahim, N. K. Fontaine, S. S. Djordjevic, B. Guan, T. Su, S. Cheung, R. P. Scott, A. T. Pomerene, L. L. Seaford, C. M. Hill *et al.*, “Demonstration of a fast-reconfigurable silicon CMOS optical lattice filter,” *Opt. Express* **19**, 13245–13256 (2011).
- [255] R. S. Guzzon, E. J. Norberg, J. S. Parker, L. A. Johansson, and L. A. Coldren, “Integrated InP-InGaAsP tunable coupled ring optical bandpass filters with zero insertion loss,” *Opt. Express* **19**, 7816–7826 (2011).
- [256] E. J. Norberg, R. S. Guzzon, J. S. Parker, L. A. Johansson, and L. A. Coldren, “Programmable photonic microwave filters monolithically integrated in InP-InGaAsP,” *J. Light. Technol.* **29**, 1611–1619 (2011).
- [257] N. Hosseini, R. Dekker, M. Hoekman, M. Dekkers, J. Bos, A. Leinse, and R. Heideman, “Stress-optic modulator in TriPleX platform using a piezoelectric lead zirconate titanate (PZT) thin film,” *Opt. Express* **23**, 14018–14026 (2015).
- [258] M. Ayata, Y. Fedoryshyn, W. Heni, B. Baeuerle, A. Josten, M. Zahner, U. Koch, Y. Salamin, C. Hoessbacher, C. Haffner *et al.*, “High-speed plasmonic modulator in a single metal layer,” *Science* **358**, 630–632 (2017).
- [259] I. T. Sorokina, E. Sorokin, and T. Carrig, “Femtosecond pulse generation from a SESAM mode-locked Cr: ZnSe laser,” in “Conf. Lasers and Electro-Optics,” (Optical Society of America, 2006), p. CMQ2.

- [260] A. Fülöp, M. Mazur, A. Lorences-Riesgo, Ó. B. Helgason, P.-H. Wang, Y. Xuan, D. E. Leaird, M. Qi, P. A. Andrekson, A. M. Weiner *et al.*, “High-order coherent communications using mode-locked dark-pulse Kerr combs from microresonators,” *Nat. commun.*, **9**, 1598 (2018).
- [261] V. Brasch, M. Geiselmann, T. Herr, G. Lihachev, M. H. Pfeiffer, M. L. Gorodetsky, and T. J. Kippenberg, “Photonic chip-based optical frequency comb using soliton Cherenkov radiation,” *Science* **351**, 357–360 (2016).
- [262] S.-W. Huang, J. Yang, M. Yu, B. H. McGuyer, D.-L. Kwong, T. Zelevinsky, and C. W. Wong, “A broadband chip-scale optical frequency synthesizer at 2.7×10^{-16} relative uncertainty,” *Sci. Adv.* **2**, e1501489 (2016).
- [263] S. Smirnov, J. Ania-Castanon, T. Ellingham, S. Kobtsev, S. Kukarin, and S. Turitsyn, “Optical spectral broadening and supercontinuum generation in telecom applications,” *Opt. Fiber Technol.* **12**, 122–147 (2006).
- [264] H. Hu, F. Da Ros, M. Pu, F. Ye, K. Ingerslev, E. P. da Silva, M. Nooruzzaman, Y. Amma, Y. Sasaki, T. Mizuno *et al.*, “Single-source chip-based frequency comb enabling extreme parallel data transmission,” *Nat. Photon.* p. 1 (2018).
- [265] G. Berrettini, A. Bogoni, F. Fresi, G. Meloni, and L. Potì, “Evolution of Optical Sampling,” in “Advances in Lasers and Electro Optics,” (InTech, 2010).
- [266] P. Andrekson, “Picosecond optical sampling using four-wave mixing in fibre,” *Electron. Lett.* **27**, 1440–1441 (1991).
- [267] S. Larochelle, Y. Hibino, V. Mizrahi, and G. Stegeman, “All-optical switching of grating transmission using cross-phase modulation in optical fibres,” *Electron. Lett.* **26**, 1459–1460 (1990).
- [268] N. Doran and D. Wood, “Nonlinear-optical loop mirror,” *Opt. Lett.* **13**, 56–58 (1988).
- [269] B. Nelson and N. Doran, “Optical sampling oscilloscope using nonlinear fibre loop mirror,” *Electron. Lett.* **27**, 204–205 (1991).
- [270] J. He and K. Chan, “All-optical actively modelocked fibre ring laser based on cross-gain modulation in SOA,” *Electron. Lett.* **38**, 1504–1505 (2002).
- [271] I. Kang and K. Dreyer, “Sensitive 320 Gbit/s eye diagram measurements via optical sampling with semiconductor optical amplifier-ultrafast nonlinear interferometer,” *Electron. Lett.* **39**, 1081–1083 (2003).
- [272] S. Kodama, T. Shimizu, T. Yoshimatsu, K. Yoshino, T. Furuta, and H. Ito, “Ultrafast optical sampling gate monolithically integrating a PD and EAM,” *Electron. Lett.* **40**, 696–697 (2004).
- [273] H. Takara, S. Kawanishi, A. Yokoo, S. Tomaru, T. Kitoh, and M. Saruwatari, “100 Gbit/s optical signal eye-diagram measurement with optical sampling using organic nonlinear optical crystal,” *Electron. Lett.* **32**, 2256–2258 (1996).

- [274] K. Parameswaran, M. Fujimura, M. Chou, and M. Fejer, "Low-power all-optical gate based on sum frequency mixing in APE waveguides in PPLN," *IEEE Photon. Technol. Lett.* **12**, 654–656 (2000).
- [275] S. Nogiwa, Y. Kawaguchi, H. Ohta, and Y. Endo, "Highly sensitive and time-resolving optical sampling system using thin PPLN crystal," *Electron. Lett.* **36**, 1727–1728 (2000).
- [276] S. Kawanishi, T. Yamamoto, M. Nakazawa, and M. Fejer, "High sensitivity waveform measurement with optical sampling using quasi-phasematched mixing in LiNbO₃/waveguide," *Electron. Lett.* **37**, 842–844 (2001).
- [277] R. Jungerman, G. Lee, O. Buccafusca, Y. Kaneko, N. Itagaki, R. Shioda, A. Harada, Y. Nihei, and G. Sucha, "1-THz bandwidth C- and L-band optical sampling with a bit rate agile timebase," *IEEE Photon. Technol. Lett.* **14**, 1148–1150 (2002).
- [278] A. H. Gnauck, P. J. Winzer, A. Konczykowska, F. Jorge, J.-Y. Dupuy, M. Riet, G. Charlet, B. Zhu, and D. W. Peckham, "Generation and transmission of 21.4-Gbaud PDM 64-QAM using a novel high-power DAC driving a single I/Q modulator," *J. Light. Technol.* **30**, 532–536 (2012).
- [279] P. A. Andrekson and M. Westlund, "Nonlinear optical fiber based high resolution all-optical waveform sampling," *Laser Photon. Rev.* **1**, 231–248 (2007).
- [280] S. Diez, R. Ludwig, C. Schmidt, U. Feiste, and H. Weber, "160-Gb/s optical sampling by gain-transparent four-wave mixing in a semiconductor optical amplifier," *IEEE Photon. Technol. Lett.* **11**, 1402–1404 (1999).
- [281] J. Li, J. Hansryd, P. O. Hedekvist, P. A. Andrekson, and S. N. Knudsen, "300 Gbit/s eye-diagram measurement by optical sampling using fiber based parametric amplification," in "Optical Fiber Communication Conference and Exhibit (OFC)," , vol. 4 (IEEE, 2001), vol. 4, pp. PD31–PD31.
- [282] S. Nogiwa, H. Ohta, Y. Kawaguchi, and Y. Endo, "Improvement of sensitivity in optical sampling system," *Electron. Lett.* **35**, 917–918 (1999).
- [283] R. Liao, Z. Wu, S. Fu, S. Zhu, Z. Yu, M. Tang, and D. Liu, "Fiber optics frequency comb enabled linear optical sampling with operation wavelength range extension," *Opt. Lett.* **43**, 439–442 (2018).
- [284] H. Ohta, N. Banjo, N. Yamada, S. Nogiwa, and Y. Yanagisawa, "Measuring eye diagram of 320 Gbit/s optical signal by optical sampling using passively modelocked fibre laser," *Electron. Lett.* **37**, 1541–1542 (2001).
- [285] R. Gebs, G. Klatt, C. Janke, T. Dekorsy, and A. Bartels, "High-speed asynchronous optical sampling with sub-50fs time resolution," *Opt. Express* **18**, 5974–5983 (2010).
- [286] Y. Liu, F. Qin, Z.-Y. Wei, Q.-B. Meng, D.-Z. Zhang, and Z.-Y. Li, "10 fs ultrafast all-optical switching in polystyrene nonlinear photonic crystals," *Appl. Phys. Lett.* **95**, 131116 (2009).

- [287] S. D. Dods and T. B. Anderson, "Optical performance monitoring technique using delay tap asynchronous waveform sampling," in "Optical Fiber Communication Conference," (Optical Society of America, 2006), p. OThP5.
- [288] Y. Liu, J.-G. Zhang, and W. Zhao, "Design of wideband, high-resolution optical waveform samplers based on a dispersion-flattened highly nonlinear photonic crystal fiber," *J. Opt.* **14**, 055201 (2012).
- [289] H. Sunnerud, M. Sköld, M. Westlund, and P. A. Andrekson, "Characterization of complex optical modulation formats at 100 Gb/s and beyond by coherent optical sampling," *J. Light. Technol.* **30**, 3747–3759 (2012).
- [290] H. Ji, H. Hu, M. Galili, L. K. Oxenløwe, M. Pu, K. Yvind, J. M. Hvam, and P. Jeppesen, "Optical waveform sampling and error-free demultiplexing of 1.28 Tbit/s serial data in a silicon nanowire," in "Optical Fiber Communication (OFC), collocated National Fiber Optic Engineers Conference (OFC/NFOEC)," (IEEE, 2010), pp. 1–3.
- [291] J. Van Erps, F. Luan, M. D. Pelusi, T. Iredale, S. Madden, D.-Y. Choi, D. A. Bulla, B. Luther-Davies, H. Thienpont, and B. J. Eggleton, "High-resolution optical sampling of 640-Gb/s data using four-wave mixing in dispersion-engineered highly nonlinear As₂S₃ planar waveguides," *J. Light. Technol.* **28**, 209–215 (2010).
- [292] M. Duguay and J.-W. Hansen, "An ultrafast light gate," *Appl. Phys. Lett.* **15**, 192–194 (1969).
- [293] T. Kanada and D. L. Franzen, "Optical waveform measurement by optical sampling with a mode-locked laser diode," *Opt. Lett.* **11**, 4–6 (1986).
- [294] S. Nogiwa, N. Yamada, and H. Ohta, "Optical sampling system using a PPLN crystal and wavelength-tunable soliton pulse," in "Lightwave Technologies in Instrumentation and Measurement Conference, 2004. Proceedings of the," (IEEE, 2004), pp. 73–78.
- [295] E. J. Post, "Sagnac effect," *Rev. Mod. Phys.* **39**, 475 (1967).
- [296] S.-C. Lin and T. G. Giallorenzi, "Sensitivity analysis of the Sagnac-effect optical-fiber ring interferometer," *Appl. Opt.* **18**, 915–931 (1979).
- [297] M. Jinno, "Effects of crosstalk and timing jitter on all-optical time-division demultiplexing using a nonlinear fiber sagnac interferometer switch," *IEEE J. Quantum Electron.* **30**, 2842–2853 (1994).
- [298] S.-S. Wang, Z.-F. Hu, Y.-H. Li, and L.-M. Tong, "All-fiber Fabry–Perot resonators based on microfiber Sagnac loop mirrors," *Opt. Lett.* **34**, 253–255 (2009).
- [299] M. Jinno and T. Matsumoto, "Nonlinear Sagnac interferometer switch and its applications," *IEEE J. Quantum Electron.* **28**, 875–882 (1992).
- [300] M. Westlund, M. Sköld, and P. A. Andrekson, "All-optical phase-sensitive waveform sampling at 40 GSymbol/s," in "Optical Fiber Communication Conference," (Optical Society of America, 2008), p. PDP12.

- [301] G. Meloni, A. Bogoni, and L. Potì, "Sub-ps resolution sampler based on FWM effect in Highly Non Linear Fibre," in "Millimeter-Wave and Terahertz Photonics," , vol. 6194 (International Society for Optics and Photonics, 2006), vol. 6194, p. 61940P.
- [302] A. J. Lowery, L. B. Du, and J. Armstrong, "Performance of Optical OFDM in Ultralong-Haul WDM Lightwave Systems," *J. Light. Technol.* **25**, 131–138 (2007).
- [303] G. Bosco, V. Curri, A. Carena, P. Poggiolini, and F. Forghieri, "On the performance of Nyquist-WDM terabit superchannels based on PM-BPSK, PM-QPSK, PM-8QAM or PM-16QAM subcarriers," *J. Light. Technol.* **29**, 53–61 (2011).
- [304] M. Nakazawa, T. Hirooka, P. Ruan, and P. Guan, "Ultrahigh-speed "orthogonal" TDM transmission with an optical Nyquist pulse train," *Opt. Express* **20**, 1129–1140 (2012).
- [305] H. Nyquist, "Certain topics in telegraph transmission theory," *Transactions of the American Institute of Electrical Engineers* **47**, 617–644 (1928).
- [306] G. Bosco, A. Carena, V. Curri, P. Poggiolini, and F. Forghieri, "Performance limits of Nyquist-WDM and CO-OFDM in high-speed PM-QPSK systems," *IEEE Photon. Technol. Lett.* **22**, 1129–1131 (2010).
- [307] S. Kilmurray, T. Fehenberger, P. Bayvel, and R. I. Killey, "Comparison of the nonlinear transmission performance of quasi-Nyquist WDM and reduced guard interval OFDM," *Opt. Express* **20**, 4198–4205 (2012).
- [308] H. N. Tan, T. Inoue, T. Kurosu, and S. Namiki, "Transmission and pass-drop operations of mixed baudrate Nyquist OTDM-WDM signals for all-optical elastic network," *Opt. Express* **21**, 20313–20321 (2013).
- [309] H. N. Tan, T. Inoue, K. Tanizawa, T. Kurosu, and S. Namiki, "All-optical Nyquist filtering for elastic OTDM signals and their spectral defragmentation for inter-datacenter networks," in "European Conference on Optical Communication (ECOC)," (IEEE, 2014), pp. 1–3.
- [310] R. Schmogrow, M. Winter, M. Meyer, D. Hillerkuss, S. Wolf, B. Baeuerle, A. Ludwig, B. Nebendahl, S. Ben-Ezra, J. Meyer *et al.*, "Real-time Nyquist pulse generation beyond 100 Gbit/s and its relation to OFDM," *Opt. Express* **20**, 317–337 (2012).
- [311] M. Yan, Z. Tao, W. Yan, L. Li, T. Hoshida, and J. C. Rasmussen, "Experimental comparison of no-guard-interval-OFDM and Nyquist-WDM superchannels," in "Optical Fiber Communication Conference," (Optical Society of America, 2012), pp. OTh1B–2.
- [312] K. Igarashi, T. Tsuritani, I. Morita, Y. Tsuchida, K. Maeda, M. Tadakuma, T. Saito, K. Watanabe, K. Imamura, R. Sugizaki *et al.*, "Super-Nyquist-WDM transmission over 7,326-km seven-core fiber with capacity-distance product of 1.03 Exabit/s· km," *Opt. Express* **22**, 1220–1228 (2014).
- [313] H. Hu, D. Kong, E. Palushani, J. D. Andersen, A. Rasmussen, B. M. Sørensen, M. Galili, H. C. H. Mulvad, K. J. Larsen, S. Forchhammer *et al.*, "1.28 Tbaud Nyquist signal transmission using time-domain optical Fourier transformation based receiver,"

- in “CLEO: Science and Innovations,” (Optical Society of America, 2013), pp. CTh5D–5.
- [314] B. Corcoran, Z. Geng, V. Rozental, L. Zhuang, M. Lillieholm, and A. Lowery, “Photonic-chip-enabled 25 Tb/s optical superchannel using cyclic spectra,” in “European Conference on Optical Communication (ECOC),” (IEEE, 2017), p. M.1.F.3.
 - [315] J. Zhang, J. Yu, Y. Fang, and N. Chi, “High speed all optical Nyquist signal generation and full-band coherent detection,” *Sci. Rep.* **4**, 6156 (2014).
 - [316] A. J. Lowery, Y. Xie, and C. Zhu, “Systems performance comparison of three all-optical generation schemes for quasi-Nyquist WDM,” *Opt. Express* **23**, 21706–21718 (2015).
 - [317] A. J. Lowery, C. Zhu, E. Viterbo, and B. Corcoran, “All-optical generation of DFT-S-OFDM superchannels using periodic sinc pulses,” *Opt. Express* **22**, 27026–27041 (2014).
 - [318] Z. Li, M. S. Erkilinc, S. Pachnicke, H. Griesser, R. Bouziane, B. C. Thomsen, P. Bayvel, and R. I. Killey, “Signal-signal beat interference cancellation in spectrally-efficient WDM direct-detection Nyquist-pulse-shaped 16-QAM subcarrier modulation,” *Opt. Express* **23**, 23694–23709 (2015).
 - [319] Z. Li, M. S. Erkilinc, L. Galdino, K. Shi, B. C. Thomsen, P. Bayvel, and R. I. Killey, “Comparison of digital signal-signal beat interference compensation techniques in direct-detection subcarrier modulation systems,” *Opt. Express* **24**, 29176–29189 (2016).
 - [320] K. Zou, Y. Zhu, F. Zhang, and Z. Chen, “Spectrally efficient terabit optical transmission with Nyquist 64-QAM half-cycle subcarrier modulation and direct detection,” *Opt. Lett.* **41**, 2767–2770 (2016).
 - [321] M. Zhu, J. Zhang, X. Yi, Y. Song, B. Xu, X. Li, X. Du, and K. Qiu, “Hilbert superposition and modified signal-to-signal beating interference cancellation for single side-band optical NPAM-4 direct-detection system,” *Opt. Express* **25**, 12622–12631 (2017).
 - [322] P. Andrekson, “Picosecond optical sampling using four-wave mixing in fibre,” *Electron. Lett.* **27**, 1440–1441 (1991).
 - [323] M. Westlund, P. A. Andrekson, H. Sunnerud, J. Hansryd, and J. Li, “High-performance optical-fiber-nonlinearity-based optical waveform monitoring,” *J. Light. Technol.* **23**, 2012–2022 (2005).
 - [324] H. Takara, S. Kawanishi, A. Yokoo, S. Tomaru, T. Kitoh, and M. Saruwatari, “100 Gbit/s optical signal eye-diagram measurement with optical sampling using organic nonlinear optical crystal,” *Electron. Lett.* **32**, 2256–2258 (1996).
 - [325] T. Richter, E. Palushani, C. Schmidt-Langhorst, R. Ludwig, L. Molle, M. Nolle, and C. Schubert, “Transmission of single-channel 16-QAM data signals at terabaud symbol rates,” *J. Light. Technol.* **30**, 504–511 (2012).

- [326] J. Schröder, L. B. Du, M. M. Morshed, B. J. Eggleton, and A. J. Lowery, “Colorless flexible signal generator for elastic networks and rapid prototyping,” in “Optical Fiber Communication Conference and Exposition and the National Fiber Optic Engineers Conference (OFC/NFOEC),” (IEEE, 2013), pp. 1–3.
- [327] A. J. Lowery, J. Schröder, and L. B. Du, “Flexible all-optical frequency allocation of OFDM subcarriers,” *Opt. Express* **22**, 1045–1057 (2014).
- [328] B. Corcoran, Z. Geng, V. Rozental, and A. J. Lowery, “Cyclic spectra for wavelength-routed optical networks,” *Opt. Lett.* **42**, 1101–1104 (2017).
- [329] B. Corcoran, C. Zhu, B. Song, and A. J. Lowery, “Folded orthogonal frequency division multiplexing,” *Opt. Express* **24**, 29670–29681 (2016).
- [330] M. M. Strasser, P. J. Winzer, and A. Napoli, “Noise and intersymbol-interference properties of OTDM and ETDM receivers,” *IEEE Photon. technol. lett.* **16**, 248–250 (2004).
- [331] R. Salem, M. A. Foster, A. C. Turner-Foster, D. F. Geraghty, M. Lipson, and A. L. Gaeta, “High-speed optical sampling using a silicon-chip temporal magnifier,” *Opt. Express* **17**, 4324–4329 (2009).
- [332] L. Zhuang, C. Zhu, B. Corcoran, Z. Geng, B. Song, and A. Lowery, “On-chip optical sampling using an integrated SOA-based nonlinear optical loop mirror,” in “European Conference on Optical Communication (ECOC),” (VDE, 2016), pp. 1–3.
- [333] J. K. Fischer, R. Ludwig, L. Molle, C. Schmidt-Langhorst, C. C. Leonhardt, A. Matiss, and C. Schubert, “High-speed digital coherent receiver based on parallel optical sampling,” *J. Light. Technol.* **29**, 378–385 (2011).
- [334] X. Chen, I. Kim, G. Li, H. Zhang, and B. Zhou, “Coherent detection using optical time-domain sampling,” in “Optical Fiber Communication Conference,” (Optical Society of America, 2008), p. JThA62.
- [335] A. O. Wiberg, C.-S. Bres, B. P. Kuo, J. X. Zhao, N. Alic, and S. Radic, “Pedestal-free pulse source for high data rate optical time-division multiplexing based on fiber-optical parametric processes,” *IEEE J. Quantum Electron.* **45**, 1325–1330 (2009).
- [336] M. Nakazawa, T. Yamamoto, and K. Tamura, “1.28 Tbit/s–70 km OTDM transmission using third-and fourth-order simultaneous dispersion compensation with a phase modulator,” *Electron. Lett.* **36**, 2027–2029 (2000).
- [337] J. Li, M. Westlund, H. Sunnerud, B.-E. Olsson, M. Karlsson, and P. A. Andrekson, “0.5-Tb/s eye-diagram measurement by optical sampling using XPM-induced wavelength shifting in highly nonlinear fiber,” *IEEE Photon. Technol. Lett.* **16**, 566–568 (2004).
- [338] D. Kong, Z. Geng, B. Foo, V. Rozental, B. Corcoran, and A. J. Lowery, “All-optical digital-to-analog converter based on cross-phase modulation with temporal integration,” *Opt. Lett.* **42**, 4549–4552 (2017).

- [339] T.-K. Chiang, N. Kagi, M. Marhic, and L. G. Kazovsky, "Cross-phase modulation in fiber links with multiple optical amplifiers and dispersion compensators," *J. Light. Technol.* **14**, 249–260 (1996).
- [340] M. B. Anderson, "Clock recovery circuit," (1999). US Patent 5,987,085.
- [341] A. J. Metcalf, V. T. Company, D. E. Leaird, and A. M. Weiner, "High-power broadly tunable electrooptic frequency comb generator," *IEEE J. Sel. Top. Quantum Electron.* **19**, 231–236 (2013).
- [342] B. R. Washburn, R. W. Fox, N. R. Newbury, J. W. Nicholson, K. Feder, P. S. Westbrook, and C. Jørgensen, "Fiber-laser-based frequency comb with a tunable repetition rate," *Opt. Express* **12**, 4999–5004 (2004).
- [343] K. Nagarjun, V. Jeyaselvan, S. K. Selvaraja, and V. Supradeepa, "Generation of tunable, high repetition rate optical frequency combs using on-chip silicon modulators," *Opt. Express* **26**, 10744–10753 (2018).
- [344] X. Chen, I. Kim, G. Li, H. Zhang, and B. Zhou, "Coherent detection using optical time-domain sampling," in "Optical Fiber Communication Conference," (Optical Society of America, 2008), p. JThA62.
- [345] C. F. Lam, "FTTH Look Ahead-Technologies & Architectures," in "European Conference on Optical Communications (ECOC)," (2010), pp. 1–18.
- [346] M. Funabashi, H. Nasu, T. Mukaihara, T. Kimoto, T. Shinagawa, T. Kise, K. Takaki, T. Takagi, M. Oike, T. Nomura *et al.*, "Recent advances in DFB lasers for ultradense WDM applications," *IEEE J. Sel. Top. Quantum Electron.* **10**, 312–320 (2004).
- [347] G. P. Agrawal and N. K. Dutta, *Semiconductor lasers* (Springer Science & Business Media, 2013).
- [348] G. P. Agrawal, *Lightwave technology: telecommunication systems* (John Wiley & Sons, 2005).
- [349] B. Dahmani, L. Hollberg, and R. Drullinger, "Frequency stabilization of semiconductor lasers by resonant optical feedback," *Opt. Lett.* **12**, 876–878 (1987).
- [350] C. Salomon, D. Hils, and J. Hall, "Laser stabilization at the millihertz level," *JOSA B* **5**, 1576–1587 (1988).
- [351] R. Abel, A. Mohapatra, M. Bason, J. Pritchard, K. Weatherill, U. Raitzsch, and C. Adams, "Laser frequency stabilization to excited state transitions using electromagnetically induced transparency in a cascade system," *Appl. Phys. Lett.* **94**, 071107 (2009).
- [352] I. T. Monroy and E. Tangdiongga, *Crosstalk in WDM communication networks*, vol. 678 (Springer Science & Business Media, 2013).
- [353] H. J. Dutton, *Understanding optical communications* (Prentice Hall PTR Upper Saddle River, NJ, 1998).

- [354] H. Mawatari, M. Fukuda, F. Kano, Y. Tohmori, Y. Yoshikuni, and H. Toba, "Lasing wavelength changes due to degradation in buried heterostructure distributed Bragg reflector lasers," *J. Light. Technol.* **17**, 918 (1999).
- [355] L. Li, Z. Tao, S. Oda, T. Hoshida, and J. C. Rasmussen, "Wide-range, accurate and simple digital frequency offset compensator for optical coherent receivers," in "Optical Fiber communication/National Fiber Optic Engineers Conference (OFC/NFOEC)," (IEEE, 2008), pp. 1–3.
- [356] M. Pelusi, F. Luan, S. Madden, D. Choi, D. Bulla, B. LutherDavies, and B. J. Eggleton, "Wavelength conversion of high-speed phase and intensity modulated signals using a highly nonlinear chalcogenide glass chip," *IEEE Photon. Technol. Lett.* **22**, 3–5 (2010).
- [357] S. Watanabe, T. Kato, R. Okabe, R. Elschner, R. Ludwig, and C. Schubert, "All-optical data frequency multiplexing on single-wavelength carrier light by sequentially provided cross-phase modulation in fiber," *IEEE J. Sel. Top. Quantum Electron.* **18**, 577–584 (2012).
- [358] L. B. Du, J. Schröder, M. M. Morshed, B. Eggleton, and A. J. Lowery, "Optical inverse Fourier transform generated 11.2-Tbit/s no-guard-interval all-optical OFDM transmission," in "Optical Fiber Communication Conference (OFC)," (Optical Society of America, 2013), pp. OW3B–5.
- [359] Z. Jiang, D. E. Leaird, and A. M. Weiner, "Spectral line-by-line pulse shaping," in "Conference on Lasers and Electro-Optics," (Optical Society of America, 2005), p. CWB4.
- [360] K. R. Parameswaran, J. R. Kurz, R. V. Roussev, and M. M. Fejer, "Observation of 99% pump depletion in single-pass second-harmonic generation in a periodically poled lithium niobate waveguide," *Opt. Lett.* **27**, 43–45 (2002).
- [361] M. Westlund, H. Sunnerud, M. Karlsson, and P. A. Andrekson, "Software-synchronized all-optical sampling for fiber communication systems," *J. Light. Technol.* **23**, 1088 (2005).
- [362] T. Umeki, T. Kazama, H. Ono, Y. Miyamoto, and H. Takenouchi, "Spectrally efficient optical phase conjugation based on complementary spectral inversion for nonlinearity mitigation," in "European Conference on Optical Communication (ECOC)," (IEEE, 2015), pp. 1–3.
- [363] B. Corcoran, C. Zhu, J. Schröder, L. Zhuang, B. Foo, M. Burla, W. P. Beeker, A. Leinse, C. G. Roeloffzen, and A. J. Lowery, "Multipass performance of a chip-enhanced WSS for Nyquist-WDM sub-band switching," *J. Light. Technol.* **34**, 1824–1830 (2016).
- [364] Z. Wang, S. Chang, C. Ni, and Y. J. Chen, "A high-performance ultracompact optical interleaver based on double-ring assisted Mach–Zehnder interferometer," *IEEE Photon. Technol. Lett.* **19**, 1072–1074 (2007).
- [365] L. Zhuang, B. Foo, C. Zhu, B. Corcoran, B. Song, and A. J. Lowery, "Ring-based interleaver for Nyquist filtering and WDM multiplexing," in "Optical Fiber Communications Conference and Exhibition (OFC)," (IEEE, 2015), pp. 1–3.

- [366] T. Zhu, Y. Hu, P. Gatkine, S. Veilleux, J. B. Hawthorn, and M. Dagenais, "Ultra-broadband high coupling efficiency fiber-to-waveguide coupler using Si₃N₄/SiO₂ waveguides on silicon," *IEEE Photonics J.* **8**, 1–12 (2016).
- [367] R. Nagarajan, M. Kato, J. Pleumeekers, P. Evans, D. Lambert, A. Chen, V. Dominic, A. Mathur, P. Chavarkar, M. Missey *et al.*, "Single-chip 40-channel InP transmitter photonic integrated circuit capable of aggregate data rate of 1.6 Tbit/s," *Electron. Lett.* **42**, 771–773 (2006).
- [368] A. Sano, T. Kobayashi, K. Ishihara, H. Masuda, S. Yamamoto, K. Mori, E. Yamazaki, E. Yoshida, Y. Miyamoto, T. Yamada *et al.*, "240-Gb/s polarization-multiplexed 64-QAM modulation and blind detection using PLC-LN hybrid integrated modulator and digital coherent receiver," in "European Conference on Optical Communication (ECOC)," , vol. 2009 (IEEE, 2009), vol. 2009, pp. 1–2.
- [369] P. Winzer, A. Gnauck, C. Doerr, M. Magarini, and L. Buhl, "Spectrally efficient long-haul optical networking using 112-Gb/s polarization-multiplexed 16-QAM," *J. Lightwave Technol.* **28**, 547–556 (2010).
- [370] T. Kobayashi, A. Sano, H. Masuda, K. Ishihara, E. Yoshida, Y. Miyamoto, H. Yamazaki, and T. Yamada, "160-Gb/s polarization-multiplexed 16-QAM long-haul transmission over 3,123 km using digital coherent receiver with digital PLL based frequency offset compensator," in "Optical Fiber Communication Conference (OFC)," (Optical Society of America, 2010), p. OTuD1.
- [371] T. Pfau, S. Hoffmann, and R. Noé, "Hardware-efficient coherent digital receiver concept with feedforward carrier recovery for M -QAM constellations," *J. Lightwave Technol.* **27**, 989–999 (2009).
- [372] T. Nakagawa, M. Matsui, T. Kobayashi, K. Ishihara, R. Kudo, M. Mizoguchi, and Y. Miyamoto, "Non-data-aided wide-range frequency offset estimator for QAM optical coherent receivers," in "Optical Fiber communication/National Fiber Optic Engineers Conference (OFC/NFOEC)," (IEEE, 2011), pp. 1–3.
- [373] J. van Howe and C. Xu, "Ultrafast optical signal processing based upon space-time dualities," *J. Light. Technol.* **24**, 2649 (2006).
- [374] B. H. Kolner, "Space-time duality and the theory of temporal imaging," *IEEE J. Quantum Electron.* **30**, 1951–1963 (1994).
- [375] C. V. Bennett and B. H. Kolner, "Aberrations in temporal imaging," *IEEE J. Quantum Electron.* **37**, 20–32 (2001).
- [376] J. van Howe, J. Hansryd, and C. Xu, "Multiwavelength pulse generator using time-lens compression," *Opt. Lett.* **29**, 1470–1472 (2004).
- [377] B. H. Kolner, "Generalization of the concepts of focal length and f-number to space and time," *J. Opt. Soc. Am. A* **11**, 3229–3234 (1994).
- [378] R. Salem, M. A. Foster, A. C. Turner, D. F. Geraghty, M. Lipson, and A. L. Gaeta, "Optical time lens based on four-wave mixing on a silicon chip," *Opt. Lett.* **33**, 1047–1049 (2008).

- [379] H. H. Mulvad, H. Hu, M. Galili, H. Ji, E. Palushani, A. T. Clausen, L. K. Oxenløwe, and P. Jeppesen, "DWDM-to-OTDM conversion by time-domain optical Fourier transformation," in "European Conference and Exhibition on Optical Communication (ECOC)," (IEEE, 2011), pp. 1–3.
- [380] M. A. Foster, R. Salem, D. F. Geraghty, A. C. Turner-Foster, M. Lipson, and A. L. Gaeta, "Silicon-chip-based ultrafast optical oscilloscope," *Nature* **456**, 81 (2008).
- [381] O. Kuzucu, Y. Okawachi, R. Salem, M. A. Foster, A. C. Turner-Foster, M. Lipson, and A. L. Gaeta, "Spectral phase conjugation via temporal imaging," *Opt. Express* **17**, 20605–20614 (2009).
- [382] D. Wang, L. Huo, Y. Xing, X. Jiang, and C. Lou, "Optical Nyquist pulse generation using a time lens with spectral slicing," *Opt. Express* **23**, 4329–4339 (2015).
- [383] P. Guan, D. Kong, K. M. Røge, H. C. H. Mulvad, M. Galili, and L. K. Oxenløwe, "Real-time all-optical OFDM transmission system based on time-domain optical Fourier transformation," in "Optical Fiber Communication Conference," (Optical Society of America, 2014), pp. W4F–1.
- [384] M. A. Foster, R. Salem, Y. Okawachi, A. C. Turner-Foster, M. Lipson, and A. L. Gaeta, "Ultrafast waveform compression using a time-domain telescope," *Nat. Photon.* **3**, 581 (2009).
- [385] J. Lancis, P. Andrés *et al.*, "Spectral imaging system for scaling the power spectrum of optical waveforms," *Opt. Lett.* **32**, 2849–2851 (2007).
- [386] E. Palushani, H. H. Mulvad, D. Kong, P. Guan, M. Galili, and L. K. Oxenløwe, "All-optical OFDM demultiplexing by spectral magnification and band-pass filtering," *Opt. Express* **22**, 136–144 (2014).
- [387] B. Li, C. Zhang, J. Kang, X. Wei, S. Tan, and K. K. Wong, "109 MHz optical tomography using temporal magnification," *Opt. Lett.* **40**, 2965–2968 (2015).
- [388] E. Palushani, H. C. H. Mulvad, M. Galili, H. Hu, L. K. Oxenlowe, A. T. Clausen, and P. Jeppesen, "OTDM-to-WDM conversion based on time-to-frequency mapping by time-domain optical Fourier transformation," *IEEE J. Sel. Top. Quantum Electron.* **18**, 681–688 (2012).
- [389] Y. Xing, Q. Wang, L. Huo, and C. Lou, "Optical time-division demultiplexing using a time-lens-assisted Mach-Zehnder modulator," *IEEE Photon. Technol. Lett.* **25**, 1503–1505 (2013).
- [390] H. Hu, J. L. Areal, H. C. H. Mulvad, M. Galili, K. Dalgaard, E. Palushani, A. T. Clausen, M. S. Berger, P. Jeppesen, and L. K. Oxenlowe, "Synchronization, retiming and OTDM of an asynchronous 10 Gigabit Ethernet NRZ packet using a time lens for Terabit Ethernet," in "European Conference and Exposition on Optical Communications," (Optical Society of America, 2011), pp. Tu–3.

- [391] H. Hu, J. L. Areal, E. Palushani, M. Galili, A. Clausen, M. S. Berger, L. K. Oxenløwe, and P. Jeppesen, "Synchronization and NRZ-to-RZ format conversion of 10 G Ethernet packet based on a time lens," in "Photonics in Switching," (Optical Society of America, 2010), p. PMD2.
- [392] T. Hirooka and M. Nakazawa, "Optical adaptive equalization of high-speed signals using time-domain optical Fourier transformation," *J. Light. Technol.* **24**, 2530 (2006).
- [393] Y. Li, W. Li, F. Ye, C. Wang, D. Liu, B. Huang, and K. Yang, "Experimental implementation of an all-optical OFDM system based on time lens," *Opt. Commun.* **284**, 3983–3989 (2011).
- [394] P. Guan, K. M. Røge, H. C. H. Mulvad, M. Galili, H. Hu, M. Lillieholm, T. Morioka, and L. K. Oxenløwe, "All-optical ultra-high-speed OFDM to Nyquist-WDM conversion based on complete optical Fourier transformation," *J. Light. Technol.* **34**, 626–632 (2016).
- [395] Z. Wu, L. Lei, J. Dong, J. Hou, and X. Zhang, "Reconfigurable temporal Fourier transformation and temporal imaging," *J. Light. Technol.* **32**, 3963–3968 (2014).
- [396] J. Schröder, F. Wang, A. Clarke, E. Ryckeboer, M. Pelusi, M. A. Roelens, and B. J. Eggleton, "Aberration-free ultra-fast optical oscilloscope using a four-wave mixing based time-lens," *Opt. Commun.* **283**, 2611–2614 (2010).
- [397] M. Kauffman, W. Banyai, A. Godil, and D. Bloom, "Time-to-frequency converter for measuring picosecond optical pulses," *Appl. Phys. Lett.* **64**, 270–272 (1994).
- [398] M. Nakazawa and T. Hirooka, "Distortion-free optical transmission using time-domain optical Fourier transformation and transform-limited optical pulses," *J. Opt. Soc. Am. B* **22**, 1842–1855 (2005).
- [399] E. Palushani, L. K. Oxenlowe, M. Galili, H. C. H. Mulvad, A. T. Clausen, and P. Jeppesen, "Flat-top pulse generation by the optical Fourier transform technique for ultrahigh speed signal processing," *IEEE J. Quantum Electron.* **45**, 1317–1324 (2009).
- [400] Y. Okawachi, R. Salem, M. A. Foster, A. C. Turner-Foster, M. Lipson, and A. L. Gaeta, "High-resolution spectroscopy using a frequency magnifier," *Opt. Express* **17**, 5691–5697 (2009).
- [401] P. Guan, S. Lefrancois, M. Lillieholm, H. H. Mulvad, K. M. Røge, H. Hu, J. Schroeder, B. Eggleton, Z. Geng, A. Lowery *et al.*, "All-optical OFDM system using a wavelength selective switch based transmitter and a spectral magnification based receiver," in "European Conference on Optical Communication (ECOC)," (IEEE, 2014), pp. 1–3.
- [402] C. Bennett, R. Scott, and B. Kolner, "Temporal magnification and reversal of 100 Gb/s optical data with an up-conversion time microscope," *Appl. Phys. Lett.* **65**, 2513–2515 (1994).
- [403] A. W. Lohmann and D. Mendlovic, "Temporal filtering with time lenses," *Appl. Opt.* **31**, 6212–6219 (1992).

- [404] H. C. H. Mulvad, E. Palushani, H. Hu, H. Ji, M. Lillieholm, M. Galili, A. T. Clausen, M. Pu, K. Yvind, J. M. Hvam *et al.*, “Ultra-high-speed optical serial-to-parallel data conversion by time-domain optical Fourier transformation in a silicon nanowire,” *Opt. Express* **19**, B825–B835 (2011).
- [405] A. J. Lowery, “Amplified-spontaneous noise limit of optical OFDM lightwave systems,” *Opt. Express* **16**, 860–865 (2008).
- [406] J. Schröder, L. B. Du, J. Carpenter, B. J. Eggleton, and A. J. Lowery, “All-optical OFDM with cyclic prefix insertion using flexible wavelength selective switch optical processing,” *J. Light. Technol.* **32**, 752–759 (2014).
- [407] J. Du and C. Shu, “Cascaded and multisection Sagnac interferometers for scalable and tunable all-optical OFDM DEMUX,” *J. Light. Technol.* **31**, 2307–2313 (2013).
- [408] A. J. Lowery, “Design of arrayed-waveguide grating routers for use as optical OFDM demultiplexers,” *Opt. Express* **18**, 14129–14143 (2010).
- [409] G. Cincotti, “Generalized fiber Fourier optics,” *Opt. Lett.* **36**, 2321–2323 (2011).
- [410] I. Kang, M. Rasras, X. Liu, S. Chandrasekhar, M. Cappuzzo, L. Gomez, Y. Chen, L. Buhl, S. Cabot, and J. Jaques, “All-optical OFDM transmission of 7 x 5-Gb/s data over 84-km standard single-mode fiber without dispersion compensation and time gating using a photonic-integrated optical DFT device,” *Opt. Express* **19**, 9111–9117 (2011).
- [411] W. Bogaerts, M. Fiers, and P. Dumon, “Design challenges in silicon photonics,” *IEEE J. Sel. Top. Quantum Electron.* **20**, 1–8 (2014).
- [412] K. Harako, D. O. Otuya, K. Kasai, T. Hirooka, and M. Nakazawa, “High-performance TDM demultiplexing of coherent Nyquist pulses using time-domain orthogonality,” *Opt. Express* **22**, 29456–29464 (2014).
- [413] D. Kong, J. Zang, M. Yu, Y. Li, S. Zhou, H. Guo, and J. Wu, “A novel detection scheme for Nyquist optical time-division multiplexed signal with coherent matched sampling,” in “Optical Fiber Communication Conference,” (Optical Society of America, 2015), pp. W3C–4.
- [414] H.-G. Weber, R. Ludwig, S. Ferber, C. Schmidt-Langhorst, M. Kroh, V. Marembert, C. Boerner, and C. Schubert, “Ultrahigh-speed OTDM-transmission technology,” *J. Light. Technol.* **24**, 4616–4627 (2006).
- [415] T. Hirooka, D. Seya, K. Harako, D. Suzuki, and M. Nakazawa, “Ultrafast Nyquist OTDM demultiplexing using optical Nyquist pulse sampling in an all-optical nonlinear switch,” *Opt. Express* **23**, 20858–20866 (2015).
- [416] E. Verdurmen, G. Khoe, A. Koonen, and H. De Waardt, “All-optical data format conversion from WDM to OTDM based on FWM,” *Microw. Opt. Technol. Lett.* **48**, 992–994 (2006).

- [417] Z. Wang, K. S. Kravtsov, Y.-K. Huang, and P. R. Prucnal, "Optical FFT/IFFT circuit realization using arrayed waveguide gratings and the applications in all-optical OFDM system," *Opt. Express* **19**, 4501–4512 (2011).
- [418] J. Azaña and M. A. Muriel, "Real-time optical spectrum analysis based on the time-space duality in chirped fiber gratings," *IEEE J. Quantum Electron.* **36**, 517–526 (2000).
- [419] M. Lillieholm, P. Guan, M. Galili, M. Møller-Kristensen, L. Grüner-Nielsen, and L. K. Oxenløwe, "Optimization and characterization of highly nonlinear fiber for broadband optical time lens applications," *Opt. Express* **25**, 12566–12580 (2017).
- [420] T. A. Strasser and J. L. Wagener, "Wavelength-selective switches for ROADMs applications," *IEEE J. Sel. Top. Quantum Electron.* **16**, 1150–1157 (2010).
- [421] S. Tibuleac and M. Filer, "Transmission impairments in DWDM networks with reconfigurable optical add-drop multiplexers," *J. Light. Technol.* **28**, 557–598 (2010).
- [422] H. H. Mulvad, L. Oxenlowe, M. Galili, A. Clausen, L. Gruner-Nielsen, and P. Jeppesen, "1.28 Tbit/s single-polarisation serial OOK optical data generation and demultiplexing," *Electron. Lett.* **45**, 280–281 (2009).
- [423] M. Gao, T. Kurosu, T. Inoue, and S. Namiki, "Efficient phase regeneration of DPSK signal by sideband-assisted dual-pump phase-sensitive amplifier," *Electron. Lett.* **49**, 140–141 (2013).
- [424] P. Guan, F. Da Ros, M. Lillieholm, N.-K. Kjølner, H. Hu, K. M. Røge, M. Galili, T. Morioka, and L. K. Oxenløwe, "Scalable WDM phase regeneration in a single phase-sensitive amplifier through optical time lenses," *Nat. Commun.* **9**, 1049 (2018).
- [425] C. Huang, N. Zhang, and C. Shu, "SBS-enhanced FWM for polarization division multiplexed signals in coherent communication systems," *Opt. Lett.* **42**, 4271–4274 (2017).
- [426] B. Vidal, M. Piqueras, and J. Martí, "Tunable and reconfigurable photonic microwave filter based on stimulated Brillouin scattering," *Opt. Lett.* **32**, 23–25 (2007).
- [427] A. H. Atabaki, S. Moazeni, F. Pavanello, H. Gevorgyan, J. Notaros, L. Alloatti, M. T. Wade, C. Sun, S. A. Kruger, H. Meng *et al.*, "Integrating photonics with silicon nanoelectronics for the next generation of systems on a chip," *Nature* **556**, 349 (2018).
- [428] J. Wang, S. Paesani, Y. Ding, R. Santagati, P. Skrzypczyk, A. Salavrakos, J. Tura, R. Augusiak, L. Mančinska, D. Bacco *et al.*, "Multidimensional quantum entanglement with large-scale integrated optics," *Science* p. 7053 (2018).
- [429] A. Pasquazi, Y. Park, J. Azaña, F. Légaré, R. Morandotti, B. E. Little, S. T. Chu, and D. J. Moss, "Efficient wavelength conversion and net parametric gain via Four Wave Mixing in a high index doped silica waveguide," *Opt. Express* **18**, 7634–7641 (2010).

- [430] M. Pu, H. Hu, L. Ottaviano, E. Semenova, D. Vukovic, L. K. Oxenlowe, and K. Yvind, “AlGaAs-on-insulator nanowire with 750 nm FWM bandwidth, -9 dB CW conversion efficiency, and ultrafast operation enabling record Tbaud wavelength conversion,” in “Optical Fiber Communication Conference (OFC),” (Optical Society of America, 2015), pp. Th5A–3.
- [431] V. Brasch, E. Lucas, J. D. Jost, M. Geiselmann, and T. J. Kippenberg, “Self-referenced photonic chip soliton Kerr frequency comb,” *Light: Science & Applications* **6**, 16202 (2017).
- [432] D. T. Spencer, T. Drake, T. C. Briles, J. Stone, L. C. Sinclair, C. Fredrick, Q. Li, D. Westly, B. R. Ilic, A. Bluestone *et al.*, “An optical-frequency synthesizer using integrated photonics.” *Nature* (2018).

